Substrate Conformal Imprint Lithography for Nanophotonics

Substrate Conformal Imprint Lithography for Nanophotonics

Substraat-Conforme Imprint Lithografie voor Nanofotonica

(met een samenvatting in het Nederlands)

Proefschrift

ter verkrijging van de graad van doctor aan de Universiteit Utrecht
op gezag van de rector magnificus, prof.dr. J.C. Stoof,
ingevolge het besluit van het college voor promoties
in het openbaar te verdedigen
op woensdag 24 maart 2010 des middags te 12.45 uur

door

Marcus Antonius Verschuuren

geboren op 17 september 1977 te Tilburg

Promotor: Prof. Dr. A. Polman
Co-promotor: Dr. H.A. van Sprang

There is plenty of room at the bottom.
Richard P. Feynman, 1959

Contents

Chapter 1

General introduction

Nanotechnology focuses on the fabrication, characterization and modeling of structures and processes on length scales below 100 nm. It is used in almost every scientific discipline. Nanotechnology is driven by the fact that materials often acquire unique properties when structured on the nanometer scale. Over the past decade many new instruments to fabricate nanostructures and study phenomena on the nanoscale have been developed. For example, scanning electron microscopy (SEM), scanning tunneling microscopy (STM), atomic force microscopy (AFM) and near-field scanning optical microscopy (NSOM) have enabled the detailed study of structural, electrical, mechanical and optical phenomena at dimensions down to the nanoscale. These studies of phenomena at the nanometer scale have opened many new application areas.

In research studies, nanostructures are often produced by electron beam lithography (e-beam) or focused ion beam milling (FIB). While e-beam and FIB can generate arbitrary patterns and are well suited to fabricate a limited numbers of samples with a small active area (typically mm^2), these techniques are relatively slow and expensive due to the serial manner in which the patterns are generated. This is a major bottleneck for the application of nano-fabricated structures on an industrial scale as this often requires many square meters of nanopatterns. In contrast, optical lithography is used readily for the fabrication of large-area integrated circuits on an industrial scale. However, this technique is not capable of patterning high density structures with nanoscale features as its resolution is limited to the diffraction limit of light.

Nanoimprinting is a versatile technique for fabricating nanostructures in which a master pattern is replicated via a stamping process, which uses physical contact to mold a material in the inverse shape of the stamp. Nanoimprint technology has the potential to economically deliver large areas of features with dimensions well below 1 micrometer. However, nanoimprint has not been used outside research and development to replicate large-area nanoscale resolution patterns due to intrinsic issues with this contact replication technique.

In this thesis we present Substrate Conformal Imprint Lithography (SCIL) as a novel large area wafer-scale nanoimprint method with nanoscale resolution. We provide a detailed description of the technique, its versatility, and the resolution that can be attained. We apply the SCIL technique in nanophotonics, the research field that studies the control of light at the nanoscale.

We characterize the SCIL technique by studying the optical functionality of nanophotonic devices incorporating nanofeatures made using SCIL. We describe the use of sub-wavelength optical gratings to improve the performance of Vertical Cavity Surface Emitting Lasers (VCSELs), vary the emission pattern of LEDs using photonic crystals, fabricate sub-wavelength hole arrays in metal films with anomalous transmission and improve the efficiency of solar cells by use of soft-imprinted nano-plasmonic back reflectors, all using nanoscale patterns made using SCIL.

In the following section we describe existing nanoimprint methods and discuss the fundamental limitations of these techniques. Next, we present Substrate Conformal Imprint Lithography and show how this technique can be used to pattern large areas with nanometer resolution. We then describe the applications scope of the SCIL technique that enables large-scale production of patterns with nanoscale resolution. In the last section we describe the outline of the thesis.

1.1 Nanoimprint lithography

Nanoimprint lithography was first demonstrated using rigid stamps to hot-emboss polymer layers[1] (NIL) or replicate layers in UV curable resists at room temperature (UV-NIL).[2] In NIL a thin polymer layer is applied on a substrate and heated to above the glass temperature of the polymer, see Fig. 1(a). Then the stamp is pressed into the soft polymer, which flows around the patterns and adopts the inverse shape of the stamp. Next, the stamp and substrate are cooled to below the glass temperature of the polymer after which the stamp is removed from the patterned polymer. In UV-NIL, see Fig. 1(b), a stamp is made from patterned silica glass which is transparent to ultra-violet light. On a substrate a thin layer of UV sensitive liquid organic resist is applied. The silica stamp is pressed in the liquid resist which fills up the features in the stamp. UV light is applied through the stamp onto the resist in which polymer monomers cross linking proceeds. After some time the resist forms a rigid solid and the stamp is released from the patterns. Both NIL and UV-NIL have demonstrated replication of 5-10 nm structures and imprinted areas up to 200 mm diameter.[3-5]

In some applications, multiple layers must be patterned, which necessitates accurate alignment of the layers. NIL uses a large temperature cycling budget which introduces stresses due to the difference in thermal expansion coefficients of the stamp, wafer and imprint tool, which makes accurate overlay alignment almost impossible to achieve. UV-NIL is better suited to achieve
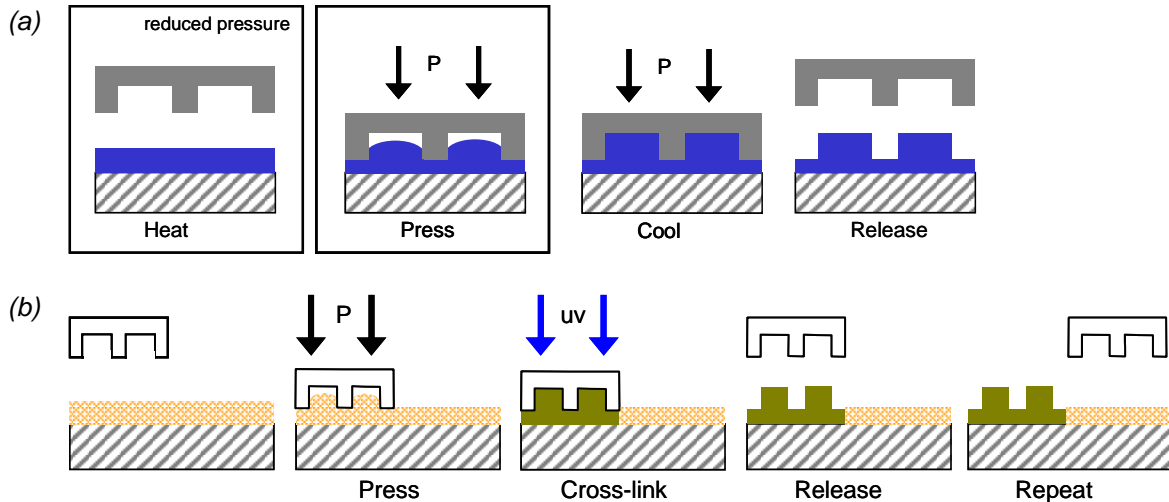
Figure 1. Schematic of nanoimprint (a) and UV-nanoimprint (b) processes.

accurate overlay alignment as it is an isothermal process (except for slight heating due to the absorbed UV light). UV-NIL has shown overlay alignment down to ~15 nm over square cm areas.[6-8]

The advantage of nanoimprinting techniques described above over e-beam lithography and focused ion beam patterning is that it can pattern large areas with nanoscale features. However, the high stiffness of the stamp and use of such a stamp in close proximity to a rigid substrate causes several disadvantages.

- Establishing conformal contact between two rigid plates is difficult as no substrate or stamp is perfectly flat. (Fig. 2(a)) To ensure proper conformal contact and avoid variation in the residual layer thickness requires the use of high imprint pressures (up to 20 bar) in NIL[4,9] or a small stamp area (max. ~8 cm^2) in UV-NIL[5].
- A particle can cause damage to the expensive stamp or substrate and lead to an exclusion area where no patterns are imprinted.[9-12] (Fig. 2(b))
- Features can become partially filled with resist due to the trapping of air inclusions or restricted resist flow.[13-16] (Fig. 2(c))
- Once the resist has hardened the rigid stamp is interlocked with a rigid resist pattern. To initiate release a substantial initial force has to be applied to the stamp. The release front then moves at a high speed which can cause damage to the stamp or imprinted features.[4,10] (Fig. 2(d)) Additionally, lateral movement of the stamp during release can cause additional damage to features in the stamp or resist.
- To prevent chemical adhesion of imprint resist to the stamp a non-stick mono-layer is applied to the stamp. During imprinting this layer wears off or gets damaged.[17-19] This requires the frequent re-application of the non-sticking layer.
- If a stamp becomes contaminated by an imprint defect (particle, resist) it has to be cleaned using harsh chemicals to remove the hardened resist.[19]
- The large thermal budget of NIL and the limited stamp area of UV-NIL limit the throughput, which is a disadvantage for large-area industrial applications.

To avoid some of the disadvantages of having two rigid plates in conformal contact, several possible solutions have been investigated. To maintain the nanometer resolution a relatively thin rigid layer holding the patterns is backed by a somewhat flexible support layer.[20-21] The advantage of this geometry is that the stamp can accommodate to substrate bow and can be removed in a peeling-like manner which reduces the required forces. A different solution that has been developed is to each time mold a new thick semi-rigid polymer stamp from the master using a UV curable liquid resist.[22] This polymer stamp is subsequently used to make one imprint on a wafer after which the stamp is discarded. In this way the master is protected against damage to
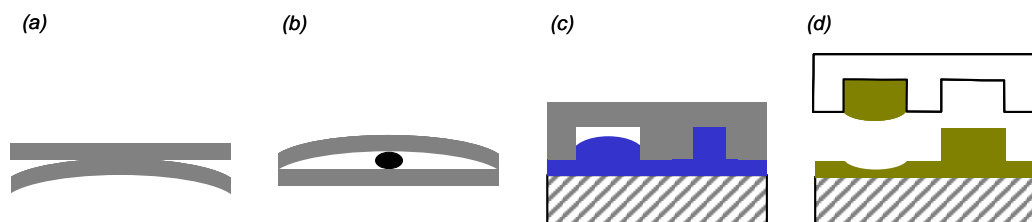
Figure 2. Schematic representation of defects which occur in NIL and UV-NIL nanoimprint. (a) Partial contact of the stamp with the wafer. (b) A particle prevents contact between stamp and substrate over an area many times the particle size. (c) Incomplete filling of features. (d) Breaking of an imprinted resist feature which remains attached to the stamp.

particles. This is a costly solution and furthermore, it still requires high imprint pressures to contact a whole wafer which deforms the stamp and can damage the wafer if particles are present.[9,22] Also, both methods have two rigid interlocking patterns which are sensitive to damage on release of the stamp from the patterned resist and require anti-sticking layers.

While the rigid stamp itself causes several problems as discussed above, the corresponding organic resist or hybrid organic-inorganic materials also have limitations as these materials are not light and temperature stable. Furthermore, they are easily consumed in a reactive ion etch (RIE) process.[23] For these materials to be used as an etch mask and transfer pattern, requires the deposition of extra layer which serve as hard mask before imprinting or an inverse imprint process which covers the imprinted polymer with a silicon containing resist.[4]

Despite the major advances in the field of hard stamp nanoimprint lithography over the last years, the basic problems sketched above have persisted. These have hindered nanoimprint to be used on a large scale outside a research or pre-production environment.

1.2 Soft lithography

As an alternative to (UV-)NIL using hard stamps as discussed above, "soft" lithography has been developed.[24] This technique uses a soft stamp made from a liquid silicone rubber, which is poured over a master pattern and thermally cured at 50 °C to form a rubber, poly-di-methyl-siloxane (PDMS) stamp, which it is peeled from the master. This silicone rubber is transparent for near-UV and visible light and temperature stable up to ~200 °C. A soft stamp can easily make conformal contact over large areas, is less sensitive to damage by particles or stamp release and multiple stamps can be made from one master at low cost.

However, soft stamp cannot be used to imprint features with nanometer resolution as the nanometer sized rubber features are too flexible and collapse under the influence of surface tension.[25-28] Furthermore, the replicated patterns display in-plane distortion due to the elasticity of the stamp.[29,30]

1.3 Substrate Conformal Imprint Lithography

Substrate conformal imprint lithography (SCIL) introduced in this thesis uses a composite stamp composed of two rubber layers on a thin glass support.[31,32] The patterns are molded in a thin layer made from a new type of stiff silicone rubber that we introduce, which allows for accurate replication of nanometer-sized structures. This layer is glued on a thin glass plate by a soft silicone rubber.[33,34] The thin glass is flexible in the out-of-plane direction, which allows conformal contact to be made. The stamp can be removed from the master in a peeling like manner with low force, while the in-plate stiffness of the glass sheet avoids pattern distortions. SCIL combines the resolution and accuracy of rigid stamps with the flexibility of soft stamp methods.

Wafer scale imprints are made using the SCIL setup which uses local pneumatic pressure to stepwise form full contact on a wafer coated with a silica based liquid sol-gel resist. After the resist has hardened the stamp is released in a smooth peeling-like action by a step wise application of vacuum.
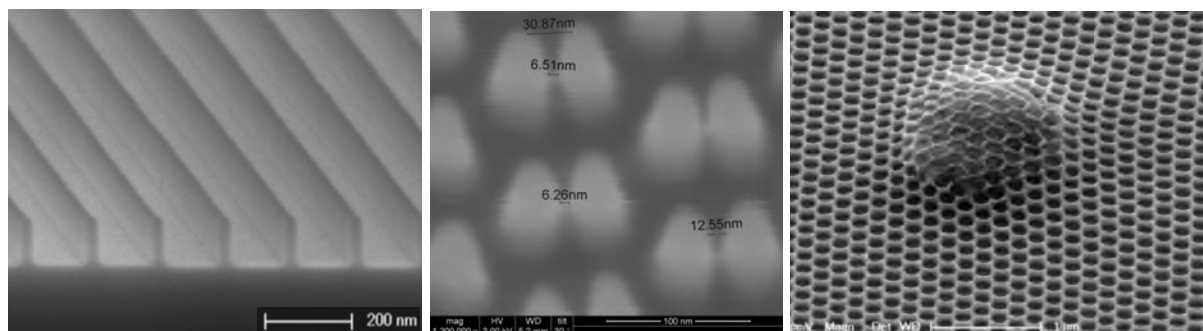
Figure 3. Examples of SCIL imprinted sol-gel patterns that will be discussed in this thesis. From left to right: cross section of 150 nm pitch grating of 25 nm wide, 100 nm high silica lines; sol-gel dots spaced 30 nm apart with a sub 10-nm spacing; and a pattern which is imprinted over a particle contaminant which was present on the substrate, demonstrating substrate conformal imprinting.

The SCIL technology has multiple advantages over methods which use rigid stamps.

- Conformal contact can be made over large areas without the use of a high pressure as the flexible stamp follows the substrate curvature.
- Micro scale air inclusions and partially filled features are avoided as silicone rubber has a high permeability for solvents and gasses which allows trapped air to diffuse into the stamp.[35]
- Particle contaminants are less problematic as the rubber can locally deform around a particle avoiding damage to the stamp or substrate.
- Release of a rubber stamp from a rigid imprinted pattern is aided by the fact that the rubber temporarily deforms on release. This avoids damage to features in the resist or stamp. This enables the replication of features with a high aspect ratio, in contrast to (UV-)NIL in which the aspect ratio is often limited to below 1.[5]
- PDMS has an inherently low surface energy and is chemically non-reactive and therefore an anti-sticking layer is not needed.

An essential advantage of PDMS stamps is that they can be used to pattern fully inorganic material systems. In this thesis we develop a novel inorganic silica forming imprint resist based on the sol-gel route.[36,37] This material allows direct patterning of silicon oxide glass with nanometer resolution. This material can be directly used as hard mask in RIE processes to transfer patterns into an underlying layer with high fidelity. Furthermore, due to the light and temperature stability of imprinted silica it can directly be used in (optical) applications. Figure 3 shows examples of SCIL imprinted sol-gel patterns which demonstrate the high resolution and robustness of the technique introduced in this thesis.

1.4 SCIL application scope

The work in this thesis has been conducted in an industrial research laboratory with a focus on bridging the gap between research and application. As will be shown, the SCIL technology potentially allows economic patterning of high-fidelity patterns with nm resolution over large areas. This is of interest for applications such as photonic crystal LEDs and organic LEDs, lasers and bio-sensors. SCIL enables at the same time the study of fundamental research topics, which are otherwise difficult to study due to the required large area nanopatterns, examples of which are light management in photo-voltaics[38,39], plasmonic phenomena in nanostructured metals [40,41], optical meta-materials, (bio)sensing, optical antenna's, quantum optics and templated nano-wire

growth[42]. Other research areas that require large-area nanostructures and which can benefit from SCIL are discrete magnetic storage[43], integrated photonics, organic electronics, microfluidics and many more.

Applying SCIL to nanophotonics serves two purposes: first of all by integrating nanoscale features using SCIL on optical devices such as LED's, lasers and solar cells we demonstrate the versatility of the SCIL technique. Second, by detailed optical characterization of these imprinted structures, we obtain information on the accuracy and reproducibility of SCIL imprinted patterns.

1.5 Outline of this thesis

This thesis describes experiments and calculations with the aim to understand the underlying processes in SCIL, to demonstrate large-area high-fidelity imprinted structures with nanometer resolution, and to apply this in nanophotonics.

In Chapter 2 we first describe the SCIL soft-nanoimprint process in detail. We introduce a novel silica sol-gel imprint resist and study the sol-gel chemistry for optimal imprint performance. Feature instabilities in soft stamps are modeled and a new soft rubber stamp material is developed which enables sub-10 nm resolution in imprinted sol-gel features. The SCIL imprint technology is explained and characterized. We show that a replicated silica grating with a pitch of 3 µm exhibits an average pitch variation over a 25×25 mm area that is less than 0.1 nm. We demonstrate overlay alignment between two SCIL imprinted layer with an accuracy below 50 nm.

Chapter 3 demonstrates the versatility of the SCIL soft-nanoimprint method demonstrating patterns on a pitch of 30 nm with a spacing as small as 6 nm. Isolated patterns with an aspect ratio up to 5 are also shown. Very wide grating lines with an aspect ratio of 1/640 are demonstrated which are planarized to within 2 nm. We show that imprinted sol-gel patterns can be transferred into underlying materials while maintaining sub-10 nm resolution. Imprinted sol-gel patterns can serve as a hard mask to pattern materials such as silicon, quartz, GaN, and Cr. We demonstrate homogeneously imprinted patterns over 150 mm diameter wafers and use the etch selectivity between the sol-gel silica and silicon to invert the pattern tone on a full wafer scale. Two new methods are demonstrated which allow the patterning of noble metals in particle arrays and sub-wavelength hole arrays. We also demonstrate that SCIL can be used to pattern a non-continuous substrate, by fabricating photonic crystal InGaN LEDs.

In Chapter 4 we demonstrate a relatively simple route towards 3D woodpile type photonic crystals using SCIL. A process is developed in which imprinted silica gratings are made that then are planarized with a polymer by a surface energy driven process. This process is repeated to produce a 3D multi layer structure. After removal of the polymer an open silica four layer woodpile type structure is left with 70 nm wide features on a 240 nm pitch, which is temperature stable up to 1000 °C.

In Chapter 5 we introduce single-mode polarization-stabilized Vertical Cavity Surface Emitting Lasers (VCSELs) which are used for optical motion detection in e.g. laser computer mice and hold future promise for microscale atomic clocks. We study the enhanced polarization stabilization mechanism of an embedded grating in one of the VCSEL laser mirrors. We compare polarization stable VCELs produced by SCIL and e-beam lithography. The SCIL lasers exhibit identical opto-electronic behavior and show that our imprint process has the same high fidelity as conventional e-beam lithography. Furthermore, we use SCIL to produced gratings with a pitch well below the laser wavelength, which cannot economically be produce using e-beam lithography due to the increased writing time. These gratings do not show diffraction and therefore increase the laser efficiency by 29 % compared to conventional diffractive gratings.

Chapter 6 demonstrates a novel fabrication route to large-area arrays of nanoscale holes in a metal film. Hole arrays find application in color filters and (bio)sensors. Optical spectroscopy shows extraordinary transmission peaks attributed to coupling of surface plasmon polaritions to the array. Using multiple sol-gel layers a solid-state index-matched nanohole array is realized which broadens the transmission peaks and further enhances transmission.

Chapter 7 studies the improved red absorption in thin-film hydrogenated amorphous silicon (a-Si:H) solar cells. The solar cells are made on a SCIL-structured silver back reflector as well as a smooth silver mirror for reference. The finished photovoltaic cells have an active silicon layer thickness of 500 nm. The energy conversion efficiency of the patterned cells is 6.2 %, an increase of 26 % over the smooth reference cells. This increase is due to an increased short circuit current, which is due to enhanced absorption in the 600-800 nm wavelength range. The patterned mirror diffracts non-absorbed light into off-normal angles, thereby increasing the optical path length and carrier generation rate in the cell.

In Chapter 8 the performance of ultra-thin silicon solar cells is studied for different plasmonic back reflector mirror geometries. Increasing the performance of ultra-thin silicon solar cells leads to cost savings and moreover, thinner a-Si:H layers suffer less of the Staebler-Wronski photo-degradation mechanism. We use SCIL to pattern substrates which a large variety of nanopatterns on which thin film a-Si:H solar cells are processed with a thickness of 160 and 340 nm. A 160 nm thick silicon cell is also made on randomly textured glass. The best patterned cells with 160 nm thick silicon exhibit an energy conversion efficiency of 6.6 %, equal to that of the best thicker cells and 37.8 % better than flat cells. Crucially, some regular patterns exhibited an improved efficiency over cells made on randomly textured glass, which we attribute to efficient coupling of backscattered light to waveguide modes in the active silicon layer of the cell.

In summary, this thesis demonstrates the top down fabrication of large-area nanoscale patterns by Substrate Conformal Imprint Lithography (SCIL) that are used to demonstrate lasers, LEDs, plasmonic hole arrays and solar cells with improved performance.

References

[1]   S.Y. Chou, P.R. Krauss, and P.J. Renstrom, *Nanoimprint lithography*, J. Vac. Sci. Technol. B **14**, 4129 (1996)

[2]   J. Haisma, M. Verheijen, K. van den Heuvel, and J. van den Berg, *Mold-assisted nanolithography: A process for reliable pattern replication*, J. Vac. Sci. Technol. B **14**, 4124 (1996)

[3]   M.D. Austin, H. Ge, W. Wu, M. Li, Z. Yu, D. Wasserman, S.A. Lyon, and S.Y. Chou, *Fabrication of 5 nm linewidth and 14 nm pitch features by nanoimprint lithography*, Appl. Phys. Lett. **84**, 5299 (2004)

[4]   H. Schift, *Nanoimprint lithography: An old story in modern times? A review*, J. Vac. Sci. Technol. B **26**, 458 (2008)

[5]   T. Balla, S.M. Spearing, and A. Monk, *An assessment of the process capabilities of nanoimprint lithography,* J. Phys. D: Appl. Phys. **41**, 174001 (2008)

[6]   N. Li, W. Wu, and S.Y. Chou, *Sub-20-nm alignment in nanoimprint lithography using Moiré fringe*, Nano Lett. **6**, 2626 (2006)

[7]   I. Yoneda, S. Mikami, T. Ota, T. Koshiba, M. Ito, T. Nakasugi, and T. Higashiki, *Study of nanoimprint applications toward 22nm node CMOS devices*, Proc. of SPIE **6921**, 692104-1 (2008)

[8]   J. Choi, K. Nordquist, A. Cherala, L. Casoose, K. Gehoski, W.J. Dauksher, S.V. Sreenivasan, and D.J. Resnick, *Distortion and overlay performance of UV step and repeat imprint lithography*, Microelectronic Eng. **78–79**, 633 (2005)

[9]   H. Gao, H. Tan, W. Zhang, K. Morton, and S.Y. Chou, *Air cushion press for excellent uniformity, high yield, and fast nanoimprint across a 100 mm field*, Nano Lett. **6**, 2438 (2006)

[10]   L. Chen, X Deng, J. Wang, K. Takahashi, and F. Liud, *Defect control in nanoimprint lithography¸* J. Vac. Sci. Technol. B **23**, 2933 (2005)

[11]   T. Bailey, B. Smith, B.J. Choi, M. Colburn, M. Meissl, S.V. Sreenivasan, J.G. Ekerdt, and C.G. Willson, *Step and flash imprint lithography: Defect analysis*, J. Vac. Sci. Technol. B **19**, 2806 (2001)

[12]   D.J. Resnick, W.J. Dauksher, D. Mancini, K.J. Nordquist, T.C. Bailey, S. Johnson, N. Stacey, J.G. Ekerdt, C.G. Willson, S. V. Sreenivasan, and N. Schumaker, *Imprint lithography for integrated circuit fabrication*, J. Vac. Sci. Technol. B **21**, 2624 (2003)

[13]   D.S. Macintyre, and S. Thoms, *A study of resist flow during nanoimprint lithography*, Microelectronic Eng. **78–79**, 670 (2005)

[14]   S. Reddy, and R.T. Bonnecaze, *Simulation of fluid flow in the step and flash imprint lithography process*, Microelectronic Eng. **82**, 60 (2005)

[15]   H. Schift, G. Kim, J. Lee, and J. Gobrecht, *3D visualization of mold filling stages in thermal nanoimprint by white light interferometry and atomic force microscopy*, Nanotechnology **20**, 355301 (2009)

[16]   D. Morihara, H. Hiroshima, and Y. Hirai, *Numerical study on bubble trapping in UV-nanoimprint lithography*, Microelectronic Eng. **86**, 684 (2009)

[17]   J. Perumal, T.H. Yoon, H.S. Jang, J.J. Lee, and D.P. Kim, *Adhesion force measurement between the stamp and the resin in ultraviolet nanoimprint lithography—an investigative approach*, Nanotechnology **20**, 055704 (2009)

[18]   M. Okada, M. Iwasa, K.-I. Nakamatsu, K. Kanda, Y. Haruyama, and S. Matsui, *Durability of antisticking layer against heat in nanoimprinting evaluated using scanning probe microscopy*, Microelectronic Eng. **86**, 657 (2009)

[19]   D. Truffier-Boutry, R. Galand, A. Beaurain, A. Francone, B. Pelissier, M. Zelsmann, and J. Boussey, *Mold cleaning and fluorinated anti-sticking treatments in nanoimprint lithography*, Microelectronic Eng. **86**, 669 (2009)

[20]   E. Roy, Y. Kanamori, M. Belotti, and Y. Chen, *Enhanced UV imprint ability with a tri-layer stamp configuration*, Microelectronic Eng. **78–79**, 689 (2005)

[21]   Z. Li, Y. Gu, L. Wang, H. Ge, W. Wu, Q. Xia, C. Yuan, Y. Chen, B. Cui, and R.S. Williams, *Hybrid nanoimprint-soft lithography with sub-15 nm resolution*, Nano Lett. **9**, 2306 (2009)

[22]   http://www.obducat.com/

[23]   L.J. Guo, *Nanoimprint lithography: Methods and material requirements*, Adv. Mater. **19**, 495 (2007)

[24]   Y. Xia, and G.M. Whitesides, *Soft lithography*, Annu. Rev. Mater. Sci. **28**, 153 (1998)

[25]   C.Y. Hui, A. Jagota, Y.Y. Lin, and E.J. Kramer, *Constraints on microcontact printing imposed by stamp deformation*, Langmuir **18**, 1394 (2002)

[27]   E. Delamarche, H. Schmid, B. Michel, and H. Biebuyck, *Stability of molded polydimethylsiloxane micro structures*, Adv. Mater. **9**, 741 (1997)

[28]   Y. Zhao, *Closely spaced polymer microstructures as a unique tool for characterization at the small scales*, Proc. IEEE 21st International Conference on Micro Electro Mechanical Systems, 459 (2008)

[29]   J.A. Rogers, K.E. Paul, and G.M. Whitesides, *Quantifying distortions in soft lithography*, J. Vac. Sci. Technol. B **16**, 88 (1998)

[30]   S. Pagliara, L. Persano, A. Camposeo, R. Cingolani, and D. Pisignano, *Registration accuracy in multilevel soft lithography*, Nanotechnology **18**, 175302 (2007)

[31] M.M.J. Decré, R. Schneider, D. Burdinski, J. Schellekens, M. Saalmink, and R. Dona, *Wave Printing (I): Towards large-area, multilayer microcontact printing*, Mater. Res. Soc. Symp. Proc. **M4.9.1** (2004)

[32] J. Schellekens, D. Burdinski, M. Saalmink, M. Beenhakkers, G. Gelinck, and M.M.J. Decré, *Wave printing (II): Polymer MISFETs using microcontact printing*, Mater. Res. Soc. Symp. Proc. **M2.9.1** (2004)

[33] T.W. Odom, J.C. Love, D.B. Wolfe, K.E. Paul, and G.M. Whitesides, *Improved pattern transfer in soft lithography using composite stamps*, Langmuir **18**, 5314 (2002)

[34] B. Michel, A. Bernard, A. Bietsch, E. Delamarche, M. Geissler, D. Juncker, H. Kind, J.P. Renault, H. Rothuizen, H. Schmid, P. Schmidt-Winkel, R. Stutz, and H. Wolf, *Printing meets lithography: Soft approaches to high-resolution patterning*, IBM J. Res. Develop. **45**, 697 ((2001)

[35] P. C. Duineveld, M. Lilja, T. Johansson, and O. Inganäs, *Diffusion of solvent in PDMS elastomer for micromolding in capillaries*, Langmuir **18**, 9554 (2002)

[36] *Sol-gel science: The physics and chemistry of sol-gel processing*, C. Jeffrey Brinker and George W. Scherer, Academic Press Inc, (1990)

[37] L.L. Hench and J.K. West, *The Sol-gel Process*, Chem. Rev. **90**, 33 (1990)

[38] K. R. Catchpole, and A. Polman, *Plasmonic solar cells*, Optics Express **16**, 21793 (2008)

[39] V.E. Ferry, M.A. Verschuuren, H.B.T. Li, R.E. I. Schropp, H.A. Atwater, and A. Polman, *Improved red-response in thin film a-Si:H solar cells with soft-imprinted plasmonic back reflectors*, Appl. Phys. Lett. **95**, 183503 (2009)

[40] A. Otto, I. Mrozek, H. Grabhorn, and W. Akemann, *Surface-enhanced Raman scattering*, J. Phys. Condens. Mat. **4**, 1143 (1992)

[41] R. Alvarez-Puebla, B. Cui, J.-P. Bravo-Vasquez, T. Veres, and H. Fenniri, *Nanoimprinted SERS-active substrates with tunable surface plasmon resonances*, J. Phys. Chem. C **111**, 6720 (2007)

[42] A. Pierret, M. Hocevar, S.L Diedenhofen, R.E Algra, E. Vlieg, E.C. Timmering, M.A. Verschuuren, G.W.G. Immink, M.A. Verheijen, and E.P.A.M. Bakkers, *Generic nano-imprint process for fabrication of nanowire arrays*, Nanotechnology **21**, 065305 (2010)

[43] J.-S. Sohn, D. Lee, E. Cho, H.-S. Kim, B.-K. Lee, M.-B. Lee, and S.-J. Suh, *The fabrication of Co–Pt electro-deposited bit patterned media with nanoimprint lithography*, Nanotechnology **20**, 025302 (2009)

Chapter 2

SCIL soft-nanoimprint of sol-gel materials

In this chapter we describe the SCIL soft-nanoimprint process using silica sol-gel resist. The sol-gel chemistry and resist is discussed and a systematic optimization of sol-gel parameters is described. The cause of feature collapse in soft stamps is investigated and a solution to this problem is given. We demonstrate a systematic study towards to a new high Young's modulus PDMS rubber of which the synthesis and characterization is described. The SCIL tooling and composite stamp fabrication is described. The SCIL method is characterized by measurements of the replication quality and induced pattern deformations. A procedure to obtain highly accurate overlay alignment is described and experiments are performed to determine the overlay accuracy of the SCIL process.

2.1 Introduction into sol-gel soft-nanoimprint

In soft-nanoimprint lithography a rubber stamp with nanoscale patterns is applied to a liquid material. The liquid subsequently reacts to form a solid material, which transfers the nanoscale patterns. Ideally this material is temperature stable, chemically inert and resistant to visible and UV light. These requirements can be met using sol-gel chemistry. In this method a solution of metal (alkoxide) precursors is applied to a substrate where it reacts to form a gel, which after drying turns into a solid. With sol-gel chemistry a wide range of metal oxides can be formed, based on e.g. silicon, germanium, boron, titanium, zirconium, hafnium, niobium, lanthanum, lead and tantalum.[1,2] Typical layer thicknesses that can be made range from 10 to 500 nm.

Figure 1 shows the characteristic processing steps in sol-gel nanoimprinting. First a thin layer of silica sol-gel imprint resist is applied on a substrate. Next a patterned silicone rubber stamp made of poly-di-methyl-siloxane (PDMS) is applied to the liquid layer (Fig. 1(a)). The filling of the features is greatly influenced by capillary forces as depicted in Fig. 1(a). Remaining air in the features diffuses into the rubber. Next, solvents are removed by diffusion into the stamp and the volume loss due to removal of the solvents is compensated by material flow under the stamp (see Fig. 1(b)). Simultaneously the silicon oxide precursors react with each other, forming an inorganic network of silicon-oxygen-silicon bonds. The reaction products of the network formation are water and alcohols, which also diffuse into the rubber stamp. The viscosity of the liquid increases as this network is formed. Eventually a gel is formed and further material flow is not possible anymore (see Fig. 1(c)). The gel contains alcohols and water which are removed from the sol-gel layer by diffusion into the stamp. Further formation of the inorganic network transforms the gel into solid silicon oxide glass (Fig. 1(d)). At this stage the stamp can be removed, which leaves a replica of the original master pattern. Using this procedure large areas of micro- and nanostructured silica can be made, simply by manually applying a rubber stamp.

After patterning, a sintering step of typically 100-1000 °C is used to densify the material. The densification during sintering of as-prepared sol-gel layers to fully dense coatings can typically range from 2 up to 10 fold. This leads to the build up of a tensile mechanical stress in the layer which can lead to the formation of cracks in the film. Thicker layers lead to higher stress build-up, which limits the layer thickness that can be made with the sol-gel method. When a sol-gel layer is structured, the sol-gel patterns will deform due to the densification.[3-6]

Much effort has gone into developing fully organic and hybrid organic-inorganic material systems that do not experience this high shrinkage and therefore can be patterned with high fidelity using (soft-)nanoimprint techniques.[7-11]
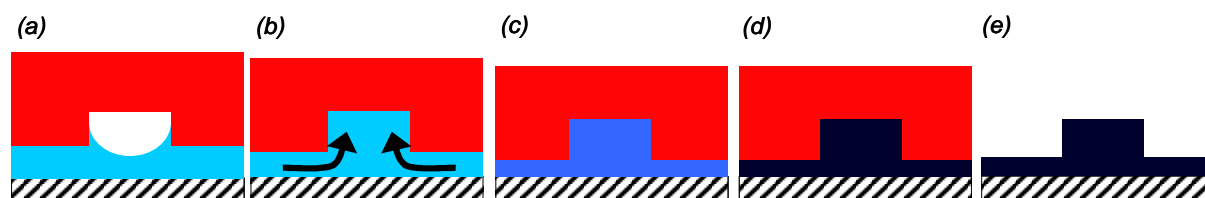
Figure 1. Schematic of the sol-gel imprinting process, (a) a solution containing alcohol, water and silicon sol-gel precursors is brought in contact with the silicon rubber stamp, (b) features fill due to capillary forces, solvents diffuse into the stamp and material flow compensates the volume loss, (c) the precursors react, forming an inorganic Si-O-Si network and eventually a silica gel, (d) remaining liquid is removed from the gel and further network formation takes place, transforming the gel into a solid silicon oxide glass. (e) The stamp is removed leaving a replica of the original master pattern.

However, the disadvantage of these materials is that they are not light and temperature stable and therefore also cannot be directly used in optical applications. Therefore these materials are not further discussed.

In this thesis we develop a novel inorganic cross-linking imprint resist via the sol-gel route that leads to films with minimal shrinkage and no cracking. It is based on silicon-oxide sol-gel chemistry and involves only a minimal amount of organic components. These materials can be patterned at room temperature and low pressure results in high fidelity nanoscale features which are resistant to visible and UV light and are temperature stable.

2.2 Silicon based sol-gel chemistry and synthesis

2.2.1 Basic silicon sol-gel chemistry

The base component in silicon sol-gel chemistry is the liquid alkoxide tetra-methyl-ortho-silicate (TMOS), $Si(OCH_3)_4$, see Fig. 2. This precursor can partly or fully react with water (hydrolysis) to yield methanol and a silicon hydroxyl group $(CH_3O)_3Si\text{-}OH$. Two silicon hydroxyl groups can react under release of water (condensation) to form a stable Si-O-Si bond, the basis of a silicon oxide glass. In practice TMOS is mixed with alcohol and water that is acidified to catalyze the hydrolysis reaction. The (partly) hydrolyzed TMOS can subsequently follow several reaction paths towards condensation. Simultaneous with the hydrolysis, condensation takes place and larger molecules are formed consisting of silicon atoms bound by oxygen and terminated by OH or alkoxy end groups. The formed molecules can be either linear or branched as TMOS has four reactive groups per silicon atom.

In Table I the possible reactions are listed which can proceed during hydrolysis of TMOS and subsequent formation of a solid layer. Reactions 1 - 3 are equilibrium reactions. The final ratio and concentration of different reactive groups depends on the initial concentration of all reactants, pH and temperature. In general, elevated temperatures and acid or basic conditions promote hydrolysis and condensation reactions.[12-15]

1.	hydrolysis	$Si\text{-}(O\text{-}CH_3) + H_2O$	$\leftrightarrow$	$Si\text{-}OH + HO\text{-}CH_3$
2.	esterification	$Si\text{-}OH + HO\text{-}CH_3$	$\leftrightarrow$	$Si\text{-}(O\text{-}CH_3) + H_2O$
3.	substitution	$Si\text{-}(O\text{-}CH_3) + HO\text{-}C_2H_5$	$\leftrightarrow$	$Si\text{-}(O\text{-}C_2H_5) + HO\text{-}CH_3$
4.	condensation	$Si\text{-}OH + HO\text{-}Si$	$\rightarrow$	$Si\text{-}O\text{-}Si + H_2O$
5.	alkoxolation	$Si\text{-}OH + Si\text{-}(O\text{-}CH_3)$	$\rightarrow$	$Si\text{-}O\text{-}Si + HO\text{-}CH_3$

Table I. Reactions of silicon alkoxides during sol-gel hydrolysis and film formation. Reactions 1, 2 and 3 are equilibrium reactions, the environment determines the balance in the reactions. Reactions 4 and 5 form the silicon oxide network.
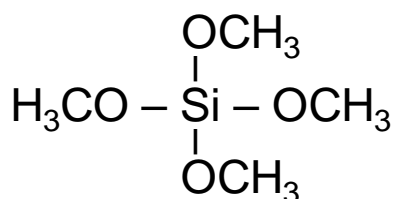

Figure 2. Chemical formula of tetra-methyl-ortho-silicate (TMOS).

When a mixture of TMOS with alcohol and water is allowed to react so that it has reached a certain degree of hydrolysis and condensation, it can subsequently be used to form thin films on a substrate by spin coating. During and after spinning of the hydrolysis mixture alcohol(s) and water are removed from the liquid by evaporation, which promotes formation of the silica network. The degree of hydrolysis and condensation of a hydrolysis mixture determines the type of solid layer that is formed:

1. Low degree of hydrolysis.
During hydrolysis a small fraction of the alkoxides hydrolyses and as a result the degree of condensation is low. When a coating is prepared from this mixture and the gel state is reached, the layer contains a high amount of alkoxide groups. To further form the network these alkoxides form Si-O-Si bonds by undergoing hydrolysis and condensation in the layer when it is in the gel or solid state. This leads to volume loss and the formation of pores due to the leaving alcohols and water as the network has already formed. During the final drying phase the gel forms a porous layer or the gel collapses under capillary forces leading to the formation of cracks in the layer.

2. High degree of hydrolysis.
If the hydrolysis degree is high, the condensation degree will be high and an extensive 3D inorganic network forms in solution. During drying this will lead to gel formation in an early stage, when most of the alcohol and water are still present. Thus the solid content of the gel is low. During drying of the gel the network collapses under capillary forces, which leads to porous, cracked coatings.

Consequently, both low and high degree of hydrolysis sol-gel layers will undergo a strong shrinkage (80-90%). When such a sol-gel system is patterned by soft imprint lithography, the final printed patterns will undergo strong shrinkage, causing a strong deformation of the original pattern.[3-6] The hydrolysis and condensation degree can also be controlled by addition of complex-forming ligands organic components such as acetylacetone, which stabilize the silicon in solution and prevent condensation.[16] However these relatively large organic molecules are incorporated in the layer and must be removed from the formed layer by annealing, which again leads to excessive volume loss. In conclusion, sol-gel systems based solely on pure metal alkoxide precursors will always lead to high shrinkage as there is not enough control over the network formation in these systems. An additional parameter is therefore needed to control the network formation. Here we use organically modified silicon precursors in the sol-gel route to influence the degree of condensation.

2.2.2 Organically modified silicon precursors

A different way of tuning the condensation degree or cross link density of silicon based sol-gel is to use organically modified silicon precursors.[17-20] These organo-silanes have at least one carbon atom covalently bound to silicon. In principle this makes it possible to link almost any organic group directly to silicon. We used the simplest organic alkoxide, methyl-tri-methoxy-silane (MTMS), CH_3-$Si(OCH_3)_3$, which is similar to TMOS, but has three reactive alkoxide groups and a methyl group, see Fig. 3. The methyl group of MTMS does not participate in the inorganic network formation. Layers that contain MTMS can be used for optical purposes as cured MTMS layers do not absorb ultra violet, visible or near infrared light. Moreover, the silicon-carbon bond in MTMS is temperature stable up to 450 °C in air.

$$OCH_3$$
$$|$$
$$H_3CO - Si - CH_3$$
$$|$$
$$OCH_3$$
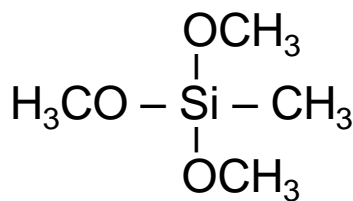
Figure 3. Chemical formula of methyl-tri-methoxy-silane (MTMS).

Substituting part of the TMOS precursors by MTMS provides an additional parameter to tune the degree of cross linking. This tunable cross link degree of a hybrid TMOS-MTMS sol-gel mixture can potentially lead to a gel point at a higher concentration of silicon precursors. This would result in a less porous material and less shrinkage of the final structures.

2.2.3 Synthesis of TMOS-MTMS hydrolysis solution and sol-gel imprint resist

Hydrolysis and imprint experiments were performed using various TMOS to MTMS ratios. The sol-gel imprint resist is synthesized in two steps. First the sol-gel "hydrolysis base" is synthesized by controlled hydrolysis and condensation of TMOS and MTMS in a water and alcohol solution under acid conditions. Hydrolysis and condensation reactions are exothermic and therefore the hydrolysis is performed in a temperature controlled water bath. Typical hydrolysis times are 10 to 120 minutes. The hydrolysis time is increased for higher MTMS to TMOS ratios. We observed when short hydrolysis times are used with pure MTMS this does not form a continuous thin layer on a substrate without breaking up into droplets. We attribute this to a lower hydrolysis rate and crosslink degree of an MTMS hydrolysis mixture, possibly due to sterical hindrance of the methyl group. The following procedure is used in the synthesis of mixtures with varying TMOS to MTMS ratios.

1. TMOS and MTMS are mixed in the appropriate molar ratio.
2. Per mol of silicon 0.33 mol of n-propanol is added to increase mixability with water.
3. Water is added to a ratio of 1 mol water per mol of alkoxide present. This water was acidified with 1 mol per liter formic acid.
4. A temperature controlled heated water bath is used to control the temperature between room temperature and 50 °C.
5. The mixture is allowed to react for 10 to 120 minutes.
6. After the reaction time the mixture is cooled to room temperature.
7. Water is added to reach 9 mol water per mol of silicon in the mixture.
8. n-propanol is added to dilute the hydrolysis sol to a concentration of 0.78 mol Si / kg hydrolysis mixture.
9. This mixture is kept at room temperature for 20 minutes and is subsequently stored at -25 °C.

Table II. TMOS-MTMS hydrolysis recipe.

Dilution with alcohol and storing at -25 °C stops condensation reactions, but substitution reactions do proceed. The hydrolysis mixture is in equilibrium after about 24 hours. The pot life of these hydrolysis mixtures is at least half a year when stored at -25 °C.

In the second step a sol-gel imprint resist solution is prepared from this mixture. Equal parts (by weights) of hydrolysis base material and n-propanol containing 2.0 weight percent 2-(2-butoxy-ethoxy)-ethyl-acetate (BEEA) are mixed. This results in a resist which contains 0.39 mol Si / kg solution. BEEA is a linear a-polar molecule which does not participate in sol-gel reactions. Due to its low vapor pressure (0.01 mBar at room temperature) BEEA remains in a spin-coated sol-gel layer after water and alcohols have evaporated. It lowers the viscosity of the sol-gel layer and

allows up to 5 minutes between spin coating of the sol-gel layer on the substrate and the application of the PDMS stamp.

Using spin coating a layer with a typical thickness of ~100 nm is applied on a silicon substrate. To ensure good wetting and adhesion of the sol-gel layer the substrates are cleaned prior to use by an oxygen plasma (barrel geometry, 200 W, 0.5 mBar, 2 min.). The spin coater is equipped with a co-rotating lid, as this allows the layer to thin to the correct thickness without changes in viscosity due to solvent evaporation. A three-stage spin coat cycle is used that will result in a sol-gel layer of ~100 nm thickness. A typical spin coat cycle is described in Table III.

1.	open lid	100 rpm, 10 sec.	low speed resist application
2.	close lid	500 rpm, 10 sec.	thinning of the resist at high speed
		1000 rpm, 2 sec.	removal of thick liquid on substrate edge
3.	open lid	300 rpm, 5 - 30 sec.	pre-drying: evaporation of water and alcohols

Table III. Three stage spin coat cycle which results in a sol-gel layer of ~100 nm.

During the drying step most of the alcohol and water evaporate while the BEEA remains in the sol-gel coating. It is estimated that after the drying step the amount of BEEA left in the sol-gel layer is ~34 volume percent, assuming the density of the silica sol-gel to be 1.3 g/cm^3 (the density of silicon oxide is 2.6 g/cm^3).

2.2.4 Imprint results for varying TMOS:MTMS hydrolysis ratios

Within one minute after spin coating the sol-gel layer is imprinted using a patterned PDMS stamp. The stamp is left in contact with the sol-gel to let the remaining BEEA and reaction products of the condensation reactions diffuse into the PDMS. Typical imprint times are 10 to 30 minutes. During the imprint time the sol-gel forms a rigid glass-like structure that does not deform during removal of the stamp, nor does it deform due to surface tension after the stamp release. The stamp is removed from the hardened sol-gel layer by gently pealing it from a side.

In Table IV an overview is given of imprint experiments with sol-gel hydrolysis mixtures of varying TMOS:MTMS ratios. The organic fraction (CH$_3$ group of MTMS) is calculated using the molar weights of fully condensed TMOS (SiO$_2$ = 60) and MTMS (SiO$_{1.5}$CH$_3$ = 67). The maximum crosslink degree of a sol-gel network is calculated by taking the mole average cross link numbers of TMOS (4) and MTMS (3). The imprint results are examined by scanning electron microscopy (SEM) and atomic force microscopy (AFM) to determine the quality of the imprinted patterns.

TMOS:MTMS ratio	Maximum crosslink degree	Organic fraction (wt. %)	Sol-gel replica quality
1 : 0	4	0	No replica obtained
1 : 0.5	3.67	8.0	No imprint / high shrinkage during imprinting
1 : 1	3.5	11.8	One to one copy of original pattern
0.5 : 1	3.33	15.5	One to one copy of original pattern
0 : 1	3	22.4	One to one copy of original pattern

Table IV. Overview of different TMOS:MTMS ratios used in imprint experiments. Organic fraction refers to the methyl group of MTMS. The maximum cross link degree was calculated from the mole average crosslink degree (4 for TMOS and 3 for MTMS).
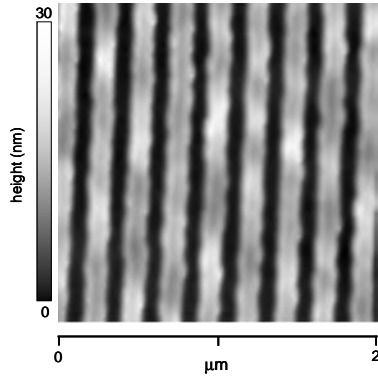
Figure 4. AFM measurement of grating pattern imprinted in a sol-gel resist with a TMOS-MTMS ratio of 1:0.5. The features in the stamp are not correctly replicated in the sol-gel: the grating height in the stamp is 70 nm while the height in the sol-gel replica is between 10 and 20 nm.

We find that sol-gel mixtures with an MTMS content less than 50% can not be patterned with high fidelity. For a TMOS:MTMS ratio of 1:0.5 features in the stamp can not be transferred into the sol-gel at all, or the resulting sol-gel feature height was only 10-20 nm, while the feature height in the stamp is 70 nm. This is illustrated by the AFM scans in Fig 4. We find that mixtures with a MTMS content above 50%, corresponding to a cross-link degree ≤3.5 (see Table IV), can all be patterned with high fidelity. Given that the organic content must be kept as low as possible, e.g. for optical and thermal applications, we conclude that a one-to-one molar ratio for TMOS to MTMS is optimal.

2.2.5 Post cure shrinkage of imprinted sol-gel patterns

We determined the shrinkage of imprinted sol-gel after curing at 200 °C and sintering at 1000 °C. We used gratings with a pitch of 240 nm that are patterned on silicon substrates using sol-gel with a TMOS-MTMS ratio of 1:1. The shape and size of the grating patterns is determined by SEM. Figure 5 shows the patterned sol-gel directly after imprinting at room temperature (a), after curing in air at 200 °C (b) and sintering in air at 1000 °C (c). From the SEM images it is found that after curing at 200 °C the shrinkage is 9 % in width and 6 % in height; after sintering at 1000 °C the total shrinkage is 14 % in width and 18 % in height.
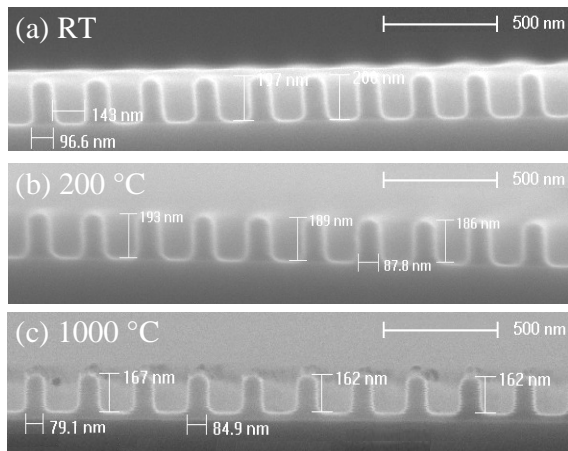
Figure 5. SEM cross section images of grating structures imprinted in a 1:1 TMOS:MTMS sol-gel layer after (a) imprinting at room temperature, (b) curing in air at 200 °C and (c) sintering in air at 1000 °C. The sol-gel lines densify and shrink at higher curing temperatures due to increased cross linking and removal of methyl groups by oxidation (> 450 °C). These combined processes remove nano-pores in the material.

The densification at 200 °C is attributed to further condensation and removal of nano-pores. Above 450 °C the methyl group of MTMS is oxidized and forms a Si-OH group which can subsequently further condensate, causing additional densification. The sol-gel reaches the density of fused silica at 1000 °C, which we confirmed by ellipsometry measurements on planar 100 nm thick sol-gel layers. The rounding of the corners observed at the bottom of the features is due to influence of the substrate, which does not shrink, and prevents sol-gel shrinkage in width close to the substrate. The residual layer under the imprinted sol-gel gratings is initially ~5 nm thick. After sintering at 1000 °C in air a ~30 nm thick silicon oxide layer has formed due to thermal oxidation of the silicon substrate.

2.3 High resolution poly-di-methyl-siloxane stamp materials

Poly-di-methyl-siloxane (PDMS or silicone rubber) is an excellent material to use in soft lithography stamps, as first demonstrated by Whitesides *et al*. They showed that PDMS is able to replicate (sub)-micro meter structures. Due to the ease of use, PDMS has become the material of choice in soft lithography applications as micro-contact printing, micro-transfer printing, replica molding, transfer molding, etc.[3] The properties of this inorganic-organic polymer are ideal for soft lithography: the low Young's modulus enables conformal contact on substrates and the rubber can be formed at room temperature. Moreover, PDMS is chemically inert, non-toxic, bio-compatible, has a low surface energy and has high permeability for gasses and solvents. Finally, PDMS is transparent in the wavelength range of ~300 nm to ~ 3 µm.

Patterned PDMS stamps are formed by molding a reactive two-component PDMS system from a master pattern. This is usually a silicon wafer patterned by standard semiconductor lithography processes such as optical lithography, electron beam lithography in combination with etching or focused ion beam milling. PDMS stamps can also be directly molded from patterned resist materials.

To aid release of the rubber stamp from the master, the surface of the master is made non-reactive towards PDMS. To do so, the surface is modified with a reactive organo-silane containing a fluorinated tail using the vapor phase deposition method. In this process the master is placed in a vacuum oven at 50 °C. Next a few drops of 1,1,2,2H-perfluorodecyl-tri-chloro-silane are placed in the oven and the system is continuously pumped to ~10^{-2} mBar for at least 16 hours.[21-23] The chloro-silane passivates Si-OH and Si-H groups on the master which otherwise react with PDMS. The long fluor-modified chains help to form an inert closed layer as the chains form a densely packed mono-layer. This passivation effect is verified by measuring the contact angle of a droplet of de-ionized water on a flat silicon surface; for low sticking of PDMS to silicon the advancing contact angle has to be in the range of 110-118°.

PDMS rubber is made by mixing and de-gassing a two-component PDMS system which is poured on the master pattern. The liquid PDMS flows into the spaces around the features in the master. A thermally activated cross link reaction converts the liquid in a rubber with the inverse shape of the master. Typical curing conditions are 24 hours in an oven at 50 °C. The rubber stamp can be released from the master by gentle peeling. The master remains unchanged and can subsequently be used to replicate additional PDMS stamps. The most widely used silicone rubber materials in soft lithography are Sylgard 184 from Dow Corning and Elastosil 601 from Wacker Chemie. These materials can be cured from room temperature up to 150 °C and form transparent PDMS rubbers with a Young's modulus between 1 and 5 MPa, depending of curing temperature and time.

2.3.1 Pattern instability in soft stamps

The advantages of soft stamps are: inexpensive, easy to fabricate and conformal contact on substrates. They also require low force to release the stamp from an imprinted pattern. However, a disadvantage of soft stamps is that as features become smaller, the surface-to-volume ratio increases and surface tension causes rounding of sharp corners. To illustrate this, Fig. 6 shows tapping mode AFM phase images of PDMS pyramids made from rubbers with a Young's modulus of 2.5 MPa (a) and 8 MPa (b) that were molded from inverted pyramids etched into a Si<100> master using etching by KOH. The KOH etches the different crystal planes of silicon at different rates and produces atomically sharp edges. As Fig. 6 shows, these edges can be observed in both PDMS stamps, but in the softer material (Fig. 6(a)) the corners are rounded under the influence of surface tension.[24]

A second disadvantage of the use of soft (low Young's modulus) stamps is that adjacent features can stick, leading to collapse of a stamp pattern. This is not an issue in isolated nanoscale features, for which PDMS has been successfully used.[25,26] However, collapse of patterns is an issue in dense patterns such as gratings and photonic crystal patterns in which the lateral feature size is comparable to the pitch. The so called pairing, the sticking of individual features, is schematically shown in Fig. 7(a). The instability of PDMS stamps is being studied extensively, both theoretically and experimentally, as it is often the limiting factor in the spatial resolution of soft lithography.[27-33]

Patterns become permanently paired if the elastic energy which is stored in deformed features is less than the energy gained by the reduction of surface energy at the contact area between two features. In Fig. 7(b) tapping mode AFM height data is shown of a collapsed grating with 115 nm high, 80 nm wide lines on a pitch of 240 nm. A 240 nm pitch pattern is schematically indicated by the dots in the cross section, which clearly shows that the grating lines have become paired. Figure 7(c) shows a SEM image of the same grating. It clearly shows regions in which two and three individual grating lines have paired.
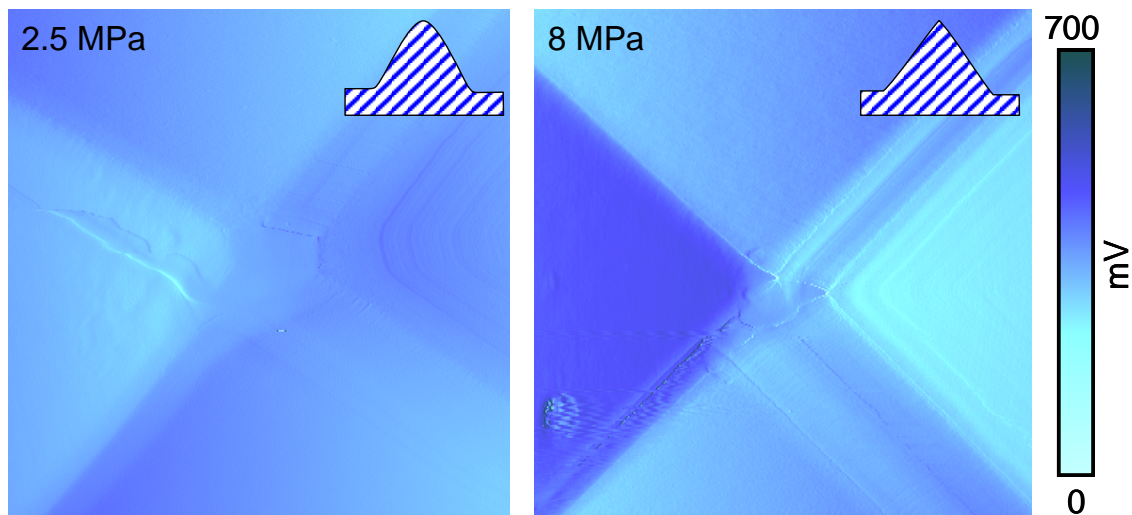
Figure 6. AFM measurements (tapping mode phase information) of PDMS replicas made from a pyramid structure formed by KOH etching of silicon. (a) Sylgard 184 PDMS with a Young's modulus of 2.5 MPa, (b) H-PDMS with a Young's modulus of 8 MPa. The base of the pyramids is 3 micron.
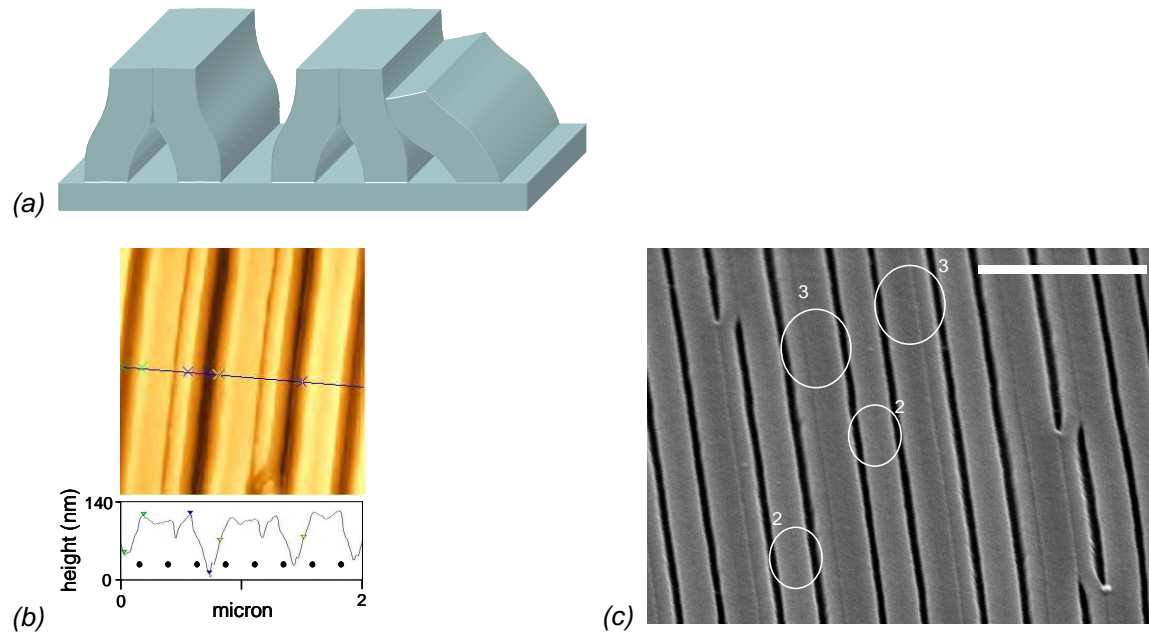
Figure 7. (a) Schematic of paired grating features, (b) AFM data: 2D height profile and line scan perpendicular to the grating lines. The dot pattern schematically shows a pitch of 240 nm. (c) SEM image of H-PDMS grating of 115 nm high, 80 nm wide lines on a pitch of 240 nm. The grating has collapsed and 2 or 3 individual lines stick together (indicated by the white circles). The scale bar in (c) is 2 µm.

We explored several routes to restore collapsed features: fluor modification of the PDMS surface to lower the surface tension, washing with low surface energy solvents such as ethanol/iso-propanol, washing with water containing a surfactant[27] and super critical CO_2 washing and drying. The last method avoids capillary forces on features during drying. None of these methods leads to restoring of the collapsed grating patterns. The data shown in this section clearly shows that soft stamp made from standard PDMS material, which is routinely used to soft-imprint micron scale features, cannot be used to fabricate structures with high density and small feature sizes.

2.3.2 Calculation of feature stability in PDMS stamps

The stability of features against collapse depends on the pattern geometry and dimensions. Using a continuum mechanical model described in Ref. 32 we calculate the elastic deformation energy and reduction of surface energy per unit grating width for two lamella making contact as depicted in Fig. 8. The elastic energy required to deform a feature is given by: $U_e = E \cdot a^2 \cdot t^3 / 2s^3$, with a, t and s as indicated in Fig. 8 and E the Young's modulus. The surface energy gained by the reduced surface area is given by: $U_s = -2\gamma_s \cdot d$, with d the height of the contact area and γ_s the surface energy. If the surface energy gained due to collapse is less than the energy required to deform the features ($2U_e - 2U_s > 0$) the patterns are stable towards lateral collapse. We use the surface energy of water (80 mJ/m^2), instead of PDMS (~20-25 mJ/m^2) because during the imprinting of sol-gel water is present, which can condense and increase the surface energy of the stamp.
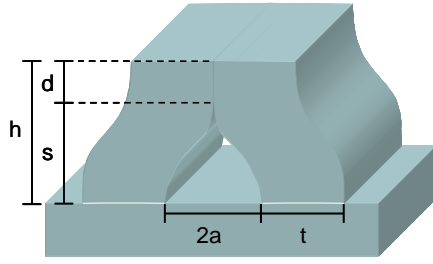
Figure 8. Schematic of a paired grating with the characteristic dimensions: feature width (t), height (h), contact height (d) and spacing (2a).

Figure 9(a) shows the calculated values of $2U_e-2U_s$ as function of d/h for a grating with low aspect ratio (t=160 nm, h=115 nm, a=40 nm) and a Young's modulus of 11 MPa. As can be seen, for the low aspect ratio grating collapse is not energetically favorable.

Figure 9(b) shows calculations for geometries with reduced spacing (a=15 nm) and increased aspect ratio (1.5 or 2) using a Young's modulus E=20 MPa. A stable geometry is found for 60 nm pitch grating with 30 nm wide, 45 nm high lines. However if the aspect ratio is increased to 2 (60 nm high lines), a negative energy is found around d/h ~0.35 and the features will collapse.

Figure 9(c) shows calculations of the minimum value of the elastic energy minus the surface energy for gratings with a aspect ratio of 2 and feature height equal to the grating pitch. It shows that for a rubber with a Young's modulus E=11 MPa the grating will become unstable and collapse below a pitch of 200 nm. For a rubber with E=40 MPa the gratings are predicted to be stable down to 50 nm pitch.

(a)

(b)

(c)
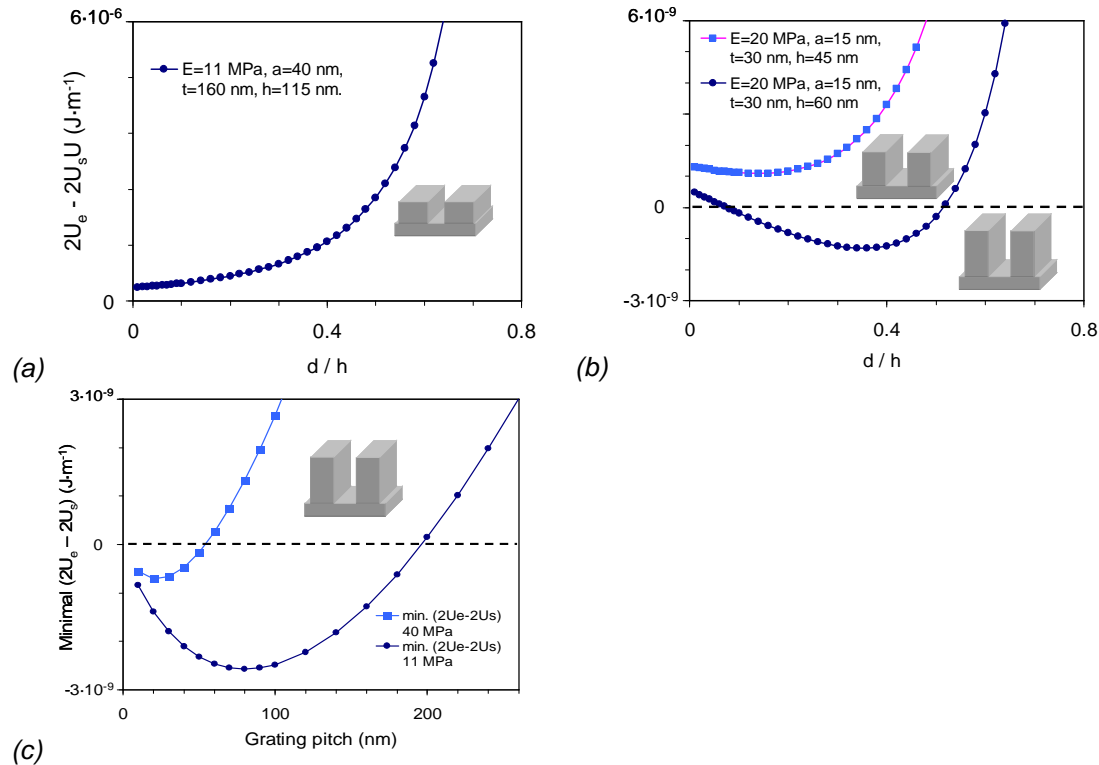
Figure 9. Calculated elastic/surface energy for two collapsed grating lines with different height, width, spacing and Young's modulus. (a) height 115 nm, width 82 nm, 240 nm pitch and E=11 MPa (low aspect ratio geometry) (b) height 45 nm, width 30 nm, 60 nm pitch (aspect ratio 1.5) and height 60 nm, width 30 nm, 60 nm pitch (aspect ratio 2) both with E=20 nm. (c) Minimal (2Ue-2Us) as function of grating pitch. Gratings have a geometry of aspect ratio 2 and feature height equal to the grating pitch.

We note that the above calculations are made using a simplified model that does not take into account the complex deformation of PDMS features (as schematically shown in Fig. 7). Finite-element modeling must be used to simulate the mechanical behavior of soft rubber patterns in complex geometries more precisely. However this falls outside the scope of this work.

The surface energy of PDMS could be lowered by chemical surface modification.[34-36] However in practice this will yield little improvement as the presence of water and the associated high capillary forces will dominate. The main conclusion from the above calculations is that stamp material with an increased modulus over the commonly used PDMS rubbers (that have E=2 – 8 MPa) is required to fabricate dense periodic patterns with high aspect ratio and nanoscale dimensions. In the following sections we introduce a novel route to fabricate stable sub-50 nm pitch patterns by increasing the Young's modulus of the PDMS stamp material.

2.3.3 Mechanically stable nanoscale PDMS patterns

Increasing the Young's modulus to make a rubber stamp more stable towards collapse is a contradictory requirement for a soft stamp. A low Young's modulus is required to achieve conformal contact over large areas, make the imprint process less sensitive to particle contaminants and to allow for low force release from imprinted features. The challenge is thus to find a material that has the advantages of PDMS combined with a Young's modulus that is just high enough to obtain stable features.

To increase resolution and avoid the inherent low modulus of PDMS rubbers, several other materials have been developed and used as stamps in soft lithography. These material systems include, siloxane-composites[37,38], (fluoridized) UV curing polymers[39-41] and thermo-plastic materials[42,43]. Although features down to 50 nm have been replicated in these materials, they have important disadvantages. UV curing polymers have to be used above their glass transition temperature, otherwise the materials are too stiff to form conformal contact on substrates. The disadvantage of a non-rubber stamp material, which is used above its glass transition temperature, is that the material will permanently deform when put under stress. Thermoplastic polymers have to be molded from a master at high temperatures (typically 150 - 250 °C) to lower the materials viscosity and let the material flow into the patterns on the master. However, during cooling of the stamp stress builds up due to the difference in thermal expansion coefficients of the master (fused silica / silicon, $0.5 – 4.5$ ppm·K^{-1}) and thermoplastic polymers ($100 – 1000$ ppm·K^{-1}), causing deformation of the stamp.

To increase the Young's modulus of PDMS a modified PDMS type called H-PDMS was developed.[44] The H-PDMS rubber has a Young's modulus E=8-12 MPa, compared to E=2-3 MPa for the often used commercial Sylgard 184 PDMS. The highest values have been obtained by using shorter cross linkers and an increased concentration of reactive groups combined with curing of the PDMS at 150 °C.[45] However, this increased modulus of H-PDMS over standard PDMS is not sufficient to obtain stable patterns below 100 nm, as shown by the collapsed gratings in Fig. 7, which are replicated in H-PDMS material. Our conclusion is that we have to further increase the Young's modulus of PDMS type materials to obtain reproducible sub-50 nm patterns over large areas. Based on our calculations we estimate that rubbers with a Young's modulus of 20 - 100 MPa are relevant for our goal. To the best of our knowledge there are no PDMS rubber type materials available that fulfill our requirements.

2.3.4 PDMS with increased Young's modulus: X-PDMS

Increasing the Young's modulus of PDMS rubbers is possible by adaptations to the silicone processing and composition. Process parameters which can be modified are: curing temperature, curing time and crosslink density. The curing temperature must be kept below 50 °C to minimize thermally induced deformations due to the difference in thermal expansion coefficient of rubber, master wafer and glass carrier (see section 2.4.1). H-PDMS is a two-component system of linear di-methyl-siloxane molecules. There are several different chemical routes to cross-link siloxanes and in this way form a rubber. The platinum catalyzed route has the advantage that there are no byproducts from the cross linking process and the reaction already proceeds at room temperature.[46] In the platinum catalyzed PDMS systems two components react to form a network: a vinyl functionalized linear di-methyl-siloxane (Fig. 10(a)) and a silicon-hydride functionalized linear di-methyl-siloxane (Fig. 10(b)). Silicon-vinyl and silicon-hydride groups can react by a platinum catalyzed addition reaction to form a network as shown in Fig. 10(c). By changing the chain length and the amount of reactive groups in each precursor, the crosslink density can be tuned to obtain rubbers with varying Young's modulus. This was done for the H-PDMS recipe.[44]

We first performed experiments using linear siloxanes of varying functionality and molecular weights to increase the Young's modulus. We could not increase the modulus over the value of the H-PDMS. The linear PDMS chains cannot effectively form a stiff 3D network due to the flexible linear molecule parts between cross link points. To increase the cross link density and the rigidity between the different cross link points, a precursor has to be used that itself is branched in several directions. Figure 11 shows an example a branched siloxane (Q-siloxane) that has quaternary branching of some silicon atoms. Adding Q-siloxanes to a linear PDMS network creates points where the network is cross-linked in multiple directions. This increases the overall crosslink density and stiffness of the network which should result in an increased Young's modulus.
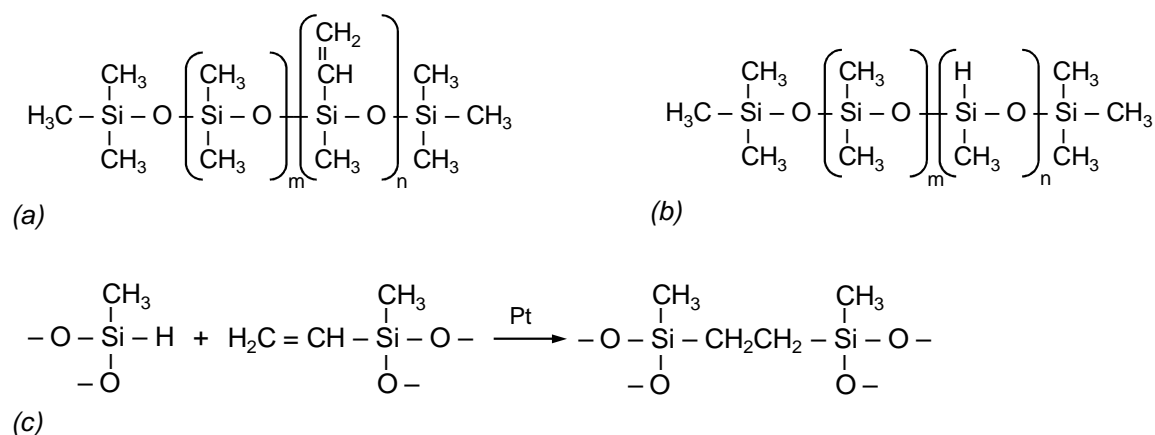
Figure 10. Chemical formulas of base siloxane molecules used in PDMS. (a) Linear di-methy-siloxane where part of the methyl groups have been replaced by reactive vinyl groups, (b) Linear di-methy-siloxane where part of the methyl groups have been replaced by reactive silicon hydride groups, (c) Platinum assisted addition reaction between a silicon hydride group and a vinyl group, forming a silicon-ethyl-silicon bond between two siloxane molecules.
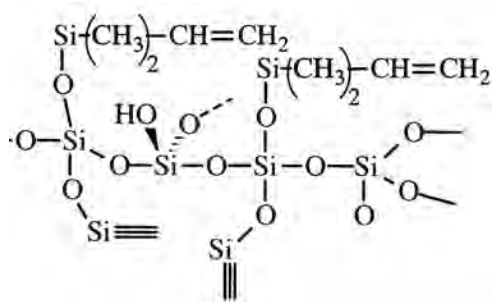
Figure 11. Chemical representation of a Q-branched siloxane precursor.

2.3.5 Preparation of Q-siloxane modified PDMS

Various modified PDMS rubbers were prepared using Q-siloxanes in combination with linear siloxane precursors. Additionally, experiments were performed using T-siloxanes (ternary branching) from which rubbers with a Young's modulus up to E=~25 MPa were prepared, however more promising results were obtained by using Q-siloxanes. Table V lists the base materials used to prepare silicon rubbers. All materials are obtained from Gelest Inc. and used as received.

Product code	Type	Functionality
VDT-731	linear vinyl siloxane	7% reactive methyl-vinyl-siloxane groups in the siloxane chain
HMS-301	linear hydride siloxane	30% reactive methyl-hydride-siloxane groups in the siloxane chain
HMS-501	linear hydride siloxane	50% reactive methyl-hydride-siloxane groups in the siloxane chain
VQX-221	Vinyl Q-siloxane	50 wt.% solution of vinyl Q-siloxanes in xylene
SIP 6831.2LC	Platinum catalyst	2.5 wt.% platinum di-vinyl-tetra-methyl-di-siloxane in xylene
SIT 7900.0	Moderator	1,3,5,7-tetra-vinyl-1,3,5,7-tetra-methyl-cyclo-tetra-siloxane

Table V. Siloxane base materials.

Figure 12 shows the developed synthesis procedure for rubber compositions consisting of vinyl Q-siloxanes, linear vinyl siloxanes, platinum catalyst and catalyst moderator. This mixture is cross linked with linear hydride siloxanes. The vinyl functional part A (see Fig. 12) is prepared by mixing linear vinyl siloxanes with a solution of Q-siloxanes in xylene to the appropriate ratio of solid Q-siloxane. The xylene solvent is evaporated from the mixture in an air purged oven at 45 °C until the solvent content is below 0.1 wt. %. Next, the platinum catalyst and moderator are added to part A. The PDMS rubber is formed by cross linking part A with linear silicon-hydride siloxanes (part B). The two components A and B are thoroughly mixed and de-gassed before curing at 50 °C.
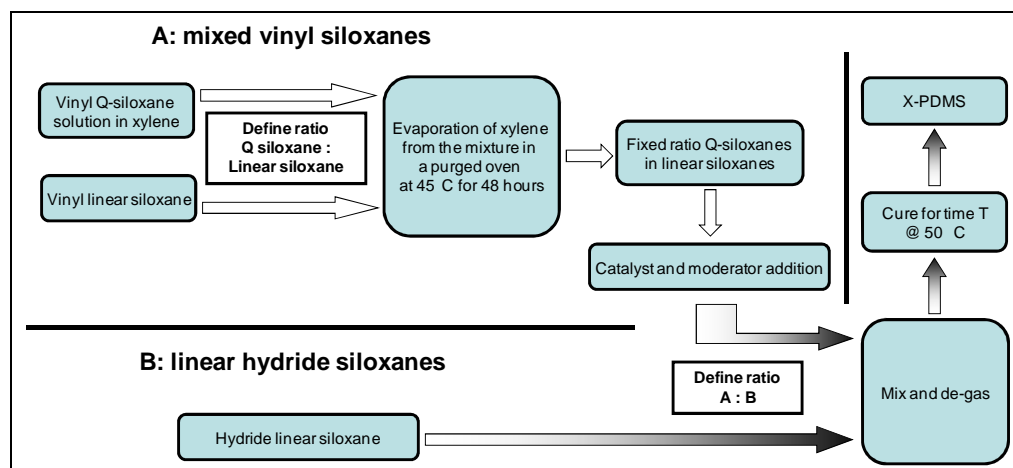
Figure 12. Schematic of the synthesis of X-PDMS composed of Q-vinyl siloxanes, linear vinyl siloxanes, platinum catalyst, catalyst moderator and linear hydride siloxanes.

For part A varying weight ratios of linear siloxanes to Q-siloxanes have been prepared ranging from 1:0.3 to 1:1. The catalyst and moderator concentration is chosen so the working time (gel formation) would be between 5 and 15 minutes after addition of the hydride siloxanes. This allows for thorough mixing and de-gassing of the viscous X-PDMS liquid. The X-PMDS liquid is subsequently poured in cylindrical moulds made from poly-tetra-fluor-ethylene (PTFE) with a diameter of 10 mm and 5 mm height. The X-PDMS in the mould is subsequently cured in an oven at 50 °C. The curing times ranged from overnight up to two weeks. The resulting X-PDMS cylinders are released from the mold after which the Young's modulus is determined by indentation measurements.

2.3.6 Young's modulus determination by indentation measurements

The Young's modulus of the formed rubber is determined by a force-displacement indentation measurement. A half sphere with a radius of 1.5 mm is used to indent the rubber while the force as function of indentation depth is monitored. The indentation depth (I_d) is a function of applied load (F), sphere radius (R), Poisson ratio (ν) and the Young's modulus (E) of the rubber. The load as function of indentation depth can be calculated using:

$$F = \frac{4E \cdot \sqrt{R}}{3(1-\nu^2)} \cdot I_d^{(3/2)} \quad .^{[47]}$$

Figure 13 shows the force versus position data for loading and unloading an X-PDMS rubber. We fit the data of the loading curve using $\nu=0.5$, a standard value for rubbers,[47] and find a Young's modulus of 69 MPa. The measured position is corrected for the linear stiffness of the load cell and taking into account an off-set, as the force will only start to increase once contact is made between rubber and sphere. The sample is measured by cyclically loading and unloading starting from 1 N up to 4 N in 4 steps. Note that the load and unload curves fully overlap, which indicates there is no hysteresis or creep in the material. This shows that the sample is a fully elastic rubber.
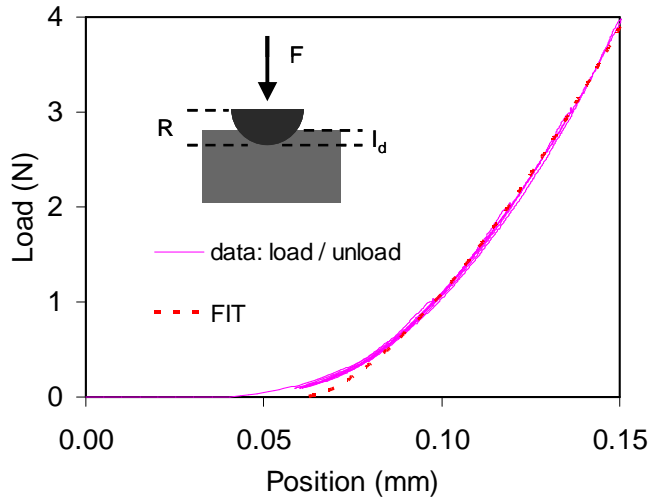
Figure 13. Force-position measurement for an X-PDMS rubber. The load and unload data are shown as well as the fit to the load data. Assuming $v=0.5$ we fit a Young's modulus E= 69 MPa.

We prepared and characterized more than 150 silicone rubber compositions containing Q-siloxanes. For each specific rubber composition the Young's modulus was determined by measuring multiple cylinders of X-PDMS. We observed that the following factors increased the Young's modulus of PDMS rubbers:

- increased Q-siloxane content
- increased functionality of the linear hydride siloxane
- increased platinum catalyst concentration
- decreased moderator concentration
- increased curing temperature
- increased curing time (at constant temperature)

Of all the possible combinations there is a limited range over which the components can be varied without compromising the process window. High Q-siloxane content leads to increased viscosity which hinders homogeneous mixing. Increased platinum catalyst concentration or decreased moderator concentration reduced the working time to only a few minutes after addition of the hydro-siloxane. An important variable is the ratio of part A (with a fixed Q-siloxane to linear-siloxane ratio) to part B. We observed that a 10% variation in A to B ratio could reduce the modulus by 50% and that the modulus of a rubber increases with prolonged curing time. Table VI shows the compositions and Young's modulus of different (optimal) X-PDMS rubbers, made using HMS-501 as part B.

Part A L:Q ratio	A:B ratio (by weight)	# days curing @ 50 °C	Young's modulus
1 : 0.625	1:0.400	4	20.7±0.9
1 : 0.7	1: 0.308	3	22.0±0.1
1 : 0.7	1: 0.325	4	61.3±3.6
1 : 0.8	1: 0.325	1	57.7±1.8
1 : 0.8	1: 0.325	11	78.7±1.8

Table VI. Young's modulus of X-PDMS rubbers made with different weight ratios of A and B and varying Q-siloxane content. The rubbers have been cured for 1 to 11 days at 50 °C. The Pt catalyst and moderator concentration is equal for each composition.
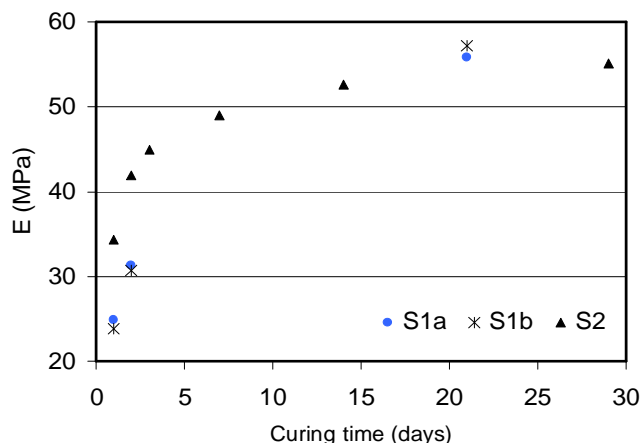
Figure 14. Young's modulus of an X-PDMS rubber as function of curing time at 50 °C for three samples of two batches with a ratio A to B 1:0.36, The composition ratio of linear- to Q-siloxane is 1:0.7 in part A, and part B is composed of HMS-501.

Figure 14 shows the modulus as function of curing time for two batches composed of a Q-siloxane to linear-siloxane ratio of 1:0.7 (part A) and HMS-501 as part B. The ratio A:B was 1:0.36. We compare samples from two different batches (S1 & S2) and two samples from the same batch (S1a & S1b). As can be seen, samples from the same batch (squares and crosses) show very reproducible behavior. The initial modulus for short curing times is quite different for the two different batches. We attribute this to small variations in the platinum and modurator concentrations between the two batches. The three samples reach about the same Young's modulus after three weeks curing (E~55 MPa). The saturation effect for long curing times is attributed to the fact that the formation of cross-links makes it increasingly difficult for reactive groups to react due to increased sterical hindrance of the formed network.

From these experiments we determined two optimal formulations of high-modulus X-PDMS rubber. These compositions reach a Young's modulus of 65 MPa and 80 MPa after curing for 5 days at 50 °C. The total compositions by weight are shown in table VII. These X-PDMS compositions result in high Young's modulus PDMS rubbers in an acceptable curing time using a curing temperature of 50 °C. The X-PDMS material is compatible with commercial PDMS and the two PDMS types can be co-cured to form composite stamps where the two PDMS types are chemically bonded.

Part A				Part B	Young's Modulus (MPa)
Vinyl linear siloxane	Vinyl Q-siloxane (solid content)	Platinum catalyst	Moderator	Hydride linear siloxane	Curing condition: 5 days 50 °C
VDT-731	VQX-221	2.5 wt% complex in xylene	Tetravinyl-tetramethyl-cyclo-tetra-siloxane	HMS-501	
1	0.7	0.025	0.045	0.553	65 ± 2
1	0.8	0.025	0.045	0.585	80 ± 1

Table VII. X-PDMS compositions by weight and resulting Young's modulus of the rubber after curing at 50 °C for 5 days.

2.3.7 Sub-50 nm imprinted sol-gel patterns using X-PDMS stamps

The Young's modulus of a X-PDMS rubber is 20-40 times higher than that of standard commercial PDMS, but is still low enough for the rubber to easily establish conformal contact on substrates. X-PDMS is also permeable to solvents, which makes it compatible with our sol-gel material in the same way as commercial PDMS. To test the resistance of X-PDMS towards feature collapse, two separate masters are prepared with e-beam lithography of ZEPP520, a positive PMMA based resist. A first pattern contains a grating of ~30 nm wide, 60 nm high lines on a pitch of 60 nm, a second pattern contains a 2D square array of 25 nm diameter ~40 nm deep holes on a pitch of 50 nm. After fluor mono-layer surface modification, composite X-PDMS stamps are molded from these masters. The X-PDMS is thoroughly mixed, de-gassed and spin-coated over the masters. This results in a 50-100 μm thick X-PDMS layer. After a pre-cure of 20 minutes at 50 °C, 1 mm thick Sylgard 184 is poured on the X-PDMS. The stamp is cured for 7 days at 50 °C before it is released form the master. The Young's modulus of the X-PDMS is ~65 MPa, as determined by force indentation measurements on a test sample from the same X-PDMS batch.

Figure 15 shows SEM images of sol-gel layers imprinted using the resulting X-PDMS stamps. Figure 15(a) show the grating with a pitch of 60 nm, showing 25-30 nm wide grating lines. Figure 15(b) shows the hole-array with a pitch of 50 nm and 20-30 nm diameter holes. Clearly, the increased modulus of the X-PDMS results in features which are more stable against collapse (compare e.g. Fig. 7) and enables the replication of dense patterns with dimensions as small as 25 nm and a pitch of 50 nm. This work proves that PDMS stamps are able to replicate high aspect ratio sub-25 nm patterns with all the advantages of soft stamps.

We believe these dimensions are not the limit of the X-PDMS rubber system for dense patterns. In fact, the resolution of e-beam resist used to fabricate the master is limiting the production of dense regular patterns with a smaller pitch. The ultimate resolution of our X-PDMS material is not only determined by the geometrical stability of patterns, but also by the ability of the rubber material to mold to a certain shape and hold this shape. Figure 16(a) shows SEM images, taken under an angle of 30 °, of a master made by e-beam lithography and etching of quartz. It contains ~30 nm diameter pillars on a pitch of 50 nm in square and hexagonal lattices. In a separate area, arrays are composed of features where during the e-beam process two dots are written next to

(a) *(b)*
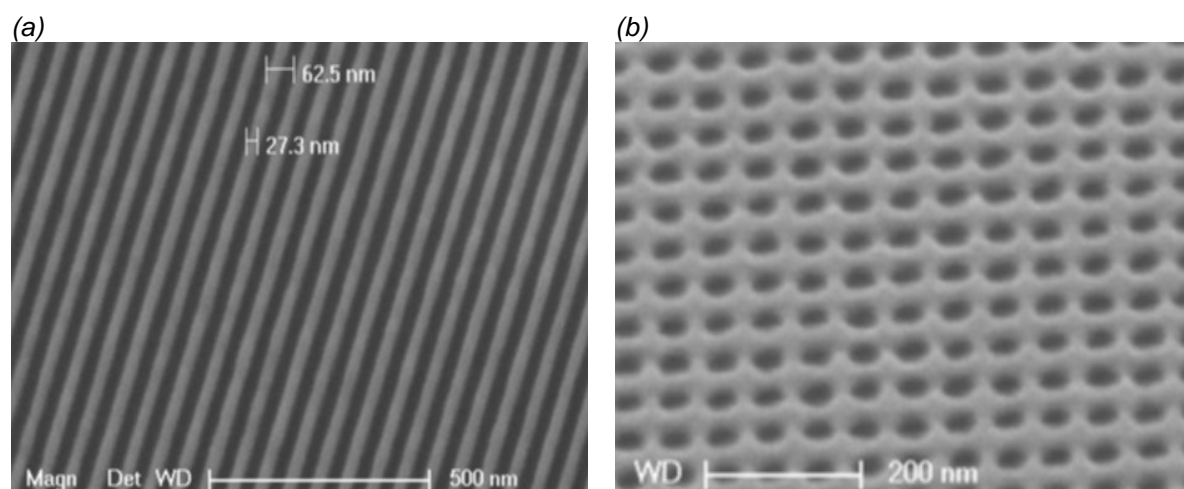
Figure 15. SEM images taken under an angle of 35° of a sol-gel layer patterned by X-PDMS stamps. (a) 60 nm pitch grating lines. (b) square array of holes with 50 nm pitch .
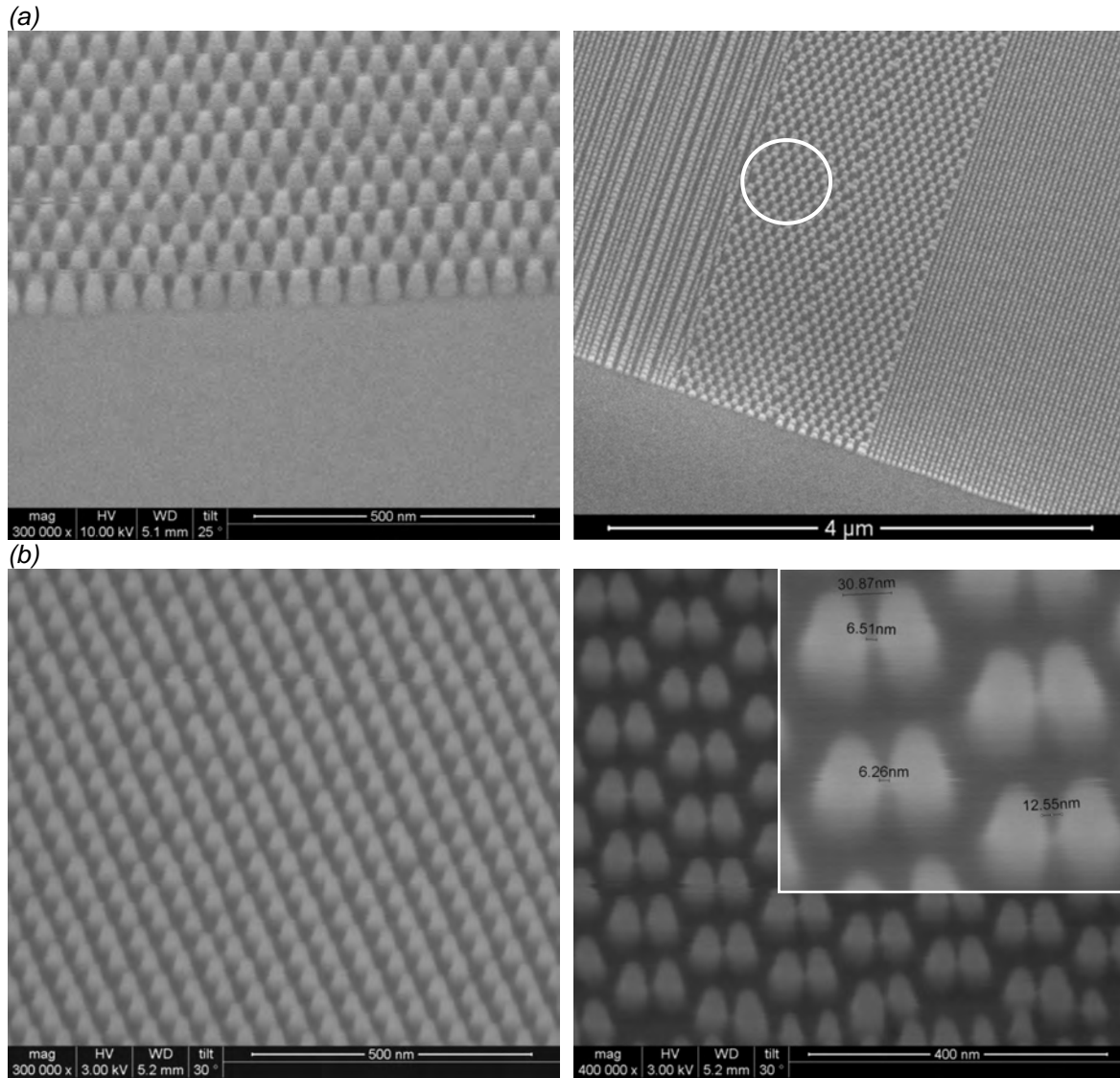
Figure 16. (a) Quartz master pattern containing ~30 nm diameter pillars on a pitch of 50 nm and pillars spaced on a pitch of 30 nm, (b) Sol-gel replica of the master patterns shown in (a).

each other. During subsequent etching these two closely spaced structures are transferred in the quartz as two separate dots, leaving a narrow gap of less than 10 nm, indicated by the circle in Fig. 16(a). This master pattern was replicated in sol-gel using an X-PDMS stamp. Figure 16(b) shows SEM images taken under an angle of 30 ° of the imprinted sol-gel patterns. As can be seen the rubber is capable of reproducibly patterning 6 nm gaps between arrays of sol-gel pillars. This indicates the potential of our material system to reproduce dense patterns on length scales below 10 nm.

2.4. Substrate Conformal Imprint Lithography method

Manually handling a rubber stamp to imprint areas larger than a few square cm leads to two problems: we observe air inclusions and pattern deformations due to deformation of the rubber stamp during handling. To avoid these problems an imprint method was developed analog to the wave printer concept.[48,49] Waveprinting was developed by Philips Research to pattern large areas using micro contact printing. Our imprint method is called Substrate Conformal Imprint Lithography (SCIL) and enables imprinting of wafer-scale areas in a single step. SCIL uses

composite soft stamps which are grafted on a thin glass plate. We use AF45 glass, which has a thermal expansion coefficient which closely matches that of silicon around room temperature. This composite layout avoids the buildup of stress during curing of the stamp and avoids deformation of the rubber as the glass provides in-plane mechanical integrity.

2.4.1 SCIL composite stamp fabrication

A typical SCIL stamp consists of a 200×200 mm square glass sheet with a thickness of 150 or 200 micron. On this glass a 150 mm diameter ~0.5 mm thick PDMS rubber stamp is grafted. This geometry allows bending of the stamp in the out-of-plane direction to conform to surface roughness and substrate bow, while pattern distortions are minimized due to the in-plane stiffness of the glass plate.

The H-PDMS and X-PDMS rubbers are less tough than commercial rubbers. As a consequence, a stamp made entirely from these high-modulus PDMS rubbers is fragile. The high modulus is also a disadvantage during imprinting when large particles are present and the "bulk" rubber has to deform to accommodate the deformation. Therefore the rubber is built up from a thin layer of high-modulus PDMS (which contains the patterns) and layer of soft and tough commercial PDMS.[50-52]

A tool was developed to fabricate SCIL composite stamps without air inclusions and ensure homogeneous heating during curing of the PDMS. It consists of two parallel vacuum chucks where the distance between the chucks is controlled by three micrometer spindles. To produce a SCIL stamp the master containing the patterns is first prepared. A 50-100 micron thick layer of X-PDMS is spin coated over the master and pre-cured for 10-20 min. at 50 °C. After the pre-cure the X-PDMS is still tacky and the coated master is placed on the bottom vacuum chuck. Next, commercial PDMS is mixed and de-gassed and a precise amount is poured on the X-PDMS coated master. Subsequently, the top vacuum chuck which holds the glass plate is lowered which causes squeezing out of the commercial PDMS over the master. The final thickness is controlled by the three spindles. To cure the (X-)PDMS to the desired modulus the whole set of vacuum chucks, master and back plate is placed in an oven at 50 °C. As the soft PDMS cures it bonds to the X-PDMS layer and the glass. After release from the tool the composite stamp can be carefully peeled from the master. The edges of the rubber stamp are carefully trimmed with a scalpel to remove any PDMS that protrudes above the plane of the patterns. Finally a rubber seal is glued on the edge of the glass. Figure 17(a) shows the schematic stamp layout and Fig. 17(b) shows photographs of two SCIL stamps demonstrating the out-of-plane flexibility and the large (150 mm diameter) stamp area which displays interference colors due to the patterns in the rubber.
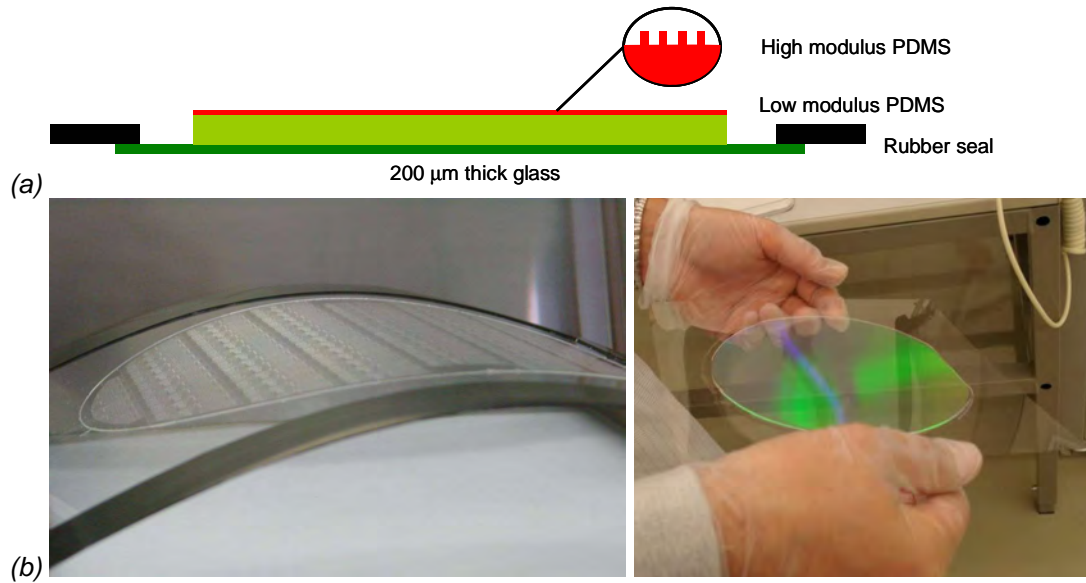
Figure 17. (a) Schematic of a SCIL composite stamp consisting of a thin glass carrier plate on which a two-layer silicone rubber stamp is attached. The top PDMS layer consists of high-modulus X-PDMS and contains the patterns. The low modulus of the bottom PDMS layer helps to make conformal contact during imprinting, (b) Photographs of SCIL stamps, showing the flexibility in the out-of-plane direction by bending the stamp. In the right picture interference colors can be seen which result from a pillar pattern with a pitch of 513 nm in the X-PDMS.

2.4.2 SCIL imprint method

The SCIL imprint module consists of a flat plate which contains multiple grooves. The composite stamp is held in place on this plate by vacuum. Parallel to the stamp a substrate with a liquid resist layer is suspended, leaving a gap of 75-125 micrometers. To bridge the gap and contact the stamp to the substrate the grooves are pressurized. Starting from one side an overpressure of typically 15-30 mBar is applied to one groove. The applied pressure makes the stamp bulge and this forms an elevated line parallel to the grooves. As more neighboring grooves are pressurized in sequence, the (stamp) line will gradually bridge the gap to the substrate and make contact. Depending on gap size and applied pressure ~10-15 grooves have to be pressurized to form the initial contact between the stamp and the substrate. Subsequently the remaining grooves are pressurized in sequence causing a gradual advance of the line contact between the stamp and the resist, see Fig. 18(a). The stamp is kept in contact until the (sol-gel) resist layer has hardened. Then the stamp is released from the imprinted features by sequentially switching the grooves back to vacuum from one side.
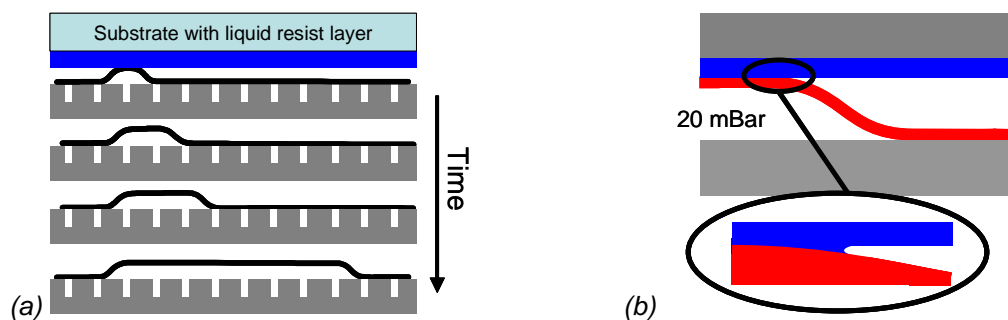
Figure 18. SCIL imprint principle. (a) Time sequence of an imprint step showing the evolution of the contact area by sequentially pressurizing the grooves, (b) Advancing capillary contact line due to wetting at both interfaces.

SCIL design constrictions

The choice of groove pitch is important to produce imprints without introducing air inclusions. The first design used 1 mm wide grooves on a pitch of 5 mm. Using this design it proved to be impossible to imprint sol-gel layers (100 nm – 10 micron thickness) without forming air inclusions. We studied the imprint process by using a glass chuck and substrate and video recording to follow the capillary front movement as the imprint was made in a sol-gel layer. From the video data it was determined that the capillary front is able to travel ~3 mm under capillary force. Therefore, for a groove plate with a pitch of 5 mm, which will advance the stamp contact 5 mm each step, air inclusions are formed because the stamp comes into contact with the sol-gel layer before the capillary front arrives. As contact between stamp and resist is made at random positions, multiple circularly expanding capillary fronts are created that can enclose air. A second design of the groove plate was made which used 1 mm wide grooves on a pitch of 2.5 mm. This allows the capillary front to travel the 2.5 mm distance of the pitch length, before random contact can occur, thus avoiding air inclusions. The final SCIL imprint tool uses a plate with 80 grooves of 1.0 mm width on a pitch of 2.5 mm. This setup allows imprinting of round substrates up to 150 mm diameter.

Imprinting: capillary force driven advancing contact line

During the imprint step the capillary force pulls the stamp into the liquid, rather than the stamp being pushed on the substrate by the air pressure under the stamp. The capillary pressure scales with surface energy and the inverse of the capillary radius. The latter is very small as at the stamp-resist-air contact line the stamp is almost parallel to the substrate due to the S-shape of the stamp (see Fig. 18(b)), which requires 20-30 mm to bridge the distance of 100 μm between the stamp and substrate (an average slope of less than 5 μm/mm). By looking through a glass substrate at the contact line interference fringes can be seen between the stamp and the substrate. From the spacing of the fringes we judge the distance between the stamp and substrate in front of the contact line to be less than 200 nm over a distance of 100-200 micron. The fact that the capillary forces drive the advancing contact line was verified by recording the moving contact line on video. From this data the speed of the moving contact line once a groove was pressurized is estimated to be 30-50 mm per second. This is much faster than the effective speed of the pressure sequence, indicating the capillary forces dominate the process.

We varied the delay time between pressurizing subsequent grooves from ~100 ms up to two seconds and found no difference in the imprint quality. The bending stiffness of the composite stamp had no substantial influence on the minimum time delay between subsequent pressurizing of grooves. This was tested for stamps with glass back plates of 150 and 200 microns thickness and stainless steel back plates of 100 micron thickness. The distance between substrate and stamp was varied between 50 and 200 micron. We found the optimum distance between stamp and substrate to be ~100 micron. This allows for substrate bow and non-flatness while it minimizes air leaks from pressurized to vacuum grooves.

Stamp release: receding contact line

The stamp is released in a controlled way from an imprinted (sol-gel) layer by sequentially switching the grooves back to vacuum. Starting from one side where the stamp is held on the groove plate, a groove is evacuated. The air under the stamp is drawn away by the groove which is open to vacuum. This quickly creates a local under-pressure at the position of the groove which is switched. As a result the ambient air pressure pushes the stamp towards the groove plate. As the stamp makes contact to the groove plate it seals the vacuum leak. The gap between groove plate and substrate is now bridged in a length that is 2.5 mm shorter than the equilibrium position of the stamp and the bending stress in the stamp is increased. The stamp relaxes to the

equilibrium position by releasing from the substrate; the actual release is thus a slow controlled peeling process. While switching a groove from overpressure to vacuum, the pressure under the area of the stamp that is still in contact to the substrate can drop from ~20 mBar to ~10 mBar, but it does not go below atmospheric pressure. In practice the minimum delay time between evacuating subsequent pressurized grooves is ~300 ms. The optimum delay time depends on the feature density and aspect ratio: dense high-aspect ratio features have increased contact area between stamp and resist and therefore higher Van der Waals contact force, requiring a more slow release than non-patterned areas. The switch delay therefore has to take into account different pattern geometries across the stamp.

2.5 SCIL imprint performance

Any imprint process can lead to the formation of defects. It is important to identify the type of errors that can be introduced and at which process step they occur. In this section we study pattern deformations which are introduced by stamp replication and the SCIL imprint process.

We distinguish two types of defects that can occur during imprinting which are related to defects of individual features.

1. Incomplete feature replication. This is mainly a concern for imprint methods which use rigid stamps and is caused by two phenomena: 1. air trapped in the features prevents the filling of the features with resist material[53,54] and 2. on stamp release, features in the resist or stamp can break.[55] In our X-PDMS SCIL process we observe that all individual features are replicated at every imprint. This is due to the fact that liquid resist can easily fill up features and trapped air diffuses into the rubber. On release, the stamp (locally) deforms to aid release of the patterned structures. To characterize this in further detail, automated processing and inspection tooling are required.

2. Particle related defects. As imprint lithography is a contact method, particles that are present on the stamp or the substrate will influence the replicated pattern. Working in a clean environment can minimize particle related defects.[56-58] Studying this in a quantitative way is difficult and requires a production type of environment which uses automated handing. We observe that particles preferentially adhere to our sol-gel imprint resist on the substrate and in this manner clean the stamp. Large-area imprints with low particle related defect densities were obtained by first imprinting sol-gel resist on two or three clean silicon wafers before a (series) of products was imprinted. This procedure clearly reduced particle related defects. This was verified by dark-field optical microscopy on sub-wavelength patterns, in which particles clearly stand out. We also used an automated wafer scale particle counter in which a defect is detected by the scattered light of a laser beam. We imprinted 5 wafers in sequence and observed that particle contaminants decreased after each imprint, which demonstrates the self-cleaning effect of soft-stamps in combination with sol-gel resist.

In the next section we elaborate on pattern deformations and magnification errors.

2.5.1 Pattern deformation: ex-situ measurements

Pattern deformations, which are introduced by the double replication step from master to stamp to imprint, are characterized by laser diffraction measurements to determine variations in the pitch of a grating. This provides information about the uniformity of the replicated patterns and resolves if there are any repetitive errors present from the SCIL replication step. Figure 19 shows the setup which is used to scan a substrate on a precision stage under a normal-incidence laser beam from a HeNe laser with a wavelength of 633 nm.
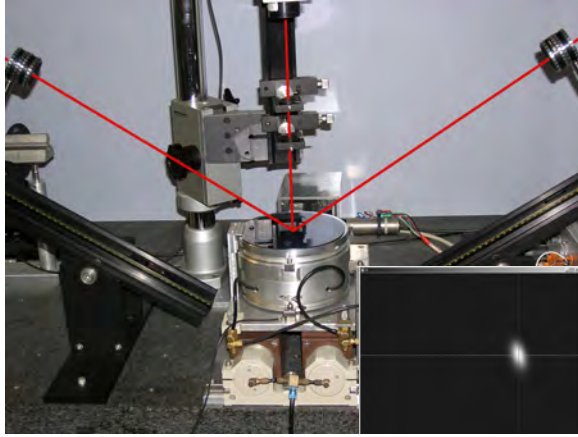
Figure 19. Photograph of the laser diffraction setup. It shows the x-y stage on which the sample is held by vacuum. Laser light is directed from above and diffracts off the gating. The two 4th diffraction orders are focused on two CCD cameras using two lenses. The inset shows a CCD image of a 4th order diffraction laser spot.

The laser beam diffracts off a 3 micron pitch grating imprinted in silica towards two CCD cameras on either side. The inset in Fig. 19 shows a CCD camera image of a diffracted 4th order laser spot. Scanning the sample under the laser spot and tracking the reflected diffraction orders on the cameras produces a two-dimensional map of the grating pitch averaged over the laser spot diameter of ~125 µm. The total scanned area is 25×25 mm^2. Figure 20 shows images of the averaged grating pitch for master (a) and sol-gel replica, with the imprint direction parallel (b) or perpendicular (c) to the SCIL grooves.

Figure 20 shows variations in average grating pitch of less than 0.1 nm (i.e. ±0.03 %) for both master and replicas. A replication fidelity corresponding to a pitch variation of less than 0.1 nm has to our knowledge never been shown for soft stamp imprint methods.[59,60] The bright vertical lines are due to stitching errors between 15×15 mm grating areas introduced in the mastering process. The isolated artifacts in the replicas (see arrows in b,c) are due to particles contaminants, which we confirmed by optical microscopy at these places. Note that due to the softness of the
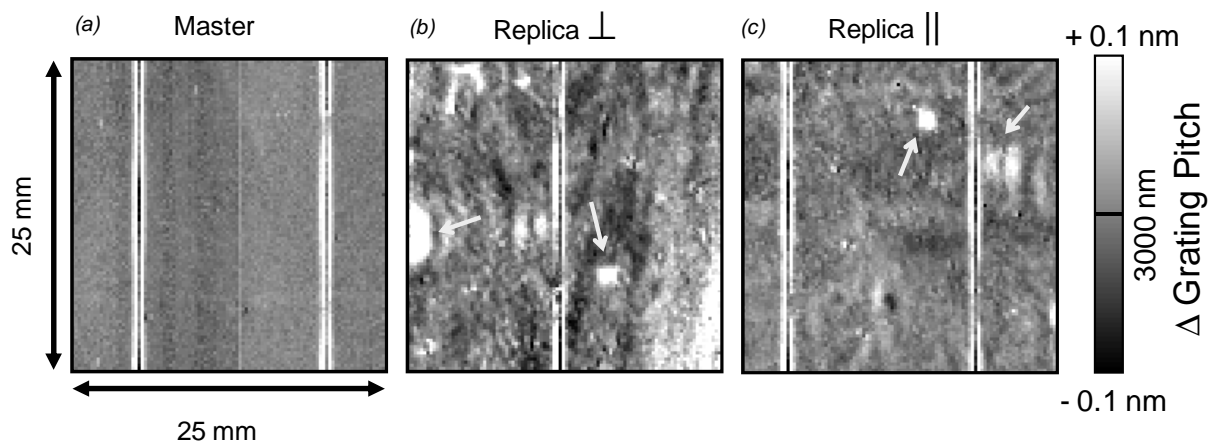
Figure 20. Two-dimensional distribution of the grating pitch measured using laser diffraction. The pitch scale bar is shown on the right hand side. The light vertical lines are stitch marks from the stepper used to produce the master pattern. The dark and bright spots are induced by particles. (a) Master pattern in silicon, (b) sol-gel replica on AF45 glass produced by imprinting the grating lines perpendicular to the SCIL grooves, (c) sol-gel replica on AF45 glass produced by imprinting the grating lines parallel to the SCIL grooves. The step wise application (2.5 mm period) of the SCIL cannot be observed in the replicas.

stamp, particles only cause pattern deformation in a small range around the particle. Comparing the images for the two imprint directions we conclude that the direction in which the grating was imprinted does not influence the deformation. Furthermore, the step wise application of the stamp by the SCIL process is not observed in the replicas.

The laser diffraction measurements shown in Fig. 20 do not give information about possible magnification errors which can be introduced during the replication steps. The absolute pitch can only be determined with a precision of ~0.5% which is limited by the measurement of the angle between the two CCD cameras. We will use a different method to quantify magnification errors more precisely in section 2.5.3.

The deformation of the stamp due to a particle contaminant is mostly dissipated in the soft intermediate PDMS layer. This localizes the deformation to the PDMS in the direct surrounding of the particle contaminant and ensures the remainder of the area is imprinted without deformations. Figure 21 shows SEM images of SCIL imprints in sol-gel resist over particles with a height up to ten times the resist layer thickness. As can be seen, the stamp imprints the patterns on and over the particle and the local deformation of the rubber stamp is clearly shown. Only a small distance away from the defect the pattern continues without distortion. The bottom right picture shows an imprint over a particle which is ~ 20 µm in height, which is too large to be fully dissipated in the rubber. This leads to an exclusion area of ~ 100 µm diameter around the particle where no patterns are imprinted. When using a rigid stamp, these type of particles would cause damage to the stamp and/or substrate, potentially generating additional particles.

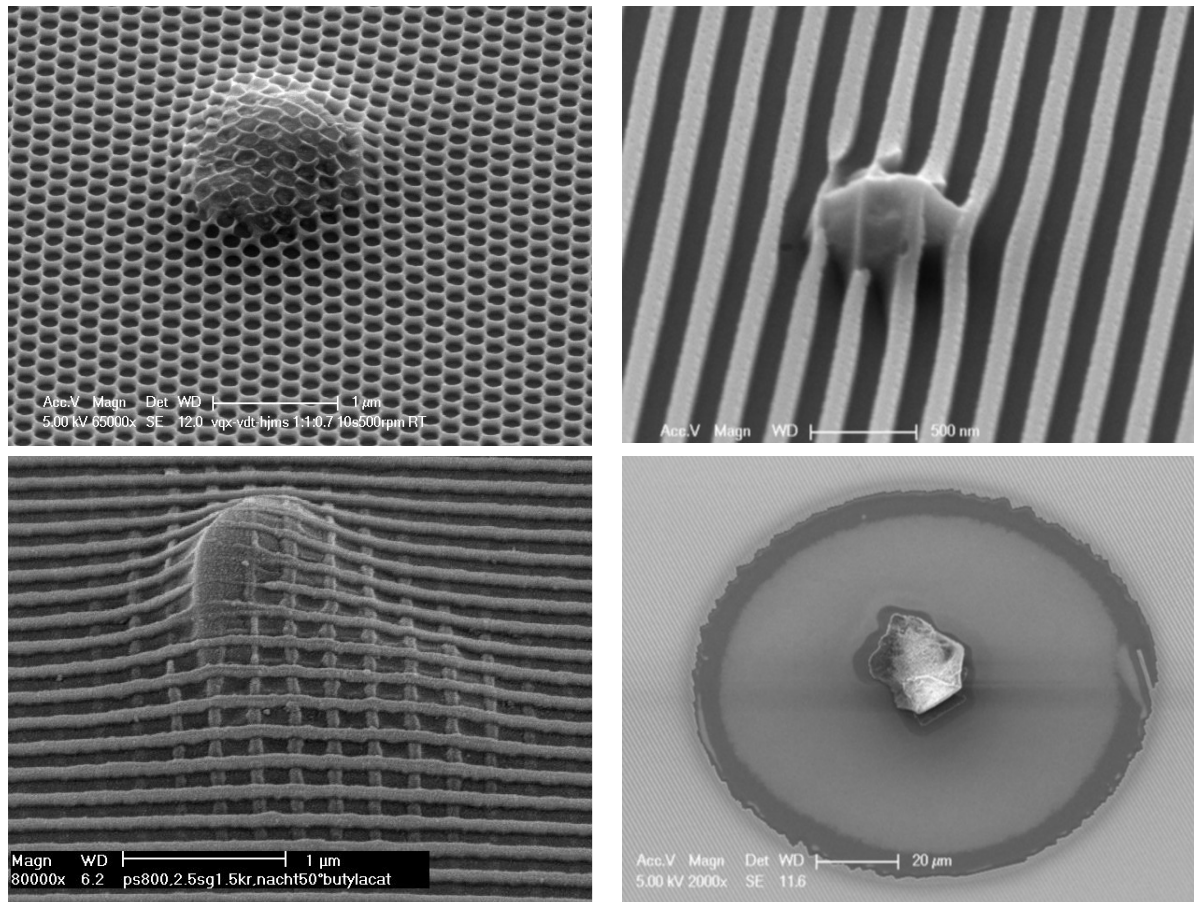*Figure 21. SEM images of sol-gel patterns made using SCIL on substrates with particle contaminants. Due to the softness of the stamp the patterns are imprinted over particles, while the surrounding pattern is undisturbed.*
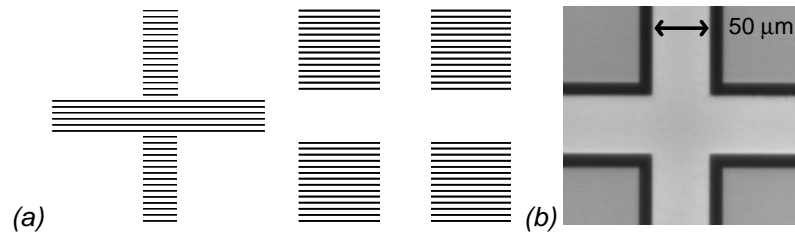
Figure 22. (a) Schematic of the cross (left) and box (right) marker, which are defined by gratings. (b) CCD image of a box-in-box alignment marker in contact.

2.5.2 Design of overlay alignment markers

Alignment marker patterns can be used to determine the absolute or relative position between a stamp and substrate and to detect pattern deformations. To provide absolute alignment down to ~1 µm box-in-box type of alignment marker is used. This consists of a 50 µm wide cross which is located on the stamp (molded from a first master). The corresponding box, an area with a gap width of 70 µm in the form of a cross, is formed by imprinting sol-gel on a substrate (stamp molded from second master). The cross and box patterns are composed of gratings with a pitch of 580 nm, see Fig. 22(a).

When illuminated with 450 nm light from an LED under an angle of 61° to the substrate normal, the -1st reflection order exits perpendicular to the substrate, see Fig. 23(a). The patterns are viewed using a long working distance objective coupled to a CCD camera. A picture of an aligned box-in-box marker in contact is shown in Fig. 22(b). This small difference in brightness of the box and cross patterns is attributed to a small difference in fill fraction or refractive index between the two gratings. The high contrast observed between grating and non-grating area enables accurate alignment of the two patterns.

2.5.3 The variation in magnification error between two stamps

The box-in-box alignment patterns can also be used to determine the difference in magnification error (defined as relative difference between master and stamp pattern) between two stamps. Magnification errors are predominantly caused by small variations in thermal thermal cycles during stamp fabrication and a difference between the thermal expansion coefficients of master and stamp. If two stamps have been prepared at different absolute temperature, the mismatch between the thermal expansion coefficient of master and glass back plate will produce a magnification error between the two stamps. Magnification errors are difficult to detect with laser diffraction (see 2.5.1) as these only measure local pattern deformations.

Figure 23. (a) Schematic cross section of the 580 nm pitch gratings used to generate high contrast alignment markers. (b) Schematic cross section of the 580 nm pitch gratings used to generate Moiré patterns. Both gratings have a depth of 90 nm and a fill fraction of $^2/_3$.

Left alignment marker   Right alignment marker

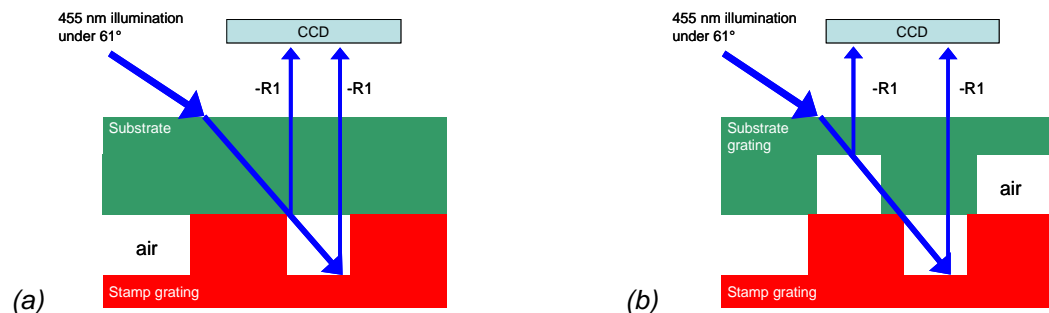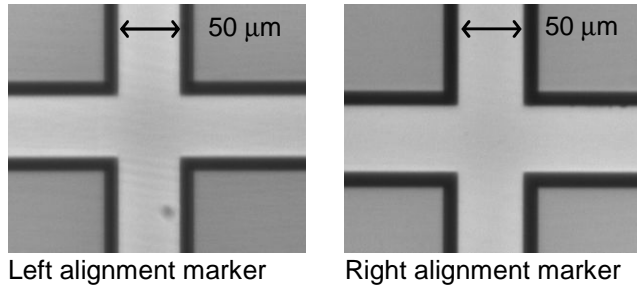*Figure 24. Two box-in-box type alignment markers in contact. The middle cross is 50 microns wide and the space between the squares is 70 micron. The distance between the left and right marker on the wafer is 70 mm.*

By comparing the alignments of two sets of box-in-box alignment markers spaced over a large distance, the magnification error can be determined. To do so, we use a stamp to imprint the box pattern on a substrate. A second stamp with the corresponding cross is then brought into contact to form the box-in-box pattern. The box-in-box markers are positioned 70 mm from each other. By simultaneously aligning the two markers, the distance between the middle cross on the substrate and the edge of the outer cross on the stamp is minimized. Figure 24 shows the aligned left and right stamp and substrate markers while in contact.

We used computer pattern recognition to measure the distances between the cross and the box in both directions where the width of the middle cross was used for calibration. The distances were found to be all equal within the measurement accuracy of $\pm\,0.25$ µm. This is much larger than the maximum position error of the e-beam generator ($\pm\,25$ nm) which was used to produce the two master patterns. The maximum magnification error between the two stamps is therefore 2×0.25 µm over 70 mm, or 7 ppm. The measured magnification error of 7 ppm is the upper value due to the uncertainty in the optical measurement of the position of the crosses in the alignment markers.

2.5.4 Design of Moiré interference alignment markers and in-situ pattern deformation characterization

Moiré interference techniques enable the detection of movements down to the nanometer level. Here, a Moiré pattern is formed by a grating on a substrate in contact with a grating in a stamp. This can result in light and dark patterns due to constructive or destructive interference of light in the two gratings.[61-65] To use Moiré patterns in the SCIL setup the optical design depicted in Fig. 23(b) was developed. The grating base period is 580 nm with a depth of 80-90 nm. The gratings are illuminated while in contact with 450 nm light from a LED under an angle of 61° to the substrate normal. Light from the 1st reflection orders of the top and bottom gratings interfere and form a Moiré pattern which is recorded using a CCD camera.

To control the period of the Moiré fringes, we use a Vernier Moiré technique in which two gratings of slightly different periods are in contact. To do so, two masters with corresponding grating patterns were produced by e-beam lithography and two SCIL stamps were molded from these masters. Using the SCIL setup the patterns in the first stamp are imprinted in sol-gel resist on thoroughly cleaned AF45 glass substrates. The second stamp, which contains the corresponding grating is then loaded in the SCIL setup and brought into contact with the first imprinted gratings. In the first experiments, using gratings with a fill fraction of ~0.5 we noticed that the contrast of the Moiré patterns changed over time. We found that this is caused by grating lines that do not stay on top of each other as shown in Fig. 23(b), but would actually sag between each other and interpenetrate. This changes the interference condition and thus the contrast of the
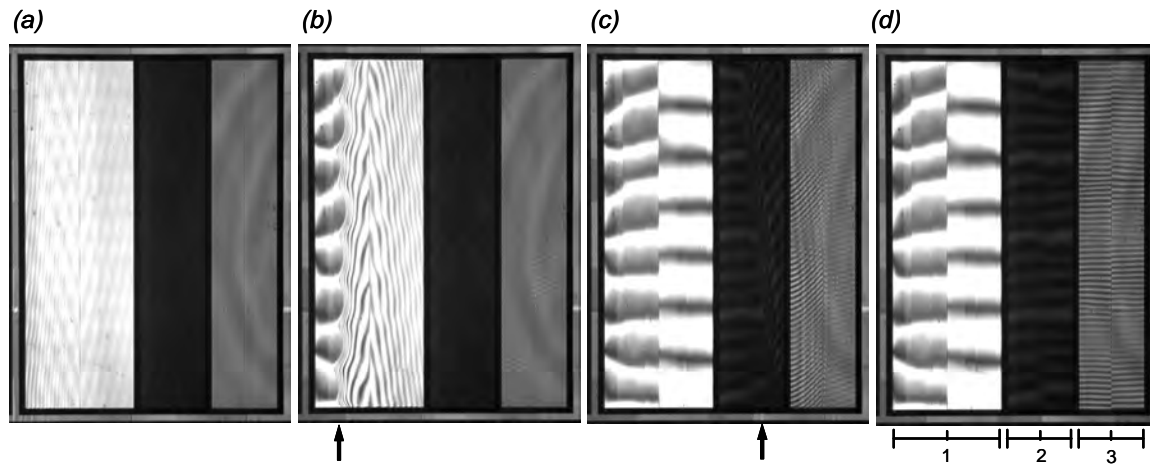
Figure 25. Three distinct pairs of Moiré patterns are formed as two grating sets are brought into contact using the SCIL setup, the contact line advancing 2.5 mm each time. (a) The stamp is in close proximity; (b)-(d) stamp in contact, with in (b) and (c) the contact line indicated by arrows; in (d) the stamp is in full contact. The numbered sections in (d) refer to grating pitches of: 1. 580/580.3 nm, 2. 2317/2320 nm, 3. 10.000/10.050 μm.

Moiré pattern. We then changed the grating duty cycle to $^2/_3$ and found that the Moiré patterns do not change contrast over a timescale of several days.

To determine absolute position errors using Moiré fringes, the absolute placement of the gratings has to be known to at least within half the grating pitch. This is due to the repetitive nature of the Moiré interference after one grating period. To enable absolute alignment down to nm accuracy, a method is needed that can detect absolute position changes from sub-mm to nm scale. Our design uses Moiré patterns with three length scales, which are subsequently aligned, starting with the coarse pattern.

Using the box-in-box alignment markers and the SCIL setup, the stamp and the substrate which contain the imprinted markers were aligned to within 1 μm. Figure 25 shows successive CDD images of a Moiré alignment marker pattern as the stamp is brought in contact with the substrate. The area over which a Moiré pattern is formed is 8×6 mm. In Fig. 25(a) the stamp is in close proximity, but not in contact, in (b) the stamp is partly in contact with the substrate (arrow indicates the position of the contact front), the contact has advanced 2.5 mm in (c) and in (d) full contact is established. In Fig. 25(d) from left to right three different Moiré patterns are observed (indicated 1,2,3) which correspond to grating pitch combinations of 580/580.3 nm, 2317/2320 nm, 10.000/10.050 μm, respectively. These three Vernier gratings are used in pairs: for each pair each time the left part of the pair has the shortest pitch located on the substrate and the right part has the shortest pitch located on the stamp. This design has the following advantages that when the patterns are moved perpendicular to the grating direction in a pair, the left and right Moiré fringes move in opposite directions. This doubles the resolution per pixel as not the absolute shift of a Moiré fringe is measured, but the relative shift between two Moiré fringes. The patterns are designed such that for absolute alignment all the fringes have to line up, as shown in Fig. 25(d). This pattern also helps to optimize the alignment procedure: if the previous alignment step accuracy is better than half the grating pitch of the next Moiré grating set, the fringes which have the smallest off-set need to be aligned next.

The following patterns and features are observed in the Moiré patterns of Fig. 25(d). The 580/580.3 nm Moiré pattern has a high contrast and shows the predicted 8 fringes. The 2317/2320 nm Moiré pattern shows a repeating pattern of 3 dim lines and a brighter fourth line. This can be explained as the 2317/2320 nm gratings are designed to reflect the fourth diffraction

order into the CCD camera. The period of the bright fringe corresponds to a period of 2317 nm (of which there are 4 over 8 mm distance). The dim fringes repeat every 580 nm, as the fourth order has four times the accuracy of the first order. The 10 μm Moiré pattern has lower contrast. The 10 μm gratings are made using areas of 5 lines with a pitch of 580 nm, which are placed on a pitch of 10.000 and 10.050 μm. In this way the 580 nm gratings diffract light into the CCD camera with a periodicity of 10.000 and 10.050 μm. The combination of 10.000 and 10.050 micron gratings results in four (low contrast) Moiré fringes over 8 mm. The high frequency Moiré fringes result from interference of the 580 nm grating areas which shift 50 nm every 10 μm. Therefore, a 580 nm fringe will repeat after 580/50 nm = 11.6 periods of 10 μm, corresponding to 116 micron. This will result in 69 fringes over a distance of 8 mm, as is observed in Fig. 25(d).

Our Moiré method magnifies position errors between the two gratings up to a factor of ~3000. Therefore pattern deformations are easily observed in distorted or shifted Moiré fringes. For example the e-beam pattern generator generates stitching errors every 0.5 mm due to an inaccuracy of ~20 nm in the stage positioning. These errors are clearly present as discontinuities in the individual fringes of the 580 nm Moiré pattern of Fig. 25(d). Besides particles and pattern edge related distortions the Moiré fringes are straight and have a regular spacing. More importantly, the Moiré pattern is identical each time when contact with the stamp is made. From ex-situ laser diffraction measurements and this in-situ Moiré method we conclude that the SCIL technique is able to reproduce patterns without introducing pattern deformations that are intrinsic to the SCIL method. Particles are the principle cause of defects but due to the elasticity of the rubber stamp these remain localized around the particle and do not influence the pattern outside the vicinity of the particle. This confirms that the thin glass carrier provides adequate in-plane stiffness in the rubber to prevent pattern deformations.

2.6 SCIL overlay alignment method

In several applications multiple layers must be made on top of each other and it is important to achieve a high alignment accuracy. For example, a 3D photonic crystal of the woodpile type is composed of multiple layers that are to be aligned to within ~30 nm with respect to each other, in order to obtain a 3D optical bandgap in the 550 nm spectral range when using a material with an index of refraction n=2.3.[66]

The substrate and stamp cannot be accurately aligned using a non-contact method as this leads to parallax errors. Alignment of the stamp and substrate while they are in contact is impossible due to the large imprint area in SCIL. We tested the reproducibility of placing a stamp from the SCIL groove plate into contact with a substrate. Using the box-in-box alignment markers from Fig. 22(b) we measured variations of ~1 μm. Therefore, this method is unsuitable for nanometer accurate overlay alignment. However, we found that when the stamp is kept in contact with the substrate over a small area, the stamp can be placed back in the original position to within 5 nm, as measured using the Moiré interference markers described above. This accuracy is obtained even as the stamp is released from the substrate over 9 cm from the measurement position, corresponding to an error of only 0.06 ppm. Our explanation for the remarkable accuracy is that the stamp in contact with the substrate forms a rigid connection. Furthermore the SCIL imprint principle allows the stamp to be applied to the substrate in a stress free manner. The reproducible stress free application of a stamp to a substrate is possible due to Van der Waals' forces that pull the PDMS stamp in contact and move the contact line forward. In effect the SCIL method acts as a controlled stamp release mechanism. As a result no external forces are applied to the stamp which would deform the pattern and result in misalignment.
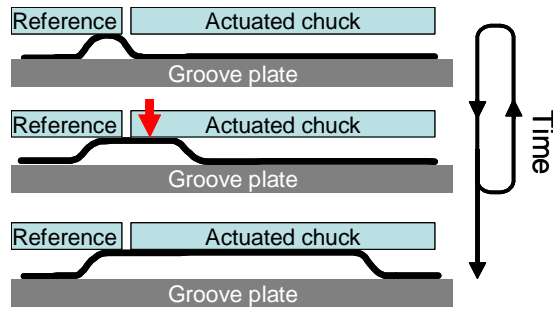
Figure 26. Method to provide overlay alignment while keeping the stamp in contact with the reference substrate. The stamp is placed in contacted with the substrate held by the chuck, and the position error measured. After retracting the stamp from the chuck, the position with respect to the reference is corrected. After making contact with the substrate, the corrected position error is measured again. Once the position is correct the pattern is imprinted by making full contact over the substrate.

Figure 26 shows a schematic of the technical realization of the developed method which is based on the highly reproducible way a stamp can be returned to a position on a substrate. The setup consists of a reference plate were the stamp is kept into contact, while the position of the chuck with respect to the reference is controlled by closed-loop piezo actuators.

The alignment method has to following sequence:

1. The stamp is in contact with reference and contact is made with the chuck.
2. The position error between stamp and substrate is measured.
3. The stamp is released from the chuck, but stays in contact with the reference.
4. The measured position error of the substrate is corrected by using the piezo actuators to position the chuck to a new position with respect to the reference.
5. The stamp is placed back into contact with the chuck and the position is measured again.
   → Steps 3 to 5 are repeated until the desired position of the substrate with respect to the stamp is obtained.
6. Once the substrate is aligned with respect to the stamp, the pattern is imprinted by fully contacting the stamp over the substrate.

2.6.1 SCIL imprint tool with incorporated substrate position control with nm resolution

Together with Philips Applied Technologies, a setup was designed and developed to enable the alignment method described above. The goal of the setup was to position a substrate with respect to the reference with nm accuracy. Figure 27(a) show the schematic of the SCIL setup and an exploded view of all the components starting from the base frame (bottom) which holds the groove plate. The aluminum reference frame is composed of the quartz reference plate, aluminum chuck frame and quartz chuck (top). Figure 27(b) shows a photograph of the SCIL setup consisting of the outer aluminum reference frame, which is actuated for coarse alignment by micrometer spindles. Piezo actuators and capacitive sensors in the frame control the position of the inner black aluminum chuck frame with the quartz chuck. The reference area in Fig. 26 is the quartz reference plate, which is attached to the outer aluminum base frame, see Fig. 27(a). The quartz reference plate is mounted in the base frame using three linear leaf springs which compensate thermal expansion differences and keep the reference plate centered; the height of the leaf spring is ~ 20 mm to provide stiffness in the vertical direction. The reference has a square opening in the middle in which the quartz chuck fits into. The quartz chuck is placed in position in the aluminum chuck frame using metal half spheres and V-grooves at three positions; the glass is secured by pneumatic actuators. This setup allows the quartz chuck to be removed from the setup to load a substrate while the stamp remains in contact with the reference quartz

plate. The chuck frame is connected to the base frame using three elbow leaf springs. These keep the quarts chuck centered in the quartz reference and allows hysteresis-free in-plane x-, y- and rotation movement of the chuck frame for up to ~100 μm with low force. The height of the leaf spring is ~ 20 mm to provide stiffness in the vertical direction. Three manual vertical micrometer spindles in the base frame control the gap between the stamp and the quartz chuck / reference. On the outside of the base frame three manual horizontal micrometer spindles can be seen which are used to align the chuck to the stamp down to ~1 μm. When the quartz chuck is placed in the setup, there is between 50 and 300 μm space between the chuck and the quartz reference plate. This allows the chuck to be positioned within this range by three piezo actuators which connect the chuck frame to the base frame. The piezo actuators have a travel range of 50 μm and their position is controlled by capacitive sensors, operated in a closed loop. The position of the chuck frame to the base frame is measured at the three positions where the piezo is actuating the chuck. These lie on the two symmetry axes of the chuck.

(a)

(b)
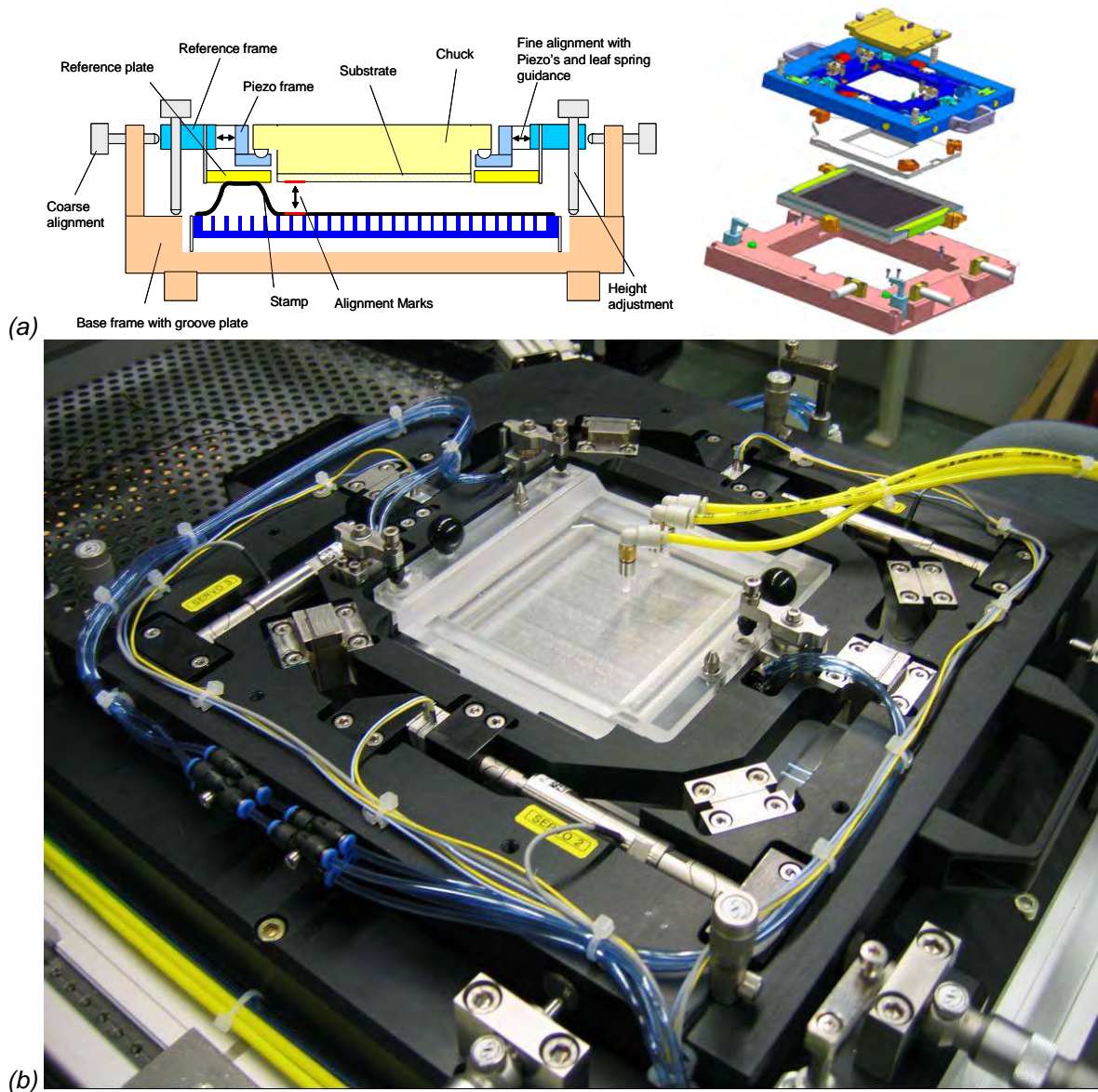
Figure 27. (a) Schematic cross section of the SCIL setup and exploded view of the complete assembly with from bottom to top: ground frame, groove plate, quartz reference plate, base frame and quartz chuck. (b) Photograph of the SCIL setup with piezo feedback controlled quartz chuck. The chuck position is controlled by piezos with respect to the black aluminum frame. The distance between the two frames is measured using a capacitive sensor on the symmetry axes of the chuck where it is actuated.
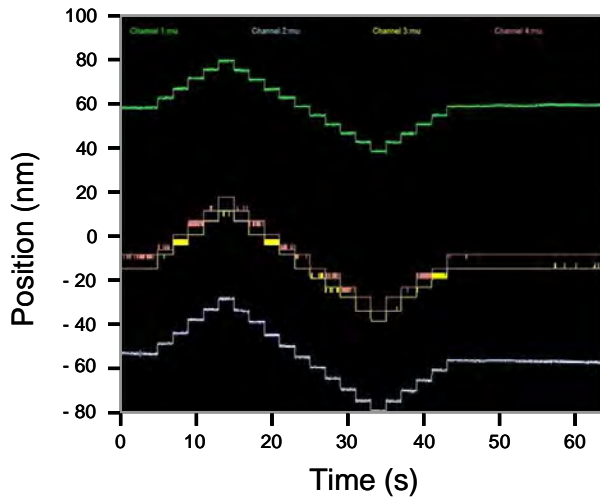
Figure 28. Comparison between the position readout of external capacitive sensors (top and bottom) to the position readout of the capacitive sensors controlling the piezos when taking 5 nm steps.

The quartz chuck is required to move without hysteresis or stick-slip behavior, which means the aluminum frame may not display these phenomena as it is positioned by the piezo actuators. We therefore compared the chuck movement, given by output of the piezo capacitive sensor, with the actual movement of the chuck, which was measured using two external capacitive sensors. The external sensors are mounted on the quartz chuck and the aluminum reference frame and measure the movement between these two components. The piezo actuators are programmed to make 20 steps of 5 nm while the positions are recorded over 60 seconds. The 5 nm steps are controlled by the piezo actuator's individual capacitive sensors.

Figure 28 shows position measurements as function of time as the stage is moved in 5 nm steps of the piezo's two capacitive sensors (middle) and two external capacitive sensors. As can be seen from the data, the external sensors exactly measured the 5 nm steps. In the measurement no stick-slip behavior is observed and there is no hysteresis present between back and forward movement. The absolute difference between the beginning and end position of the external sensors is caused by thermal drift in the mounts which hold the external sensors. These measurements are performed for all three piezo's actuators and confirmed that the chuck moves reproducibly and without hysteresis over distances of 30 µm. In practice, the stamp is in contact with the quartz reference plate and not the aluminum reference frame. We compared the position of the quartz reference plate and the quartz chuck in the same manner as for the quartz chuck and the aluminum base frame. The results showed identical performance as for the measurement for the distance between the aluminum frame and quartz chuck. The high stiffness of the system allows this indirect measurement to be used and rely on the output of the piezo actuator's capacitive sensors to accurately monitor the movement of the chuck with respect to quartz reference plate.

The alignment scheme depicted in Fig. 26 can introduce an uncertainty in the position reproducibility, as the stamp has to bridge the gap between the reference plate and the substrate. This is done while the closed loop piezo system controls the position of the chuck with respect to the reference plate. We measured the reproducibility of the whole system by using the Moiré alignment markers, imprinted on a substrate which was loaded on the quartz chuck. We found that we could reproducibly place the stamp back to within 5 nm on the actively controlled substrate/chuck after it was released. This demonstrates the robust overlay principle and very high accuracy of the SCIL imprint method.

2.7 Overlay alignment results

Figure 29 shows the design of the alignment markers patterns for the substrate (a) and stamp (b) used in overlay alignment experiments. The top left and right markers have box-in-box and Moiré type patterns, the top centre pattern has only Moiré type markers. The left and right Moiré markers are sensitive in the y direction and used for alignment in y direction and rotation control.

The centre marker is used to align the x direction only. The distance between the two y markers is 70 mm and these are located on a line 35 mm above the substrate centre. The stamp also contains five 2×2 mm grating areas arranged within a 3×3 cm square as indicated in Fig. 29(b). Within each square area gratings with a 240 nm pitch are oriented in two perpendicular directions to enable the detection of alignment errors in two directions.

To perform overlay alignment, the position of the stamp with respect tot the substrate has to be determined. This procedure is performed in a semi-automated manner using a Matlab program. First the left and right box-in-box markers are imported simultaneously and the number of pixels between the middle cross and the surrounding box is measured in x- and y-direction at four positions around the middle of the cross pattern. The width of the middle cross (50 μm) is used to calibrate the measurement. From the measured offsets the alignment error in the centre of the substrate and the rotation error around the centre is calculated. Subsequently these values are used to calculate the piezo actuator movement to correct for the misalignment and rotation error. Using typically 2-3 iterations, where each time the stamp is retracted from the substrate but kept in contact with the reference, the detected offset in the centre of the substrate is reduced to less than 200 nm (as calculated by the program). This corresponds to the maximum resolution of our box-in-box alignment procedure.

The box-in-box alignment ensures the pattern overlay error is less than 2 μm, which allows that the Moiré images can be used to further align the patterns. From the three alignment marker positions Moiré patterns are imported in the Matlab program and analyzed, see Fig. 30. For each Moiré pattern pair, two line scans are obtained by averaging 50 pixels in the vertical direction. For the 10 μm Moiré patterns the high frequency oscillations are filtered out using a Fourier transfer. The resulting four fringes corresponding to the 10/10.05 μm Moiré pattern and are plotted in the top right panel. Moiré patterns for the 2317/2320 nm Moiré are plotted in the bottom panel of Fig. 30(b) without filtering. To align the patterns, two fringes are manually selected by dragging a box over the fringe peak (see bottom panel in (b)).

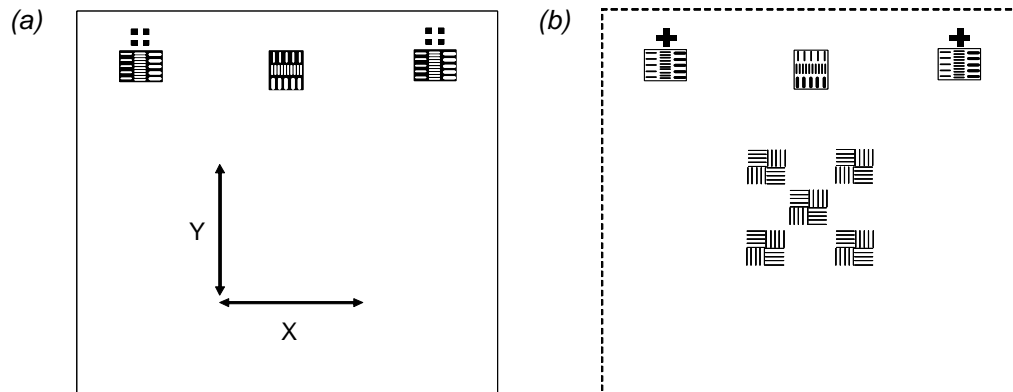*Figure 29. Schematic of the position of the alignment markers on the substrate (a) 100x100 mm AF45 glass with imprinted alignment markers. (b)100×100mm area on the stamp with corresponding alignment markers and test patterns consisting of 240 nm pitch gratings in two directions.*
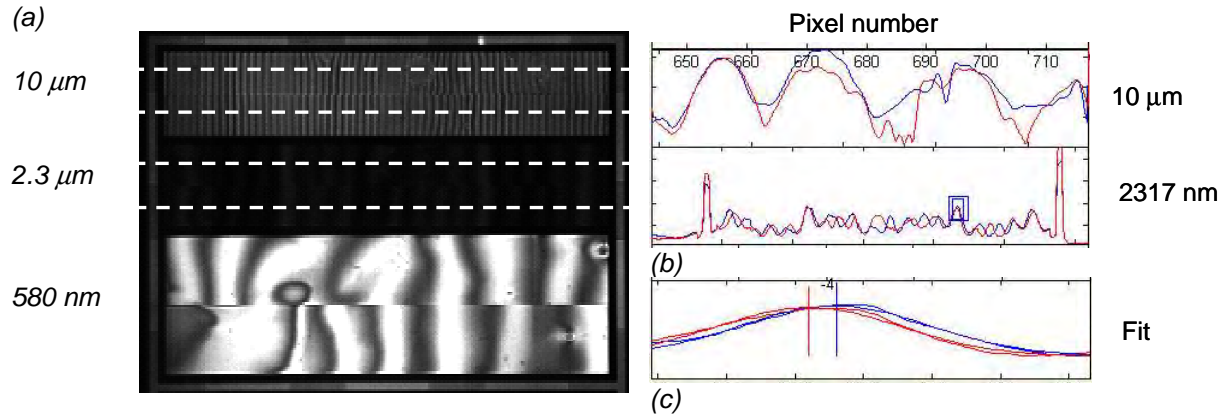
Figure 30. (a) CCD image of Moiré interference patterns with the grating periods indicated. (b) Line scan taken through the data in (a), indicated by dashed lines. (c). Zoom in of data from 2.3 μm grating in (b, see box) with Gaussian fit. The detected offset is 4 pixels corresponding to 20 nm.

From the selected data in the box the peak is fitted using a Gaussian and the peak position determined, see Fig. 30(c). The number of pixels between the two Gaussian peaks is determined and the pixel size calibrated using the known fringe spacing. This procedure is performed for the outer two Moiré markers which gives the sample rotation and off set in y-direction. From the middle marker an offset in x-direction is determined. Subsequently, in the same manner as used for the box-in-box markers the piezo actuator movement is calculated to correct the measured misalignment. In our system the resolution of a measured Moiré pattern is given by the number of CCD pixels per Moiré fringe. In theory the resolution per pixel in the three different Moiré fringes is: ~50 nm for the 10 micron, 5 nm for the 2.3 micron and 2.5 nm for the 580 nm Moiré patterns, respectively. In practice the alignment is dependent on the pattern quality which is mostly influenced by particles. This as can be seen in the bottom part of Fig. 30(a) where a particle distorts the pattern. To minimize particle induced alignment errors it is important to align identical fringes in subsequent imprints.

To assess the alignment performance of the whole system we aligned the stamp containing the 240 nm gratings to the substrate. To do so, the alignment markers imprinted on the substrate are first covered with tape and sol-gel resist is then spin coated over the substrate. After removal of the tape the markers are free of sol-gel resist. The substrate is loaded in the SCIL setup and aligned to the stamp. This is done by only pressurizing the stamp at the alignment marker position, bringing the stamp in direct contact with the substrate at that position. After 3 iterations the residuals in the offset are minimized. Next, the rest of the substrate is contacted, thereby imprinting the gratings. To obtain contrast during later SEM inspection, the centre area of the imprinted 240 nm gratings is covered with 10 nm of molybdenum using sputter deposition. Next, sol-gel resist is applied again and a second alignment performed, after which the same grating pattern was imprinted over the first molybdenum coated layer. Both imprints have thus been separately aligned towards the alignment markers imprinted on the bare substrate.

This procedure was first performed by using the box-in-box alignment markers. Figure 31(a) shows a SEM image taken under an angle of 45° of the corresponding two aligned layers. As can be seen, each grating layer contains horizontally and vertically oriented grating lines. The bottom layer can be distinguished by the light color due to the molybdenum. The lines are well aligned in two directions between the first and second grating layer. The alignment error is determined by measuring the offset between the first and second grating in two directions. For the image in Fig. 31(a) this is 21 nm in the horizontal and 55 nm in de vertical direction respectively. Figure

31(b) shows an overlay error map for the five grating positions, assuming the first layer was perfectly aligned. The square corresponds to the area of the five regions which contain gratings, see Fig. 29(b) and the overlay error is represented by the distance between the two squares, with the length scale indicated (100 nm scale bar). From Fig. 31(b) it can be seen that the maximum misalignment between the two grating layers is 110 nm (top right pattern). The maximum rotation error is found to be 1.3×10^{-6} rad. As these errors are the sum of two separate alignment runs, the alignment error for a separate run therefore is less than 55 nm. From this data the magnification error between the first and second imprint can be calculated. We expect the error to be the result of thermal expansion variations which are symmetric around the substrate centre. Therefore, the data for the second imprint in Fig. 30(b) are translated so that the residual overlay error is zero in the middle. The remaining off-sets for the other four points are then a measure for pattern distortion and magnification errors. We find a maximum magnification error of 1.2 ppm in the x direction and 2.4 ppm in the y direction. This is highly accurate as no active temperature control was used and there was a day between the two aligned imprints runs.

The misalignment found in Fig. 31 is due to a combination of magnification errors and alignment errors. Comparing the maximum misalignment in Fig. 31(b) of 110 nm with the magnification error over a 30×30 mm area of 72 nm (assuming the 2.4 ppm error found above), we calculate that the maximum alignment error amounts to ~40 nm. Improvement in overlay accuracy can be expected as magnification errors can be eliminated by using a temperature controlled environment during imprinting. Furthermore, the currently used alignment process only analyzes the alignment patterns and minimizes the offsets. This process can be improved by using Moiré interference markers as described above. This work is in progress. These results show our SCIL alignment method in combination with the Moiré alignment procedure can reach 20 nm overlay precision over an area of 1×1 cm^2.

Finally we study the reproducibility of the imprint process for a given stamp. Over a four-year period we have made over 3000 imprints in sol-gel resist using the same stamp which contains 150 nm high, 130 nm wide lines on a pitch of 580 nm. By comparing the SEM images of sol-gel imprints over time we do not see any degradation of the pattern over time. Using a grating pattern in two directions makes it possible to determine the reproducibility of individual features, as a single feature can be located. Figure 32 shows SEM images of two overlay alignment tests for the same position. The patterns in Fig. 32(a) are made after ~24 imprints and in (b) after ~40 imprints. This shows that even the smallest features, measuring only ~15 nm wide are replicated each time with high fidelity. These results confirm the robustness of our SCIL imprint method in the replication of large area nanoscale features.
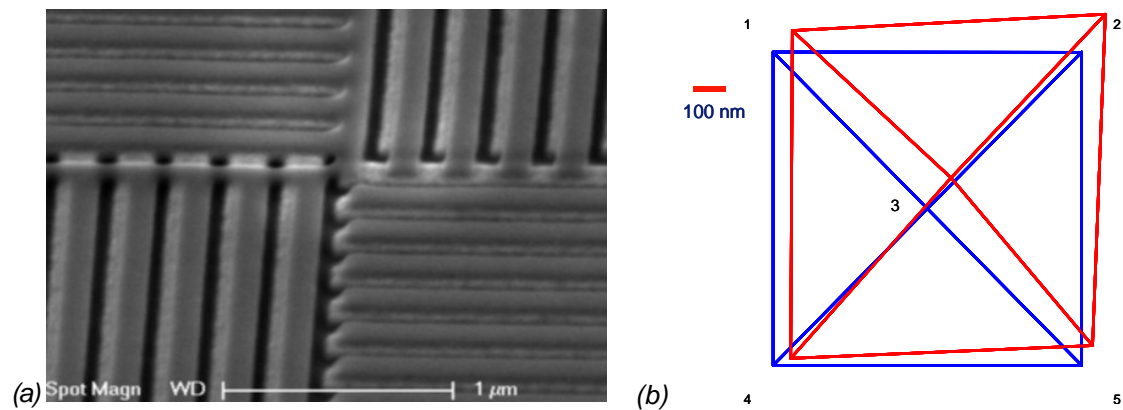

Figure 31. (a) SEM image of two aligned grating patterns in silica taken under a tilt of 45° of two aligned and imprinted gratings. (b) Schematic representation of the overlay error for five positions on the substrate.
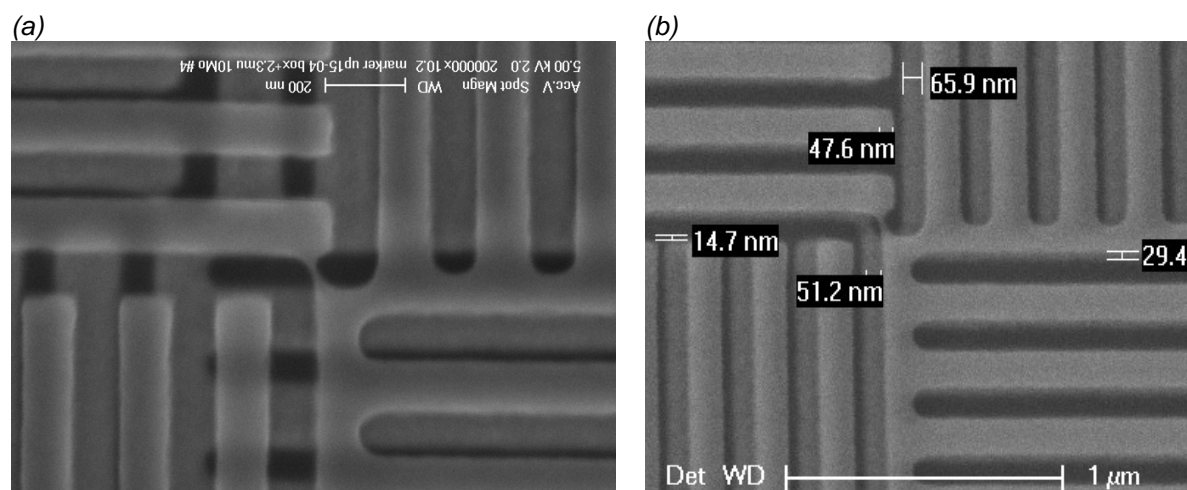
Figure 32. SEM images of two overlaid grating patterns in silica taken at the same position after (a) ~24 imprints and (b) ~40 imprints.

The high reproducibility and low pattern distortions found using the SCIL process have to our knowledge never been achieved by other soft imprint techniques. In fact, the reproducibility and overlay performance of soft stamp imprint techniques has only been marginally studied. A study using PDMS stamps cured against a thick glass support and Moiré pattern analysis found relative distortions of just under a micron over an area as small as 0.25 cm^2.[58] Using the waveprint principle[48] and micro-contact printing to pattern gold on glass, an average distortion of 0.7 μm was found over an area of 10×10 cm; a resulting overlay error up to 2 μm was achieved over this area[49]. A recent study reported overlay errors of ~2.3 μm using H-PDMS stamps and ~0.5 μm when using a high modulus polymer (2600 MPa) as a stamp. These results were obtained over an area of only 50×50 μm.[59]

2.8 Sol-gel imprint resist optimization

In section 2.2 details of the sol-gel chemistry and processing for soft imprinting were shown. In this section we present further details on the optimization of the sol-gel imprint process. The imprint process of a sol-gel layer takes place in two steps. First, the solvents are removed and second, the sol-gel has to form a rigid inorganic network by condensation between two Si-OH groups or a Si-OH and Si-OC$_x$ (alkoxide) group.

2.8.1 Influence of the low vapor pressure solvents on the imprint time

As described in section 2.2.3 the sol-gel imprint resist is prepared from the hydrolysis base material and n-propanol containing 2.0 wt. % 2-(2-butoxyethoxy)-ethyl-acetate (BEEA), low vapor pressure solvent (LVPS). We studied several LVPS for use in the sol-gel imprint process. Criteria for the choice of these solvents are:

- Compatibility with sol-gel chemistry (acid or basic chemicals can not be used as this will lead to uncontrolled condensation. Alcohols can form the corresponding alkoxides).
- Avoid excess swelling of the PDMS stamp material.
- The vapor pressure must be ~20-100 times less than that of the majority solvents to ensure the high boiling solvent will be the last remaining liquid in the sol-gel resist while water and n-propanol are mostly removed.
- Non-toxic.

Three solvents were selected and tested for their influence on the imprint time: 1,2-propanediol, 2-(2-butoxyethoxy)-ethyl-acetate (BEEA) and methyl-benzoate (MBZ). The solvents' physical properties are listed in table VIII.

Solvent name	Boiling point (°C)	Vapour pressure @ 20°C (mBar)	Solvent type
1,2-propanediol	187	0.01	polar molecule
2-(2-butoxyethoxy)-ethyl-acetate (BEEA)	245	<0.013	Linear, semi-polar molecule
Methyl-benzoate (MBZ)	199	0.25	Aromatic, slightly polar molecule

Table VIII. Physical properties of low vapor pressure solvents used in sol-gel imprint resists.

To determine the influence of the LVPS on the imprint time a fresh solution of imprint resist is prepared each time. Equal weights of the same sol-gel hydrolysis batch are mixed with 1-propanol, containing 2 wt. % of LVPS. This imprint resist is used within two hours to imprint spin coated sol-gel layers of 70 nm thickness. The stamp consists of a 50-100 µm thick H-PDMS layer with ~2 mm Sylgard 184 as backing. The H-PDMS contains a grating pattern of 580 nm pitch, a fill fraction of 0.3 and depth of 130 nm. For each sol-gel mixture with a different LVPS the imprint time is varied and the resulting sol-gel patterns are studied by SEM.

Figure 33 shows SEM images in cross section and top view of the grating under an angle of ~45° for sol-gel imprint resists which contained (a) 1 wt. % 1,2-propanediol and (b) 1 wt. % MBZ. It shows that as the imprint times become longer the gratings are better defined with sharp corners and a more defined roughness. This roughness is present in the master pattern and is replicated with high fidelity. For shorter imprint times (2.5 min. for MBZ, 5 min. for 1,2-propanediol) the network formation has not progressed to such an extent that a glass-like solid has formed.

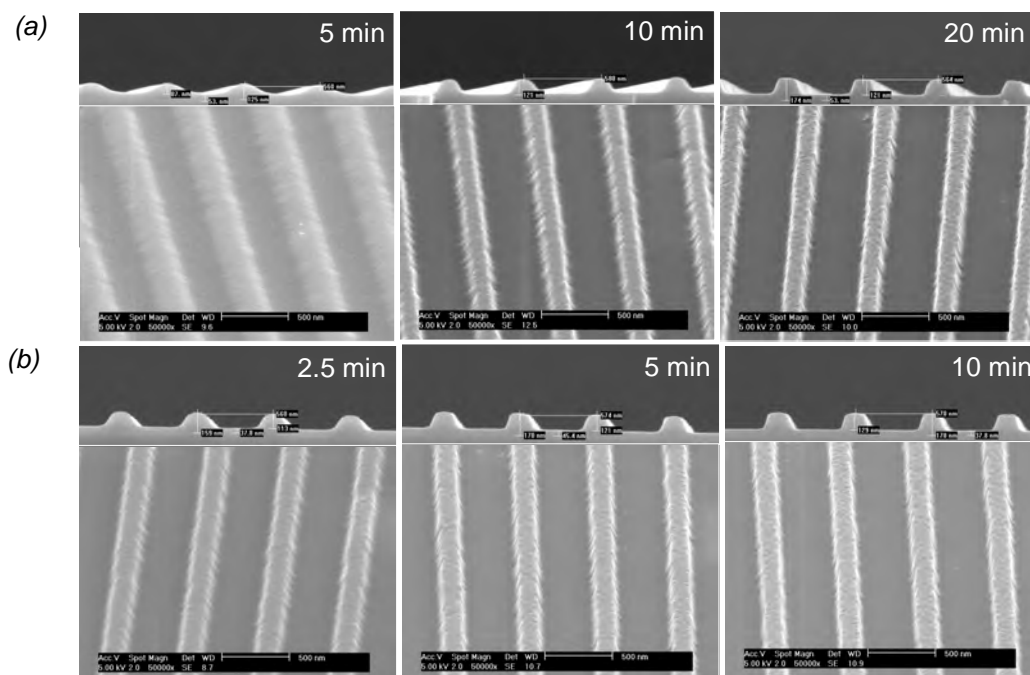*Figure 33. SEM images (cross section and top view) of sol-gel gratings made using 1,2-pronanediol (a) and MBZ (b) produced with varying imprint times. The influence of the low vapor pressure solvent can be clearly observed. Samples with 1,2-propanediol required at least 20 minutes to form high fidelity imprints. Sol-gel with methyl-benzoate form high fidelity patterns in less than 10 minutes.*

The sol-gel layer then is a highly viscous liquid or gel and as a result of surface tension sharp corners become rounded. Using resists which contained MBZ high quality replicas could be obtained using imprint times of less than 10 minutes, see Fig. 33(b). Similar results were obtained for BEEA (data not shown). A sol-gel resist containing 1,2-propanediol required at least 20 minutes to form a high fidelity replica. To explain the different behavior between 1,2-propanediol and the two other solvents we determined the time it takes the LVPS to diffuse into the PDMS. To approximate imprint conditions and the amount of LVPS that remains after spin coating, a mixture of water, 1-propanol and LVPS in the same proportions as in a sol-gel resist is spin coated on a silicon wafer. After the spin coat drying cycle (see Table III) a thin layer of LVPS is present on the substrate which is then is imprinted using the 580 nm grating stamp. At first the grating becomes index matched by the LVPS and is therefore not visible. Over time the LVPS is absorbed in the PDMS which removes the index matching condition and diffraction colors clearly visible by eye appear. The time between imprinting a layer of HBS and appearance of diffraction colors is ~2 minutes for all three low vapor pressure solvents in Table VIII. The imprint time is thus mainly determined by the sol-gel to form an inorganic network. The increased imprint time when using 1,2-propanediol is attributed to the formation of silicon-propanediol alkoxides during the last phase of the spin coat cycle and during the imprint. These alkoxides cannot condensate and suppress the network formation. The two other solvent cannot have substitution reactions with the sol-gel resist (see Table I) and therefore exhibit a shorter imprint time.

The pot life of the imprint resist is also influenced by the low vapor pressure solvent. Sol-gel imprint resists which contained BEEA or MBZ can be stored at -20 °C up to half a year and used without influencing the imprint results. Resists which contained 1,2-propanediol can only be used on the day of resist preparation. After a longer time, even when storing at -25 °C, the quality of the imprint is reduced. For example a sol-gel grating with a height of 70 nm directly after preparation of the resist reduces to a height of ~10 nm after a day. A possible mechanism could be that 1,2-propanediol exchanges both its alcohol groups with silicon alkoxide groups from different siloxane chains, effectively increasing the crosslink density. During the imprint process the highly cross-linked sol-gel reaches its gel point at a low solid content. After stamp release this results in strong shrinkage of the sol-gel features.

For the remaining experiments we used BEEA or MBZ as the high boiling solvent, with the exception of the fabrication of 3D photonic crystal templates. In this process multiple grating layers are patterned on top of each other and 1,2-propanediol is used because it does not dissolve the planarizing polymer.

2.8.2 Influence of sol-gel synthesis on the imprint time

The influence of time and temperature during the hydrolysis step on the condensation degree is studied by ^{29}Si nuclear magnetic resonance spectroscopy (NMR). NMR can be used to determine the fraction of silicon atoms that have chemical oxygen bonds to (multiple) other silicon atoms.[67,68] The variation of this ratio can provide insight in the condensation degree.
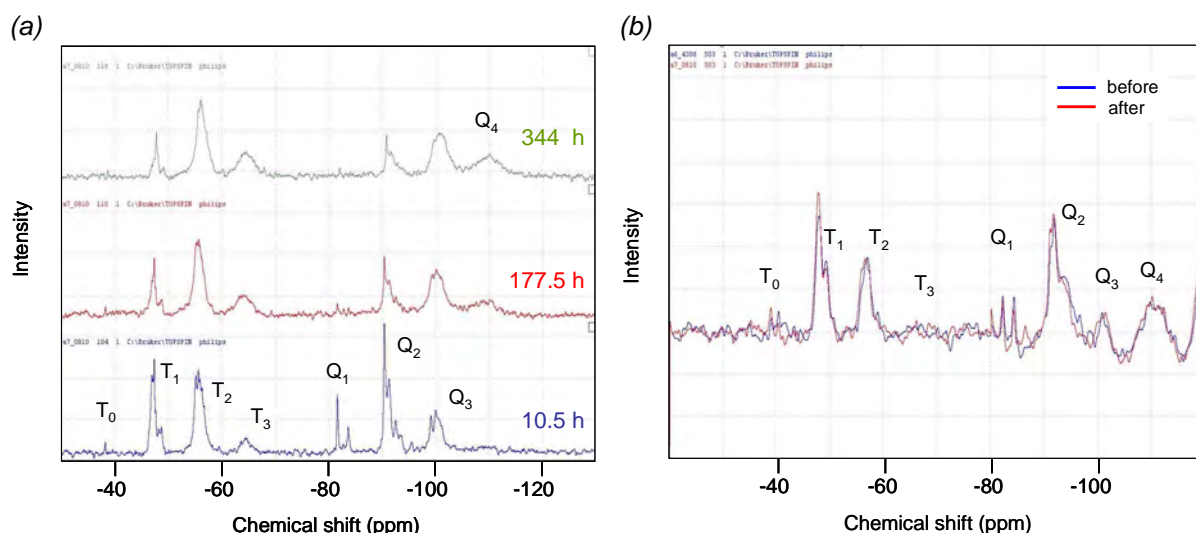
Figure 34. ^{29}Si NMR-spectra of a TMOS-MTMS (1:1) solution in n-propanol. (a) NMR spectra after 10.5, 177.5 and 344 hours at 25 °C, respectively. (b) NMR spectra before and after storing the sample for three months at -25 °C.

Figure 34 shows ^{29}Si NMR spectra of hydrolysis mixtures consisting of a 1:1 molar ratio of TMOS and MTMS and a water/silicon molar ratio of 9. The hydrolysis was performed with 1 M formic acid and a water/alkoxide ratio of 1:1. After the hydrolysis time of 30 minutes at 36 °C the mixtures are diluted with n-propanol to a concentration of 0.78 M Si/kg sol. The NMR spectra are measured while the sol-gel sample is cooled to -5 °C to suppress aging. In Fig. 34 peaks labeled "T" correspond to MTMS molecules with 0, 1, 2 and 3 Si-O-Si bonds to other silicon atoms, respectively. Similarly "Q" referes to the degree of bonding in TMOS. The peaks of TMOS and MTMS can be distinguished and do not overlap due to the methyl group which is covalently bound to silicon that shifts the NMR signal.

The aging (increased condensation) of a sol-gel mixture can be studied by comparing NMR spectra over time. Aging will result in a more condensed and cross-linked network with increased T_3 and Q_4 peak areas. This is clearly shown in Fig. 34(a) that show data for a hydrolysis mixture that is stored at 25 °C for 10.5, 177.5 and 344 hours. The peak areas corresponding to T_1, T_2, Q_1 and Q_2 decrease while those of T_3, Q_3 and Q_4 increase. When the same hydrolysis mixture is stored at -28 °C the shift to higher condensation degrees is not observed, as is seen in Fig. 34(b). This demonstrates that storage of sol-gel mixtures at low temperatures is essential for potlife.

We studied the influence of the sol-gel condensation degree on the minimum imprint time. To do so, hydrolysis batches are prepared at a controlled temperature using a thermostated water bath and allowed to react for varying times. Every time the same amount of sol-gel is prepared consisting of a 1:1 molar ratio of TMOS and MTMS with a molar water/silicon ratio of 9. The hydrolysis is performed with 1 M formic acid and a water/alkoxide ratio of 1:1. After the defined hydrolysis time the mixtures are diluted with n-propanol to a concentration of 0.78 M Si/kg sol. The resulting hydrolysis mixtures are stored in a freezer at -25 °C for at least 24 hours before ^{29}Si NMR is performed to determine the condensation degree. Figure 35 shows the condensation degree of TMOS and MTMS derived from the corresponding peak areas in NMR spectra. The hydrolysis temperature and time differs for varying the samples as indicated in the figure.

TMOS

MTMS

(a)   *(b)*
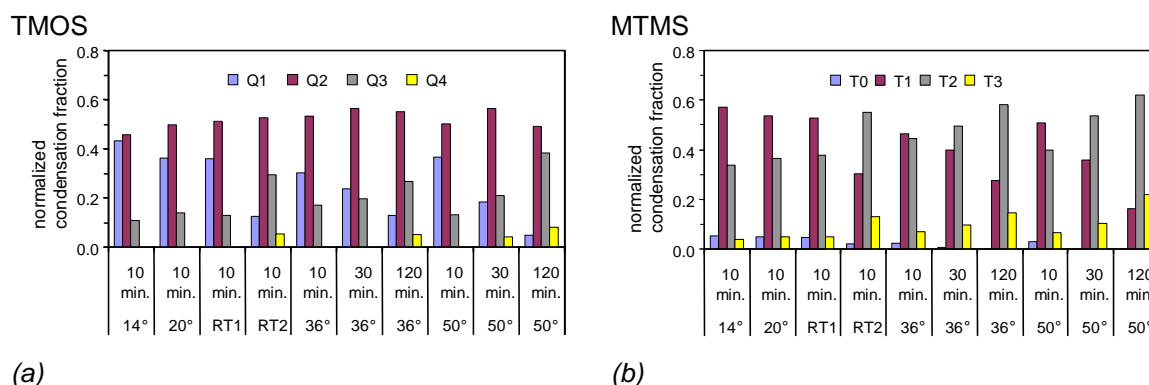
Figure 35. Normalized condensation fraction for the TMOS (a) and MTMS (b) precursors determined from the corresponding peak integrals in the NMR spectra for different hydrolysis temperature and time. Temperature is controlled by a water bath. Samples RT1 and RT2 had no active temperature control.

As can be seen from Fig. 35 longer hydrolysis times and higher temperatures increase the amount of higher coordinated silicon atoms. The formation of highly coordinated species become increasingly difficult due to increased sterical hindrance, and requires higher temperatures and more time. The samples RT1 and RT2 did not have active temperature control and as a result of the exothermic hydrolysis reaction reach a temperature of ~40-50 °C in about 1-2 min. after which the temperature slowly decreases. From the condensation fractions in Fig. 35 the degree of condensation (AF$_t$) can be calculated for TMOS and likewise for MTMS.

$$AF_t = 0 \cdot \frac{Q_0}{Q_t} + 1 \cdot \frac{Q_1}{Q_t} + 2 \cdot \frac{Q_2}{Q_t} + 3 \cdot \frac{Q_3}{Q_t} + 4 \cdot \frac{Q_4}{Q_t}$$

Degree of condensation (AF$_t$) for TMOS, with Q$_i$ the integral of the corresponding peak in the NMR spectrum and Q$_t$ the total peak integrals.

The results are shown in Fig. 36. As can be seen, the average the average condensation degree increases with increased temperatures and hydrolysis times.

Next, we determined the minimum imprint time of each hydrolysis mixture. Therefore a fresh imprint resist was prepared by mixing equal weights of a sol-gel hydrolysis mixture with 1-propanol, which contained 2 weight percent of methyl-benzoate. This mixture was used within
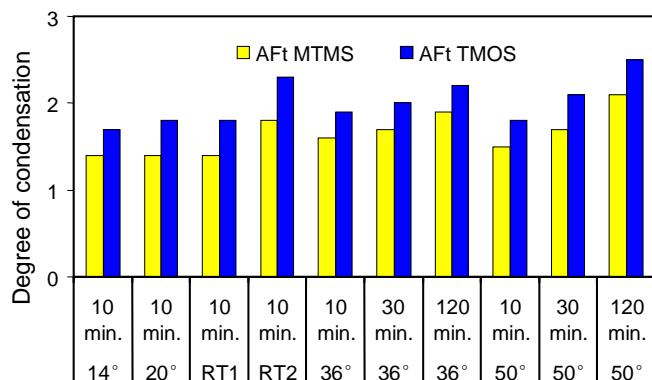
Figuur 36. Degree of condensation of TMOS and MTMS for hydrolysis mixtures prepared using varying temperatures and times. The maximum condensation degree is 4 for TMOS and 3 for MTMS.

two hours to imprint 70 nm thick sol-gel layers with a 1D-grating pattern of 580 nm pitch, fill fraction $^1/_3$, and height 130 nm (equal to the stamp used in Fig. 33). The imprint time was varied for each hydrolysis mixture and the resulting sol-gel pattern was studied by SEM. If the sol-gel had not reached the glass point the features would re-flow and sharp edges would not be present due to surface tension rounding. All the hydrolysis mixtures could be imprinted in 10 to 15 minutes with high fidelity, except for the mixture which was hydrolyzed for two hours at 50 °C, which could not be imprinted at all. During the experiments we noticed that the relative humidity, ambient temperature and age of the imprint resist influenced the imprint result more substantially than the variation in the degree of condensation. We therefore focused on the resist composition and the role water plays in the formation of the inorganic network.

2.8.3 The influence of water and alcohol on the sol-gel equilibrium state

As shown above, the condensation degree of a sol-gel system can be stabilized by cooling. However, a sol-gel system is in dynamic equilibrium (see Table I) and in solution hydrolysis and esterification proceed even at low temperature. We found there was a profound effect on the minimum imprint time as a function of alcohol dilution and water content. This is schematically indicated in Fig. 37 which describes imprint results for different water content and resist dilution.

Adding water to the imprint resist significantly reduces the imprint time of resist that has been stored at -25 °C. We explain this as follows. The imprint resist is prepared from the base hydrolysis mixture diluted with an equal amount of amount of alcohol. The increased imprint time can be explained by the shift in equilibrium from hydroxyl to non-reactive alkoxide groups (see esterification reaction in Table I). As a result the formation of the inorganic network is hindered, leading to a long imprint time. Adding water increases the reactive hydroxyl group fraction (see hydrolysis reaction Table I) leading to a fast condensation reactions and thus shorter imprint times.

2.8.4 Effect of water on sol-gel imprint performance

While a high water to silicon ratio is required for a shorter imprint time, a high water content has also disadvantages as it increases the surface tension which promotes spontaneous de-wetting of a thin sol-gel coating on a substrate. This effect can be suppressed by using up to 3 wt. % BEEA in the resist which lowers the surface tension. The BEEA will be the last solvent to be removed from the sol-gel material during spin coating due to its low vapor pressure.
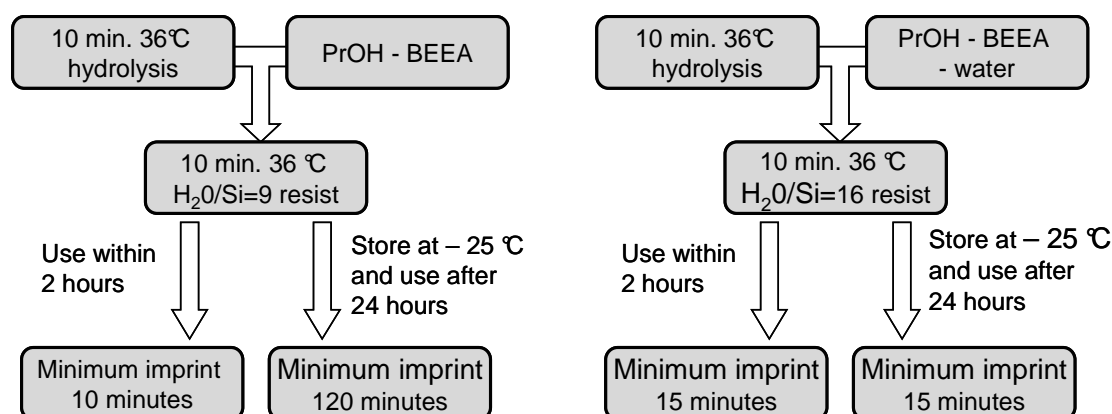

Figure 37. Diagram summarizing experiments on the effect of sol-gel dilution and molar silicon/water ratio on the minimum imprint time.

Furthermore, a sol-gel resist with relatively high water content will lead to a coating with a relatively high Si-OH content. During the imprinting of sol-gel the water that is formed in the sol-gel layer during cross-linking must be adsorbed by the PDMS stamp. However, while water has a relative high diffusion coefficient in PDMS, as it is a small molecule, the polar water molecule has low affinity with the a-polar PDMS. The amount of water that can be absorbed in PDMS is below 0.2 wt. %, compared to the absorption of 1 wt. % for methanol, 5 wt. % for ethanol [69] and up to ~10 wt. % n-propanol, which we determined by absorption experiments. The limited water absorption of PDMS leads to problems when multiple imprints are made is short succession using a high water content sol-gel resist in combination with a SCIL stamp with an impermeable glass support plate. As a result, after ~10 imprints the required imprint time is increased as the stamp becomes saturated with water. The remaining water in the sol-gel layer prevents condensation reactions to proceed. We did not observe this saturation effect for PDMS stamps without glass support, as water is removed through the top of the stamp. When a SCIL stamp with glass support plate was flushed with dry nitrogen for ~5 minutes after 3-4 imprints a saturation effect was not observed. We conclude that if the stamp becomes saturated a short nitrogen flush removes water from the SCIL stamp.

Based on the knowledge and practical experience described above, we formulated the following criteria for an optimized sol-gel imprint resist:

- High water to silicon ratio in the resist to increase the amount of Si-OH groups (reaction 1, Table I)
- Remove water during the drying cycle of spin coat step to increase the condensation degree in the sol-gel resist layer. (reaction 4, Table I)
- Substitute alcohol groups in the dilution solvents for solvents which cannot exchange with sol-gel. (avoid reaction 2&3, Table I)
- Substitute higher alcohols for lower alcohols to allow faster re-hydrolysis of formed alkoxide groups in the resist layer.

Various solvents and hydrolysis mixtures were prepared based on the recipe in Table II and benchmarked on: minimum imprint time, wetting behavior and performance under different relative humidity conditions. This resulted in two optimized resist formulations:

Resist A	Resist B
Hydrolysis I	Hydrolysis II
• 120 min. 36 °C using 1M formic acid • Dilution with n-propanol to 0.78 M Si / kg. and $H_2O/Si = 9$	• 120 min. 36 °C using 1M formic acid • Dilution with ethanol to 0.78 M Si / kg. and $H_2O/Si = 9$
Imprint resist	Imprint resist
• Dilution 1:1 with hydrolysis mixture I. • Dilution composition: 8.8 wt. % water, 25 wt. % acetonitrile, 2 wt. % BEEA and remainder diethyl-acetal.	• Mix mixtures I+II in ratio 1:9, then dilute 1:1. • Dilution composition: 8.8 wt. % water, 25 wt. % acetonitrile , 2 wt. % BEEA and remainder diethyl-acetal.

Table IX, Synthesis route of two optimized imprint resists based on the recipe in Table II.

Resists A and B have a water to silicon ratio of 15. Acetonitrile is hygroscopic and removes water as it evaporates. Diethylacetal is added because it has a low surface tension and vapor pressure equal to n-propanol. The resist compositions are optimized to have good wetting and form a uniform layer using spin coating. Both resists can be used to produce high fidelity imprints in thick (~100 nm) and thin (~20 nm) sol-gel layers on silicon substrates in less than 5 minutes.

The condensation degree of the sol-gel layer after the spin coat step is quite different for the two resists. Using resist A, the formed sol-gel has a relatively low condensation ratio, is liquid even without the use of BEEA and can be imprinted with high fidelity. In constrast, resist B requires the BEEA to keep the highly condensed sol-gel layer in a soft gel state for it to be patterned. This high condensation degree is obtained due to the high concentration of ethoxy groups in the sol-gel. These hydrolyze and condensate more easily as acetonitrile efficiently removes water from the layer. When using resist B and more precise timing of the spincoat drying step, high fidelity imprints can be made in less than 3 minutes. This is possible as the inorganic network is already almost completely formed upon imprinting. Resist B thus requires a more critical timing but the resulting imprint time is shorter.

2.8.5 Effect of the substrate on sol-gel imprint performance

Finally, we studied the effect of the substrate on the imprint performance. Comparing Si and GaAs substrates we found that using the same imprint resist high fidelity imprint are made in 10 minutes on silicon, but two hours are required when imprinting on a GaAs substrate. We used Fourier-transform infrared spectroscopy (FT-IR) to monitor the progress of chemical reactions in the sol-gel layer during solidification on several substrates.[70] The spectra are recorded by first taking a background spectrum of a substrate in ambient air, after which the sol-gel layer is applied on the substrate by spin coating and the sample is studied by FT-IR in ambient air to record transmission spectra of the sol-gel layer. Figure 38 shows FT-IR transmission spectra taken of a 100 nm thick sol-gel layer made using resist A as described in Table IX, taken after ~0.5 min. and 11 min. after spincoating, respectively. The absorption peaks are labeled with the corresponding molecular vibrations.

A broad absorption peak is found around 3300 cm^{-1} corresponding to Si-O-H groups. We further distinguish silicon-methyl groups of MTMS, Si-O-Si and Si-O bonds. As the sol-gel forms a silica network we see the Si-OH absorption peak decrease due to condensation. The Si-O-Si absorption peak (~1070 cm^{-1}) increases and shifts to a lower wavenumber, due to the overlap with a silicon-alkoxide absorption peak (~1160 cm^{-1}), which decreases in time due to
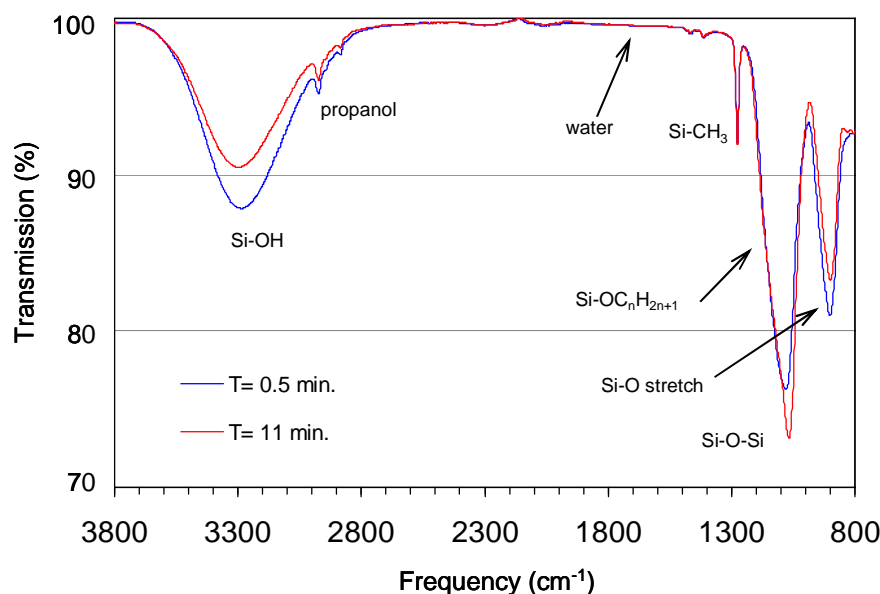

Figure 38. FT-IR transmission spectra of a ~100 nm thick sol-gel layer on silicon taken after ~0.5 min. and 11 min. in ambient air.

condensation reactions. The silicon-methyl peak is stable and can serve as a reference peak. The Si-O stretch absorption peak decreases, while an increased absorption is expected, but the absorption of this band drops as it becomes incorporated in the silica network.

By measuring reflectivity spectra of the sol-gel layer on a substrate the reactions in the sol-gel layer can be monitored on substrates that are IR transparent. The relative amount of (reactive) groups is then monitored by recording multiple spectra in time and determining the surface area of each peak. Figure 38 shows reflection measurements of the evolving peak area over time corresponding to the Si-O-Si vibration in the sol-gel layer. The peak area is integrated from 1010 to 1090 cm^{-1} to minimize interference with the absorption peak corresponding to silicon alkoxide groups. For each measurement we used resist A of Table IX and applied a 100 nm thick layer which was dried for 20 seconds at 300 rpm and 20 seconds at 1000 rpm before the sample is loaded in the FT-IR spectrometer. We used Si (including native oxide), GaAs (with or without plasma treatment), a sputter deposited layer of Al_2O_3 on silicon and a plasma grown Si_3N_4 layer on silicon.

From the data in Fig. 39 it is clear that the substrate substantially influences the condensation rate of the sol-gel system. A SiO_2 interface (native oxide on silicon) starts with the highest condensation degree, which steadily increases by 50 % over 10 minutes. A silicon nitride layer shows an initial condensation degree that is somewhat lower compared to native silicon oxide, for longer times the condensation degree is increased over that for the Si substrate. For alumina, GaAs and plasma treated GaAs surfaces the initial condensation degree is low and remarkably, on these surfaces the formation of a Si-O-Si network is very slow compared to that for silica and silicon nitride surfaces. The plasma treatment of the GaAs wafer increases the condensation degree compared to non-treated GaAs, indicating an effect of the surface chemistry. On the alumina surface the degree of silica network formation first increases and then seems to be hydrolyzed again as the corresponding Si-O-Si peak area decrease over time. A possible explanation for the different initial condensation degree and speed of Si-O-Si network formation between the samples can be a (catalytically formed) acid environment. For example, on the
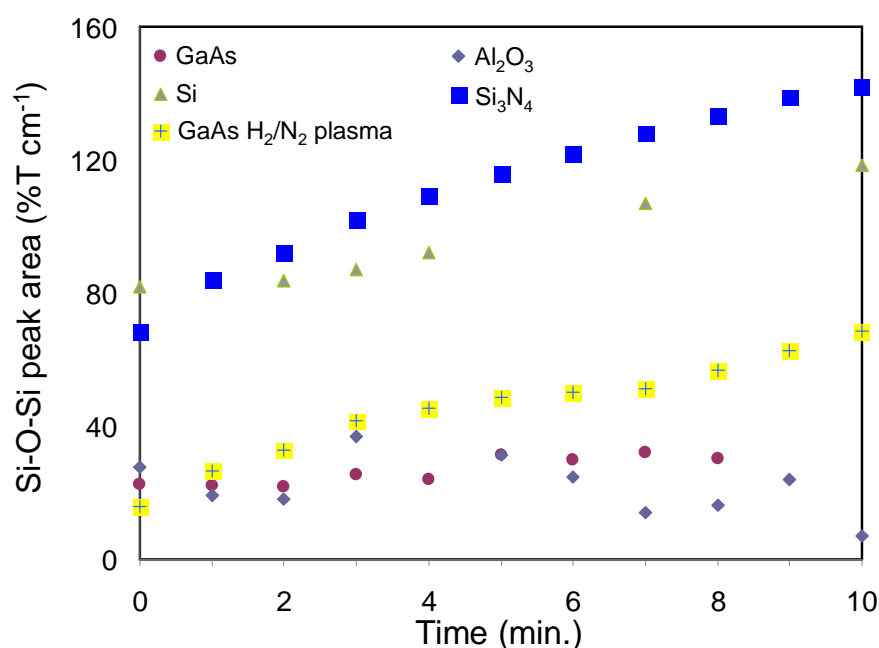

Figure 39. Peak area of the (1010-1090 cm^{-1}) band corresponding to the Si-O-Si stretch vibration measured in reflection FT-IR spectroscopy of a 100 nm thick sol-gel layer on different substrates.

aluminum oxide surface a specific combination of Al_2O_3 and SiO_2 can form acid generating sites in the presence of water. It is known that an alumina-silica compound can acid catalyze hydrocarbon reactions.[71] On a GaAs surface As_2O_3 can be present which can form the strong arsenic acid (H_3AsO_4) that affects the condensation reaction. The nitrogen / hydrogen plasma (partly) passivates the GaAs surface and prevents the formation of the arsenic acid. These measurements indicate that a sol-gel resist which is optimized for one substrate type does not necessarily perform optimally on other surfaces. This has to be taken into account when other substrates than silicon are used in sol-gel imprint lithography.

2.9 Conclusions

We demonstrated substrate conformal imprint lithography as a flexible large area nanoimprint technology. By using a composite stamp composed of thin glass with soft rubber an on top a stiff rubber wafer scale imprints can be made using low pressure and capillary action which results in minimal in-plane pattern distortions. A newly developed high Young's modulus rubber prevents instability of nm sized features. The whole stamp is still flexible enough to allow conformal contact and pattern over particle contaminants without inducing damage to the stamp or substrate. The new stiff rubber in combination with a silica sol-gel based imprint resist is used in combination with SCIL to imprint sub-10 nm silica patterns at room temperature. An optimized sol-gel resist can be patterned on a silicon substrate within 3 minutes using SCIL. The SCIL technique applies a stamp to a substrate with minimal distortions. An overlay alignment process and tooling has been developed which allows the positioning of a substrate with respect to a stamp with nm precision, without the use of active temperature control. Using this setup and box-in-box alignment markers we demonstrated sub-50 nm overlay alignment using imprinted sol-gel layers.

References

[1]   *Sol-gel science: The physics and chemistry of sol-gel processing*, C. Jeffrey Brinker and George W. Scherer, Academic Press Inc. (1990)

[2]   L.L. Hench, and J.K. West, *The sol-gel process*, Chem. Rev. **90**, 33 (1990)

[3]   C. Marzolin, S.P. Smith, M. Prentiss, and G.M. Whitesides, *Fabrication of glass microstructures by micromMolding of sol-gel precursors*, Adv. Mater. **10**, 571 (1998)

[4]   Y. Xia, and G.M. Whitesides, *Soft-lithography*, Annu. Rev. Mater. Sci. **28**, 153 (1998)

[5]   V.K. Parashar, A. Styah, E. Cuche, C. Depeursinge, and M.A.M. Gijs, *Diffractive optical elements in titanium oxide for MOEMS applications*, Proc. IEEE International Conference on Solid State Sensors, Actuators and Microsystems, 1482 (2003)

[6]   M. Li, H. Tan, L. Chen, J. Wang, and S.Y. Chou, *Large area direct nanoimprinting of SiO_2–TiO_2 gel gratings for optical applications*, J. Vac. Sci. Technol. B **21**, 660 (2003)

[7]   O.J.A. Schueller, G.M. Whitesides, J.A. Rogers, M. Meier, and A. Dodabalapur, *Fabrication of photonic crystal lasers by nanomolding of solgel glasses*, Appl. Optics **38**, 5799 (1999)

[8]   W.-S. Kim, J.-H. Lee, S.-Y. Shin, B.-S. Bae, and Y.-C. Kim, *Fabrication of ridge waveguides by UV embossing and stamping of sol-gel hybrid materials*, IEEE Photonics Tech. Lett. **16**, 1888 (2004)

[9]   S. Jeong, S.-J. Ahn, and J. Moon, *Fabrication of patterned inorganic–organic hybrid film for the optical waveguide by microfluidic lithography*, J. Am. Ceram. Soc. **88**, 1033 (2005)

[10]   M. Okinakaa, K. Tsukagoshi, and Y. Aoyagi, *Direct nanoimprint of inorganic-organic hybrid glass*, J. Vac. Sci. Technol. B **24**, 1402 (2006)

[11] D.J. Kang, B.-S. Bae, and J. Nishii, *Fabrication of thermally durable sub-wavelength periodic structures upon inorganic–organic hybrid materials by nano-imprinting*, Japanese J. of Appl. Phys. **46**, 3704 (2007)

[12] R. Aelion, A. Loebel, and F.J. Eirich, *Hydrolysis of ethyl silicate*, Am. Chem. Soc. **72**, 5705 (1950)

[13] M.P.J. Peeters, T.N.M. Bernards, and M.J. van Bommel, *^{17}O-NMR of sol-gel processes of TEOS and TMOS*, J. Sol-Gel Sci. Techn. **13**, 71 (1998)

[14] H. Dong, M. Lee, R.D. Thomas, Z. Zhang, R.F. Reidy, and D.W. Mueller, *Methyltrimethoxysilane sol-gel polymerization in acidic ethanol solutions studied by ^{29}Si NMR Spectroscopy*, J. Sol-Gel Sci. Techn. **28**, 5 (2003)

[15] H. Dong, Z. Zhang, M.-H. Lee, D.W. Mueller, and R.F. Reidy, *Sol-gel polycondensation of methyltrimethoxysilane in ethanol studied by ^{29}Si NMR spectroscopy using a two-step acid/base procedure*, J. Sol-Gel Sci. Techn. **41**, 11 (2007)

[16] V.G. Kessler, G.I. Spijksma, G.A. Seisenbaeva, S. Håkansson, D.H.A. Blank, and H.J.M. Bouwmeester, *New insight in the role of modifying ligands in the sol-gel processing of metal alkoxide precursors: A possibility to approach new classes of materials*, J. Sol-Gel Sci. Techn. **40**, 163 (2006)

[17] Y. Haruvy, I. Gilath, M. Maniewictz, and N. Eisenberg, *Sol-Gel prepared glass for refractive and diffractive micro-optical elements and arrays*, J. Sol-Gel Sci. Techn. **13**, 547 (1998)

[18] A. Sayah, V.K. Parashar, and M.A.M. Gijs, *Micro-replication of optical lensen in glass using a novel sol gel technology*, Proc. IEEE 15th International Conference on Micro Electro Mechanical Systems, 516 (2002)

[19] W. Que, and X. Hu, *Sol-gel derived titania/γ-glycidoxypropyltrimethoxysilane and methyltrimethoxysilane hybrid materials for optical waveguides*, J. Sol-Gel Sci. Techn. **28**, 319 (2003)

[20] C. Peroz, C. Heitz, E. Barthel, E. Søndergård, and V. Goletto, *Glass nanostructures fabricated by soft thermal nanoimprint*, J. Vac. Sci. Technol. B **25**, L27 (2007)

[21] M. Beck, M. Graczyka, I. Maximova, E.-L. Sarwea, T.G.I. Linga, M. Keilb, and L. Monteliusa, *Improving stamps for 10 nm level wafer scale nanoimprint lithography*, Microelectronic Eng. **61-62**, 441 (2002)

[22] G.-Y. Jung, Z. Li, W. Wu, Y. Chen, D.L. Olynick, S.-Y. Wang, W.M. Tong, and R.S. Williams, *Vapor-phase self-assembled monolayer for improved mold release in nanoimprint lithography*, Langmuir **21**, 1158 (2005)

[23] T. Zhang, B. Kobrin, M. Wanebo, R. Nowak, R. Yi, J. Chinn, M. Bender, A. Fuchs, and M. Otto, *Vapor deposited release layers for nanoimprint lithography*, SPIE Microlithography 6151-44 (2006)

[24] C.Y. Hui, A. Jagota, Y.Y. Lin, and E.J. Kramer, *Constraints on microcontact printing imposed by stamp deformation*, Langmuir **18**, 1394 (2002)

[25] F. Hua, A. Gaur, Y. Sun, M. Word, N. Jin, I. Adesida, M. Shim, A. Shim, and J.A. Rogers, *Processing dependent behavior of soft imprint lithography on the 1–10-nm scale*, IEEE transactions on nanotechnology **5,** 301 (2006)

[26] R. Lin, and J.A. Rogers, *Molecular-scale soft imprint lithography for alignment layers in liquid crystal devices*, Nano Lett. **7**, 1613 (2007)

[27] E. Delamarche, H. Schmid, B. Michel, and H. Biebuyck, *Stability of molded polydimethylsiloxane micro structures*, Adv. Mater. **9**, 741 (1997)

[28] K.G. Sharp, G.S. Blackman, N.J. Glassmaker, A. Jagota, and C.-Y. Hui, *Effect of stamp deformation on the quality of microcontact printing: Theory and experiment*, Langmuir **20**, 6430 (2004)

[29]   K. J. Hsiaa, Y. Huang, E. Menard, J.-U. Park, W. Zhou, J. Rogers, and J. M. Fulton, *Collapse of stamps for soft lithography due to interfacial adhesion*, App. Phys. Lett. **86**, 154106 (2005)

[30]   Y.Y. Huang, W. Zhou, K.J. Hsia, E. Menard, J.-U. Park, J.A. Rogers, and A.G. Alleyne, *Stamp collapse in soft lithography*, Langmuir **21**, 8058 (2005)

[31]   Y. Zhang, C.-W. Lo, J.A. Taylor, and S. Yang, *Replica molding of high-aspect-ratio polymeric nanopillar arrays with high fidelity*, Langmuir **22**, 8595 (2006)

[32]   Y. Zhao, *Closely spaced polymer microstructures as a unique tool for characterization at the small scales*, IEEE 21st International Conference on Micro Electro Mechanical Systems, 459 (2008)

[33]   J. Lee, Y.-K. Yun, Y. Kim, and K. Jo, *PDMS nanoslits without roof collapse*, Bull. Korean Chem. Soc. **30**, 1793 (2009)

[34]   R.B.A. Sharpe, D. Burdinski, J. Huskens, H.J.W. Zandvliet, D.N. Reinhoudt and B. Poelsema, *Chemically patterned flat stamps for microcontact printing*, J. Am. Chem. Soc. **127**, 10344 (2005)

[35]   X. Duan, V.B. Sadhu, A. Perl, M. Péter, D.N. Reinhoudt, and J. Huskens, *Bifunctional, chemically patterned flat stamps for microcontact printing of polar inks*, Langmuir **24**, 3621 (2008)

[36]   X. Duan, Y. Zhao, A. Perl, E. Berenschot, D.N. Reinhoudt, and J. Huskens, *High-resolution contact printing with chemically patterned flat stamps fabricated by nanoimprint lithography*, Adv. Mater. **21**, 2798 (2009)

[37]   N.Y. Lee, J.R. Lim, M.J. Lee, J.B. Kim, S.J. Jo, H.K. Baik, and Y.S. Kim, *Hydrophilic composite elastomeric mold for high-resolution soft lithography*, Langmuir **22**, 9018 (2006)

[38]   P. Choi, P.-F. Fu, and L.J. Guo, S*iloxane copolymers for nanoimprint lithography*, Adv. Funct. Mater. **17**, 65 (2007)

[39]   S.-J. Choi, P.J. Yoo, S.J. Baek, T.W. Kim, and H.H. Lee, *An ultraviolet-curable mold for sub-100-nm lithography*, J. Am. Chem. Soc. **126**, 7744 (2004)

[40]   J.P. Rolland, E.C. Hagberg, G.M. Denison, K.R. Carter, and J.M. De Simone, *High-resolution soft lithography: Enabling materials for nanotechnologies*, Angew. Chem. **116**, 5920 (2004)

[41]   T.T. Truong, R. Lin, S. Jeon, H.H. Lee, J. Maria, A. Gaur, F. Hua, I. Meinel, and J.A. Rogers, *Soft lithography using acryloxy perfluoropolyether composite stamps*, Langmuir **23**, 2898 (2007)

[42]   D. Trimbach, K. Feldman, N.D. Spencer, D.J. Broer, and C.W.M. Bastiaansen, *Block copolymer thermoplastic elastomers for microcontact printing*, Langmuir **19**, 10957 (2003)

[43]   G. Csucs, T. Kunzler, K. Feldman, F. Robin, and N.D. Spencer, *Microcontact printing of macromolecules with submicrometer resolution by means of polyolefin stamps*, Langmuir **19**, 6104 (2003)

[44]   H. Schmid, and B. Michel, *Siloxane polymers for high-resolution, high-accuracy soft lithography*, Macromolecules **33**, 3042 (2000)

[45]   C. Pina-Hernandez, J.-S. Kim, L.J. Guo, and P.-F. Fu, *High-throughput and etch-selective nanoimprinting and stamping based on fast-thermal-curing poly(dimethylsiloxane)s*, Adv. Mat. **19**, 1222 (2007)

[46]   http://www.gelest.com/literature.asp (reactive silicones brochure)

[47]   *Contact mechanics*, K.L. Johnson, Cambridge University press. (1985)

[48]   M.M.J. Decré, R. Schneider, D. Burdinski, J. Schellekens, M. Saalmink, and R. Dona, *Wave Printing (I): towards large-area, multilayer microcontact printing*, Mater. Res. Soc. Symp. Proc. **M4.9.1** (2004)

[49] J. Schellekens, D. Burdinski, M. Saalmink, M. Beenhakkers, G. Gelinck, and M.M.J. Decré, *Wave printing (II): Polymer MISFETs using microcontact printing*, Mater. Res. Soc. Symp. Proc. **M2.9.1** (2004)

[50] T.W. Odom, J.C. Love, D.B. Wolfe, K.E. Paul, and G.M. Whitesides, *Improved pattern transfer in soft lithography using composite stamps*, Langmuir **18**, 5314 (2002)

[51] B. Michel, *Printing meets lithography*, The Industrial Physicist August/September **16** (2002)

[52] B. Michel, A. Bernard, A. Bietsch, E. Delamarche, M. Geissler, D. Juncker, H. Kind, J.P. Renault, H. Rothuizen, H. Schmid, P. Schmidt-Winkel, R. Stutz, and H. Wolf, *Printing meets lithography: Soft approaches to high-resolution patterning*, IBM J. Res. Develop. **45**, 697 (2001)

[53] D.S. Macintyre, and S. Thoms, *A study of resist flow during nanoimprint lithography*, Microelectronic Eng. **78–79**, 670 (2005)

[54] S. Reddy, R.T. Bonnecaze, *Simulation of fluid flow in the step and flash imprint lithography process*, Microelectronic Eng. **82**, 60 (2005)

[55] H. Schift, *Nanoimprint lithography: An old story in modern times? A review*, J. Vac. Sci. Technol. B **26,** 458 (2008)

[56] T. Bailey, B. Smith, B.J. Choi, M. Colburn, M. Meissl, S.V. Sreenivasan, J.G. Ekerdt, and C.G. Willson, *Step and flash imprint lithography: Defect analysis*, J. Vac. Sci. Technol. B **19**, 2806 (2001)

[57] D.J. Resnick, W.J. Dauksher, D. Mancini, K.J. Nordquist, T.C. Bailey, S. Johnson, N. Stacey, J.G. Ekerdt, C.G. Willson, S.V. Sreenivasan, and N. Schumaker, *Imprint lithography for integrated circuit fabrication*, J. Vac. Sci. Technol. B **21**, 2624 (2003)

[58] L. Chen, X. Deng, J. Wang, K. Takahashi, and F. Liu, *Defect control in nanoimprint lithography*, J. Vac. Sci. Technol. B **23**, 2933 (2005)

[59] J.A. Rogers, K.E. Paul, and G.M. Whitesides, *Quantifying distortions in soft lithography*, J. Vac. Sci. Technol. B **16**, 88 (1998)

[60] S. Pagliara, L. Persano, A. Camposeo, R. Cingolani, and D. Pisignano, *Registration accuracy in multilevel soft lithography*, Nanotechnology **18**, 175302 (2007)

[61] G. Kylberg, *Measurement of interference fringe separation by a moiré technique*, J. Scientific Instruments (Journal of Physics E) **2**, 676 (1968)

[62] J. Liut, H. Furuhashit, A. Toriit, R. Sharmaz, V.T. Chitnisj, B.P. Singhs, J. Yamadat, and Y. Uchidat, *Automatic mask alignment in the theta direction using Moiré sensors*, Nanotechnology **6**, 135 (1995)

[63] D.C. O'Shea, and W.S. Rockward, *Light modulation from crossed phase gratings*, Optics Letters **23**, 491 (1998)

[64] N. Li, W. Wu, and S.Y. Chou, *Sub-20-nm alignment in nanoimprint lithography using Moiré fringe*, Nano Letters **6**, 2626 (2006)

[65] M. Mühlberger, I. Bergmair, W. Schwinger, M. Gmainer, R. Schöftner, T. Glinsner, C. Hasenfuß, K. Hingerl, M. Vogler, H. Schmidt, and E.B. Kley, *A Moiré method for high accuracy alignment in nanoimprint lithography*, Microelectronic Eng. **84**, 925 (2007)

[66] B. Gralak, M.J.A. de Dood, G. Tayeb, S. Enoch, and D. Maystre, *Theoretical study of photonic band gaps in woodpile crystals*, Phys. Rev. B **67**, 066601 (2003)

[67] H. Dong, M. Lee, R.D. Thomas, Z. Zhang, R.F. Reidy, and D.W. Mueller, *Methyltrimethoxysilane sol-gel polymerization in acidic ethanol solutions studied by ^{29}Si NMR spectroscopy*, J. Sol-Gel Sci. Techn. **28**, 5 (2003)

[68] H. Dong, Z. Zhang, M.-H. Lee, D.W. Mueller, and R.F. Reidy, *Sol-gel polycondensation of methyltrimethoxysilane in ethanol studied by ^{29}Si NMR spectroscopy using a two-step acid/base procedure*, J. Sol-Gel Sci. Techn. **41**, 11 (2007)

[69]   P.C. Duineveld, M. Lilja, T. Johansson, and O. Inganäs, *Diffusion of solvent in PDMS elastomer for micromolding in capillaries*, Langmuir **18**, 9554 (2002)

[70]   T.N.M. Bernards, M.J. van Bommel, and J.A.J. Jansen, *The effect of HF in a two-step sol-gel process of TEOS*, J. Sol-Gel Sci. Techn. **13**, 749 (1998)

[71]   X. Gao, I.E. Wachs, *Structural characteristics and reactivity properties of highly dispersed Al_2O_3/SiO_2 and $V_2O_5/Al_2O_3/SiO_2$ catalysts*, J. Catal. **192**, 18 (2000)

Chapter 3

Substrate conformal imprint lithography: robust wafer scale nanopatterns

We demonstrate a new wafer-scale nanofabrication technique offering nanometer resolution called Substrate Conformal Imprint Lithography (SCIL). This technique makes use of composite imprinting stamps composed of a patterned rubber layer with high Young's modulus on a thin glass support. The in-plane stiffness of the stamp avoids pattern deformation over large areas, while out-of-plane flexibility allows conformal contact to underlying surface features. The stamp is used in conjunction with a novel sol-gel imprint resist material that allows nanoscale features to be replicated in a layer of rigid silica at room temperature. We demonstrate better than 10 nm resolution in imprinted grating patterns of lines and individual pillars with high aspect ratio (up to 5:1). Gaps as small as 6 nm can be reproduced and the average pitch variation in replicated patterns is measured to be less than 0.1 nm over 6 cm^2. These imprinted patterns can be used as an etch mask to pattern underlying silicon and quartz substrates while maintaining sub-10 nm resolution.

3.1 Introduction

Nanoimprint lithography is a replication technique where patterns are transferred through an embossing principle. It allows the high throughput fabrication of three-dimensional nanostructures over large areas. Nanoimprint can enable the practical use of emerging nanotechnology designs in many application areas, including solid-state lighting[1,2], lasers[3,4], sensors[5,6] and photovoltaics[7,8]. The first demonstrations of nanoimprint lithography used rigid stamps to hot-emboss polymer layers[9] (NIL) or layers of UV-curable resists [10](UV-NIL). These methods realized 25 nm resolution already in 1996 and have demonstrated patterns down to 5 nm.[11] NIL and UV-NIL promised a route to cost effective fabrication of large area nanostructures. However, the deployment of rigid stamp nanoimprint technology has been hindered by the sensitivity of contact to the presence of particle contamination and wafer inhomogeneities. Soft-nanoimprint lithography was simultaneously introduced as an alternative to imprinting with rigid stamps.[12] Soft stamps proved more durable than rigid stamps and less sensitive to particle contaminants and wafer inhomogeneities. Additionally, multiple soft stamps can be replicated from a single master pattern. However, the resolution of soft-nanoimprint lithography has not previously been shown to match the performance of rigid stamp imprinting. This is commonly attributed to nanoscale elastic deformation of the soft rubber features of the stamp. These deformations have additionally prohibited the alignment and overlay of multiple layers.

Several combinations of rigid and soft stamp concepts have been previously studied. Soft stamps have been made on rigid supports to reduce pattern distortion over wafer scales, but these designs do not offer nanoscale resolution.[13] Thin rigid stamps have been made on soft and flexible supports to allow conformal contact over large areas[14,15], but these designs remain vulnerable to particle contaminants that can cause damage to the stamp surface.[16-18] Other alternative composite stamps combining rigid and soft materials require high pressure or high temperature processing conditions, do not allow for conformal contact[19], or exhibit creep which permanently deforms the nanopatterns[20].

Here we present a new high throughput wafer scale soft-nanoimprint method that can address all of these challenges called Substrate Conformal Imprint Lithography (SCIL). Our method uses composite flexible large-area rubber stamps made from a quaternary siloxane-modified poly-di-methyl-siloxane (PDMS) material with a high Young's modulus. This rubber is laminated to a thin glass carrier providing high in-plane stiffness while maintaining out-of-plane flexibility. We use this stamp to replicate patterns in a novel silica sol-gel based resist composed of tetra-methyl-ortho-silicate (TMOS) and methyl-tri-methoxy-silane (MTMS) that we have developed to minimize post-imprint shrinkage. The combination of the improved stiffness of the stamp rubber and the high silica content of the imprint resist leads to feature sizes smaller than 10 nm. We demonstrate the versatility of SCIL through examples of dense, high-aspect ratio nanoscale pattern replication in quartz, silicon, InGaN, and metal layers over large areas with sub-nm variations.

In soft-nanoimprint lithography, a rubber negative stamp is first molded from a master pattern that is typically generated using conventional electron, ion-beam, or optical lithography, or by interference lithography. The stamp rubber must be sufficiently soft (Young's modulus E<< 1 GPa) to enable conformal contact over large areas. Silicone-based poly-di-methyl-siloxane (PDMS) rubbers are most commonly used as they are chemically inert, have low surface energy, and have a high permeability for gasses and solvents. Additionally these materials are non-toxic, bio-compatible, and optically transparent to visible light. However, silicone rubbers typically

have a low Young's modulus (1-3 MPa) which causes collapse of the stamp features at micrometer scales. To solve this problem a high modulus (8 MPa) silicone rubber (H-PDMS) was previously developed, which allowed patterning down to ~200 nm scales before feature collapse occurred.[21] Further improvement in the resolution of soft-nanoimprint lithography requires the development of a new stamp materials with increased stiffness. However, these materials must still allow conformal contact and low temperature processing.

We have developed a suitable high-modulus silicone rubber which is made from a combination of vinyl-modified linear di-methyl-siloxanes (as in H-PDMS) and vinyl-modified quaternary siloxanes. The latter component increases the intrinsic crosslink density in the rubber and thereby the Young's modulus. The mixture is cross linked with hydride modified linear siloxanes using a platinum catalyzed vinyl-hydride addition reaction.[13] By changing the linear to quaternary siloxane ratio, we synthesize rubbers with Young's modulus up to 80 MPa. The rubber material with the highest attained stiffness (X-PDMS) allows the faithful replication of dense sub-10 nm features while still providing conformal contact over a full wafer.

3.2 Substrate Conformal Imprint Lithography

Before the rubber negative stamp is molded from the master pattern, the surface of the master is coated with a monolayer of 1,1,2,2-H-perfluoro-decyl-tri-chloro-silane through vapor phase deposition to prevent the possible adhesion of the X-PDMS material.[22] The X-PDMS components are thoroughly mixed and de-gassed and a 50-100 μm thick layer is formed over the master by spin coating for 30 seconds at 1000 rpm and forms a tacky layer after a pre-cure for 15 minutes at 50 °C. Next, low-modulus PDMS (Sylgard 184) is poured over the X-PDMS layer on the master. This PDMS is squeezed between the master and a 200 μm thick AF45 glass support plate to form a uniform layer of ~0.5 mm thickness. The "master – X-PDMS – PDMS – glass" sandwich is cured for 24 hours in an oven at 50 °C. The rubber negative stamp is then released from the master by gentle peeling and excess PDMS protruding above the pattern plane is trimmed. Using this procedure multiple stamps can be molded from the master without additional reapplication of the fluor monolayer. Our stamp replication method ensures that the rubber stamp is always attached to a mechanically stable carrier with high in-plane stiffness to maintain pattern fidelity. The out-of-plane flexibility of the thin glass support plate allows for substrate inhomogeneity and enables wafer-scale conformal contact. The soft PDMS rubber layer allows local conformation around particle contaminants which avoids damage to stamp or substrate.

Wafer-scale imprints are made using the composite stamps and a specially designed SCIL imprint tool. The stamp is held in the imprint tool by a flat plate with 80 grooves under low vacuum as shown in Fig. 1(a). The substrate to be patterned is coated with a liquid sol-gel resist and aligned in the imprint tool parallel to the stamp at an initial spacing of ~100 μm. The stamp is then brought into contact with the substrate by sequentially pressurizing the grooves to an overpressure of ~20 mbar (starting from the side). This procedure gently curves the composite stamp over a length of ~2 cm until a line contact forms with the substrate. As the remaining grooves are sequentially pressurized, capillary forces pull the stamp into the resist and the line contact continually moves forward while avoiding air inclusions, as in Fig. 1(b). The stamp is kept in contact as the liquid resist cross-links to form a solid silica replica. The composite stamp is then released from the patterned resist by sequentially evacuating grooves from one side, resulting in a controlled peeling like release from the imprinted patterns.
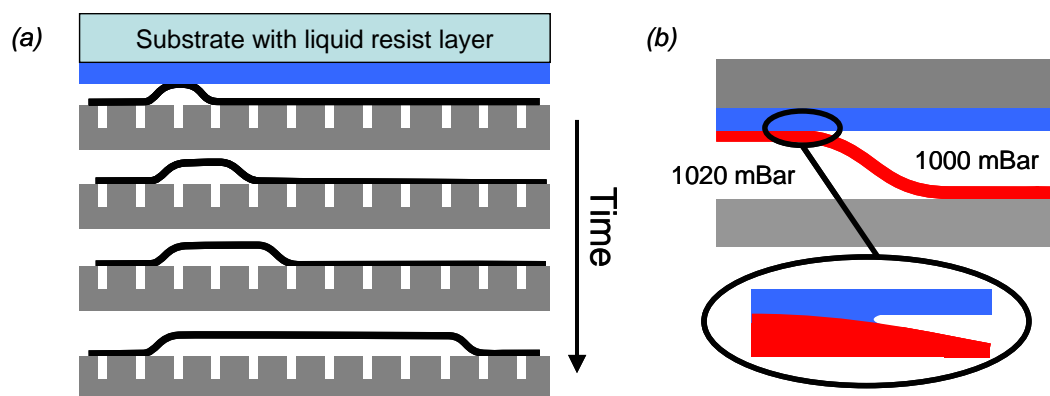
Figure 1. Substrate Conformal Imprint Lithography (SCIL) principle. A rubber composite stamp is imprinted into a substrate covered with a liquid resist layer by sequentially pressurizing an array of grooves in the stamp actuator plate. Low imprint pressure is used and minimal force is required for release by peeling. (a) Time sequence of an imprint step showing the evolution of the contact area by the sequential pressurization of the grooves. (b) Advancing capillary contact line due to wetting at both interfaces.

The sol-gel resist precursor developed in this work is prepared from tetra-methoxy-ortho-silicate (TMOS) and methyl-tri-methoxy-silane (MTMS) in a 1:1 molar ratio. This mixture is hydrolyzed for 30 minutes at room temperature using a 1:1 molar ratio of alkoxide-groups:water (the water is acidified with 1 M formic acid). After the hydrolysis reaction additional water is added to obtain a 9:1 total molar ratio of water:silicon. The hydrolyzed mixture is then stabilized by dilution with n-propanol to reach a concentration of 0.78 mol Si / kg and stored at -20 °C. The final sol-gel imprint resist material is prepared by mixing equal masses of the n-propanol diluted precursor and 1 weight-percent 1,2-propanediol.

Resist layers with a thickness ranging from 10 to 200 nm are formed by spin coating. Volatile components evaporate during the drying of the resist, leaving mainly silicon oxide oligomers and non-volatile 1,2-propanediol. The remaining 1,2-propandiol keeps the sol-gel liquid after spin coating during the ~1 minute transfer of the substrate to the SCIL imprint tool. When the composite stamp is in contact with the substrate, 1,2-propanediol diffuses into the PDMS rubber stamp which increases the concentration of reactive silicon-hydroxyl and silicon-alkoxide groups. These subsequently condense to form an inorganic network of Si-O-Si bonds while the reaction products (water and alcohols) are removed by diffusion into the stamp. After 10 minutes contact at room temperature the stamp can be removed from the glass sol-gel structure. The resulting sol-gel patterns are composed of ~90 weight-percent silicon oxide and remaining organic components.

Figure 2(a) shows secondary electron microscope (SEM) images of imprinted silica nano-gratings of 150 nm pitch, 25 nm width and 100 nm height on a silicon substrate. This demonstrates that high-aspect ratio nanoscale features can be made directly using the X-PDMS stamp material. Similar structures would be impossible to fabricate directly using conventional (H-)PDMS. Figure 2(b) shows silica pillars with a diameter of 130 nm and a height of 650 nm, demonstrating that individual high-aspect ratio features can be printed with high fidelity. In Fig. 2(c), 100 nm tall silica pillars of 30 nm diameter are shown on a pitch of 50 nm, demonstrating the fabrication of high density patterns. Figure 2(d) shows an array of paired silica pillars separated by sub-10 nm gaps on a pitch of 30 nm. This pattern is a 1-to-1 replica of the master pattern as verified by SEM, demonstrating that the X-PDMS stamp is able to hold and replicate sub-10 nm features. All of the structures are replicated as intended and no periodic defects such as consistently missing or broken features are observed. The high aspect ratio structures are
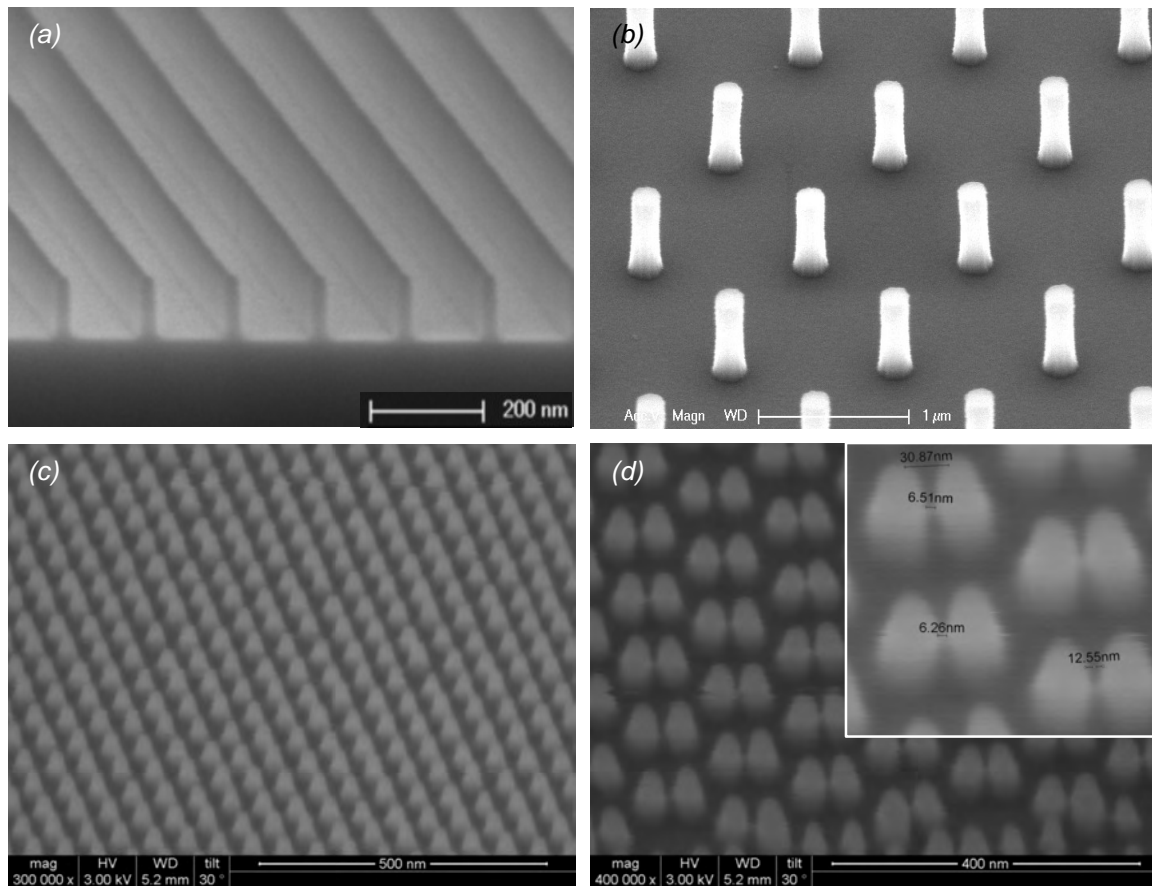
Figure 2. Directly replicated high aspect ratio patterns in silica. (a) Silica grating with 25 nm wide, 100 nm high lines at a pitch of 150 nm. (image taken 10° out of plane). (b) Silica pillars, diameter 130 nm, height 650 nm. (c) 30 nm diameter, 100 nm high silica pillars on a 50 nm pitch. (image taken under 30°). (d) Array of paired pillars on a pitch of 30 nm, separated by sub-10 nm gaps.

relatively easy to replicate as the rubber stamp will temporarily deform to accommodate the release of the rigid silica structures. These replicated patterns demonstrate that our high-Young's modulus X-PDMS silicone rubber is capable of faithfully replicating dense, high aspect ratio sub-10 nm features over large areas.

A single composite rubber stamp containing 580 nm pitch gratings with 130 nm wide lines was used to make over 3000 imprints and cleaned numerous times in a solution of diluted 1 wt. % hydrogen fluoride. We did not observe any variation in the replicated patterns (height, width, shape) over the course of this experiment. This shows that an inexpensive rubber stamp can be durable. The direct patterning of light- and temperature-stable silicon oxide could be useful for IR, optical, and UV components such as gratings, photonic crystals, diffractive optical elements, graded index coatings, and templates for bit-patterned-media. This demonstrates, for the first time, a robust and potentially cost-effective large-area imprint lithography with nanometer resolution.

The patterns in Fig. 2 have a high surface-to-volume ratio. This is a favorable geometry to imprint because features are rapidly filled with imprint resist by capillary forces while air trapped in the features diffuses into the rubber. In contrast, low aspect ratio structures are more difficult to replicate as the resist has to flow over long distances in channels with restricted height.
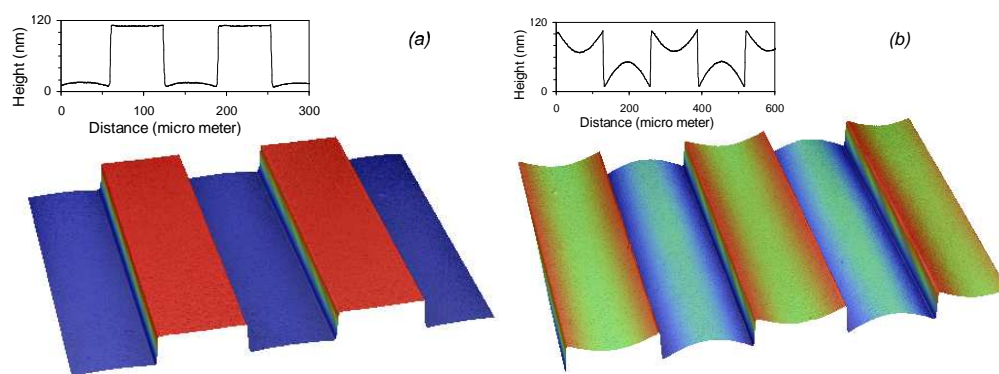
Figure 3. Extremely low aspect ratio grating prepared by SCIL. White light interferometry surface profile of 100 nm high gratings with a pitch of (a) 128 μm and (b) 256 μm meter replicated in a 100 nm thick sol-gel layer. Line scans are shown taken perpendicular to the grating lines. Note the scale difference in vertical and horizontal axes.

Figure 3 shows white light surface profilometry measurements of replicated very low aspect ratio gratings with pitches of 128 and 256 μm and 100 nm height. These structures were simultaneously imprinted in a sol-gel imprint resist layer of 100 nm thickness. Line scans are taken perpendicularly to the grating lines. In Fig. 3(a) the raised areas of the 128 μm pitch grating are flat to within 2 nm while the recessed areas are flat to within 7 nm. The difference in flatness between the two levels can be explained by the more constricted material flow between the substrate and stamp in the recessed regions (sol-gel thickness 50 nm) and the raised areas (sol-gel thickness 150 nm). In Fig. 3(b), 256 μm pitch grating patterns are shown to be level to within only 40 nm, demonstrating the limit of this geometry for the SCIL technique. During the imprint process we observed that both grating periods were index matched when the stamp was in contact with the resist, meaning that both gratings were in complete contact with the liquid resist. This implies that capillary pressure is high enough to distort the rubber, leading to the observed curved pattern. This demonstrates that external high imprint pressures are not required due to the strong capillary action.

Previous work on the direct patterning of sol-gel materials reported volume shrinkages of tens of percents at room temperature, resulting in deformed features after stamp release.[12,23-25] In this work, the combination of MTMS and TMOS led to a controlled reduction of the cross link density in our imprint resist material. This allowed us to maximize the amount of inorganic silica in the liquid sol-gel during patterning and greatly reduce post-imprinting shrinkage. We compared the dimensions of grating patterns immediately after imprinting and after sintering at 1100 °C to completely convert the sol-gel to dense silica (as confirmed by ellipsometry on planar layers). Even after sintering at these high temperatures the grating patterns are preserved. This allows us to bound shrinkage in the modified sol-gel imprint resist to only 16% in width and 18% in height for grating lines similar to those shown in Fig. 2(a). This feature shrinkage suggests that the initial sol-gel density is almost 70%.

3.3 High resolution pattern transfer

An imprinted sol-gel pattern is an ideal hard mask to transfer patterns into a substrate using reactive-ion etching (RIE). After optimizing the initial resist layer thickness, the residual layer remaining under the recessed features after imprinting is typically <10 nm. This thin layer is removed using a fluorine RIE-based breakthrough etch. We achieve a highly anisotropic etch of the sol-gel material at a rate of 30 nm/min using CF_4 and N_2 in a 1:2 flow ratio at a pressure of 12 mTorr and a RF-power of 50 W. After the breakthrough etch, the underlying layer between the

imprinted sol-gel features is exposed. This layer can subsequently be patterned by further etch steps. Figure 4 shows SEM images of the 50 nm pitch imprinted sol-gel patterns shown in Fig. 2(c) after transfer by etching into (a) silicon and (b) quartz. The silicon was etched to a depth of ~75 nm using a Cl_2/N_2 gas mixture at 40 mTorr and a RF-power of 100 W. The remaining sol-gel etch mask can be seen on top of the silicon pillars. To transfer imprinted patterns into quartz a 10 nm thick chromium transfer layer was first deposited on the quartz substrate wafer by sputter deposition. The sol-gel patterns were replicated on top of the chromium layer and the residual sol-gel layer removed by fluorine RIE. A Cl_2/O_2 RIE process is used to pattern the chromium layer and a subsequent CHF_3 based RIE etch transfers the pattern to a depth of 100 nm into the quartz substrate (removing the sol-gel etch mask as well). Note that the gaps between the etched pillars in Fig. 4(b) are smaller than 10 nm, demonstrating that the nanoscale features shown in Fig. 2(d) are fully transferred into the quartz substrate.

The uniformity of the residual resist layer thickness is important for the reliable transfer of the imprinted features into the underlying layer during RIE. Using interference lithography a master pattern was made on a 150 mm diameter silicon wafer consisting of 360-375 nm diameter holes with a depth of 180 nm, on a square lattice with a pitch of 513 nm. Using the SCIL process this pattern was replicated in sol-gel on a 150 mm diameter silicon wafer. A fluorine breakthrough etch removed 25 nm of sol-gel material to expose the underlying silicon substrate. Subsequently a Cl_2/N_2 based RIE at a pressure of 40 mT for was used to transfer the hole pattern to a depth of ~260 nm into the silicon. The sol-gel etch mask was then removed in diluted HF. Figure 5 shows photographs of (a) the master hole pattern, (b) the SCIL stamp containing sol-gel pillars and (c) the replicated hole pattern after etching into the silicon wafer and removing the sol-gel resist. The homogeneous interference colors seen in the photograph reveal that the pattern is homogeneously transferred over the entire silicon wafer area. The clear reproduction of the hole patterns can also be seen in the SEM images of the master and the replicated structures, shown in the inset in Fig. 5(a) and 5(c).

(a)

(b)
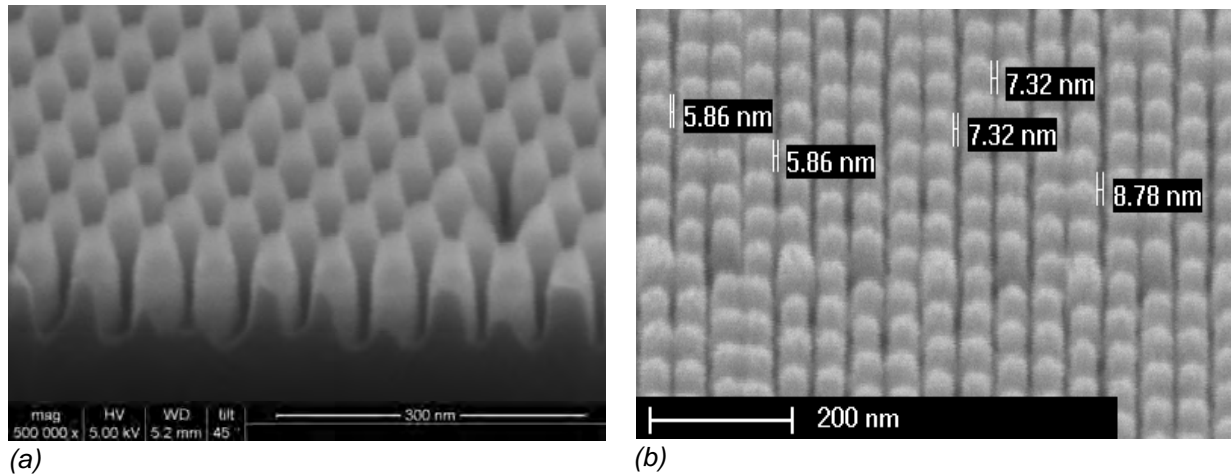
Figure 4. SCIL imprinted hard mask: 50 nm pitch pillars etched in silicon and quartz. The ~ 20 nm thick residual layer is first removed by CF_4 RIE after the patterns are transferred into silicon (a) and quartz (b). The pattern in (a) is etched in silicon by using Cl_2/N_2 RIE the oxide etch mask can be seen on top of the silicon pillars. In (b) the sol-gel pattern is used to pattern a chrome layer after which the pattern was transferred into quartz using CHF_3 RIE.

Figure 5. Wafer scale imprint and pattern transfer by SCIL. Uniform interference color bands in the (a) pattern master, (b) SCIL stamp, and (c) replicated pattern demonstrate the uniformity of a hole pattern (diameter 370 nm, pitch 513 nm) through the SCIL imprint process.

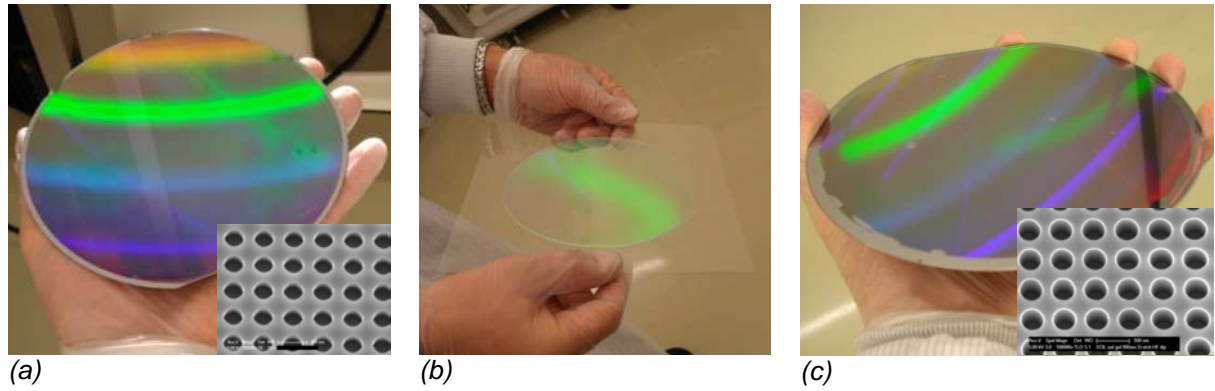To further demonstrate the flexibility of the SCIL technique we show that etch selectivity between silica and silicon can be used to invert a pattern tone. The SEM images and schematic cross section shown inset in Fig. 6 illustrate an inversion of the hole pattern shown in Fig. 5. First, the hole pattern was imprinted on a silicon wafer (a). Then the residual sol-gel resist layer was removed by CF_4 RIE and the pattern was transferred into the silicon substrate by Cl_2 RIE (b). A HF wet etch was then performed, followed by spin-coating a 100 nm thick sol-gel layer to planarize the surface. A CF_4 RIE of the sol-gel is used to expose the surrounding silicon leading to a planarized structure of holes in silicon filled with sol-gel (c). Next, the silicon surrounding the infilled holes is RIE etched using Cl_2 below the depth of the holes to invert the pattern (d). A final wet HF etch removes the sol-gel etch mask (e). As can be seen in Fig. 6(e), a regular array of silicon pillars results with a fill fraction corresponding to the original hole pattern. The height of the pillars can be determined by the duration of the final silicon RIE etch.
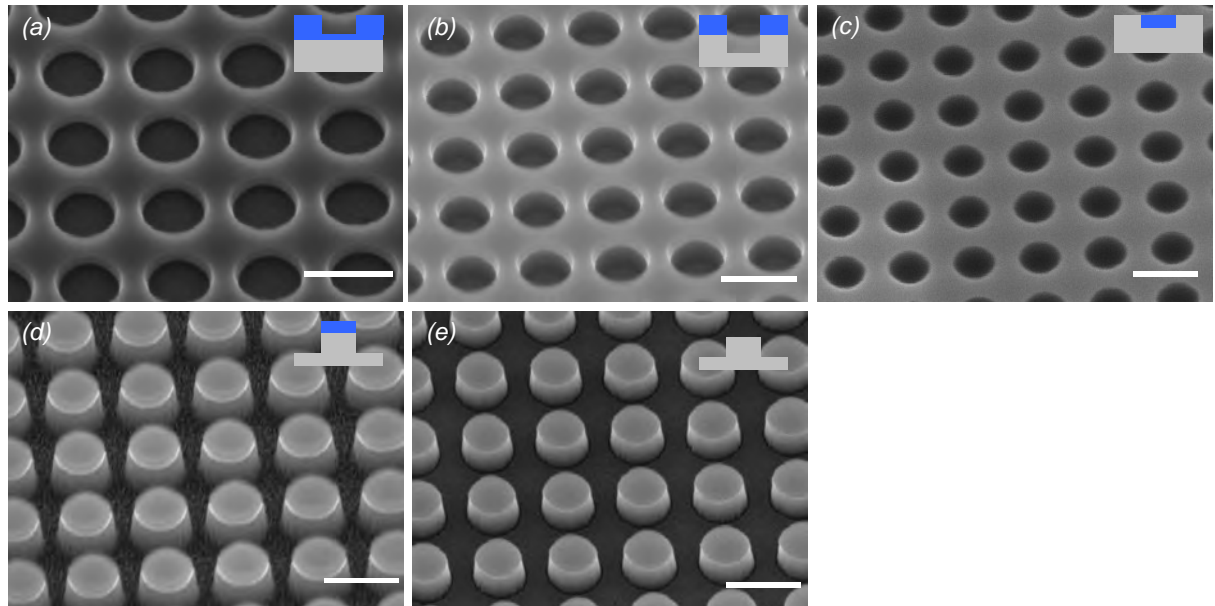
Figure 6. Pattern tone inversion using SCIL. A patter of holes is imprinted in silica sol-gel resist on a silicon substrate (a) and transferred into the silicon by RIE (b). The silica etch mask is first removed by a wet etch before the hole patterns are planarized by a layer of spin coated sol-gel. This layer is subsequently RIE etched until the silicon is exposed between the silica filled holes (c) Using a selective Cl_2/N_2 silicon etch the surrounding silicon is etched to below the silica plug, inverting the patter tone (d) after which the silica dot mask is removed by a wet etch (e). This process inverts the hole pattern to a pillar pattern with equal fill fraction. Scale bar represents 500 nm.

3.4 Pattern deformation characterization

To minimize pattern deformations on a wafer scale, the rubber stamp is always attached to a rigid support. To study the pattern distortion over a large area we measured the variations in the pitch of a grating replicated using SCIL on a 150 mm diameter wafer. A 3 μm pitch master grating was made using an ASML wafer stepper to illuminate resist with 365 nm light. Grating areas of 15×15 mm were stitched to populate the whole wafer. This pattern was transferred to a depth of 90 nm in the silicon by RIE. A composite stamp was prepared as described above from the silicon master. Using SCIL the grating was replicated in sol-gel on AF 45 glass. The pitch of the master and sol-gel replica grating was determined by illuminating the grating perpendicular to the surface using a He-Ne laser at a wavelength of 632.8 nm with a spot diameter of 125 μm. The pitch variation was determined by measuring the variation in the angle between the reflected -4th and +4th diffraction orders using two CCD cameras. By scanning the laser spot over the sample and tracking the reflected diffraction orders on the two cameras, we produced a two-dimensional map of the grating pitch averaged over the beam spot size. Figure 7 shows images of the grating pitch for the master (a) and the sol-gel replica, when the imprint direction (see Fig. 1) is applied parallel (b) or perpendicular (c) to the SCIL grooves. As can be seen from the figure, the variation in average grating pitch for both the master grating and the replica grating is less than 0.1 nm. The bright lines are due to stitching errors between the 15×15 mm grating areas, introduced in the mastering process. Isolated artifacts in the replicas (indicated by arrows) are due to contamination of the imprinted substrate by dust particles, as confirmed by optical microscopy at those locations. Note that these particle contaminants only cause pattern deformation in a small region around the particle. By comparing the images for the two imprint directions we conclude that the imprint direction does not influence the deformation of the replicated grating. The step wise application of the stamp is also not detectable. To our knowledge, the demonstrated average pitch variation of less than 0.1 nm represents a replication fidelity that has never been shown before using soft stamp imprint methods.[26,27]

Particle-induced deformation stress is accommodated in the soft intermediate PDMS layer before it reaches the thin glass plate which supports the rubber. This localizes the deformation to the immediate surrounding region of the particle contaminant and ensures the remainder of the pattern is imprinted without deformations. The localized deformation of the rubber stamp can be clearly inferred from Fig. 8, which shows SEM images of two substrates imprinted using SCIL

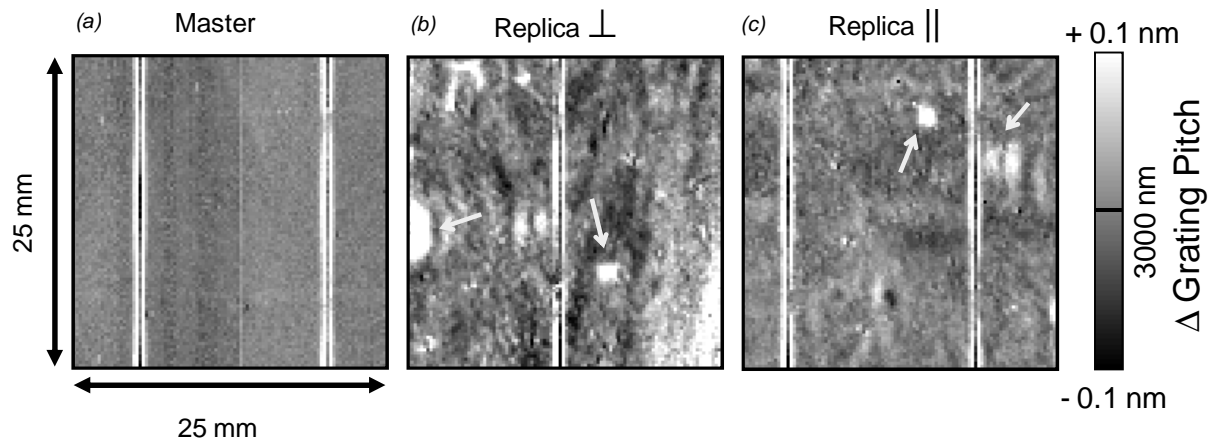*Figure 7. Less than 0.1 nm average pitch variation over large areas. The two-dimensional spatial distribution of the grating pitch of the master pattern (a) and sol-gel replicas imprinted either perpendicular (b) or parallel (c) to the grating orientation shows pattern fidelity better than 0.1nm over cm scales. The grating pitch ranges from 2999.9 to 3000.1 nm, as measured using a HeNe laser diffraction technique.*
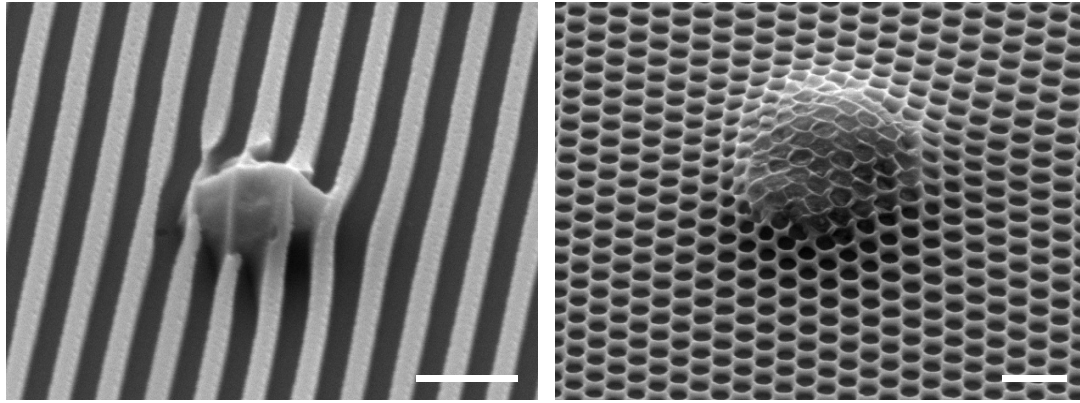
Figure 8. Conformal imprinting over particle contaminants. SEM images of patterns in sol-gel imprinted over particle contaminants which were present on the substrate surface during the imprint process. The soft stamp conforms to the local topography and replicates the pattern on and directly around the particle. The white scale bar represents 500 nm.

over particle contaminants with heights up to ten times the imprint resist layer thickness. As can be seen from Fig. 8 the stamp actually imprints the pattern on top of and over the particle contaminant. At a small distance away from defect the pattern continues without distortion. These images also demonstrate the self-cleaning principle of soft stamps. When using a rigid stamp, this type of defect would cause damage to the stamp or to the substrate and potentially generate additional particles.

3.5 Photonic crystal LEDs

Solid-state lighting is a potential major market for nanoimprint lithography. Photonic crystal patterns etched in the active semiconductor layer of an LED can enable high light extraction efficiency over a narrow angular range, surpassing the brightness that can be achieved by using a randomly roughened surface.[2] Ideally, the photonic crystal would be patterned into the semiconductor LED layer stack over the full wafer directly after the epitaxial growth. However, for a photonic crystal LED to exhibit the desired emission pattern, the photonic crystal lattice dimensions must be precisely tuned to the LED emission wavelength. As the emission wavelengths of fabricated LEDs always vary due to wafer scale inhomogeneities during the epitaxial growth process, process-integrated photonic crystals patterning after epitaxial growth is not possible.

As we have demonstrated in the examples given above, the flexibility of the SCIL stamp allows it to follow roughness and height variation when imprinting nanoscale features onto substrates. Here we show that we can faithfully imprint photonic crystal patterns on a non-continuous substrate. By pre-selecting LEDs with similar peak emission wavelengths these can be patterned with the matched photonic crystal lattice and create the desired emission profiles and light extraction. A 3" diameter silicon sub-mount wafer contains high power InGaN flip chip LEDs with an area of 1 mm^2 each on a square staggered pitch of 1.7 mm. The total area of the wafer containing LEDs to be patterned is ~40×65 mm^2. The height variation between the surfaces of the LEDs is up to 20 μm. A 150 nm thick sol-gel layer is applied over the whole wafer by spray coating, using a needle valve and high pressure air to nebulize the liquid imprint resist. The spray coat head makes four passes over the wafer to apply a reasonable homogeneous coverage of sol-gel resist (the droplets are further planarized by capillary forces). Directly after spray coating the wafer is loaded in the SCIL tool and imprinted. The stamp makes contact only with the tops of the LED chips. The photonic crystal pattern consists of ~365 nm diameter holes in a square array

with a pitch of 513 nm (similar to the patterns shown in Fig. 5). After imprinting, a RIE etch is applied to the whole wafer to remove ~50 nm of residual sol-gel material. Next, the sol-gel patterns are transferred into the GaN to a depth of ~300 nm using Cl_2/N_2 RIE at a pressure of 40 mT. Figure 9(a) shows a photograph of the imprinted and etched LED wafer. Interference colors resulting from the hole pattern can be seen on the individual LED chips. In Fig. 9(b) an SEM image of the corner of one LED is shown, confirming that the patterns have been imprinted and etched in the GaN up to the edge of each LED chip. The inset shows a high magnification SEM image of the etched holes in which the residual sol-gel etch mask can be distinguished at the surface.

The emission pattern of one LED was measured by contacting the diode with needle probes and driving it at 50 mA. An optical fiber integrated with lenses creating a focus at the centre of the LED was scanned over a range of azimuthal and axial angles. A linear CCD camera and a grating spectrometer were used to record spectra at each angular position. Figure 9(c) shows the angle-averaged emission spectrum of the LED, which peaks at 480 nm. In Fig. 9(d) the normalized far-field angular emission profiles are shown to vary with azumuthal angle. Data are shown for

(a)

(b)

(c)

(d)
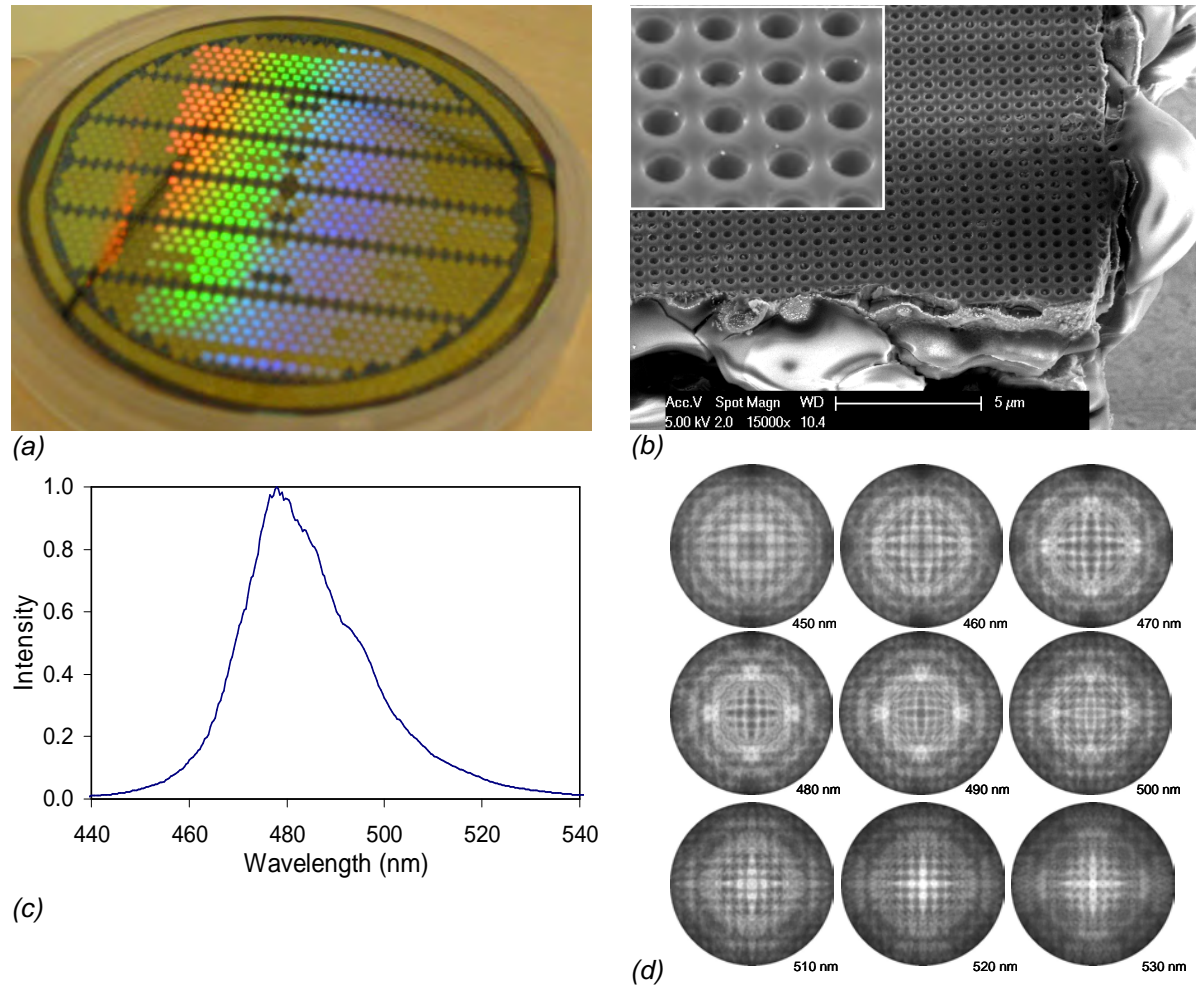
Figure 9. (a) SCIL patterned photonic crystal LEDs. (a) Photograph of a 3" diameter silicon sub-mount wafer covered with 1 mm² InGaN LEDs showing interference colors of the imprinted hole pattern. (b) SEM image of a corner of an imprinted and etched LED, the inset shows a high magnification image of the etched holes (both images are taken under an angle of ~40°). (c) Integrated normalized emission spectrum of the photonic crystal LED at a drive current of 50 mA. (d) Electro luminescence far-field angular distribution of a photonic crystal LED. The centre of the circle corresponds to emission normal to the LED surface, the edge corresponds to emission under an angle of 80° to the surface normal.

several different wavelengths in the range of 450-530 nm. The square symmetry of the photonic crystal pattern can be inferred from the symmetry of the far-field emission patterns in Fig. 9(d). Bright circles in these patterns correspond to Fabry-Perot resonances of light traveling normal to the ~4 μm thick GaN active layer. The photonic crystal etched into the LED shifts the angular emission pattern as the wavelength is changed. An increased brightness can be achieved when the photonic crystal diffraction pattern overlaps with the Fabry-Perot mode close to the normal. For this device, this condition occurs around an emission wavelength of 530 nm. In this present design the InGaN layer thickness is ~4 μm thick while the holes are ~300 nm deep. The LED emission is therefore not expected to be strongly coupled to the photonic crystal. However, our results clearly indicate a route towards control over the angular emission using photonic crystal patterns applied using the SCIL process. Future work will focus on LED samples with thinner GaN layer thickness and deeper holes to increase coupling.

3.6 Noble metal patterning using SCIL

Finally, we demonstrate the use of SCIL to fabricate metallic nanostructures. A ~100 nm thick layer of polymethylmethacrylate (PMMA, 50 K) is applied on a silicon substrate by spin coating and baked on a hotplate at 150 °C for 15 minutes. Sol-gel patterns are defined on top of the PMMA layer using the SCIL process and the residual imprint resist layer is removed by fluorine based RIE etching. A low-pressure oxygen RIE is then used to transfer the sol-gel pattern into the underlying PMMA layer. The oxygen RIE stops when the substrate is reached. A brief over-etch is intentionally applied to laterally etch the PMMA under the sol-gel etch mask. Next, gold is deposited over the patterned sol-gel / PMMA layer by electron-beam evaporation under normal incidence. A lift-off process is performed in acetone at 50 °C which quickly dissolves the remaining PMMA. This releases the imprinted sol-gel layer covered with metal which is suspended by PMMA and leaves a pattern of metal nanoparticles of controlled thickness on the substrate. Figure 10(a) shows an SEM image of 100 nm thick gold dots patterned using this method in a honeycomb arrangement and Fig. 10(b) shows ~150 nm diameter, 100 nm thick gold dots similarly patterned in a quasicrystal arrangement. The gold patterns are slightly tapered due to the buildup of metal on the sol-gel mask which narrows the effective diameter of the holes by shadowing during the deposition. The large-area nanoscale lift-off process presented here can be used to fabricate plasmonic light coupling and trapping layers for large-area photovoltaics[7] or sensors based on surface enhanced Raman spectroscopy.[28,29]

(a) (b)

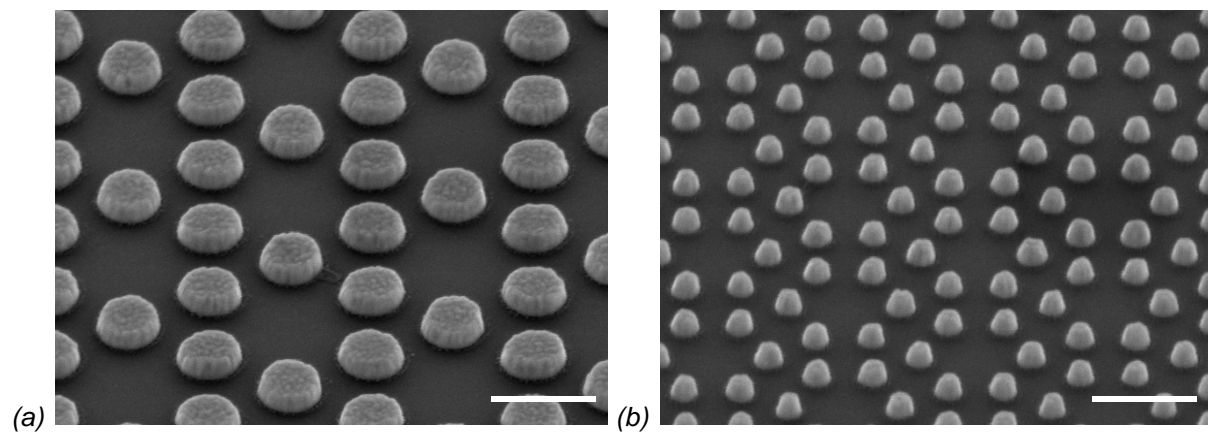*Figure 10. Gold metal particles by a SCIL lift-off method. The pattern is imprinted in sol-gel on top of a ~100 nm PMMA layer and the pattern transferred in the PMMA by oxygen RIE. Next metal is evaporated and the PMMA/sol-gel mask removed by dissolution of the PMMA in a lift-off procedure. Gold metal dots of 100 nm height in (a) honeycomb arrangement (b) quasi-crystal arrangement. The scale bar represents 500 nm.*

In the previous example, we used SCIL and lift-off to fabricate a positive tone pattern of metal dots. The inversed pattern, a noble metal hole array, is also of interest due to the surface plasmon polarition mediated extraordinary transmission of light. Arrays of nanoscale holes in metal films are also of interest as nanoscale light concentrators to be used in bio-sensors, plasmonic solar cells, and angle insensitive color filters. Unfortunately, the lift-off procedure is not well suited for the fabrication of arrays of holes as the process can require the use of a thin (2-5 nm) adhesion layer of titanium or chromium which is known to strongly absorbs surface plasmons. Also, a lift-off process would release many metal dots corresponding to the holes in the metal layer. A large fraction of these dots will adhere to the array during processing, causing increased scattering losses and reduced coupling to surface plasmons. Alternative methods are necessary to use nanoimprint lithography to produce arrays of nanoscale holes in a metal film. However the methods demonstrated previously have resulted in fragile freely floating arrays[30] or in structures in which the holes were not fully continuous through the film[5], leading to additional resonances and limiting total transmission. We have developed a SCIL-based process to fabricate nano-hole arrays over large areas on any substrate, where we avoid absorbing adhesion layers and do not generate dots than might otherwise adhere to the hole array.

Our process begins with the replication of a square array (780 nm pitch) of high aspect ratio silica pillars with a diameter of 150 nm using SCIL, similar to those as shown in Fig. 2(b). These pillars are overcoated with 250 nm gold using sputter deposition. A sputter process deposits an equal amount of material per unit area and thus results in relatively thin and porous metal deposition on the pillar sides. The full metal thickness is deposited on the substrate between the pillars and on the tops of the pillars. Next, ~130 nm gold is removed using a thio-urea and iron-sulphate based wet etch solution (etch rate ~32 nm/min.). This short etch process removes all the metal from the sides and tops of the pillars due to the high surface-to-volume ratio in these regions and leaves ~120 nm of gold on the substrate between the pillars. The pillars defining the holes are then removed in a short etch using 1 wt. % hydrogen fluoride in water, forming a regular hole-array on the underlying substrate. Figure 11(a) shows a SEM image of a hole array fabricated using this method on glass, which shows regular circular holes in a smooth metal film. The diameter of the holes is enlarged to 180 nm due to a combination of shadowing effects during sputter deposition and erosion during the wet etch process steps.

We characterized the hole array by angle-resolved transmission measurements. Light from an incandescent lamp was coupled in to a 200 μm multimode fiber and the fiber output was focused to a ~300 μm diameter spot on the sample. The transmitted light was collected by a fiber-coupled grating spectrometer with a CCD detector. The numerical aperture of the incident and transmitted light beam was limited to <0.01. The substrate was placed onto a rotation mount with the rotation axis aligned with the (0, 1) direction of the hole array. Polarization filters were placed in the the incident and transmitted beam paths to select light polarized perpendicular to this direction (p-polarization). The transmission was normalized to the transmission measured through a region where no metal was present.

Figure 11(b) shows the transmission of the hole array as function of the angle of incidence (horizontal axis) and illumination wavelength (vertical axis). The measurements show several extraordinary transmission peaks related to surface plasmon excitation by different grating orders on both sides of the array. The broad minima and maxima in the transmission spectra are caused by Fano resonances of directly transmitted light and SPP mediated transmitted light.[31,32]
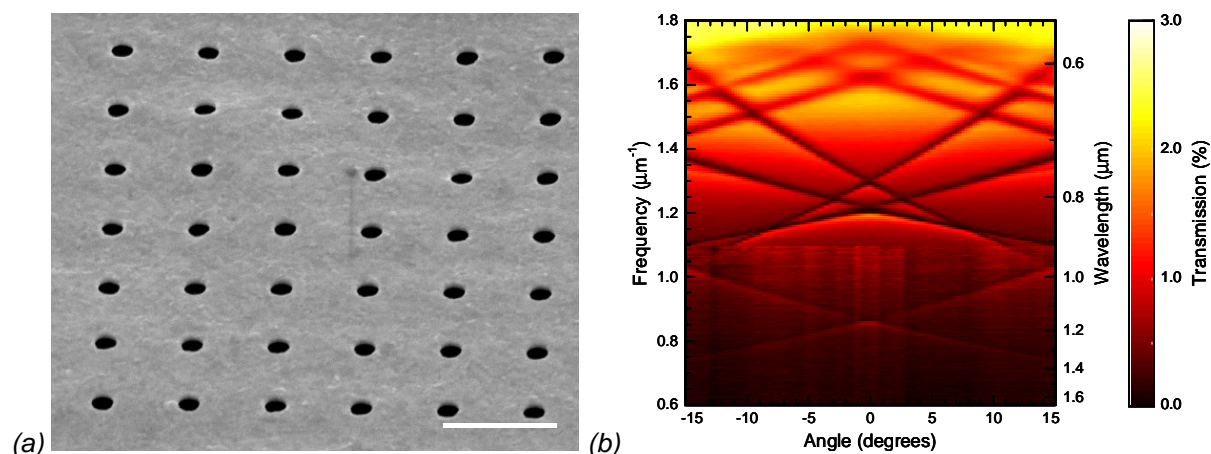
Figure 11. Array of nanoholes in a optically thick gold layer. (a) SEM image of a square array of 180 nm diameter holes in a ~120 nm thick gold film. The white scale bar represents 1 μm. (b) Optical transmission versus frequency and incidence angle for the array.

The different slopes of the dark bands in Fig. 11(b) correspond to the different dispersion on the glass side and air side of the hole array.[33] The normalized transmission reaches a maximum of 3.2 % for 649 nm light. Together with SEM inspection these transmission measurements indicate that the nanohole array is homogeneous and free of metallic particles.

3.7 Conclusions

We demonstrate Substrate Conformal Imprint Lithography (SCIL), a novel soft-nanoimprint technique offering sub-10 nm resolution over 150 mm diameter substrates. The newly developed high modulus X-PDMS stamp material enables the highest resolution dense pattern replication reported to date for a soft imprint fabrication technique while still allowing conformal contact to be made across a full wafer. In-plane pattern distortions are avoided by lamination of the stamp to a thin glass carrier during stamp replication. This flexible composite stamp allows a silica based sol-gel imprint resist to be patterned with high fidelity. We demonstrate the direct replication of nanostructures with aspect ratios of up to 5:1, feature pitches as small as 30 nm, and a minimum feature size of 6 nm. Large area imprints with minimal pattern distortions and without air inclusions are made at ambient pressure and room temperature. The sol-gel imprint process is shown to be driven primarily by capillary pressure allowing imprinting over large particle contaminants without damage to the stamp or to the substrate.

The sol-gel resist exhibits record low shrinkage and is light and temperature stable, which makes it appropriate for use as a directly patterned hard mask in subsequent RIE pattern transfer processes. Imprinted sol-gel patterns can be transferred into silicon and silica by this method while preserving sub-10 nm resolution. By using the etch selectivity between the sol-gel imprint resist and silicon the imprinted patterns can be uniformly inverted at wafer scale. Procedures have also been developed to pattern arrays of metal nanoparticles and holes in gold over large areas.

The combination of uniform wafer scale patterning with sub-10 nm resolution and minimal in-plane pattern distortion has never before been demonstrated using a room temperature conformal imprint technique. Together with the use of a fully inorganic imprint resist the SCIL process opens up many new possibilities in emerging application areas which rely on large-area nanopatterning, such as solid-state lighting, lasers, sensors and photovoltaics.

References

[1]   J.J. Wierer, M.R. Krames, J.E. Epler, N.F. Gardner, M.G. Craford, J.R. Wendt, J.A. Simmons, and M.M. Sigalas, *InGaN/GaN quantum-well heterostructure light-emitting diodes employing photonic crystal structures*, Appl. Phys. Lett. **19**, 3885 (2004)

[2]   J.J. Wierer, A. David, and M.M. Megens, *III-nitride photonic-crystal light-emitting diodes with high extraction efficiency*, Nature Photonics **3**, 163 (2009)

[3]   H. Altug, D. Englund, and J.Vučković, *Ultrafast photonic crystal nanocavity laser*, Nature Phys. **2**, 484 (2006)

[4]   S.A. Moore, L. O'Faolain, T.P. White, and T.F. Krauss, *Photonic crystal laser with mode selective mirrors*, Optics Express **16**, 1365 (2008)

[5]   V. Malyarchuk, F. Hua, N.H. Mack, V.T. Velasquez, J.O. White, R.G. Nuzzo, and J.A. Rogers, *High performance plasmonic crystal sensor formed by soft nanoimprint lithography*, Optics Express **13**, 5670 (2005)

[6]   J.M. McMahon, J. Henzie, T.W. Odom, G.C. Schatz, and S.K. Gray, *Tailoring the sensing capabilities of nanohole arrays in gold films with Rayleigh anomaly-surface plasmon polaritons*, Optics Express **15**, 18119 (2007)

[7]   K. R. Catchpole, and A. Polman, *Plasmonic solar cells*, Optics Express **16**, 21793 (2008)

[8]   V.E. Ferry, M.A. Verschuuren, H.B.T. Li, R.E. I. Schropp, H.A. Atwater, and A. Polman, *Improved red-response in thin film a-Si:H solar cells with soft-imprinted plasmonic back reflectors*, Appl. Phys. Lett. **95**, 183503 (2009)

[9]   S.Y. Chou, P.R. Krauss, and P.J. Renstrom, *Nanoimprint lithography*, J. Vac. Sci. Technol. B **14**, 4129 (1996)

[10]   J. Haisma, M. Verheijen, K. van den Heuvel, and J. van den Berg, *Mold-assisted nanolithography: A process for reliable pattern replication*, J. Vac. Sci. Technol. B **14**, 4124 (1996)

[11]   M.D. Austin, H. Ge, W. Wu, M. Li, Z. Yu, D. Wasserman, S.A. Lyon, and S.Y. Chou, *Fabrication of 5 nm linewidth and 14 nm pitch features by nanoimprint lithography*, Appl. Phys. Lett. **84**, 5299 (2004)

[12]   Y. Xia, and G.M. Whitesides, *Soft Lithography*, Annu. Rev. Mater. Sci. **28**, 153 (1998)

[13]   H. Schmid, and B. Michel, *Siloxane polymers for high-resolution, high-accuracy soft lithography*, Macromolecules **33**, 3042 (2000)

[14]   E. Roy, Y. Kanamori, M. Belotti, Y. Chen, *Enhanced UV imprint ability with a tri-layer stamp configuration*, Microelectr. Engin. **78–79**, 689 (2005)

[15]   Z. Li, Y. Gu, L. Wang, H. Ge, W. Wu, Q. Xia, C. Yuan, Y. Chen, B. Cui, and R.S. Williams, *Hybrid nanoimprint-soft lithography with sub-15 nm resolution*, Nano Lett. **9**, 2306 (2009)

[16]   L. Chen, X Deng, J. Wang, K. Takahashi, and F. Liud, *Defect control in nanoimprint lithography¸* J. Vac. Sci. Technol. B **23**, 2933 (2005)

[17]   H. Schift, C. Spreu, M. Saidani, M. Bednarzik, and J. Gobrecht, *Transparent hybrid polymer stamp copies with sub-50-nm resolution for thermal and UV-nanoimprint lithography*, J. Vac. Sci. Technol. B **27**, 2846 (2009)

[18]   J. Perumal, T.H. Yoon, H.S. Jang, J.J. Lee, and D.P. Kim, *Adhesion force measurement between the stamp and the resin in ultraviolet nanoimprint lithography - an investigative approach*, Nanotechnology **20**, 055704 (2009)

[19]   H. Gao, H. Tan, W. Zhang, K. Morton, and S.Y. Chou, *Air cushion press for excellent uniformity, high yield, and fast nanoimprint across a 100 mm field*, Nano Lett. **6**, 2438 (2006)

[20] T.T. Truong, R. Lin, S. Jeon, H.H. Lee, J. Maria, A. Gaur, F. Hua, I. Meinel, and J.A. Rogers, *Soft lithography using acryloxy perfluoropolyether composite Stamps*, Langmuir **23**, 2898 (2007)

[21] E. Delamarche, H. Schmid, B. Michel, and H. Biebuyck, *Stability of molded polydimethylsiloxane microstructures*, Adv. Mater. **9**, 741 (1997)

[22] G.-Y. Jung, Z. Li, W. Wu, Y. Chen, D.L. Olynick, S.-Y. Wang, W.M. Tong, and R.S. Williams, *Vapor-phase self-assembled monolayer for improved mold release in nanoimprint lithography*, Langmuir **21**, 1158 (2005)

[23] C. Marzolin, S.P. Smith, M. Prentiss, and G.M. Whitesides, *Fabrication of glass microstructures by micro-molding of sol-gel precursors*, Adv. Mater. **10**, 571 (1998)

[24] V.K. Parashar, A. Styah, E. Cuche, C. Depeursinge, and M.A.M. Gijs, *Diffractive optical elements in titanium oxide for MOEMS applications*, Proc. IEEE International Conference on Solid State Sensors, Actuators and Microsystems **1482** (2003)

[25] M. Li, H. Tan, L. Chen, J. Wang, and S.Y. Chou, *Large area direct nanoimprinting of SiO_2–TiO_2 gel gratings for optical applications*, J. Vac. Sci. Technol. B **21**, 660 (2003)

[26] J.A. Rogers, K.E. Paul, and G.M. Whitesides, *Quantifying distortions in soft lithography*, J. Vac. Sci. Technol. B **16**, 88 (1998)

[27] S. Pagliara, L. Persano, A. Camposeo, R. Cingolani, and D. Pisignano, *Registration accuracy in multilevel soft lithography*, Nanotechnology **18**, 175302 (2007)

[28] A. Otto, I. Mrozek, H. Grabhorn, and W. Akemann, *Surface-enhanced Raman scattering*, J. Phys. Condens. Mat. **4**, 1143 (1992)

[29] R. Alvarez-Puebla, B. Cui, J.-P. Bravo-Vasquez, T. Veres, and H. Fenniri, *Nanoimprinted SERS-active substrates with tunable surface plasmon resonances*, J. Phys. Chem. C **111**, 6720 (2007)

[30] E.-S. Kwak, J. Henzie, S.-H. Chang, S.K. Gray, G.C. Schatz, and T.W. Odom, *Surface plasmon standing waves in large-area subwavelength hole arrays*, Nano Lett. **5**, 1963 (2005)

[31] A. Krishnan, T. Thio, T.J. Kim, H.J. Lezec, T.W. Ebbesen, P.A. Wolff, J. Pendry, L. Martin-Moreno, and F.J. Garcia-Vidal, *Evanescently coupled resonance in surface plasmon enhanced transmission*, Optics Comm. **200**, 1 (2001)

[32] C. Genet, M.P. van Exter, and J. P. Woerdman, *Fano-type interpretation of red shifts and red tails in hole array transmission spectra*, J. Opt. Soc. Am. A **22**, 998 (2005)

[33] D. Stolwijk, E.F.C. Driessen, M.A. Verschuuren, G.W. 't Hooft, M.P. van Exter, and M.J.A. de Dood, *Enhanced coupling of plasmons in hole arrays with periodic dielectric antennas*, Optics Lett. **33**, 363 (2008)

Chapter 4

Fabrication of wafer-scale 3D optical photonic crystals by soft-nanoimprint lithography

We present a novel method to fabricate 3D woodpile photonic crystals for visible light (240 nm pitch) using a new wafer-scale nano-imprint method with sub-50 nm resolution. Gratings are imprinted in a sol-gel layer that is planarized to print subsequent layers to build up a 3D photonic crystal structure. Replicated test patterns (with a pitch of 3 micron) exhibit an averaged pitch variation of less than 0.1 nm over a 25×25 mm area. The 3D woodpile structure is stable up to 1050 °C in air, which facilitates infiltration of the structure with dielectrics of a high index of refraction. We demonstrate overlay alignment between two imprinted layers with a misalignment of <100 nm over an area as large as 3×3 cm; with a magnification error as small as 1.2-2.4 ppm. Using an optimized alignment procedure 20 nm overlay alignment may be reached for an area as large as 1 cm^2. We demonstrate the fabrication of a four layer woodpile scaffold from which a photonic crystal with a bandgap in the visible can be fabricated.

4.1 Introduction

Photonic crystals are regular arrangements of dielectric materials that interact strongly with light.[1] They can be used to control spontaneous emission, confinement and dispersion of light. Two dimensional photonic crystals are already used to modify the emission properties of LEDs and lasers.[2,3] The effectiveness of 2D structures is limited as these crystals only interact strongly with light in two directions. Complete control over spontaneous emission requires three dimensional photonic crystals. The availability of 3D photonic crystals will enable directional light generation in LEDs and low-threshold lasing.

Two commonly used 3D photonic crystal geometries are the inverted opal[4] and woodpile geometry.[5] Inverted opals can be made using self-assembly of colloids (polystyrene, silica) followed by infiltration of a high-index material.[6] This fabrication method cannot be well integrated with the device processing as the active optical components have to be embedded in the crystal. Furthermore, for an inverted opal structure to exhibit a complete bandgap at optical frequencies requires an index of refraction contrast which can only be achieved using highly absorbing semiconductors. Woodpile structures are build up in a layer-by-layer fabrication process that is well integrated with active planar device processing. Also, they require a refractive index contrast that is much lower than required for inverted opals, the use of a variety of non-absorbing dielectric materials.[7] Woodpile photonic crystals have been demonstrated made from silicon[8], GaAs[9] and recently TiO_2[10]. These structures were made using a time-consuming layer-by-layer electron-beam lithography, etching and planarization processes or a wafer fusion process that makes these structures impractical to use at a large scale. Building a woodpile photonic crystal for visible wavelengths presents severe technical challenges due to the smaller length scales: a woodpile crystal with an optical bandgap centered at 550 nm requires a 240 nm pitch with a line width of 70 nm made from a material with an index of refraction of n=2.3. Moreover, to achieve a bandgap each layer has to be aligned with accuracy of ~30 nm.[7,11]

To enable applications which benefit from the special optical properties of 3D woodpile photonic crystals, new fabrication methods are needed which can effectively pattern sub-100 nm features over large areas. Nano imprint lithography is an emerging method which is able to pattern large areas with a resolution down to 10 nm.[12] Here, we present a new soft stamp nano imprint method termed Substrate Conformal Imprint Lithography (SCIL), which enables wafer-scale patterning with sub-50 nm resolution using inexpensive rubber stamps. Uniquely, SCIL delivers extremely low pattern deformations on wafer scales which allows for potential wafer scale sub-20 nm overlay alignment.

Here, we use SCIL and the template inversion method to directly pattern silica sol-gel gratings at room temperature. These layers are subsequently planarized with polymer using a relatively simple self-assembly method. By repeating these steps we can fabricate a temperature-stable 3D scaffold of silica, which can be filled up with high-quality high-index material using high-temperature low pressure chemical vapor deposition (LPCVD).[13] This process is relatively simple and the number of processing steps is small.

4.2 Substrate Conformal Imprint Lithography

Soft stamp methods have shown to be able to replicate sub-10 nm features[14] but overlay alignment with an accuracy below 0.5 micron has never been demonstrated.[15,16] However in a woodpile crystal the alignment of subsequent layers is essential to obtain an optical bandgap. Replicating a single layer with a minimum of pattern deformations is a prerequisite to obtain

accurate overlay alignment. SCIL minimizes pattern deformations by using a composite stamp of rubber on thin glass. In this manner the rubber is always attached to a carrier, which is either the master (from which it was molded) or the glass sheet, which both have high in-plane stiffness. As the glass carrier is thin, the composite stamp is flexible in the out-of-plane direction, which allows for substrate non-flatness and enables wafer scale conformal contact. The rubber allows for local deformation around particle contaminants which avoids damage to stamp or substrate.

Two master gratings (typical area cm^2) of 240 nm pitch were made on 150 mm silicon wafers by electron beam lithography of negative tone hydrogen-silsesquioxane (HSQ) and positive tone PMMA based ZEPP520. To prevent adhesion of the rubber, the surface of the masters is modified with a mono-layer of 1,1,2,2-H-perfluoro-decyl-tri-chloro-silane, applied by vapor phase deposition for 24 hours.[17] Poly-di-methyl-siloxane (PDMS) rubber stamps can be directly molded from the fluor-modified e-beam resist.

The grating patterns on the silicon wafer are molded in PDMS that has a high Young's modulus, as described in ref.[18,19]. After mixing and de-gassing the components, a 50-100 micron thick H-PDMS layer is formed over the masters by spin coating for 30 seconds at 1000 rpm. After a pre-cure for 15 minutes at 50 °C a defined amount of soft PDMS (Sylgard 184) is poured on the master. This PDMS is squeezed between the master and 200 micron thick AF45 glass to form a uniform layer of ~0.5 mm thickness. The "master – PDMS – glass" sandwich is cured for 24 hours in an oven at 50 °C. The stamp is released from the master by gentle peeling. Multiple stamps can be molded from the master without additional application of the fluor mono-layer.

The stamps are used to imprint substrates up to 150 mm diameter with our SCIL setup. This consists of a flat plate with grooves to hold the composite stamp in place by vacuum, as shown in Fig. 1(a). A substrate coated with a layer of a liquid resist is placed parallel to the stamp with a spacing of ~100 microns. Starting from one side the grooves are pressurized to an overpressure of ~20 mbar. This results in the stamp being gently curved after which it forms a line contact on the substrate. As more grooves are sequentially pressurized capillary forces pull the stamp in the resist and the line contact moves forward which avoids air inclusions, see Fig. 1(b). The stamp is kept in contact until the resist is hardened. Next the grooves are evacuated which results in controlled release of the contact line from the imprinted patterns.
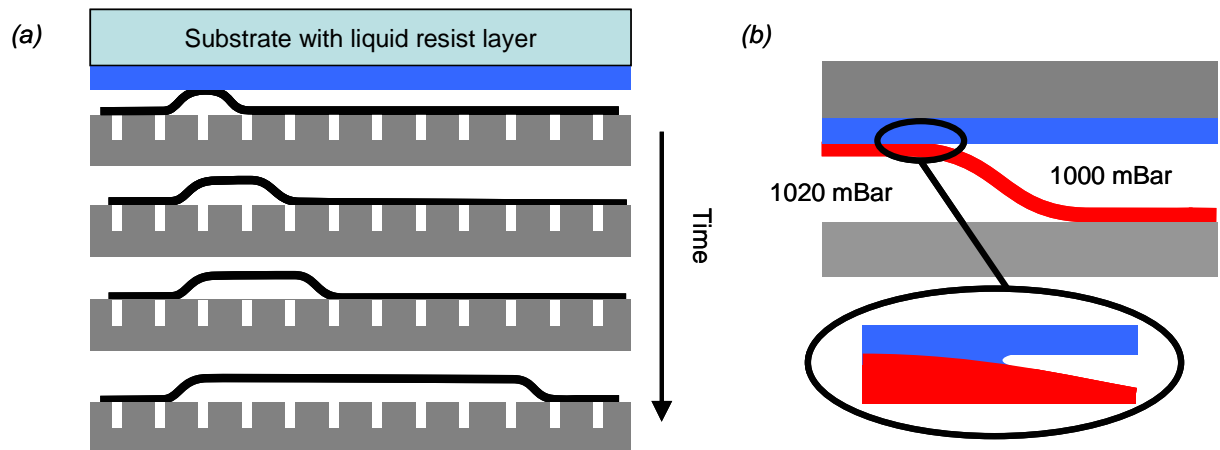

Figure 1. SCIL imprint principle. (a) Time sequence of the imprint step showing the evolution of the contact area by sequential pressurized grooves; (b) the capillary contact line advances due to wetting at both interfaces.

4.3 Room temperature direct patterning of silica sol-gel by SCIL

We used a sol-gel based imprint resist which is a pre-polymerized solution of silicates. The stamp is applied to a thin liquid sol-gel layer on a substrate. The high permeability of PDMS allows solvents and reaction products to diffuse into the rubber. As a result the sol-gel resist layer becomes a solid by forming an inorganic silica network.

The sol-gel base is prepared from tetra-methoxy-ortho-silicate (TMOS) and methyl-tri-methoxy-silane (MTMS) in a 1:1 molar ratio. This is hydrolyzed for 10 minutes at room temperature with an equal molar ratio of water to reactive alkoxide groups using water that was acidified with 1 M formic acid. After the hydrolysis reaction additional water is added to obtain a total molar ratio of water:silicon = 9:1. The mix is subsequently stabilized by adding n-propanol to dilute the sol to a 0.78 mol Si / kg hydrolysis mixture and stored in the freezer. Each time the sol-gel imprint resist was freshly prepared by mixing equal masses of hydrolysis mixture with n-propanol and addition of 1 weight percent 1,2-propanediol.

Typical resist layers are 10 to 200 nm thick and are formed by spin coating. During spin coating the volatile components of the imprint resist evaporate, leaving mainly silicon oxide oligomers and the non-volatile 1,2-propanediol. The remaining propandiol keeps the sol-gel liquid after spin coating and within a minute the stamp was applied in the sol-gel layer using the SCIL setup. Next the 1,2-propanediol diffuses into the stamp which increases the concentration of reactive groups (silicon-hydroxyl and silicon-alkoxides). These condensate to form an inorganic network of Si-O-Si bonds while the reaction products (water and alcohols) are also removed by diffusion into the stamp. After 10 minutes at room temperature the stamp can be removed from the sol-gel structures. The resulting sol-gel patterns are composed of ~ 88 wt. % silicon oxide and remaining organic components. Additional curing promotes additional formation of the inorganic network which is stable in air up to 450 °C; higher curing temperatures convert the material to pure silica.

Figure 2 shows secondary electron microscope (SEM) images of the master grating in HSQ (a) and a sol-gel replica cured at 200 °C in top-view (b) and cross section (c). The sol-gel grating is homogeneous and no defects like broken or deformed features are observed. The observed roughness in HSQ lines of the master grating is due to the high writing current used to reduce e-beam writing time. As can be seen from Fig. 2 the small details in the master pattern are perfectly copied in the sol-gel replica, which proves the high fidelity of our sol-gel imprint process.

4.4 Large area pattern uniformity

The double replication method of SCIL (master → stamp, stamp → sol-gel) can potentially introduce pattern distortions. Deformations over large areas were characterized by measuring
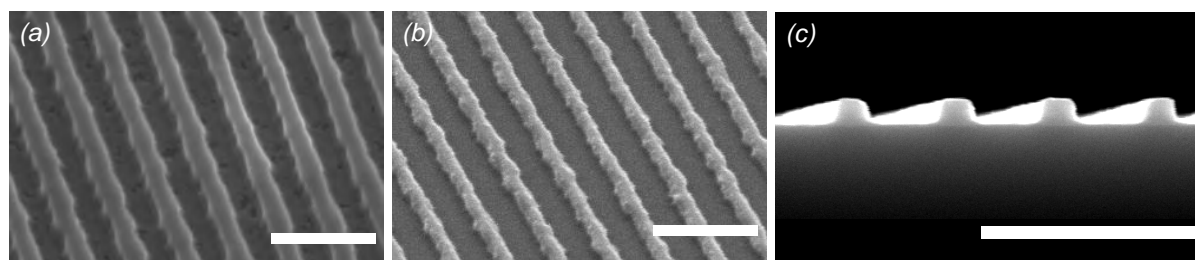

Figure 2. SEM images of (a) master grating in HSQ resist and (b,c) sol-gel replica (top view (b); cross section (c)). Scale bar is 500 nm.

variations in the pitch of a large-area grating made using SCIL. A 3 micron pitch master grating was made on a 150 mm silicon wafer using an ASML wafer stepper to illuminate resist with 365 nm light. Grating areas of 15×15 mm were stitched to populate the whole wafer. This pattern was transferred to a depth of 90 nm in the silicon using reactive ion etching (RIE). The composite stamp was replicated from the silicon master using the same procedure as described in chapter 2. Using SCIL the 3 micron grating was replicated in sol-gel on a silicon wafer.

The pitch of the master and sol-gel replica grating was determined by laser diffraction. This was done by illuminating the grating perpendicular to the surface using a He-Ne laser with a wavelength of 632.8 nm with a spot diameter of 125 micrometer. The pitch variation was determined by measuring the variations in the angle between the reflected -4th and +4th diffraction orders using two CCD cameras. Scanning the laser spot over the sample and tracking the reflected diffraction orders on the camera produces a two-dimensional map of the grating pitch averaged over the beam spot size. The measured area is 25×25 mm^2. Figure 3 shows images of the average grating pitch for master (a) and sol-gel replica, with the imprint direction (see Fig. 1) parallel (b) or perpendicular (c) to the SCIL grooves. As can be seen from the figure, the variation in the average grating pitch for both master and replica is less than 0.1 nm (i.e. ±0.03 %). The bright lines are due to stitching errors between the 15×15 mm grating areas, introduced in the mastering process. The isolated artifacts in the replicas (see arrows) are due to dust particles, which was confirmed by optical inspection at these places. Note that due to the softness of the stamp, particles only cause pattern deformation in a small range around the particle. Comparing the images for the two imprint directions we conclude that the direction in which the grating was imprinted does not influence the deformation. The observed replication errors in the imprinted patterns do not exhibit a cumulative error; for example a cumulative error of only 0.1 nm over a distance of 3 micron, would lead to a 33 nm absolute error over 1 cm, which is much larger that the 0.1 nm error found in Fig. 3(b,c). The replication fidelity we obtain of pitch variation of less than 0.1 nm has to our knowledge never been shown for soft stamp methods. These two components combined have the potential to achieve sub-20 nm overlay over square cm areas.
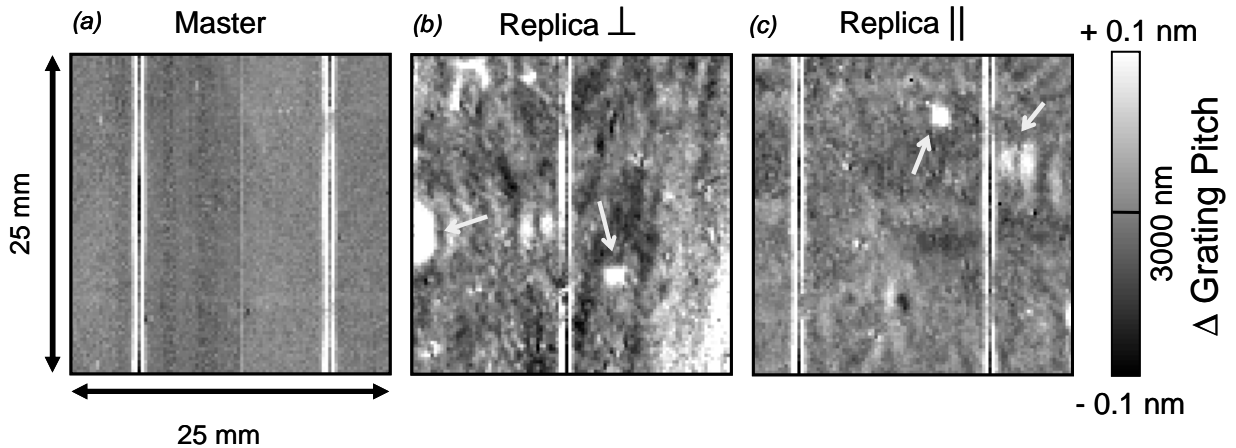

Figure 3. Two-dimensional distribution of the grating pitch measured using laser diffraction, indicated by the scale bar on the right hand side of (a) master and the sol-gel replicas, printed (b) perpendicular and (c) parallel to the grating direction. A 633 nm laser with a spot diameter of 125 μm was used, the measured area is 15×15 mm, the grating pitch ranges from 2999.9 to 3000.1 nm.

4.5 2D to 3D: multi layer imprinting

The previous sections demonstrated that direct patterning of sol-gel materials using SCIL delivers high-quality gratings over large areas with minimal distortions. Figure 4 shows the process flow used to imprint grating layers on top of each other to fabricate a 3D structure. The cycle is repeated until the desired number of grating layers is reached.

The process consists of the following steps:

1. A controlled amount of sol-gel imprint resist is applied on an AF45 glass substrate by spin coating (corresponding to a layer thickness of 35 nm when cured at 200 °C).
2. The sol-gel is patterned in 15 minutes with a 240 nm pitch grating using the SCIL setup.
3. After release of the stamp the sol-gel grating is cured at 200 °C for 20 minutes in air.
4. After imprinting a residual layer remains under the imprinted gratings, that must be removed to obtain an open 3D structure. Using SEM it is found that, with the appropriate amount of resist applied in step 1, the residual layer thickness is 10-15 nm over the entire imprinted area. It is removed by CF_4 reactive ion etching (RIE) for 30 seconds using a recipe of 10 sccm CF_4 and 20 sccm N_2, at a pressure of 12 mT and RF power of 50 W. This results in a linear etch rate of 30 nm per minute for un-patterned sol-gel layers. The process leaves 70 nm high grating lines.
5. Before the second layer can be patterned by the imprint process, the first grating layer has to be planarized while preserving the sol-gel grating topology and dimensions. We use spinodal de-wetting[20] and capillary forces to planarize a grating with polymer. To do so, a mono-layer of hexa-methyl-di-silazane is applied by vapor phase deposition, followed by a post cure at 80 °C, to render the surface hydrophobic (low surface energy).
6. A controlled amount of a solution of polystyrene (MW 206k Aldrich) in n-butylacetate is spin coated over the grating, resulting in the grating being in-filled and covered by polymer. Figure 5(a) shows atomic force microscopy (AFM) scans of the sol-gel grating after deposition of the polymer. Clearly the polymer has filled the spaces between the grating lines, leaving a residual height variation of ~25 nm.
7. The closed polymer film is broken up by heating it above the polymer glass transition temperature for 10 minutes at 150 °C. Spinodal de-wetting initiates at points where the polymer layer is thinnest, which is at the edge of the grating lines. Due to the low surface energy, the polymer withdraws from the top of the grating lines and capillary forces lead to filling of the space between the lines. Figure 5(b) shows AFM data of the grating after spinodal de-wetting has taken place. The residual height variation is only ~5 nm.
8. A low-power oxygen plasma, followed by rinsing with de-ionized water is used to improve adhesion of the next sol-gel layer on the planarized grating surface.

Subsequent grating layers are patterned by repeating steps 1 through 8. Figure 5(c) shows the residual height modulation after imprinting a second grating perpendicular to the first grating, and removal of the residual layer (step 4). The line scan is taken between the lines of the second
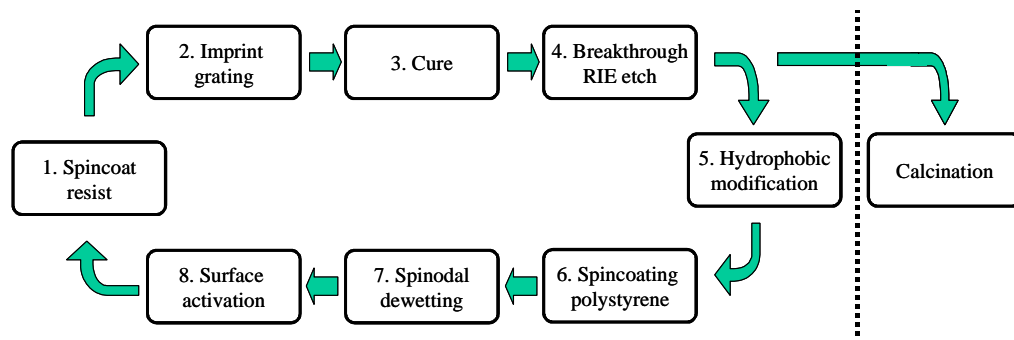

*Figure 4. Process flow used to produce open multi-layer structures.*

grating, in a direction perpendicular to the first grating layer (dashed line in AFM image). It confirms that the first layer was planarized within 5 nm and that imprinting subsequent layers does not affect the previous layer.

Calcination. After the last grating layer is imprinted and opened by RIE etching (step 4) all the polymer used for planarization of the sol-gel gratings is removed by calcination. Figure 5(d) shows a SEM image of a structure with four grating layers in alternating direction calcined in air at 550 °C for two hours. The scale bar indicates 500 nm. As can be seen, the polymer is clearly removed, resulting in an open silica 3D grating structure.

4.6 High temperature behavior of imprinted sol-gel patterns

To infill the sol-gel 3D template with a high-index dielectric, high temperatures (up to 1000 °C) are typically required. Up to 450 °C densification occurs due to removal of nano-pores by condensation of Si-OH groups. Heating the patterned sol-gel to 1000 °C will oxidize the silicon-methyl groups in MTMS to silicon hydroxyl groups which can subsequently further condensate and sinter the sol-gel to dense silica. It is therefore important to assess the shrinkage that occurs in an imprinted structure after sintering.

High aspect ratio gratings (width 95 nm, height 180 nm) with a pitch of 240 nm were patterned in sol-gel on silicon substrates. Figure 7 shows SEM cross sections of sol-gel gratings directly after imprint patterning (a) and sintering at 1050 °C in air (b). The grating lines show a shrinkage of 16 % in width and 18 % in height. The shrinkage is reproducible and can therefore be corrected for in designing the dimensions of the master grating. A four-layer photonic crystal was also made on a silicon substrate and heated to 1050 °C in air. The densification of the sol-gel will
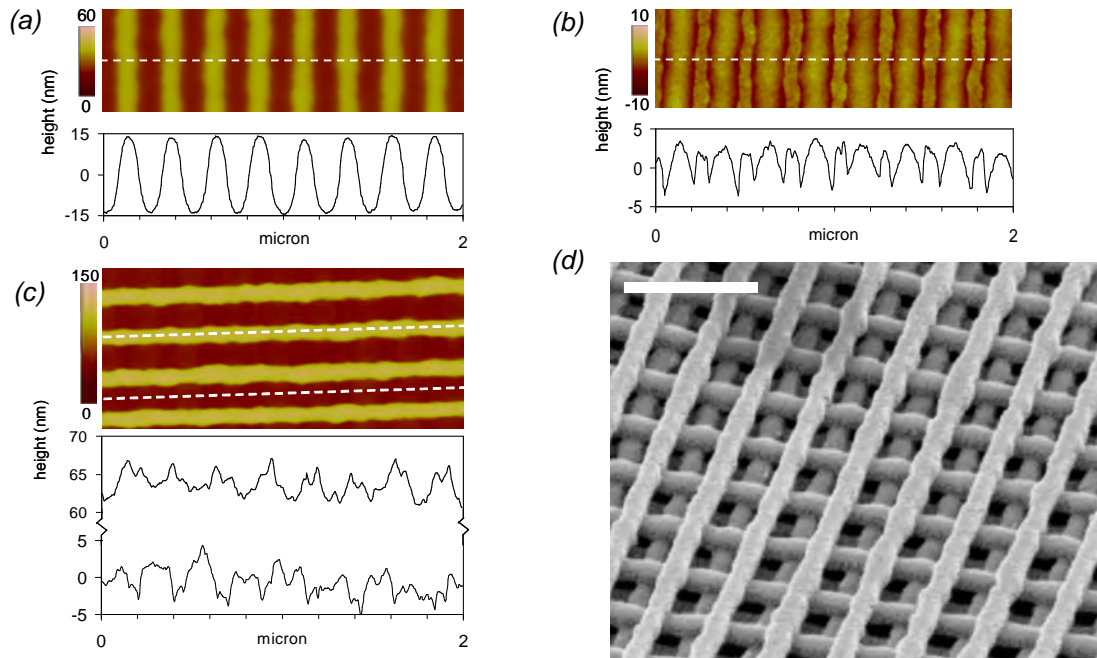
Figure 5. AFM height data. Both two-dimensional images and characteristic line scans normal to the grating are shown. (a) Grating height after spin coating polystyrene onto a grating layer, (b) grating height after spinodal de-wetting of polymer. The sol-gel lines can clearly be distinguished from the polymer. (c) Data of two perpendicularly oriented imprinted gratings after the RIE breakthrough etch. The height variations in the first grating layer are ~ 5 nm after patterning of the second grating layer and the lines of the second grating are flat within 5 nm. (d) SEM image of a four layer silica sol-gel grating stack after polymer burn out at 550 °C. The scale bar indicates 500 nm.
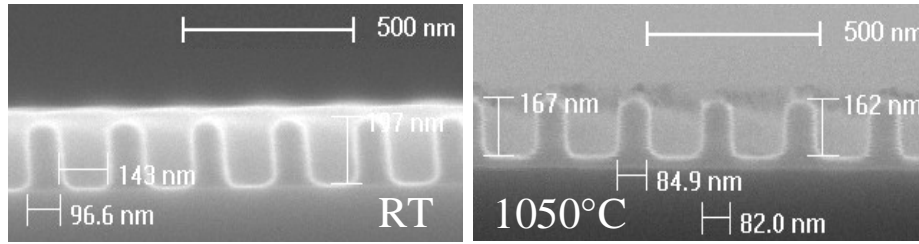
Figure 7. SEM cross section images of a sol-gel grating on silicon after imprinting (a) and after annealing at 1100 °C (b). The sol-gel lines densify and shrink after annealing due to increased cross linking and removal of methyl groups by oxidation.

induce stress in the material, which could lead to cracks or layer delamination. However none of these effects have been observed. A possible reason is that the small feature size and open structure permit stress relaxation, which occurs less easily in larger features or continuous layers.

The observed shrinkage in our sol-gel material is low compared to previous work done on patterning inorganic sol-gel systems, in which volume shrinkages of tens of percents are reported already at room temperature resulting in deformed features after stamp release.[21,22] In this work, the addition of MTMS to TMOS leads to a controlled reduction of the sol-gel cross link density which allows patterning of a high sol to liquid ratio.

The above sections show the feasibility of fabricating high-quality 3D structures. In the next section we investigate the required accuracy in the superposition of the patterns in the various layers (overlay alignment).

4.7 SCIL overlay alignment

To realize an optical bandgap for wavelengths around 550 nm, a woodpile photonic crystal requires a variation of < 20 nm in the overlay alignment of layers 1 and 3, 2 and 4 etc. Moreover, for a sample with an area of 1x1 cm this means the rotation error between every other layer should be less than 10^{-6} rad. We study these limits by using our SCIL setup to align and imprint two grating layers. This requires two stamps, see Fig. 8(a), one which has only box-in-box type alignment markers 75 mm apart and a second stamp which contains corresponding alignment markers and gratings. The stamp with the gratings is composed of five 2×2 mm grating areas arranged within a 30×30 mm square as indicated in Fig. 8(a, stamp 2). Within each square 240 nm pitch grating areas are made, oriented in two perpendicular directions to enable the detection of alignment errors in two directions.
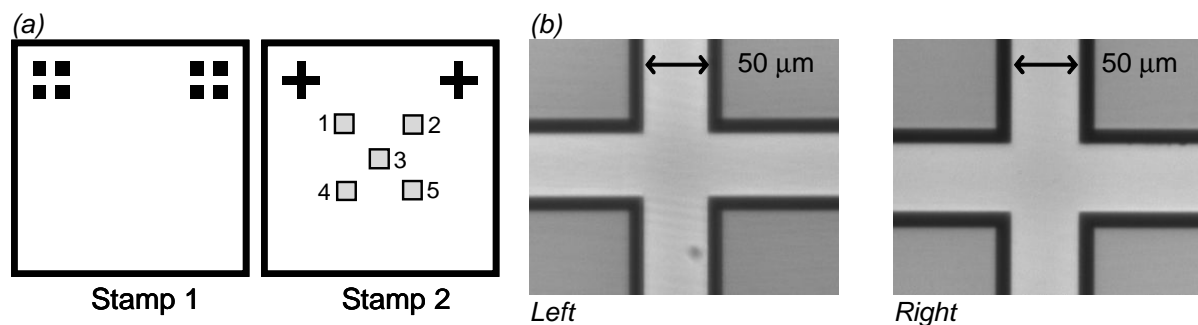

Figure 8. (a) Schematic layout of the two stamps used for overlay alignment tests. Stamp 1 has only alignment patterns. Besides alignment patterns, stamp 2 also has grating patterns defined in the five gray squares in the centre of the stamp. These are used to determine overlay errors. (b) CCD images of the left and right box-in-box alignment markers. The stamp is in contact with the substrate after alignment has been performed.

The SCIL imprint tool is equipped with closed-loop piezo-electric actuators to control the position of a glass chuck which holds the substrate. First the alignment pattern of the first stamp is imprinted on 0.7 mm thick 100×100 mm AF45 glass. Next the second stamp is loaded in the SCIL tool. The imprinted alignment markers are first covered with tape and sol-gel resist is then spin coated over the substrate. After removal of the tape the markers are free of sol-gel resist. The alignment markers on the stamp and substrate can be imaged through the glass chuck and substrate using a long working-distance objective and CCD camera. Figure 8(b) shows CCD images of two (aligned) markers on the left and right side of the substrate. Parallax errors are avoided by measuring the alignment markers when they are in contact. This is done by only pressurizing the stamp at the alignment marker position. A pattern recognition program is used to detect the deviations from the ideal aligned position, the dark lines around the middle bright cross are of equal size. To correct the determined position error the stamp is released from the substrate and the chuck re-positioned using the piezo actuators. Next contact is re-established at the marker positions and the offset determined. After 3 iterations the residuals in the offset are minimized. Now the rest of the substrate is contacted, thereby imprinting the gratings.

To obtain contrast during later SEM inspection, the first imprinted grating layer is covered with 10 nm of molybdenum using sputter deposition. Next, sol-gel resist is applied again and a second alignment performed, after which the same grating pattern was imprinted over the first molybdenum coated layer. Both imprints have thus been separately aligned with respect to the alignment markers imprinted with stamp 1. Figure 9(a) shows a SEM image taken under an angle of 45° of the two aligned layers. As can be seen, each grating layer contains horizontally and vertically oriented grating lines. The bottom layer can be distinguished by the light color due to the molybdenum. The lines of the first and second grating layers are well aligned both directions. The alignment error is determined by measuring the offset between the first and second grating in two directions. For the image in Fig. 9(a) this is 55 nm in the horizontal direction and 21 nm in de vertical direction, respectively. Figure 9(b) shows an overlay error map for the five grating positions, assuming the first layer was perfectly aligned. The square corresponds to the area of the five regions which contain gratings, see Fig. 8(a) and the overlay error is represented by the distance between the two squares, with the length scale indicated (100 nm scale bar). From Fig. 9(b) it can be seen that the maximum misalignment between the two grating layers is 110 nm (top right pattern). The maximum rotation error is found to be 1.3×10^{-6} rad. As these errors are the sum of two separate alignment runs, the alignment error for a separate run therefore is less than 55 nm. From this data the magnification error between the first and second imprint can be calculated. The data for the second imprint in Fig. 9(b) are translated so that the residual overlay error is zero for the centre point. The remaining off-sets for the other four points are then a measure for pattern distortion and magnification errors. We expect that magnification errors are most probably induced by thermal variation during imprinting and are therefore likely symmetric around the centre of the substrate. We find a maximum magnification error of 1.2 ppm in the x direction and 2.4 ppm in the y direction. This is highly accurate as no active temperature control was used and there was a day between the two aligned imprints runs.
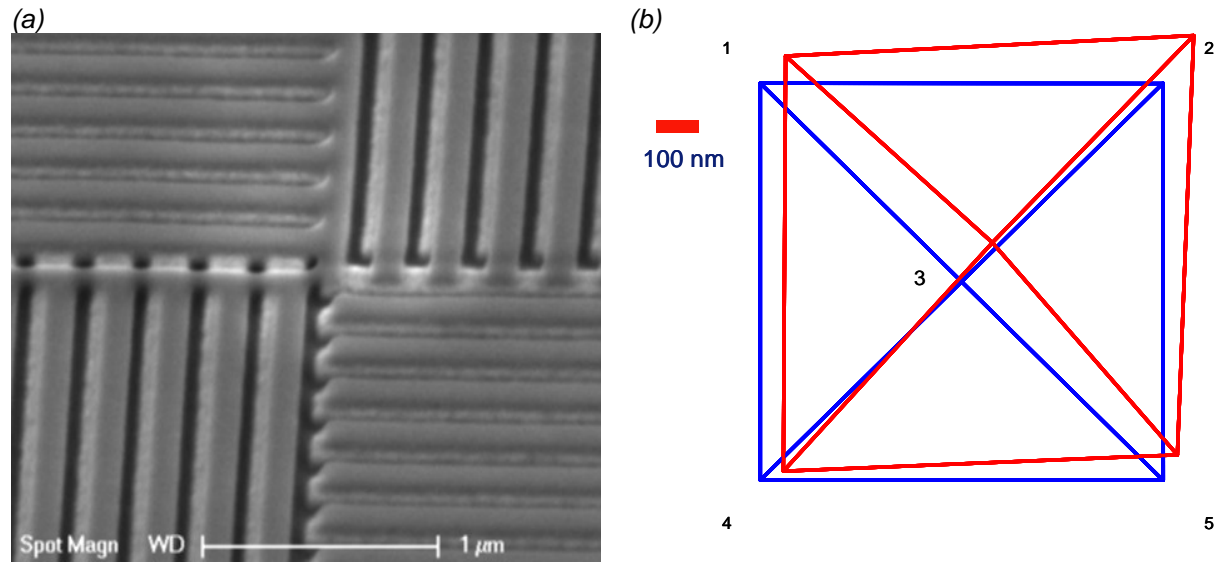
Figure 9. (a) SEM image taken under a tilt of 45° of two aligned and imprinted gratings. The bright lines are from the first imprinted grating the darker lines from the second imprint. (b) Schematic of the overlay error for five positions over the substrate over an area of 3x3 cm. The numbers correspond to the grating areas on the stamp in Fig. 8.

Comparing the maximum misalignment in Fig. 9(b) of 110 nm with the magnification error over a 30×30 mm area of 72 nm (assuming a 2.4 ppm error), we calculate that the maximum alignment error amounts to ~40 nm. Improvement in overlay accuracy can be expected as magnification errors can be eliminated by using a temperature controlled environment during imprinting. Furthermore, the currently used alignment process only analyses the alignment patterns and minimizes the offsets. This process can be improved by using more accurate Moiré interference alignment markers to accurately measure misalignment. If the alignment error could be minimized the present SCIL technique with the 2 ppm magnification error may reach ~20 nm overlay precision over an area of 1×1 cm^2 while this area can be increased with active thermal control.

4.8 Conclusions

We present a new and relatively simple route for the fabrication of 3-D photonic crystals. We demonstrate a 4-layer woodpile silica scaffold that can be infiltrated with a high-index material to form a photonic crystal with a complete bandgap in the visible. The replication process using soft stamps shows excellent quality in transferring sub-50 nm features in silica sol-gel material. Due to the mainly inorganic composition of our imprint resist it can be sintered up to 1050 °C in air while maintaining feature fidelity. SCIL enables large area replication of patterns which are nearly free of deformations. We observe an average local pattern distortions of less than 0.1 nm in a grating with a 3 micron pitch, over an areas as large 25×25 mm. The corresponding magnification error is 1.2-2.4 ppm. These results are two orders of magnitude better than any previously reported work on overlay and magnification errors for a soft lithography method.[15,16] By using SCIL and box-in-box alignment markers to align two layers, we aligned two layers within 100 nm over an area of 3×3 cm^2. These results enable the fabrication of optical 3D photonic bandgap crystals with an overlay error less than 20 nm over a 1×1 cm^2 area. Work on this topic is currently being pursued.

References

[1] E. Yablonovitch, *Inhibited spontaneous emission in solid-state physics and electronics*, Phys. Rev. Lett. **58**, 2059 (1987)

[2] J.J. Wierer, M.R. Krames, J.E. Epler, N.F. Gardner, M.G. Craford, J.R. Wendt, J.A. Simmons, and M.M. Sigalas, *InGaN/GaN quantum-well heterostructure light-emitting diodes employing photonic crystal structures*, Appl. Phys. Lett. **89**, 3885 (2004)

[3] S.A. Moore, L. O'Faolain, T.P. White, and T.F. Krauss, *Photonic crystal laser with mode selective mirrors*, Optics Express **16**, 1365 (2008)

[4] J.E.G.J. Wijnhoven, and W.L. Vos, *Preparation of photonic crystals made of air spheres in titania*, Science **281**, 802 (1998)

[5] S.-Y. Lin, and J. G. Fleming, *A three-dimensional optical photonic crystal*, J. of Lightwave Tech. **17**, 1944 (1999)

[6] E. Graugnard, V. Chawla, D. Lorang, and C. J. Summers, *High filling fraction gallium phosphide inverse opals by atomic layer deposition*, Appl. Phys. Lett. **89**, 211102 (2006)

[7] B. Gralak, M.J.A. de Dood, G. Tayeb, S. Enoch, and D. Maystre, *Theoretical study of photonic band gaps in woodpile crystals*, Phys. Rev. B **67**, 066601 (2003)

[8] J.G. Fleming, and S.-Y. Lin, *Three-dimensional photonic crystal with a stop band from 1.35 to 1.95 μm*, Optics Let. **24**, 49 (1999)

[9] S. Noda, K. Tomoda, N. Yamamoto, and A. Chutinan, *Full three-dimensional photonic bandgap crystals at near-infrared wavelengths*, Science **289**, 604 (2000)

[10] G. Subramania, Y.-J. Lee, A.J. Fischer, and D.D. Koleske, *Log-pile TiO_2 photonic crystal for light control at near-UV and visible wavelengths*, Adv. Mat. **21**, 1 (2009)

[11] M.J.A. de Dood, B. Gralak, A. Polman, and J.G. Fleming, *Superstructure and finite-size effects in a Si photonic woodpile crystal*, Phys. Rev. B **67**, 035322 (2003)

[12] S.Y. Chou, P.R. Krauss, W. Zhang, L. Guo, and L. Zhuang, *Sub-10 nm imprint lithography and applications*, J. Vac. Sci. Technol. B **15**, 2897 (1997)

[13] N. Tétreault, G. von Freymann, M. Deubel, M. Hermatschweiler, F. Pérez-Willard, S. John, M. Wegener, and G.A. Ozin, *New route to three-dimensional photonic bandgap materials: Silicon double inversion of polymer templates*, Adv. Mater. **18**, 457 (2006)

[14] F. Hua, A. Gaur, Y. Sun, M. Word, N. Jin, I. Adesida, M. Shim, A. Shim, and J.A. Rogers, *Processing dependent behavior of soft imprint lithography on the 1–10-nm scale*, IEEE Transactions on Nanotechnology **5**, 301 (2006)

[15] J.A. Rogers, K.E. Paul, and G.M. Whitesides, *Quantifying distortions in soft lithography*, J. Vac. Sci. Technol. B **16**, 88 (1998)

[16] S. Pagliara, L. Persano, A. Camposeo, R. Cingolani, and D. Pisignano, *Registration accuracy in multilevel soft lithography*, Nanotechnology **18**, 175302 (2007)

[17] G.-Y. Jung, Z. Li, W. Wu, Y. Chen, D.L. Olynick, S.-Y. Wang, W.M. Tong, and R.S. Williams, *Vapor-phase self-assembled monolayer for improved mold release in nanoimprint lithography*, Langmuir **21**, 1158 (2005)

[18] H. Schmid, and B. Michel, *Siloxane polymers for high-resolution, high-accuracy soft lithography*, Macromolecules **33**, 3042 (2000)

[19] T.W. Odom, J.C. Love, D.B. Wolfe, K. E. Paul, and G.M. Whitesides, *Improved pattern transfer in soft lithography using composite stamps*, Langmuir **18**, 5314 (2002)

[20] R. Xie, A. Karim, J.F. Douglas, C.C. Han, and R.A. Weiss, *Spinodal dewetting of thin polymer films*, Phys. Rev. Lett. **81**, 1251 (1998)

[21] C. Marzolin, S.P. Smith, M. Prentiss, and G.M. Whitesides, *Fabrication of glass microstructures by micro-molding of sol-gel precursors*, Adv. Mat. **8**, 571 (1998)

[22] M. Li, H. Tan, L. Chen, J. Wang, and S.Y. Chou, *Large area direct nanoimprinting of SiO_2–TiO_2 gel gratings for optical applications*, J. Vac. Sci. Technol. B **21**, 660 (2003)

Chapter 5

Increased performance of polarization stable VCSELs by monolithic sub-wavelength gratings produced by soft-nanoimprint lithography

We present a novel method to fabricate polarization-stable oxide-confined single-mode GaAs based vertical cavity surface emitting lasers (VCSELs) emitting at 850 nm using a new soft lithography nanoimprint technique. A monolithic surface grating is etched in the output mirror of the laser cavity using a directly imprinted silica based sol-gel imprint resist as etch mask. The opto-electronic performance of these devices is compared to VCSELs fabricated by state-of-the-art electron-beam lithography. The lasers made using the soft-nanoimprint technique show single-mode TM lasing at a threshold and laser slope similar to that of devices made by e-beam lithography. The soft-nanoimprint technique also enables the fabrication of gratings with sub-wavelength pitch, which avoids diffraction losses in the laser cavity. The resulting single-mode VCSEL devices exhibit 29 % enhanced efficiency compared to devices equipped with diffractive gratings.

5.1 Introduction

Single-mode vertical cavity surface emitting lasers (VCSELs) find application in tunable diode laser absorption spectroscopy[1,2], laser based optical mouse sensors, optical encoders and rubidium atomic clocks for GPS systems[3,4]. These applications require single-mode and single-polarization emission. Due to the symmetry of a VCSEL device the laser does not have a geometrically defined single polarization orientation.[5-10] Emission occurs along both the <100> and <010> GaAs crystal planes. As a result the polarization can spontaneously switch between these two directions during operating of the laser, which is not desired. One method to avoid the switching of the polarization mode during laser operation is to apply a monolithic surface grating to one of the dielectric distributed Bragg reflector (DBR) mirrors of the VCSEL laser cavity.[11,12] A grating exhibits different reflection coefficients for TE and TM polarized light. The polarization mode with the higher reflectivity and thus the higher cavity quality factor will have the lowest threshold pump current for gain. As a result the polarization with the highest reflectivity will become the dominant lasing mode. Currently polarization locked VCSELs use gratings made by standard electron beam lithography.[13] Grating pitches are typically as large as 550 nm, as smaller pitches would increase the e-beam writing time and thus costs. This large pitch causes diffraction of a significant fraction of light and as a result the efficiency of stabilized VCSELs is reduced. Depending on the laser design and mirror reflectivity, which determines the number of round trips, the efficiency loss can be up to 50 %.
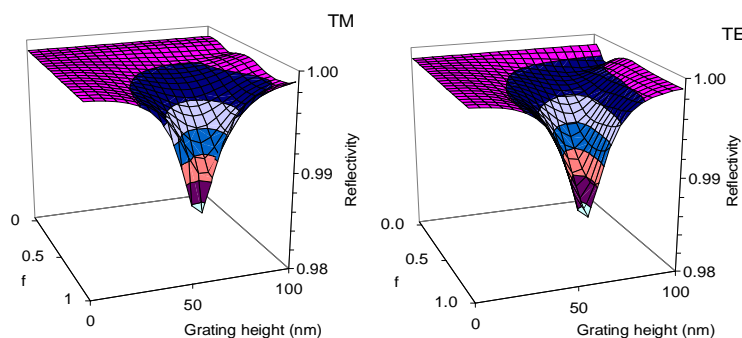
Chu *et al.* proposed to use sub-wavelength transmission gratings, that do not exhibit higher order diffraction, in an external cavity design to stabilize the VCSEL polarization.[14] As this is not a monolithic integrated solution cavity length and temperature are more difficult to control and laser operation is less stable. Johan *et al.* used e-beam lithography to pattern sub-wavelength gratings in an integrated approach.[15] However this solution requires a very well aligned localized grating on the output mirror which is difficult to produce. Moreover this method is not well suited for mass production. Here, we demonstrate polarization stabilized VCSELs using monolithic surface gratings with a period below the diffraction limit and measure polarization-stable lasing with improved efficiency. To pattern the gratings a novel soft-nanoimprint technique is used which enables application over large areas at low cost.

Soft imprint techniques use a rubber stamp which offers advantages with respect to rigid stamp methods as the soft stamp can conform to substrate bow and surface defects and full wafers can be imprinted without damage to stamp or substrate. Release of the stamp from an imprinted pattern does not involve high forces as the stamp can be removed by a peeling action; contrary to rigid stamps which require substantial force to initiate release. Previously, soft stamp imprint methods could not reproduce patterns below 100 nm with high fidelity due to deformations of the rubber features. These imprint methods also yielded pattern distortion on a wafer scale, which hampers overlay alignment during subsequent production processes.[16-18]

Here, we use a new soft stamp method called Substrate Conformal Imprint Lithography (SCIL), which offers wafer-scale replication with sub-50 nm resolution and minimal pattern deformations on wafer scales at high throughput. It also enables room temperature patterning of sol-gel materials which results in stable silicon oxide patterns which can directly be used as a hard mask.[19]
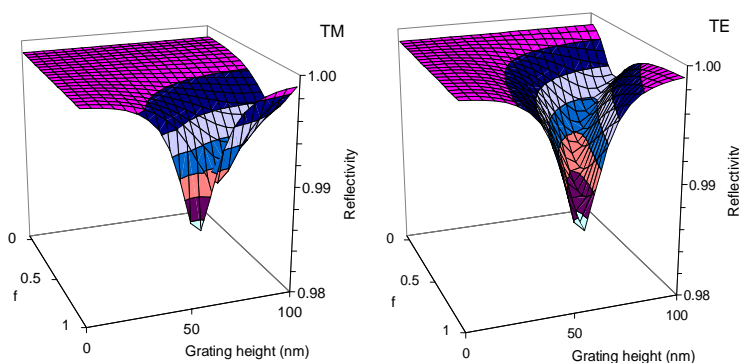
5.2 Experimental studies

5.2.1 Sub-wavelength grating design and rigorous coupled wave analyses

In this work we study GaAs/AlGaAs VCSELs that operate at 850 nm. The grating is made in GaAs (refractive index n=3.63) and is integrated with the VCSEL DBR mirror, see Fig. 1(a). The maximum grating pitch at which no higher-order diffraction occurs at λ=850 nm in the GaAs grating is given by $d = \lambda / n = 234$ nm. No diffraction occurs at the grating-air interface at this pitch. The effective refractive index of a grating layer for the two polarization orientations can be estimated using an effective medium approximation, using: $\varepsilon_\perp = (\varepsilon_1 \varepsilon_2) / (f \varepsilon_1 + (1-f) \varepsilon_2)$ and $\varepsilon_\parallel = f \varepsilon_2 + (1-f) \varepsilon_1$, with ε_1=1, ε_2= 13.81. Figure 1(b) shows the effective refractive index for TE and TM polarizations, calculated for perpendicular incidence on a grating in GaAs as a function of fill fraction (f=0: air, f=1: GaAs). A large difference in effective index is found for the two polarizations, which will result in a large variation in the reflectivity of the DBR, as we calculate in the next paragraph.

The reflectivity, transmission and diffraction of a DBR mirror with an integrated grating were calculated as function of grating pitch, height and fill fraction. We used the GSolver RCW software package, which uses rigorous coupled wave analysis to calculate the diffraction efficiency of a grating.[20] The reflectivity of the top DBR mirror towards the cavity side was simulated, coming from GaAs. The top DBR mirror consists of 24 pairs composed of 60 nm AlGaAs (n=3.13) and 65 nm GaAs (n=3.63) each, covered with a spacer layer of 120 nm GaAs, see schematic in Fig. 1(a). The GaAs grating layer with varying pitch, height and fill fraction is made on top of the spacer layer. In the simulation it is assumed there is no absorption in the materials. We simulated two grating pitches, 550 nm (which has diffraction orders in reflection) and 150 nm (which exhibits no diffraction). In Figs. 2(a) and (b) the 0th order reflectivity of 850 nm light for the orthogonal (TE) and perpendicular (TM) polarization to the grating are plotted as function of grating layer thickness and fill fraction, for 550 nm and 150 nm pitch gratings respectively.

Figure 1. (a) Schematic of top DBR cavity laser mirror with integrated grating. The arrows indicate diffraction into higher order grating modes. (b) Effective refractive index for TE and TM polarizations, calculated using an effective medium approximation, for perpendicular incidence on gratings in GaAs as function of fill fraction (f=0: air, f=1: GaAs).

(a) 550 nm pitch

(b) 150 nm pitch

Figure 2. (a) Schematic of top DBR cavity laser mirror with integrated grating. The arrows indicate diffraction into higher order grating modes, (b) TM and TE polarization reflectivity of a 24 pair DBR with 550 nm pitch grating at λ=850 nm as function of grating fill fraction (f) and grating depth, (c) TM and TE polarization reflectivity of a 24 pair DBR with 150 nm pitch grating at λ=850 nm as function of grating fill fraction (f) and grating depth.

In Fig. 3(a) the difference between TM and TE reflectivity is plotted for 550 nm and 150 nm gratings. Figure 3(b) plots the fraction of light that is diffracted in higher order modes for 550 nm gratings as function of grating height and fill fraction. In theory any difference in TE and TM reflection will result in polarization stabilization. In practice a minimum reflectivity is required for lasing; for polarization locking under all driving conditions the difference in TE and TM reflectivity must then be maximized. Figure 2 shows that the 24-pair DBR with only the 120 nm GaAs spacer layer (data for grating height = 0) has a reflectivity of 99.90 %. Adding the grating layer and taking f=0, reaches a minimum reflectivity of 98.70 % for both polarizations for a GaAs top layer thickness of 55 nm. At this thickness, the total GaAs layer on the DBR, see Fig. 1(a), corresponds to an optical thickness of one wavelength. Tuning the thickness and fill fraction of the grating layer will thus give a maximum modulation in DBR reflectivity of 1.2%. Figure 3(a) shows that for both grating pitches the TM – TE reflectivity contrast increases with increasing thickness and then decreases. For a grating height up to 60 nm the TM mode has the highest reflectivity; for large fill fraction and grating layer thickness over 60 nm, TE mode has the highest reflectivity.

It can also be seen that the reflectivity contrast is largest for the 150 nm pitch grating. In Fig. 3(b) the sum of the reflectivity of higher order grating reflections for the TM mode is plotted as function of grating height and fill fraction for 550 nm pitch. The diffraction losses first increase and then decrease with increasing grating height and fill fraction. The increase is due to an increased scatter cross section, the decrease is due to the higher reflectivity of the DBR/grating combination for increased thickness (see Fig. 2(a)). Figure 3(b) indicates that to minimize diffraction the grating has to have limited height and fill fraction.
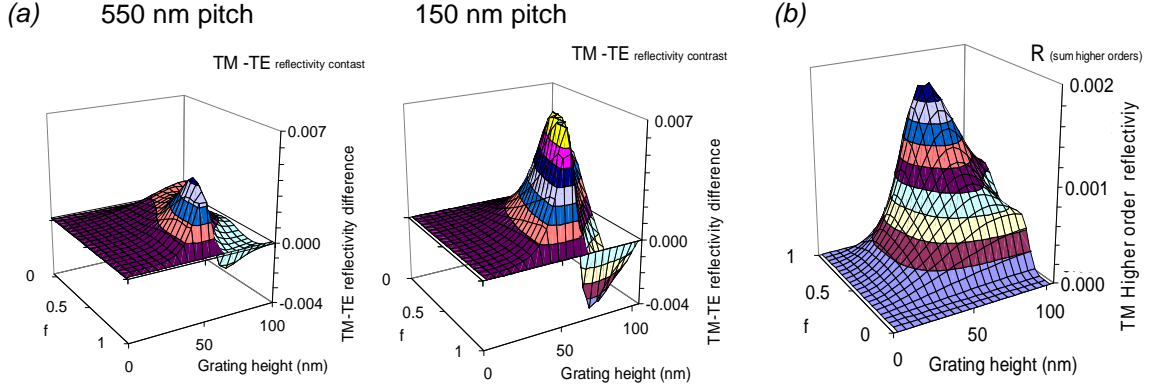
Figure 3. (a) Difference between TM and TE reflectivity at λ=850 nm as function of grating fill fraction and depth for 550 nm and 150 nm gratings on a 24 pair DBR, (b) Fraction of TM polarized light reflected in higher grating orders as function of grating fill fraction and depth for 550 nm gratings on a 24 pair DBR.

The reflectivity of the top mirror is mainly determined by the number of DBR pairs. Optimizing the DBR/grating mirror for a polarization-controlled laser requires on the one hand maximum contrast between the reflectivity for TM and TE polarization (Fig. 3(a)), and on the other hand sufficiently high absolute reflection to obtain a high cavity Q. Here we choose a 550 nm grating pitch design with a thickness of 50 nm and fill fraction of 0.3 which results in a reflectivity of 99.83 % with a TM-TE contrast of $7x10^{-4}$. This reflectivity is sufficient to obtain acceptable laser threshold and sufficiently stabilize the TM mode. For this configuration the diffraction losses are $2.8x10^{-4}$ (Fig. 3(b)). This fraction appears relatively low but these losses occur at each optical round trip and correspond to 24.8 % of the out-coupled laser intensity.

To compare the performance of 150 nm pitch gratings to diffractive 550 nm gratings we compare structures with equal absolute TM reflectivity of 99.83 %. This reflectivity is obtained for a 150 nm grating at 50 nm height and 0.55 fill fraction (Fig. 2(b)). Using this sub-wavelength design we expect a reduced laser threshold as no light is lost in higher order diffraction modes, causing a reduced cavity Q. The polarization suppression is expected to increase, as the reflection contrast is increased to $2.5x10^{-3}$, compared to $7.0x10^{-4}$ in the 550 nm design (Fig. 3(a)).

Next, we will describe the fabrication of 150 nm and 550 nm pitch gratings by soft-nano imprint lithography and direct e-beam patterning. The performance of the electrically driven VCSELs will be compared for both designs.

5.2.2 Soft stamp fabrication

The two master grating patterns are prepared on 150 mm diameter silicon wafers using a Jeol 100 kV e-beam pattern generator to pattern ZEPP 520 PMMA based positive tone e-beam resist. From these masters two poly-di-methyl-siloxane (PDMS) stamps are molded which are subsequently used to replicate the grating patterns in sol-gel resist.

The ZEPP resist thickness was 100 nm for the 550 nm pitch grating, f=0.3 (line width 165 nm) and 50 nm thickness for the 150 nm pitch grating, f=0.55 (line width 83 nm). The gratings are written over a 3" diameter area, in 15 micron diameter circles, placed in a 2D array of 200 micron pitch. At the same time alignment markers were defined over the 3" area to align subsequent layers to the grating areas during VCSEL processing. After development of the resist the surface was modified to ease release of the PDMS stamp. This was done by applying

1,1,2,2-H-perfluoro-decyl-tri-chloro-silane by vapor phase deposition for 24 hours.[21] The PDMS stamps were directly molded from the fluor-modified e-beam resist.

The grating patterns on the silicon wafer are molded in PDMS that has a Young's modulus that is higher than that of conventional rubbers, as described in Ref. [22]. After mixing and de-gassing the components, a 50-100 micron thick H-PDMS layer is formed over the masters by spin coating for 30 seconds at 1000 rpm. After a pre-cure for 15 minutes at 50 °C a defined amount of soft PDMS (Sylgard 184) is poured on the master. This PDMS is squeezed between the master and 200 micron thick AF45 glass to form a uniform layer of ~0.5 mm. The "master – PDMS – glass" sandwich is cured for 24 hours in an oven at 50 °C. The stamp is released from the master by gentle peeling. Multiple stamps can be molded from the master.

Pattern deformations are avoided as during stamp preparation the rubber is always attached to a carrier, either the master or the glass sheet, which both have high in-plane stiffness. As the glass support is thin, the composite stamp is flexible in the out of plane direction, which allows for substrate non-flatness. The rubber also allows local deformation around particle contaminants, thereby avoiding damage to stamp or substrate.

5.2.3 Wafer-scale grating replication

Wafer-scale imprints are made with SCIL using a flat plate with 80 vacuum grooves, which hold the composite stamp in place. A resist coated substrate is placed parallel to the stamp with a spacing of ~100 microns. Starting from one side the evacuated grooves are pressurized to ~20 mbar overpressure. This results in the stamp being gently curved, to bridge the 100 micron gap, after which it forms a line contact on the substrate. As more grooves are sequentially pressurized, capillary forces pull the stamp into the resist and the line contact moves forward which avoids the formation of air inclusions. The stamp is kept in contact until the resist is hardened. Next, the grooves are sequentially evacuated which results is a controlled release of the stamp from the imprinted patterns. With this method replicated patterns exhibit merely sub-nm deformation over large areas, as demonstrated in Ref. [19].

The following imprint process was used to replicate both grating designs. A silica based sol-gel was used as imprint resist, of which the preparation is described in Ref. [19]. The sol-gel resist was applied by spin coating on the as-grown VCSEL layer stack on 3" GaAs wafers. The layer thickness was optimized to leave a residual layer after imprinting of ~10 nm. Directly after the spin coat cycle the substrate with the liquid sol-gel was loaded in the SCIL tool and the stamp applied in the sol-gel. The sol-gel cross-links as the remaining solvents and reaction products like water and alcohols are removed from the resist by diffusion into the stamp. After 15 minutes the sol-gel solidified by forming a three dimensional inorganic network. The stamp was removed from the patterned substrate and a post cure at 70 °C was applied to the sol-gel patterns. The resulting grating patterns are composed of silicon oxide (88 wt. %) and remaining organic components and stable in air until 450 °C. This provides a stable inorganic etch mask to pattern the underlying GaAs layer.

The residual layer under the imprinted gratings is removed by CF_4 reactive ion etching (RIE). A recipe of 10 sccm CF_4 and 20 sccm N_2 is used, at a pressure of 12 mT and RF power of 50 W. This results in a linear etch rate of 30 nm per minute for patterned sol-gel layers. Both gratings were etched 40 seconds to remove 20 nm of sol-gel resist and expose the GaAs. This leaves a ~80 nm thick silica etch mask for the 550 nm grating and a ~30 nm thick silica sol-gel mask for the 150 nm grating.

5.2.4 VCSEL device processing

In order to exclude the effect of variations in the MBE growth, wafers from the same growth run were used and processed into VCSELs. The laser stack is grown on 3" GaAs wafers and consists of a 32 pair DBR (n-type, GaAs/AlGaAs), a GaAs resonant mode cavity with 3 GaAs quantum wells between AlGaAs barriers and a 24 pair DBR (p-type, GaAs/AlGaAs) with a 170 nm GaAs layer on top (120 nm spacer, 50 nm for the grating). For single mode operation current confinement is provided by a high-aluminum content AlGaAs layer, placed between the quantum wells and the p-type DBR. This layer is selectively oxidized from the side during processing and provides current and mode confinement.[23-25] Modulated doping was used in the DBRs to reduce optical absorption while maintaining low electrical resistance.

A first batch of samples was patterned with 550 nm gratings by the SCIL sol-gel process and as a reference, by direct e-beam patterning of PMMA resist. A second batch was patterned with 550 nm gratings by e-beam and 150 nm gratings replicated in sol-gel by SCIL. In this manner the quality of the SCIL process can be compared to e-beam fabrication and the performance difference between diffractive and non-diffractive gratings can be measured.

Both batches were processed into single-mode VCSELs using the same processing steps. The first process transfers the sol-gel / PMMA grating patterns in the GaAs semiconductor using RIE etching with chlorine. After the GaAs is etched to a target depth of 50 nm, the sol-gel etch-mask is selectively removed in aqueous HF and the e-beam resist stripped using organic solvents.

The transfer etch determines the final DBR mirror reflectivity, which is influenced by grating depth and fidelity. Figure 4(a,b) shows atomic force microscope (AFM) height data taken perpendicular to the GaAs grating lines after removal of the etch masks. The etch depth in GaAs is 38 nm for the e-beam grating and 58 nm for the grating made using nanoimprint. This difference is due to the fact that the polymer of the e-beam resist reacts with the chlorine etch-chemistry which influences the etch rate. As both samples were etched for the same time, the resulting depth of the GaAs grating with the sol-gel mask is larger. For the 150 nm grating (Fig. 4(b)) the target depth of 50 nm is reached. Note that a silica sol-gel etch mask (thickness of only 30 nm) is sufficient to etch the GaAs to the target depth, as silica has a high etch selectivity in the chlorine RIE etch. In the AFM data of the 150 nm grating the corners at the bottom appear rounded. This is due to the finite size of the AFM tip. Figure 4(c) shows a photograph of the wafer with 550 nm grating in GaAs made by SCIL, clearly showing diffractive colors. The uniform color confirms the wafer scale pattern transfer. Figure 4(d) shows a scanning electron microscope micrograph (SEM) image of a finished VCSEL with an imprinted 150 nm pitch grating in the exit aperture. From Fig. 4 it is clear that the gratings made using SCIL have high fidelity and have identical lateral size control as the patterns made by e-beam lithography.

Next, the wafers were processed into VCSELs using the imprinted alignment markers to align the subsequent layers to the grating areas. The process steps where: RIE mesa etching, lateral oxidation of high Al-containing layer for current and mode confinement, p-and n-contact formation, polyimide passivation and bond-pad definition. Finally, the wafers were diced into individual VCSEL devices for electrical and optical characterization.
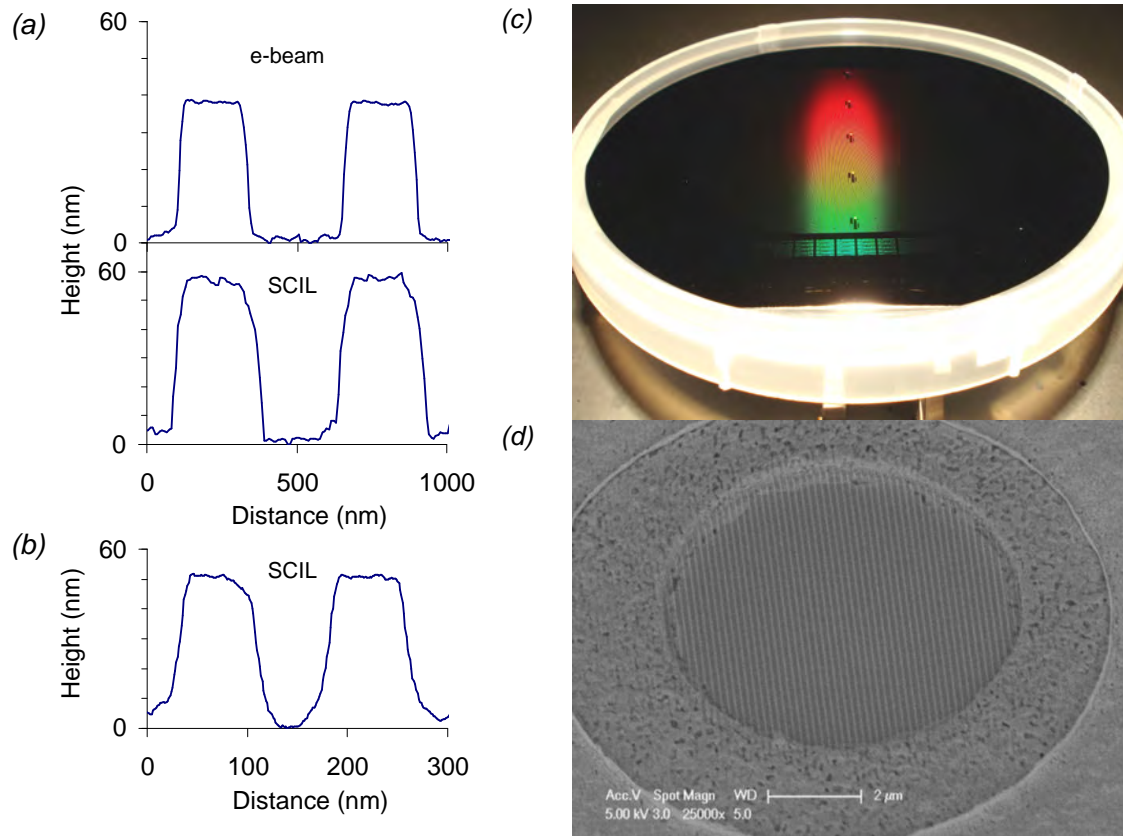
Figure 4. Height profile from AFM measurements of gratings etched in the top GaAs layer of the DBR, (a) Gratings of 550 nm pitch by e-beam lithography and SCIL, (b) grating of 150 nm pitch by SCIL, (c) Photograph of 3" diameter GaAs wafer with laser stack with the imprinted and etched 550 nm gratings showing large-area conformality.(d) SEM image taken under 40° of the output aperture of a finished VCSEL with an imprinted 150 nm pitch grating and the surrounding p-contact metal.

5.3 Opto-electronic device analysis

The yield of VCSEL lasers was comparable for the nano imprint and the e-beam process. All resulting VCSEL devices exhibited single-mode operation. For non-stabilized lasers the polarization direction is randomly spread over the (<100> and <010>) crystallographic orientations of GaAs and results in a 1:1 spread in polarization direction. The laser polarization was measured by positioning a rotating polarizer between the VCSEL and an integrating sphere. All the lasers exhibited linear TM polarized lasing and during cycling of the laser current no polarization rotations were measured. This demonstrates the successful stabilization of the laser polarization using our soft-nanoimprint method.

Figure 5 shows current-voltage (I-V) and current-output (I-P) graphs as well as VCSEL emission spectra at 2.5 mA drive current for lasers of the first wafer batch with 550 nm pitch gratings made by e-beam lithography (a) and SCIL (b). Both devices have the dominant laser mode emitting at λ=853.3±0.1 nm and are single mode as can be seen from the side mode suppression ratio of -18 dB and -20 dB for e-beam and SCIL respectively. The lasing characteristics of the VCSEL made with an imprinted grating are almost identical to the reference VCSEL which had the grating defined by e-beam lithograph. The I-V and I-P curves are comparable, with a threshold current of 0.84 mA and laser slope of 0.59 mW / mA (e-beam) and a threshold current of 0.80 mA and laser slope of 0.55 mW / mA (SCIL) respectively. The optical output power at 3 mA drive current is 1.14 mW (e-beam) and 0.97 mW (SCIL). The small variation in the I-P

behavior between the two samples is attributed to the different etch depths of the gratings, see Fig. 4. This leads to an increased reflection of the DBR for the SCIL gratings. For the imprinted VCSEL this results in a decreased threshold current and accompanied reduced laser slope. The almost identical opto-electronic behavior of these resonant devices demonstrates that the SCIL imprint method is capable of reproducing deep sub-micron features with equal high fidelity as state-of-the-art electron beam lithography.

Figure 6 shows I-V and I-P graphs as well as VCSEL emission spectra at 2.5 mA drive current for lasers of the second wafer batch with 550 nm pitch gratings made by e-beam lithography (a) and 150 nm pitch gratings made by SCIL (b). Both devices have the dominant laser mode emitting at λ=855.8±0.05 nm and are single mode as can be seen from the side mode suppression ratio of -20 dB. From the I-V and I-P graphs it is clear that the performance of VCSELs with a sub-wavelength grating is superior compared to VCSELs with a diffractive grating. The threshold current is reduced from 0.9 mA for the 550 nm pitch grating laser, to 0.6 mA for the 150 nm pitch grating laser. And at the same time the laser slope increased from 0.61 mW / mA for the diffractive grating VCSEL to 0.85 mW / mA for the sub-wavelength grating VCSEL. This reduction in threshold current and simultaneous increase in laser slope can only be explained by the reduction of losses in the laser cavity as there is no diffraction at the interface of the 150 nm grating. Power in the reflected 0th order is increased compared to the 550 nm grating samples which experience diffraction, leading to a reduction is threshold. As the optical losses in the cavity are reduced, the number of emitted photons excited per injected electron increase, leading to an increased laser slope.
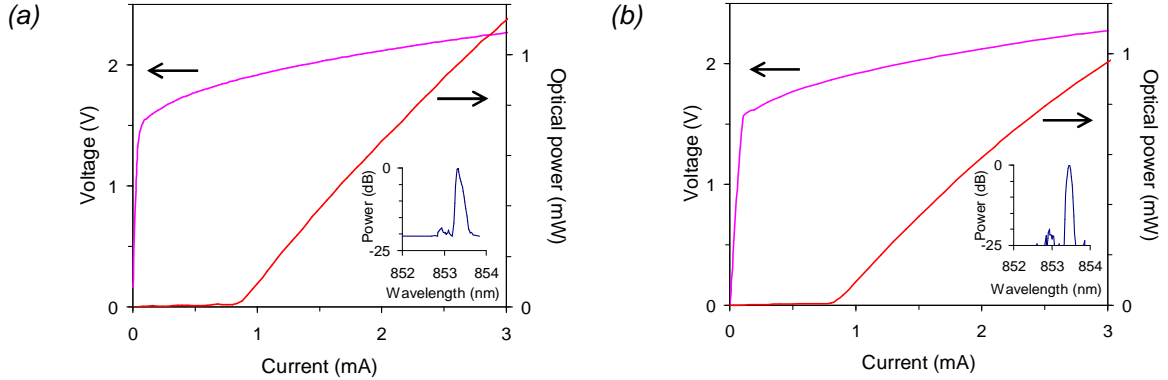
Figure 5. Current-voltage and Current-Output power characteristics for VCSELs with 550 nm gratings fabricated by (a) e-beam, (b) SCIL. Laser spectra obtained at 2.5 mA driving current are shown as insets.
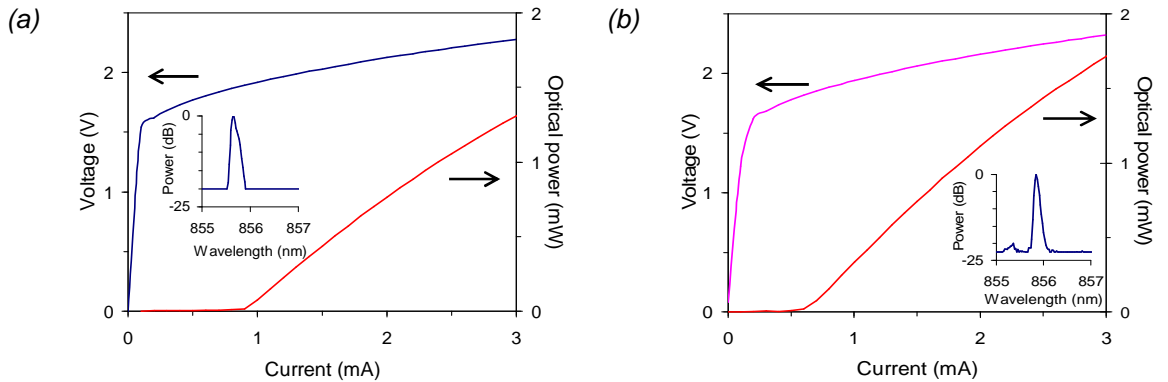
Figure 6. Current-voltage and Current-Output power characteristics for VCSELs with, (a) 550 nm pitch gratings fabricated by e-beam, (b) 150 nm pitch gratings fabricated by SCIL. Laser spectra obtained at 2.5 mA driving current are shown as insets.

The above data thus clearly shows that using non-diffractive gratings to stabilize the polarization in VCSELs results in substantial increased efficiency, compared to devices with diffractive gratings. The overall efficiency at 3 mA drive current was increased from 19.2 % for 550 nm gratings to 24.7 % for 150 nm gratings, a relative increase of 29 %.

The yield of VCSEL lasers directly after processing of the devices was comparable for devices patterned by e-beam and soft-nanoimprint. We also studied the influence of the SCIL soft-nanoimprint process on the lifetime of VCSEL laser devices. As any semiconductor device, single mode VCSEL lasers are sensitive to impurities that can diffuse in the semiconductor material and to damage by electrostatic discharge, which does not always show up directly but over time can lead to abrupt failure of a VCSEL. For lasers made by e-beam and SCIL an accelerated lifetime test was performed using 2 mA drive current at a temperature of 140 °C. Figure 7 shows the normalized optical output of the same device, measured at room temperature after 1-day time intervals. The acceleration factor at these conditions is ~100, which corresponds for the longest tested device (10 days) to three years of continuous operation at standard conditions. The light output of VCSELs made by SCIL and e-beam reduces at approximately the same rate for the first few days. For larger times the SCIL laser has a significantly higher power. No abrupt devices failures were observed, which indicates that our imprint method does not induce any damage to the sensitive semiconductor device during processing.

5.4 Summary and conclusions

Single-mode TM polarization stabilized GaAs VCSELs operating at λ=850 nm have been made by using a soft rubber stamp based nanoimprint method in combination with sol-gel resist to pattern gratings in the surface mirror. VCSELs prepared by nanoimprint show equal performance as reference devices produced by e-beam lithography in terms of emission wavelength, side mode suppression ratio, threshold current, laser slope, output power and lifetime. Imprinted gratings with sub-wavelength pitch do not diffract laser light and VCSEL lasers with these gratings show a combination of reduced threshold current, increased laser slope and increased output power. Overall these VCSEL lasers show a 29 % increased efficiency compared to the lasers with a conventional diffractive grating. This work demonstrates that the SCIL soft-nanoimprint method is capable of delivering nanoscale patterns over wafer scale areas with equal quality as electron beam lithography. The new technique enables the fabrication of large area nano-patterns at high speed and low cost, a key benefit which cannot be delivered by electron beam lithography.
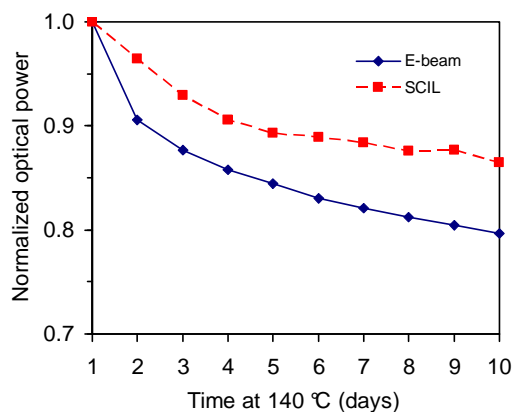
Figure 7. Optical output power of VCSELs with 550 nm pitch gratings made by e-beam and SCIL as function of time at 140 °C and 2 mA drive current. The optical power is measured at room temperature after 1 day intervals.

References

[1] M. Lackner, G. Totschnig, G. Loeffler, H. Hofbauer, and F. Winter, *In-situ laser spectroscopy of CO, CH$_4$, and H$_2$O in a particle laden laboratory-scale fluidized bed combustor*, Thermal Science **6**, 13 (2002)

[2] I. Linnerud, P. Kaspersen, and T. Jaeger, *Gas monitoring in the process industry using diode laser spectroscopy*, Applied Physics B **67**, 297 (1998)

[3] S. Knappe, V. Shah, P.D.D. Schwindt, L. Hollberg, J. Kitching, L.A. Liew, and J. Moreland, *A microfabricated atomic clock*, Appl. Phys. Lett **85,** 1460 (2004)

[4] R. Lutwak, D. Emmons, W. Riley, and R. M. Garvey, *The chip-scale atomic clock – coherent population trapping vs. conventional interrogation*, Proceedings of the 34th Annual Precise Time and Time Interval Systems Applications Meeting **539** (2002)

[5] T. Ohtoshi, T. Kuroda, A. Niwa, and S.Tsuji, *Dependence of optical gain on crystal orientation in surface-emitting lasers with strained quantum wells*, Appl. Phys. Lett. **65**, 1886 (1994)

[6] K. Tateno, Y. Ohiso, C. Amano, A. Wakatsuki, and T. Kurokawa, *Growth of vertical-cavity surface-emitting laser structures on GaAs (311)B substrates by metalorganic chemical vapor deposition*, Appl. Phys. Lett. **70**, 3395 (1997)

[7] O. Tadanaga, K. Tateno, H. Uenohara, T. Kagawa, and C. Amano, *An. 850-nm InAlGaAs strained quantum-well vertical-cavity surface-emitting laser grown on GaAs (311)B substrate with high-polarization stability*, IEEE Photon. Tech. Lett. **12**, 942 (2000)

[8] K.D. Choquette, and R.E. Leibenguth, *Control of vertical-cavity laser polarization with anisotropictransverse cavity geometries*, IEEE Photon. Techn. Lett. **6**, 40 (1994)

[9] B. Weigl, M. Grabherr, C. Jung, R. Jäger, G. Reiner, R. Michalzik, D. Sowada, and K.J. Ebeling, *High performance oxide confined GaAs VCSELs*, IEEE J. Select. Topics Quantum Electron. **3**, 409 (1997)

[10] P. Dowd, P.J. Heard, J.A. Nicholson, L. Raddatz, I.H. White, R.V. Penty, J.C.C. Day, G.C. Allen, S.W. Corzine, and M.R.T. Tan, *Complete polarisation control of GaAs gain-guided top-surface emitting vertical cavity lasers*, Electron. Lett. **33**, 1315 (1997)

[11] P. Debernardi, and G.P. Bava, *Coupled mode theory: a powerful tool for analyzing complex VCSELs and designing advanced device features*, IEEE Journal of Selected Topics In Quantum Electronics **9**, 905 (2003)

[12] J.M. Ostermann, P. Debernardi, C. Jalics, A. Kroner, M.C. Riedl, and R. Michalzik, *Surface gratings for polarization control of single- and multi-mode oxide-confined vertical-cavity surface-emitting lasers*, Optics Communications **246**, 511 (2005)

[13] M. Grabherr, R. King, R. Jäger, D. Wiedenmann, P. Gerlach, D. Duckeck, and C. Wimmer, *Volume production of polarization controlled single-mode VCSELs*, Proceedings of the SPIE Vertical-Cavity Surface-Emitting Lasers XII, Volume **6908-02** (2008)

[14] S.Y. Chou, S. Schablitsky, and L. Zhuang, *Subwavelength transmission gratings and their applications in VCSELs*, Proceedings of the SPIE, Optoelectronic integrates circuits **3290**, 0277-786, 73 (1997)

[15] J.S. Gustavsson, Å. Haglund, J.A. Vukušić, J. Bengtsson, P. Jedrasik, and A. Larsson, *Efficient and individually controllable mechanisms for mode and polarization selection in VCSELs, based on a common, localized, sub-wavelength surface grating*, Optics Express **15**, 6626 (2005)

[16] J.A. Rogers, K.E. Paul, and G.M. Whitesides, *Quantifying distortions in soft lithography*, J. Vac. Sci. Technol. B **16**, 88 (1998)

[17] S. Pagliara, L. Persano, A. Camposeo, R. Cingolani, and D. Pisignano, *Registration accuracy in multilevel soft lithography*, Nanotechnology **18**, 175302 (2007)

[18] C. Moraes, Y. Sun, and C.A Simmons, *Solving the shrinkage-induced PDMS alignment registration issue in multilayer soft lithography*, J. Micromech. Microeng. **19**, 065015 (2009)

[19] M. Verschuuren and H. van Sprang, *3D photonic structures by sol-gel imprint lithography*, Mater. Res. Soc. Sym. Proc. **1002**, N03 (2007)

[20] M.G. Moharam, and T.K. Gaylord, *Coupled-wave analysis of reflection gratings*, Applied Optics **20**, 240 (1981)

[21] G.Y. Jung, Z. Li, W. Wu, Y. Chen, D.L. Olynick, S.Y. Wang, W.M. Tong, and R.S. Williams, *Vapor-phase self-assembled monolayer for improved mold release in nanoimprint lithography*, Langmuir **21**, 1158 (2005)

[22] H. Schmid, and B. Michel, *Siloxane polymers for high-resolution, high-accuracy soft lithography*, Macromolecules **33,** 3042 (2000)

[23] D.L. Huffaker, C.C. Lin, J. Shin, and D.G. Deppe, *Resonant cavity light emitting diode with an Al_xO_y/GaAs reflector*, Appl. Phys. Lett. **66**, 3096 (1995)

[24] B. Weigl, M. Grabherr, R. Michalzik, G. Reiner, and K.J. Ebeling, *High power single mode selectively oxidized vertical cavity surface emitting lasers*, IEEE Photon. Tech. Lett. **8**, 971 (1996)

[25] M. Grabherr, R. Jäger, R. Michalzik, B. Weigl, G. Reiner, and K.J. Ebeling, *Efficient single-mode oxide-confined GaAs VCSEL lasers emitting in the 850-nm wavelength regime*, IEEE Photon. Tech. Lett. **9**, 1304 (1997)

Chapter 6

Large area replication of high quality nanohole arrays in gold using soft-nanoimprint lithography

We present a novel soft-nanoimprint method to replicate sub-wavelength, nanoscale hole arrays in optically thick films of gold. We fabricate large-area high-fidelity arrays of 180 nm diameter holes on a square lattice of 780 nm pitch. Optical angular transmission measurements show that the produced hole arrays are free of fabrication related defects and show high fidelity extra ordinary transmission peaks mediated by surface plasmon polaritons. Metal hole arrays on glass exhibit separate dispersion transmission bands due different effective index of the SPP modes on opposing sides of the hole array. As the dielectric surrounding of a hole array is made more symmetric, the transmission peaks are broadened and increased. A hole array with equal dielectric surrounding is fabricated which exhibits a ~2 times increased peak transmission compared to a regular hole array on glass.

6.1 Introduction

Metal films perforated with an array of sub-wavelength holes have intrigued researchers since the discovery that these arrays show extraordinary transmission of light.[1,2] It is generally accepted that the enhanced transmission is mediated by surface plasmon polaritions (SPPs), electromagnetic waves that are bound to a metal-dielectric interface.[3] On a smooth interface these waves cannot be excited directly because their momentum is larger than that of light incident from free space. Diffraction from a regular array of holes enables efficient resonant excitation of the plasmon modes and which assist in transmission. Arrays with nanoholes are increasingly studied as color filters[4] and nanoscale light concentrators for application in bio-sensors[5] and solar cells[6]. To realize such applications at a large scale a fabrication method is required that is able to pattern hole arrays with designed geometry, hole size and pitch at large area and low cost. In some applications arrays of different geometry are to be integrated with e.g. detectors or micro fluidics and therefore must be aligned with existing patterns or substrates.

So far nanohole arrays have been made using focused ion beam (FIB) to mill holes in planar films, or electron beam lithography in combination with metal lift-off, which are both relatively slow and expensive. Interference lithography is also being used but is limited in that it produces patterns of the same period and variation in pattern is more difficult to obtain in once sample. Moreover, the metal lift-off procedure itself in combination with lithographic patterning has disadvantages to fabricate metal hole arrays for plasmonic applications. Often it requires the use of a thin (2-5 nm) adhesion layer of titanium or chromium, which strongly absorbs surface plasmons. But more importantly, the lift-off process releases metal dots corresponding to holes in the metal layer, a large fraction of which typically adheres to the array, causing increased losses due to scattering and reduced coupling to SPPs.

Recently, nanoimprint lithography was introduced to produce arrays of nanoscale holes in a metal film. However the methods used so far resulted in fragile freely floating arrays[7] or to structures in which the holes were not fully continuous through the film, which can lead to unwanted resonances and limited total transmission[8,9].

Here, we introduce a new novel method to produce large area sub-wavelength nanohole arrays using a soft-nanoimprint method. Our Substrate Conformal Imprint Lithography (SCIL) technique uses soft composite stamps which allow for wafer-scale patterning of sub-50 nm features with very low distortions.[10] Previous soft-stamp methods where not capable of producing details below 100 nm and suffered from in-plane distortions on wafer scales.[11,12] So far, we have demonstrated the use of SCIL to fabricate regular free standing nanostructures in silica and silicon. Here, we use SCIL to directly pattern optically transparent silica patterns over large areas with high resolution. We describe a new relatively simple route to produce high-fidelity hole arrays that can be applied to any substrate type. We demonstrate its use to fabricate hole arrays in gold films without using a lift-off process. Our method yields large area arrays which are free of scattering particles or defects. Optical transmission spectrometry is presented, demonstrating the high optical quality of the imprinted nanohole arrays.

6.2 Fabrication of nanohole arrays using soft-nanoimprint lithography

Soft-nanoimprint lithography requires a rubber stamp which is molded from a master pattern. The master pattern contains an array of dots which is generated using a Jeol 100 kV e-beam pattern generator on a 150 mm diameter silicon wafer in 150 nm thick hydrogen-silses-quioxane (HSQ). In a 0.5×0.5 mm area 150 nm diameter dots are placed in a square array with a pitch of

780 nm. After development of the HSQ an array of dots remains. The surface of this master pattern is made non-reactive by applying a monolayer of a fluoro-silane by vapor phase deposition.[13] From this pattern a soft silicone rubber, poly-di-methyl-siloxane, (PDMS) stamp is molded. A composite stamp is made from a layer of higher modulus PDMS, containing a pattern of holes, on a layer of soft PDMS.[14,15] Next, we use this stamp to create a second master pattern with the same pitch and diameter, but higher aspect ratio structures. This process is schematically indicated in Fig. 1. First a silicon wafer was sputter coated with a 50 nm thick layer of chromium after which a ~1 micron thick layer of HPR-504 positive photo resist was applied by spin coating. This layer was baked for 30 minutes on a hot-plate at 250 °C, after which a ~700 nm thick cross-linked resist layer remains. On top of this layer a precise amount of silicon sol-gel imprint resist [10] is applied by spin coating. Directly after spin coating the first stamp molded from the HSQ dots is applied in the sol-gel resist. After 30 minutes the sol-gel resist has formed a rigid silica-like material and the stamp was removed by gentle pealing, leaving the structure as shown in Fig. 1(a). The residual sol-gel layer under the feature was removed by a CF_4/N_2 anisotropic reactive ion etch (RIE), Fig. 1(b). The remaining sol-gel resist serves as a mask during a subsequent oxygen RIE etch of the organic resist layer, see Fig. 1(c). The remaining sol-gel etch mask is removed in 1 weight percent hydrofluoric acid (HF) solution, Fig. 1(d). Figure 1(e) shows a secondary electron micrograph (SEM) image of the resist pillars. The pillars are straight, have smooth side walls and are uniform in height and diameter.

Next, this high aspect ratio resist pattern is used as a master to mold a second composite soft PDMS stamp using the same procedure as for the first stamp. This second stamp is then used to produce nanohole arrays in a gold film. Figure 2 shows SEM images of the different stages of the fabrication of the nanohole array. On AF45 glass substrates a ~100 nm thick sol-gel layer is imprinted with the second stamp. After the sol-gel has solidified, the stamp is carefully removed leaving an array of silica pillars which are transparent to near-UV, visible and near-infrared light, which are then cured in an oven at 200 °C in air. Figure 2(a) shows a SEM image of the resulting 650 nm high silica pillars. Figure 2(b) shows the sample after 250 nm gold is deposited over the pillars by sputter deposition. The amount of gold deposited on the pillar sides is about 100 nm, judging from the increased pillar diameter in Fig. 2(b). Next a thio-urea / iron-sulphate based wet etch is used to remove the metal from the pillar top and side walls.[16] This mixture has an etch rate on our flat sputtered gold of ~32 nm / min. at room temperature. Figure 2(c) shows the sample after three minutes of wet etching and clearly shows that all the metal is removed from the pillar sides as well as the top of the pillar. The short etch time required to remove all the metal from the pillars is attributed to porosity of the metal on the pillar sides and the high surface to volume ratio of the (250 nm thick) metal on top of the pillar. The wet etch removes ~120 nm from the planar metal layer, leaving a ~130 nm thick gold layer with holes at the pillar position.
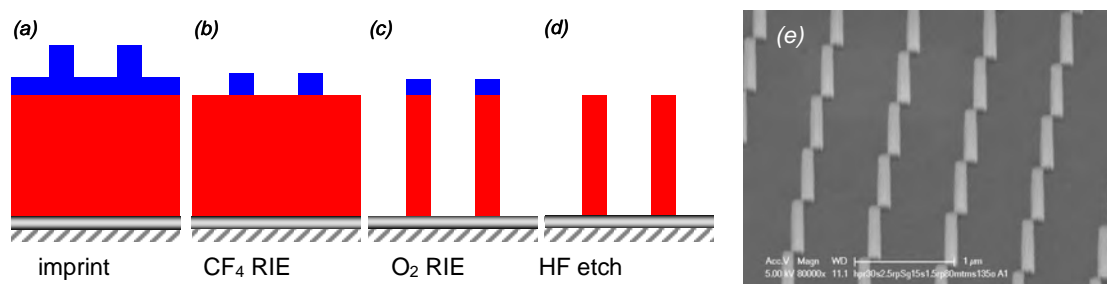
Figure 1. Schematic of the process steps used to obtain high aspect ratio pillars: (a) imprinted sol-gel resist on the cross-linked HPR-504, (b) after the removal of the residual sol-gel layer by RIE etching, (c) high aspect ratio organic resist pillars are formed by oxygen RIE, (d) wet etching removes the sol-gel etch mask, (e) SEM image of the final high aspect ratio resist pillars.
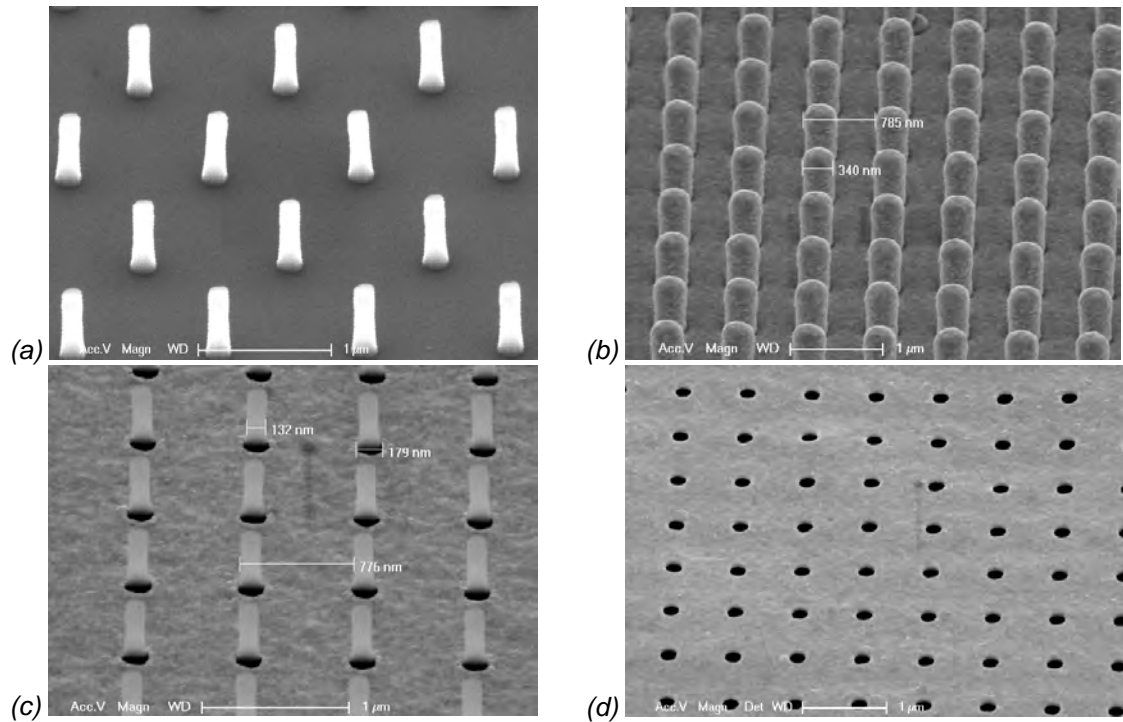
Figure 2. SEM images at different stages in the nanohole array fabrication (images taken under an angle of ~40°). (a) Imprinted sol-gel pillars, (b) imprinted sol-gel pillars after sputter coating with 250 nm gold, (c) the metal is removed from the pillars and a hole array remains with ~500 nm high silica pillars protruding from the holes, (d) silica pillars are removed by etching in diluted aqueous HF.

The sol-gel pillars are then removed by a short etch in 1 weight percent HF. Figure 2(d) shows the gold nano hole array after the sol-gel pillars are removed. The SEM image clearly shows that the square array is well reproduced. The hole diameter is enlarged to 180 nm compared to the initial diameter of the sol-gel pillar (Fig. 2(a)), which we attribute to a combination of shadow effects during sputter deposition and the removal of metal by the wet gold etch. Replicating thinner pillars would allow to decrease the hole diameter further if desired.

The procedure described above leads to a metal hole array on a glass substrate, i.e. an asymmetric dielectric environment. We also studied the fabrication of array geometries with a more symmetric dielectric surrounding with the aim to increase the peak transmission. To do so we used the same procedure as shown in Fig. 2. In a second sample the sol-gel pillars were left un-etched, filling the holes in the metal with sol-gel. For a third sample, after the last etch step, Fig. 2(d), a 340 nm thick sol-gel coating was applied on top of the array. This layer fills up the holes and a uniform sol-gel layer on top the array is formed with a refractive index of $n \approx 1.42$, as measured on a planar substrate using ellipsometry. A fourth sample was made by first coating the AF45 glass substrate (refractive index $n \approx 1.54$) with a 2 μm thick sol-gel layer. On this sol-gel layer the gold hole array was defined using the same procedure as above, followed by over-coating with a ~2 μm thick sol-gel layer. This then leads to a symmetric dielectric surrounding with index $n \approx 1.42$ on both sides of the hole array.

6.3 Optical characterization

Angle-resolved optical transmission spectra were measured for hole arrays with the four different dielectric surroundings. An incandescent lamp was coupled to a 200 μm multimode fiber of which the output was focused to a ~300 μm diameter spot on the sample. The transmitted light

was sent to a fiber-coupled grating spectrometer. For visible to near-infrared wavelengths (500-1000 nm) we used a CCD detector (resolution 1.2 nm). For near-infrared wavelengths (900-1700 nm) we used an InGaAs array (resolution 3 nm). The numerical aperture of the incident and transmitted light beam was limited to <0.01. Polarizers were placed in parallel parts of the incident and transmitted beams. The substrate was placed onto a rotation mount with the rotation axis aligned with the (0, 1) direction of the hole array. The wave vector and polarization of the incident light were perpendicular to this direction (p-polarization).

Figure 3 shows transmission spectra at normal incidence for the four different hole arrays with 180 nm diameter holes and a pitch of 780 nm in ~130 nm thick gold with (a) a conventional hole array on AF45 glass, (b) hole array with sol-gel pillars protruding from the holes, (c) hole array on glass with a 340 nm sol-gel on top and (d) hole array surrounded by ~2 μm thick sol-gel layers. The transmission is normalized to the transmission measured on an area where there is no metal present. As can be seen from Fig. 3(a) the hole array exhibits extraordinary transmission as high as 3.2%. Several transmission peaks are observed in Fig. 3(a) corresponding to the (1,0) and (1,1) SPP modes at the air side of the array and the (1,0), (2,0) and (1,1) modes corresponding to SPP modes at the glass side of the array. As the refractive index on top on the array is increased these modes shift and broaden. In Fig. 3(b) the sample with sol-gel pillars remaining, transmission of the (1,1) air mode is highly suppressed while the (2,0) glass mode decreases slightly but broadens. The transmission of the (1,0) air mode and the (1,1) and (1,0) glass modes increase. The presence of the pillars in the holes also causes a small red shift of 8-13 nm in the
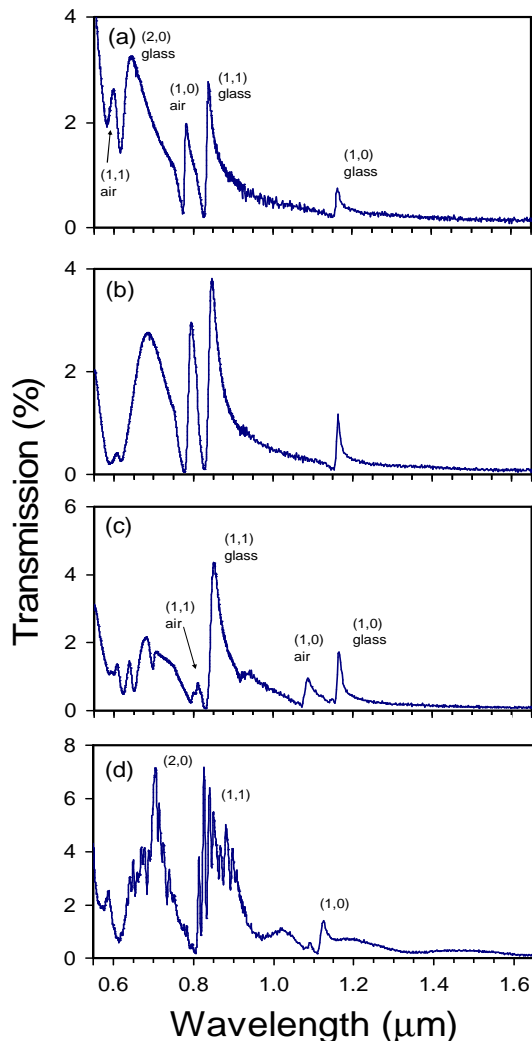
Figure 3. Optical transmission spectra of a square array of 180 nm diameter holes on a 780 nm pitch in a ~150 nm thick gold film measured normal to the gold array. (a) normal hole-array with air on top, (b) hole-array with sol-gel pillars protruding from the holes, (c) a hole-array on glass with a 340 nm sol-gel on top and (d) a hole array surrounded by ~2 micron thick sol-gel layers.

peak transmissions of the (1,1) glass, (1,0) air and (1,1) air mode. We attribute this to the presence of sol-gel material inside the hole, which red-shifts the Fano-resonances.[17,18] The peak of the (2,0) glass mode exhibits a red shift of 44 nm due to the decreased transmission of the (1,1) air mode of which the red tail overlaps with the (2,0) glass mode. Reduction of the (1,1) air mode transmission therefore shift the (2,0) glass mode towards the red. In Fig. 3(c) the two modes observed at 1090 nm and 813 nm are attributed to the red shifted original (1,0) and (1,1) air modes. The fact that these modes do not fully overlap with the (1,0) and (1,1) glass modes indicates that the dielectric environment is not fully symmetric. Figure 3(d) shows three main peaks corresponding to the (1,0), (1,1) and (2,0) glass modes, indicating the dielectric layers on both sides are index matched. These peaks have broadened significantly and except for the (1,0) peak, the transmission maximum has increased considerably. In this sample the (2,0) mode exhibit extraordinary transmission of 7.1 %, compared to the hole area coverage of only 4.2 %. The broadened and increased transmission indicates that coupling between the two sides of the array is increased.[17,19] Furthermore, the spectrum of Fig. 3(d) shows that the (1,1) and (2,0) SPP transmission peaks exhibit a multitude of sharp lines of reduced transmission. These are ascribed to Fabry-Perot resonances in the 2 μm thick top sol-gel layer, as will be discussed below.

To understand the origins of the transmission minima and maxima and the fine structure in the spectra it is useful to look at the angular dependence of the transmission. Figure 4 shows intensity plots of the transmission as a function of angle of incidence (horizontal axis) and wavelength (vertical axis) for the normal hole array on glass (a) and the array with protruding pillars (b). The transmission at normal incidence (0°) corresponds to the transmission spectra in Fig. 3(a,b). It shows a structure of transmission peaks, separated by dark bands. These minima and maxima in the transmission spectra are caused by Fano-resonances of directly transmitted light and SPP mediated transmitted light. We find an effective index on the glass side of 1.5. The different slopes of the dark bands in Fig. 4 corresponds to the different dispersion on the glass side and air side.[20] Figure 4(b) shows that the presence of the pillars increases the transmission of the hole array over the entire angular range. This is attributed to the increase of the effective hole area due to the presence of sol-gel material. In combination with a complex coupling geometry by the protruding sol-gel pillars this leads to a transmission increase.[20] The well separated dispersion curves in the transmission measurements of Fig. 4 clearly show that the gold hole arrays have an asymmetrical dielectric environment.

Figure 5(a) shows an intensity scale plot of the transmission as a function of the angle of incidence and wavelength for the hole array on a glass substrate with a 340 nm thick sol-gel layer on top of the array (as in Fig. 3(c)). As can be seen from the transmission peaks and Fano-minima, deposition of a 340 nm thick sol-gel layer on top of the array does not result in a fully index matched sample. Sets of two distinct split dispersive modes are visible, corresponding to the Au/sol-gel/air interfaces and Au/glass substrate interface. The effective index of the Au/sol-gel/air mode is found to be n≈1.4, which is due to the partial extent of the evanescent SPP mode to air, while the glass mode experiences the refractive index of AF45 glass, n≈1.52 and therefore this configuration cannot be matched using a sol-gel layer. Besides the broad transmission minima caused by Fano interference the spectra also contain more narrow transmission minima for wavelengths below 950 nm. We attribute these lines to the fundamental TE waveguide modes in the top sol-gel layer.[21]
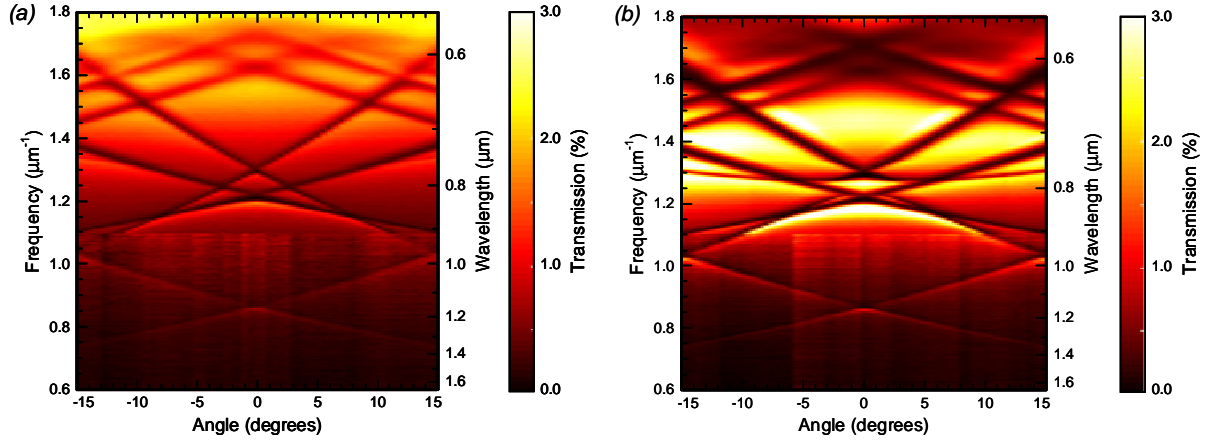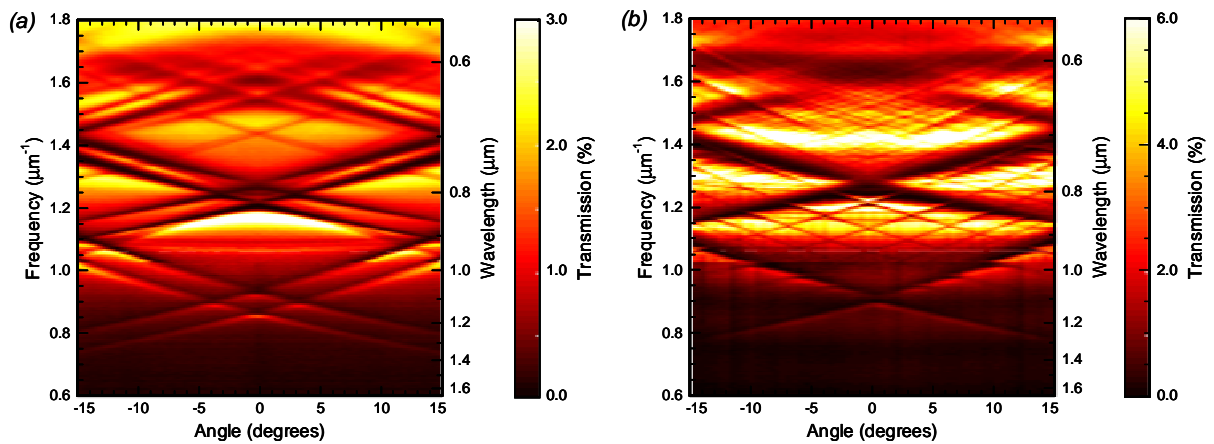
Figure 4. Angular optical transmission spectra of a square array of 180 nm diameter holes on a pitch of 780 nm in a ~150 nm thick gold film (a) hole-array on glass, (b) hole array on glass with sol-gel pillars in the holes which protrude ~500 nm above the gold film.

Figure 5(b) shows an intensity scale plot of the transmission as a function of the angle of incidence and wavelength for the hole array embedded in sol-gel layers of ~2 micron thickness (as in Fig. 3(d)). As can be seen from the transmission minima, the sol-gel encapsulated hole array exhibits a single SPP mode, because of index matching. The transmission maxima correspond to the glass SPP modes in the asymmetric arrays. The (1,0) and (1,1) modes have broadened substantially compared to the SPP glass transmission modes in the other samples. The (2,0) glass mode has the transmission peak for normal incidence around 700 nm and exhibits low dispersion with a transmission maximum of 7.1 %. While the thin sol-gel layer in Fig. 5(a) displays only waveguide modes for wavelengths below 820 nm, the 2 micron thick dielectric layer shows much more waveguide modes for wavelengths up to 1.2 micron. Depending on the phase of these modes there will be destructive interference, apparent as sharp locally reduced transmission in Fig. 5(a,b). The constructive interference is visible as the sharp bright lines in the broad SPP-Fano resonance transmission dip in the index matched sample. These waveguide modes exhibit relatively low losses as evident from the relatively narrow transmission features. This confirms the high quality of the arrays and the absence of scatter losses. The light is eventually absorbed due to the finite reflection at the sol-gel/gold interface.

Figure 5. Angular optical transmission spectra of a square array of 180 nm diameter holes on a pitch of 780 nm in a ~150 nm thick gold film (a) hole-array on glass, covered with a 340 nm thick sol-gel layer, (b) a gold array embedded in ~2 μm thick sol-gel layer on both sides.

The waveguide modes on solid state index matched hole array sample have not been observed in previous work which studied index matching of hole arrays. In these experiments bulk index matching liquids were used and thus no wave guide modes were possible in a thin layer on or below the array.[17,19] Also, in one of these studies the arrays had a considerably smaller area (~10×10 µm) which required optics with a much higher numerical aperture which would broaden the wave guide modes.[17] In our dielectrically symmetric sample the line width of the resonances is ~10 nm which corresponds to a propagation length of ~110 µm and ~92 µm for waveguide modes overlapping with the (2,0) and (1,1) SPP modes, respectively.

As Fig. 5(b) shows, index matching of the dielectric surrounding increases the resonant transmission from ~3 % to 7 %. For optimized transmission, the thickness of the sol-gel layers can be optimized so that coupling to waveguide modes is suppressed at the wavelengths of interest. The (2,0) mode around 700 nm offers a flat dispersion, high transmission peak which can be of interest in a angle-independent color filter. Conventional diffraction based color filters are much more sensitive to the incident angle of the light. An interesting observation is that the pillar array supports relatively high and narrow SPP transmission modes without additional transmission features caused by the waveguide modes in the index matched arrays. By optimizing the pillar height and diameter the transmission may be increased, from which the use of hole arrays in applications could benefit.

6.4 Summary and conclusions

We have demonstrated a novel method to fabricate high fidelity gold nanohole arrays over large areas using a cost effective soft-nanoimprint method. We fabricated nanohole arrays with both asymmetric and symmetric dielectric surrounding. Arrays with sol-gel pillars protruding from the holes show increased transmission. The asymmetric arrays show split dispersive bands in the angle-resolved transmission spectra. Index-matched hole arrays exhibit a single SPP transmission mode at corresponding wavelengths. The symmetric hole arrays show a maximum transmission up to 7.1 %, compared to a hole area of only 4.2 %. The addition of a relatively thin dielectric layer introduces slab waveguide modes which cause a regular modulation in the transmittance, depending on the layer thickness. The optical measurements demonstrate the high fidelity nanohole arrays which can be made with SCIL to directly pattern silica glass, metal deposition and wet chemical etching.

References

[1]   T. W. Ebbesen, H. J. Lezec, H. F. Ghaemi, T. Thio, and P. A. Wolff, *Extraordinary optical transmission through sub-wavelength hole arrays*, Nature **391**, 667 (1998)

[2]   H. F. Ghaemi, T. Thio, D. E. Grupp, T. W. Ebbesen, and H. J. Lezec, *Surface plasmons enhance optical transmission through subwavelength holes*, Phys. Rev. B **58**, 6779 (1998)

[3]   C. Genet, and T. W. Ebbesen, *Light in tiny holes*, Nature **455**, 39 (2007)

[4]   J.L. Skinner, A.A. Talin, and D.A. Horsley, *A MEMS light modulator based on diffractive nanohole gratings*, Optics Express **16**, 3701 (2008)

[5]   J.M. McMahon, J. Henzie, T.W. Odom, G.C. Schatz, and S.K. Gray, *Tailoring the sensing capabilities of nanohole arrays in gold films with Rayleigh anomaly surface plasmon polaritons*, Optics Express **15**, 18119 (2007)

[6]   H.A. Atwater, and A. Polman, Nature Materials **9**, 21 (2010)

[7]   E.-S. Kwak, J. Henzie, S.-H. Chang, S.K. Gray, G.C. Schatz, and T.W. Odom, *Surface plasmon standing waves in large-area subwavelength hole arrays*, Nano Letters **5**, 1963 (2005)

[8]   V. Malyarchuk, F. Hua, N.H. Mack, V.T. Velasquez, J.O. White, R.G. Nuzzo, and J.A. Rogers, *High performance plasmonic crystal sensor formed by soft nanoimprint lithography*, Optics Express **13**, 5669 (2005)

[9]   T.T. Truong, J. Maria, J. Yao, M.E. Stewart, T.-W. Lee, S.K. Gray, R.G. Nuzzo, and J.A. Rogers, *Nanopost plasmonic crystals*, Nanotechnology **20**, 434011 (2009)

[10]   M. Verschuuren, and H. van Sprang, *3D photonic structures by sol-gel imprint lithography*, Mater. Res. Soc. Sym. Proc. **1002**, N03 (2007)

[11]   J.A. Rogers, K.E. Paul, and G.M. Whitesides, *Qualifying distortion in soft lithography*, J. Vac. Sci. Technol. B **16**, 88 (1998)

[12]   C. Moraes, Y. Sun, and C.A Simmons, *Solving the shrinkage-induced PDMS alignment registration issue in multilayer soft lithography*, J. Micromech. Microeng. **19**, 065015 (2009)

[13]   G.-Y. Jung, Z. Li, W. Wu, Y. Chen, D.L. Olynick, S.-Y. Wang, W.M. Tong, and R.S. Williams, *Vapor-phase self-assembled monolayer for improved mold release in nanoimprint lithography*, Langmuir **21**, 1158 (2005)

[14]   H. Schmid, and B. Michel, *Siloxane polymers for high-resolution, high-accuracy soft lithography*, Macromolecules **33**, 3042 (2000)

[15]   T.W. Odom, J.C. Love, K.E. Paul, D.B. Wolfe, and G.M. Whitesides, *Improved pattern transfer in soft lithography using composite stamps*, Langmuir **18**, 5314 (2002)

[16]   D. Burdinski, and M.H. Blees, *Thiosulfate- and thiosulfonate-based etchants for the patterning of gold using microcontact printing*, Chem. Mater. **19**, 3933 (2007)

[17]   A. Krishnan, T. Thio, T.J. Kim, H.J. Lezec, T.W. Ebbesen, P.A. Wolff, J. Pendry, L. Martin-Moreno, and F.J. Garcia-Vidal, *Evanescently coupled resonance in surface plasmon enhanced transmission*, Optics Comm. **200**, 1 (2001)

[18]   C. Genet, M.P. van Exter, and J. P. Woerdman, *Huygens description of resonance phenomena in subwavelength hole arrays*, J. Opt. Soc. Am. A **22**, 998 (2005)

[19]   M.J.A. de Dood, E.F.C. Driessen, D. Stolwijk, and M.P. van Exter, *Observation of coupling between surface plasmons in index-matched hole arrays*, Phys. Rev. B **77**, 115437 (2008)

[20]   D. Stolwijk, E.F.C. Driessen, M.A. Verschuuren, G.W. 't Hooft, M.P. van Exter, and M.J. A. de Dood, *Enhanced coupling of plasmons in hole arrays with periodic dielectric antennas*, Optics Lett. **33**, 363 (2008)

[21]   M.J.A. de Dood, E.F.C. Driessen, D. Stolwijk, M.P. van Exter, M.A. Verschuuren, and G.W. 't Hooft, *Index matching of surface plasmons*, Proceedings of the SPIE **6987**, 6987113 (2008)

Chapter 7

Improved red-response in thin film a-Si:H solar cells with soft-imprinted plasmonic back reflectors

The impact of controlled nanopatterning on the Ag back contact of an n-i-p a-Si:H solar cell was investigated experimentally and through electromagnetic simulation. Compared to a similar reference cell with a flat back contact, we demonstrate an efficiency increase from 4.5 % to 6.2 %, with a 26 % increase in short circuit current density. Spectral response measurements show the majority of the improvement between 600 and 800 nm, with no reduction in photocurrent at wavelengths shorter than 600 nm. Optimization of the pattern aspect ratio using electromagnetic simulation predicts absorption enhancements over 50 % at 660 nm.

7.1 Introduction

Effective light trapping is a critical component of solar cell development. In typical thin film cells the thickness of the absorbing layer is governed by a tradeoff: the absorber must be optically thick to absorb a significant fraction of the incident photons, but must also be of sufficient quality to enable minority carrier collection lengths larger than the material thickness. These dual requirements largely define current cost per Watt of photovoltaic power. Thin film Si solar cells using hydrogenated amorphous Si (a-Si:H) and nanocrystalline Si (nc-Si:H) are among the most well-developed thin film photovoltaic materials, but suffer from low diffusion lengths, and much work has been devoted to the optimization of surface texturing for light management. These surfaces are typically textured metal-oxide films, including SnO_2 in superstrate cells[1] and sputtered films of Ag or Al and ZnO:Al in substrate cells[2,3], where optimization of rms roughness has been explored but the topography is otherwise random. Surface texturing has also been achieved by incorporating roughness in electrically passive materials, such as plastic substrates[4] and glass superstrates[5].

Recently plasmonic nanostructures have garnered attention as a method for enhancing absorption in thin film photovoltaic absorber layers.[6-9] While the introduction of additional metal structures can increase the Ohmic losses in the cell, through appropriate tailoring of the size, shape, and position of the nanostructures these losses can be minimized to enable overall spectral enhancement of photovoltaic performance. Compared to rough substrates, designed patterns allow for improved light management and controlled coupling of incident free space radiation to propagating guided wave.[10,11] There are non-optical device benefits to optimization of the improved light management as well: reducing the surface topography relative to a randomly structured rear contact improves semiconductor film conformity and thereby electronic quality.[12]

A significant challenge is the fabrication of large-area patterns with precisely controlled nanoscale dimensions. In previous reported work, researchers have employed methods with varying degrees of size and position ordering, including island annealing[7], colloidal metal particles[8], and porous anodized aluminum oxide templates[13,14]. Here we utilize nanoimprint lithography to pattern the back contact of an n-i-p a-Si:H solar cell, and report on the enhancements in solar cell response relative to a planar reference cell using current density-voltage (J-V) and spectral response measurements. We also use full wave finite-difference time-domain (FDTD) simulations to model the spectral response and optimize the shape of the nanopatterned back reflector. We focus mainly on the red part of the spectrum, 600 - 800 nm, where a-Si:H is weakly absorbing and the effect of light trapping is most pronounced.

7.2 Large area plasmonic cell fabrication

Large-area nanopatterns were replicated using substrate conformal imprint lithography (SCIL), a method that offers the advantages of inexpensive soft poly(dimethyl)siloxane (PDMS) stamps and delivers sub-50 nm resolution with wafer-scale pattern fidelity.[15] The master pattern is a silicon wafer with 365 diameter holes, 200 nm deep, on a square lattice of pitch 513 nm, made using laser interference lithography. The surface of the master wafer is first modified with a fluoro-silane anti-adhesion monolayer. Next a 50 micron thick layer of high modulus PDMS layer is spin coated over the master and pre-cured, then bonded onto a 200 micron thick glass sheet using low modulus PDMS[16] and released from the master.

The pattern from the stamp is then transferred to the substrate. A 150 nm thick sol-gel based resist is applied by spin-coating over a 150 mm silicon wafer. The wafer is placed parallel to the stamp, at 100 micron distance. The stamp is attached by vacuum to a plate with grooves, which are sequentially pressurized to 20 mbar to contact the resist-coated wafer. The sol-gel reacts at room temperature in 10 minutes to form a solid. The grooves are then sequentially evacuated, which results in a smooth release of the stamp from the imprinted patterns. The stamps can be used for over 2000 sol-gel imprints without observed pattern degradation. The replicated sol-gel hole array is 88 wt-% silicon oxide, non-absorbing, and stable in air up to 450°C.

To form the back contact, the patterned sol-gel layer is sputter-coated with 200 nm Ag(1%Pd), as illustrated in the scanning electron micrograph (SEM) image in Fig. 1(a). The metal holes are 225 nm in diameter after coating. The back contact for a flat reference cell was made by evaporating 200 nm of Ag on glass. Both cells were then processed side-by-side in the remaining steps to ensure identical deposition conditions. A 100 nm ZnO:Al spacer layer was sputtered on top of the Ag contact, followed by standard n-i-p a-Si:H cell deposition using 13.56 MHz PECVD with an intrinsic layer thickness of 500 nm.[17] An 80 nm indium tin oxide (ITO) top contact was sputtered on top, which also serves as an antireflection coating. Finally a metal grid was evaporated over the ITO using a contact mask. The active area of the cell is 0.13 cm^2. Fig. 1(b) shows a cross section of a cell after fabrication on top of the patterned cell, made using focused ion beam (FIB) milling. The different layers can be clearly identified, and the holes are conformally coated with Ag and ZnO:Al.

7.3 Electro-optical cell characterization and electrodynamic simulation

Figure 2 illustrates the current-voltage characteristics of the flat and patterned n-i-p a-Si:H cells, for the best cell of each type. The J-V characteristics were measured with a solar simulator under one sun illumination (AM1.5G, 100 mW/cm^2). The patterned cell exhibits a 26 % higher short circuit current density (J_{sc}) than the flat cell, demonstrating an increased optical path length in the device. The open circuit voltage (V_{oc}) shows a slight decrease, by 2 %. Combined, there is a significant increase in efficiency from 4.5 % to 6.2 % due to the patterned metal back contact. Several cells of each type were measured, with a variance in the absolute efficiency of 0.1 for the reference cell and 0.13 for the patterned cell. It is interesting to note that the patterned cell does not suffer from a reduced series resistance or fill factor.
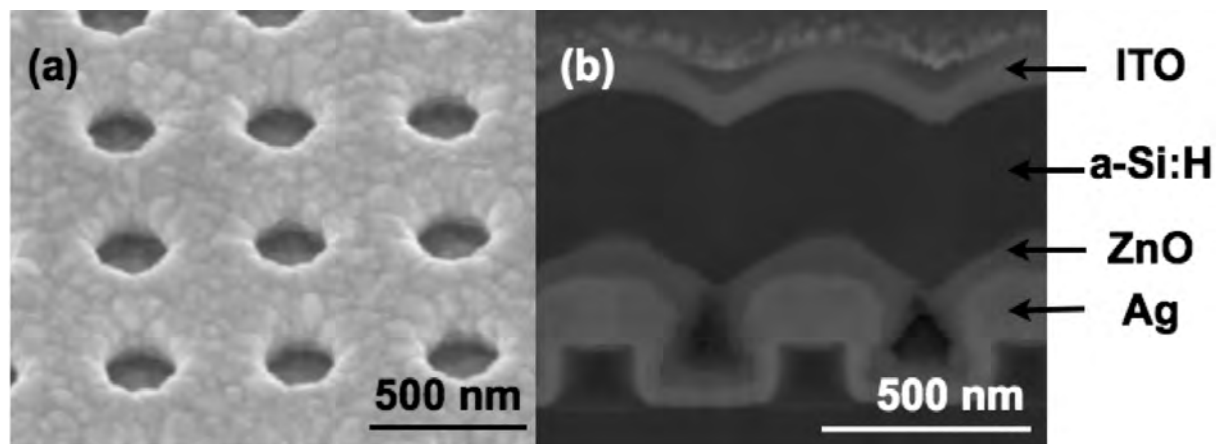
Figure 1. (a) SEM image of a nanoimprinted pattern of holes after overcoating with Ag. The coated holes are 225 nm in diameter, 240 nm deep, and have a pitch of 513 nm. (b) SEM image showing a FIB cross section of a fully fabricated n-i-p a-Si:H solar cell grown on the patterned back contact.
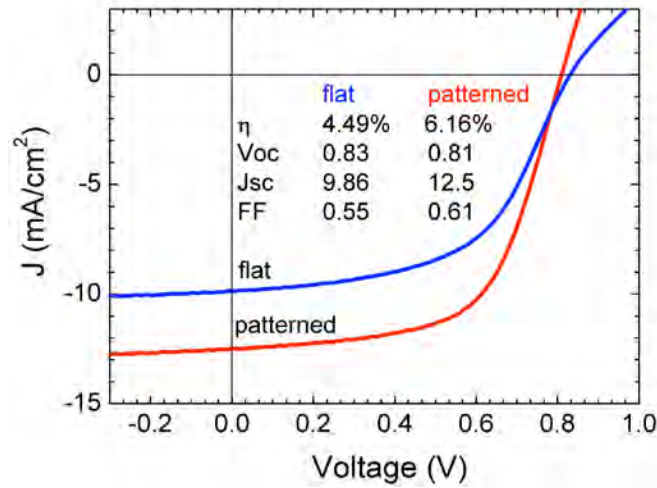
Figure 2. Best JV measurements of the flat reference and patterned n-i-p a-Si:H cells. Inset shows the cell characteristics for each device.

To better understand the nature of the enhancement, we measured spectral response curves for the two sets of devices. Fig. 3(a) shows the spectral response measured under a reverse bias of -1 Volt, which facilitates comparison to optical simulation results by sweeping out all of the generated electrons. At wavelengths shorter than 550 nm there is little difference between the flat and patterned cells. This contrasts with designs for light trapping incorporating metal nanoparticles on top, which often see a decrease in efficiency in this part of the spectrum.[7, 9] At these wavelengths most of the light is absorbed in the 500 nm thick i-a-Si:H layer before interacting with the scattering layer. At wavelengths longer than 600 nm there is a significant difference in photocurrent between the two cells. Integrating over the 600 - 800 nm region a 51 % increase in photocurrent is found.
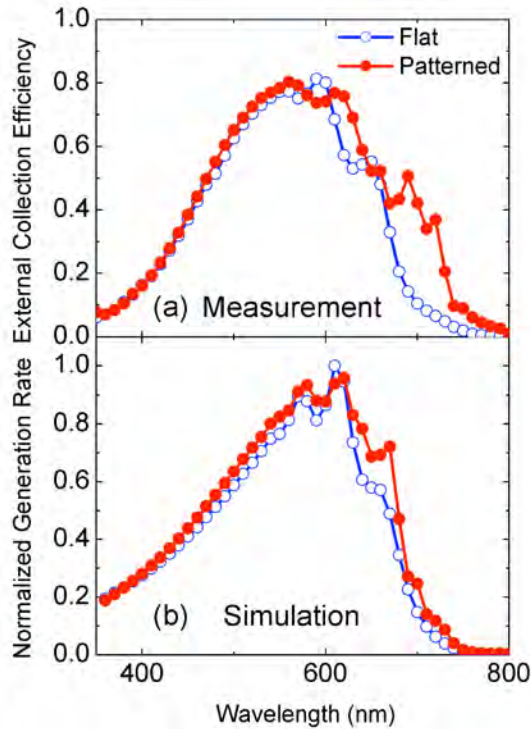
Figure 3. (a) Measured spectral response curves for the flat and patterned cells under bias voltage = -1 V. (b) Simulated normalized electron generation rates for flat and patterned cells.
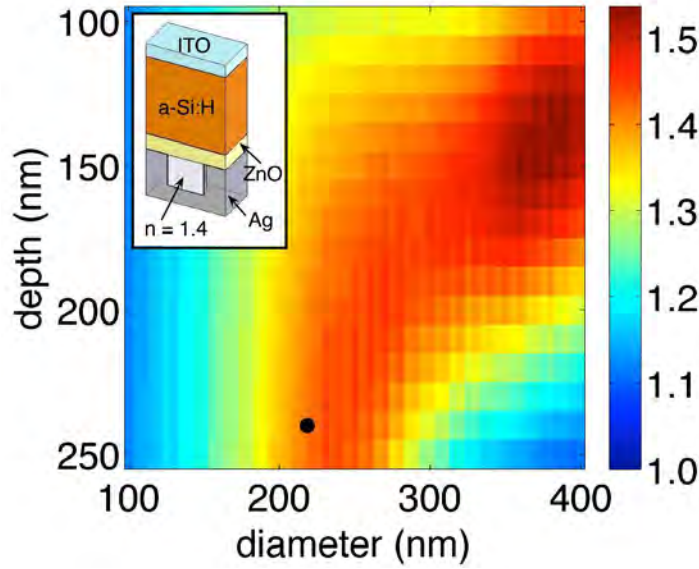
Figure 4. Calculated absorption enhancement for different Ag hole diameters and depths at λ = 660 nm. The solid dot represents the experimental configuration. Inset: geometry of the simulation cell.

We also use electrodynamic modeling to understand the optical absorption and optimize the dimensions of the nanostructured back reflector design. Simulations are done using three-dimensional full field FDTD simulation, using a rendered Si/ZnO:Al/Ag structure that is an approximation to the experimental back reflector geometry as found in SEM (Fig. 3(b)). The thin n and p layers (approximately 20 nm) were neglected, with the entire 500 nm a-Si:H layer taken as intrinsic and optically active. The complex refractive index data for the ZnO:Al, a-Si:H, and ITO layers were based on previously measured optical constants, and for Ag based on a Lorentz-Drude model using literature coefficients[18]. As a simple topological approximation to the experimentally-observed patterned structure, the interior of the hole was modeled with an effective index of n=1.4, between that of ZnO and vacuum, as illustrated in the inset of Fig. 4. The normalized optical generation rate G_{opt} was calculated at each wavelength from the divergence of the Poynting vector according to $G_{opt} = \frac{1}{2\hbar\omega}\Re[\nabla \cdot \mathbf{S}] = \frac{\epsilon''|\mathbf{E}|^2}{2\hbar}$, where ϵ'' is the imaginary part of the complex permittivity, $\mathbf{E}$ is the electric field and G_{opt} was integrated over the simulation volume containing a-Si:H.[19, 20]

Fig. 3(b) illustrates the calculated normalized generation rate over the range of the solar spectrum where a-Si:H is absorbing. As this is exclusively an optical model and does not account for the efficiency of carrier collection, the results are most comparable to a spectral response measurement under reverse bias. The overall spectral shape for both the flat and patterned cells corresponds well to the measured spectral response data, reproducing the predominant spectral peaks and shoulders, indicating that the optical absorption model is reasonable for comparison to the experimental data. A clear enhanced red response is calculated for the patterned cell, though slightly less pronounced than in the experiment. Given that the model correctly predicts the experimental results, it was used to search for an optimized scattering pattern design. Fig. 4 shows the calculated absorption enhancement due to light trapping for a range of hole diameters and depths at λ= 660 nm. The experimental configuration, which is shown by the solid dot, has an enhancement of 42 % compared to the control sample. Increasing the diameter of the hole further to 370 nm and reducing the depth to 140 nm will increase the absorption enhancement in the a-Si:H to 54 %.

7.4 Conclusions

In conclusion, we have shown that including periodic nanostructures on the back contact of an n-i-p a-Si:H solar cell enhances the red response of the device, predominantly through a 26 % increase in J_{sc}. The overall cell efficiency improves from 4.5 % to 6.2 % due to the patterns. We observe that the photocurrent enhancements are largest at wavelengths longer than 600 nm; no decrease in performance is found at shorter wavelengths. The nanopatterns were made using an inexpensive and scalable process that allows for exact control of the feature size, shape, and arrangement. Optical electromagnetic modeling compares well to the experimental data, and predict further optimization of the pattern is possible. This combination of these features makes this a model system for investigating the achievable photovoltaic efficiency improvements due to controlled light management.

References

[1] K. Sato, Y. Gotoh, Y. Wakayama, Y. Hayashi, K. Adachi, and H. Nishimura, *Highly textured SnO$_2$:F TCO films for a-Si solar cells*, Rep. Res. Lab. Asahi Glass Co. Ltd. **42**, 129 (1992)

[2] R.H. Franken, R.L. Stolk, H. Li, C.H.M. van der Werf, J.K. Rath, and R.E.I. Schropp, *Understanding light trapping by light scattering textured back electrodes in thin film n-i-p silicon solar cells*, J. Appl. Phys. **102**, 014503 (2007)

[3] J. Müller, B. Rech, J. Springer, and M. Vanecek, *TCO and light trapping in silicon thin film solar cells*, Sol. Energy **77**, 917 (2004)

[4] F.-J. Haug, T. Söderström, O. Cubero, V. Terrazzoni- Daudrix, and C. Ballif, *Plasmonic absorption in textured silver back reflectors of thin film solar cells*, J .Appl. Phys. **104**, 064509 (2008)

[5] K. Niira, H. Senta, H. Hakuma, M. Komoda, H. Okui, K. Fukui, H. Arimune, and K. Shirasawa, *Thin film poly-Si solar cells using PECVD and cat-CVD with light confinement structure by RIE*, Sol. Energy Mater. Sol. Cells **74**, 247 (2002)

[6] V.E. Ferry, L.A. Sweatlock, D. Pacifici, and H.A. Atwater, *Plasmonic nanostructure design for efficient light coupling into solar cells*, Nano Lett. **8**, 4391 (2008)

[7] F.J. Beck, A. Polman, and K.R. Catchpole, *Tunable light trapping for solar cells using localised surface plasmons*, J. Appl. Phys. **105**, 114310 (2009)

[8] D. Derkacs, S.H. Lim, P. Matheu, W. Mar, and E.T. Yu, *Improved performance of amorphous silicon solar cells via scattering from surface plasmon polaritons in nearby metallic nanoparticles*, Appl. Phys. Lett. **89**, 093103 (2006)

[9] K.R. Catchpole, and A. Polman, *Design principles for particle plasmon enhanced solar cells*, Appl. Phys. Lett. **93**, 191113 (2008)

[10] C. Eisele, C.E. Nebel, and M. Stutzmann, *Periodic light coupler gratings in amorphous thin film solar cells*, J. Appl. Phys. **89**, 7722 (2001)

[11] C. Haase, and H. Stiebig, *Thin-film silicon solar cells with efficient periodic light trapping texture*, Appl. Phys. Lett. **91**, 061116 (2007)

[12] R.E.I. Schropp, J.K. Rath, and H. Li, *Growth mechanism of nanocrystalline silicon at the phase transition and its application in thin film solar cells*, J. Cryst. Growth, **311**, 760 (2009)

[13] K. Nakayama, K. Tanabe, and H.A. Atwater, *Plasmonic nanoparticle enhanced light absorption in GaAs solar cells*, Appl. Phys. Lett. **93**, 121904 (2008)

[14] H. Sai, and M. Kondo, *Effect of self-orderly textured back reflectors on light trapping in thin-film microcrystalline silicon solar cells*, J. Appl. Phys. **105**, 094511 (2009)

[15] M. Verschuuren, and H. van Sprang, *3D photonic structures by sol-gel imprint lithography*, Mater. Res. Soc. Sym. Proc. **1002**, N03 (2007)

[16] T.W. Odom, J.C. Love, D.B. Wolfe, K.E. Paul, and G.M. Whitesides, *Improved pattern transfer in soft lithography using composite stamps*, Langmuir **18**, 5314 (2002)

[17] R.E.I. Schropp, and M. Zeman, *Amorphous and microcrystalline silicon solar cells: modeling, materials, and device technology,* Kluwer Academic Publishers, Boston/Dordrecht/London (1998)

[18] A.D. Rakic, A.B. Djurisic, J.M. Elazar, and M. L. Majewski, *Optical properties of metallic films for vertical-cavity optoelectronic devices*, Appl. Opt. **37**, 5271 (1998)

[19] M.D. Kelzenberg, M.C. Putnam, D.B. Turner-Evans, N.S. Lewis, and H.A. Atwater, *Predicted efficiency of Si wire array solar cells*, Proc. 34th IEEE PVSC (2009)

[20] A.D. Yaghjian, *Internal energy, Q-energy, Poynting's pheorem, and the stress dyadic in dispersive material*, IEEE Trans. Antennas Propag. **55**, 1495 (2007)

Chapter 8

Light trapping in ultrathin a-Si:H solar cells incorporating plasmonic back reflectors

Thin-film solar cells offer the benefits of reduced materials and fabrication costs as well as the advantages of light-weight, flexible devices.[1] For these geometries to exhibit efficient current generation, light trapping schemes are essential to capture the red and near-infrared portion of the solar spectrum.[2,3] Here we demonstrate an ultrathin amorphous Si solar cell that is integrated with plasmonic light trapping structures built into the metallic back contact. The nanopatterns allow the a-Si:H cells to be ultrathin (160 nm), yielding cells with short circuit current densities exceeding that of cells containing randomly textured back contacts due to near-field coupling to waveguide modes of the a-Si:H layer. The nanopatterns are fabricated via an inexpensive and scalable imprinting technique that could be adopted into standard solar cell production. We use amorphous Si as a test platform for photonic nanopattern design, but our approach is broadly applicable to other thin-film solar cell material systems.

8.1 Introduction

Thin film solar cells made from hydrogenated amorphous Si (a-Si:H) are attractive candidates for large-scale photovoltaic applications because Si is highly abundant and can be deposited on flexible substrates using processes that are compatible with roll-to-roll processing.[4] Since minority carrier diffusion lengths are very short in a-Si:H, the cells are often made with a p-i-n or n-i-p structure where the intrinsic absorbing layer is hundreds of nanometers thick and carrier transport is dominated by drift. Ultrathin films, where the thickness of the absorber layer is significantly reduced, would offer further cost and performance advantages. However, the use of thin absorbing layers reduces the short-circuit current density (J_{sc}) due to the decreased optical path length in the semiconductor. Strategies for increasing J_{sc} generally involve the incorporation of surface texturing to scatter incident light into off-normal angles. In thick, wafer-based photovoltaic cells, such surface texturing can lead to a maximum intensity enhancement of $4n^2$ at wavelengths near the band edge, where n is the index of refraction of the semiconductor.[5] For thin and ultrathin film cells where the total device thickness may be less than a wavelength, light trapping has previously been accomplished through randomly roughened back reflectors.[2]

The incorporation of plasmonic metal nanostructures in thin film solar cells is a promising route to enhanced J_{sc} in photovoltaics because the strong light-matter interaction in plasmonic nanostructures enables large scattering cross sections. Many of the photovoltaic designs reported to date that incorporate plasmonic nanostructures focus on the deposition of metal nanoparticles on the front surface of the cell. This can lead to preferential scattering of the incident light into the semiconductor over an increased angular range, thereby enhancing the optical path length.[6-12] While 10-20 fold enhancements of photocurrent have been reported in such solar cells for near-bandedge light, many of these devices suffer from reduced photocurrent from the blue part of the solar spectrum due to destructive interference.[9,12] The advantages of these designs must also be weighed against those achievable with standard or broadband antireflection coatings.[13,14] A second strategy is to build the scattering nanostructures directly into the back contact of the device. In this geometry, the incident blue light is absorbed before interacting with the back contact scatterers, while the red light that is poorly absorbed in a single pass through the cell is strongly scattered (Fig. 1(a)).[15-18] These back scatterers are designed to couple incident light into waveguide modes of the absorbing semiconductor layer, reducing the thickness requirements by redirecting the absorption path into the plane of the solar cell. As opposed to cells with purely grating-based reflectors[19,20], these designs also take advantage of the high scattering cross sections of plasmonic nanostructures. Provided that the structures are well-designed over the scale of a wavelength, the absorption enhancements can exceed those from random surface topography.

8.2 Fabrication of ultra-thin plasmonic back reflector solar cells

A significant challenge to the incorporation of plasmonic nanostructures in photovoltaics is fabrication: the feature sizes are typically 10s to 100s of nanometers, while photovoltaic cell dimensions may be in the m^2 range. Techniques for large area metal nanostructure formation include island annealing[7] or deposition through alumina templates[12], while smaller test devices may use electron-beam lithography or focused ion beam patterning. In this work, we have fabricated cm^2-scale n-i-p a-Si:H solar cells using soft-nanoimprint lithography[21] to incorporate plasmonic nanostructures in the Ag/ZnO back contact of the cell (Fig. 1(b)). This technique offers the capability to form large-area nanopatterns with precise control over both the dimensions and the spacing of the plasmonic scattering structures, and is amenable to roll-to-roll processing.[22] In our case, the patterns are printed into a sol-gel silica layer using substrate

conformal imprint lithography (SCIL)[23], which is then overcoated with Ag and ZnO:Al to form the back contact (Fig. 1(c)). A single substrate containing solar cells with nanopatterns of varying diameter and pitch as well as reference cells with flat back contacts is used to avoid variations between different deposition runs when comparing cell performance. Additionally, multiple copies of each cell design and reference are distributed over the substrate to reduce the possible effects of wafer-scale spatial inhomogeneity. Two different intrinsic layer thicknesses, corresponding to total a-Si:H thicknesses (including the n- and p- doped layers) of 340 nm and 160 nm were deposited on two wafers with identically prepared back contact patterns. Fig. 1d shows a cross section scanning electron microscopy (SEM) image of a fully fabricated nanopatterned cell having an a-Si thickness of 160 nm. The individual layers are clearly resolved. The ultrathin a-Si:H layer is conformal to the nanopatterned contacts, with no cracks or voids observed in the layer that could adversely influence the performance.[24] In addition to the substrates patterned by imprint lithography, a randomly textured substrate of Asahi U-type glass[25], a common photovoltaic substrate with known roughness and topography, was used to fabricate a 160 nm thick a-Si:H cell under the same deposition conditions as the nanopatterned substrate.

Since each successive layer is conformally deposited, the underlying back contact structure for both the patterned and the randomly textured devices is transferred to the top interface of the cell. Figure 2 shows tapping mode atomic-force microscopy (AFM) scans on the indium tin oxide (ITO) top contact for both the imprint-patterned cell (a) and the randomly textured Asahi sample (b). The imprinted substrate AFM scan reveals the underlying 175 nm diameter nanopatterns that are imprinted into the sol-gel glass layer, and transferred to the back contact of the cell at a pitch of 500 nm. In contrast, the randomly textured Asahi glass shows an uncorrelated distribution of height variations.
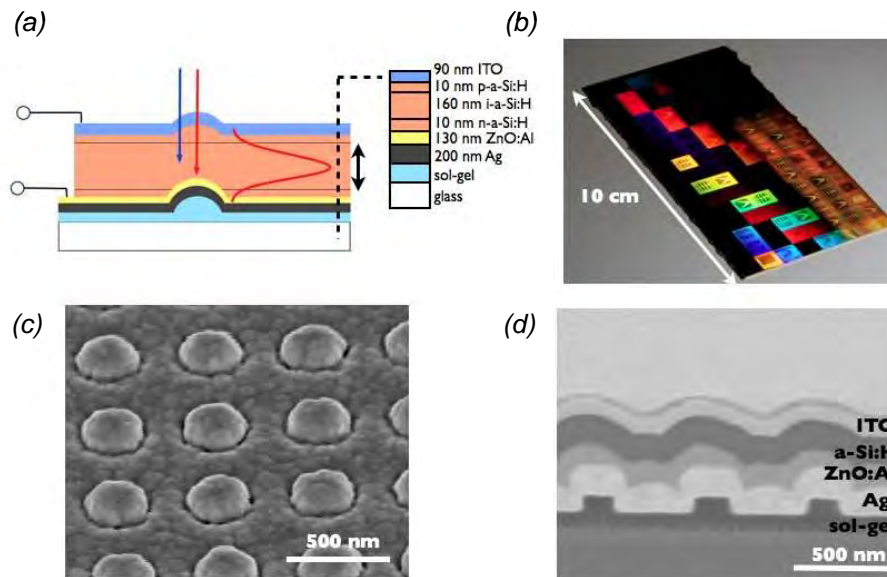
Figure 1. Plasmonic light trapping solar cell design. (a) Schematic cross section of the patterned solar cell. Patterns are made on the rear glass substrate, and there is conformal deposition of all layers over the patterns through the top ITO contact. Incident blue and red arrows indicate that blue light is absorbed before reaching the back contact while red light is scattered into modes of the solar cell. (b) Photograph of finished SCIL imprint patterned solar cell substrate. Each colored square is a separate device, with different particle diameter and pitch. (c) SEM of Ag overcoated patterns showing 290 nm diameter particles with 500 nm pitch (d) SEM image of a cross section of a fabricated cell, made using focused ion beam milling. Note that the ultrathin a-Si:H layer constitutes only a small part of the cell.
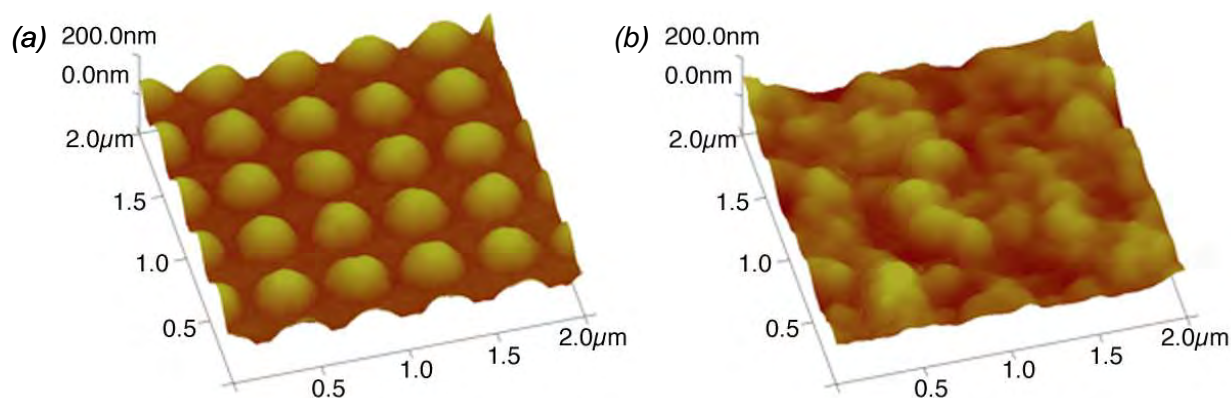
Figure 2. Surface topography of nanopatterned and randomly textured solar cells. Tapping-mode AFM images of the top ITO contacts for two of the cells compared in this study. The underlying Ag/ZnO nanostructure is transferred through each layer conformally, so that both the front and back contacts are structured. (a) Patterned cell with 500 nm pitch, (b) Cell on randomly textured Asahi U-type glass substrate.

8.3 Electo-optical characterization

Figure 3 shows current density/voltage (J-V) measurements taken under 100 mW cm^{-2} AM1.5 illumination for the 340 nm (a) and 160 nm (b) thick cells, all for cells with a plasmonic scatterer diameter of 250 nm. In Fig. 3(a), data for 500 nm and 700 nm pitch are shown together with the flat reference. In Fig. 3(b), data for the randomly textured Asahi glass cells are also shown. For the 340 nm cells, the open circuit voltage (V_{oc}) is in the 840-850 mV range for all devices, indicating that there is no significant difference in semiconductor and contact quality across the substrate. Data taken for several Ag particle diameters (200 nm, 225 nm, 250 nm, 290 nm) all show similar J_{sc}, V_{oc}, and fill factor characteristics, with a slight increase in performance for larger diameter scatterers. Further details are provided in the Supplementary Information. However, a higher J_{sc} is found for cells with a 500 nm pitch than for cells with a 700 nm plasmonic scatterer pitch. For the 500 nm pitch samples, J_{sc} improves by 27 % compared to the flat cell. The highest efficiency recorded among cells with the 340 nm thick a-Si:H layer (η=6.6 %) was found for a plasmonics scatterer pitch of 500 nm and a diameter of 250 nm. For the thinner cells (Fig. 3(b)), V_{oc} is increased in comparison to the thicker cells, to around 880 mV.
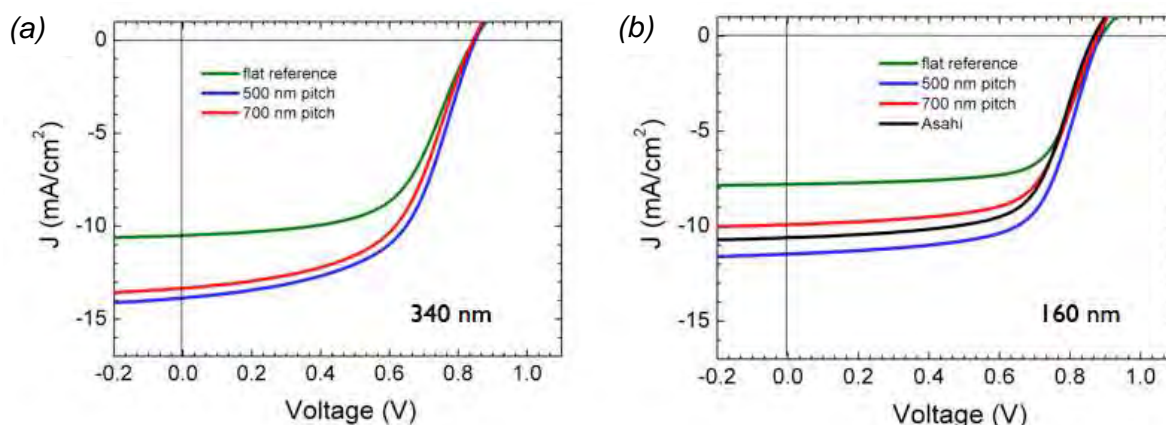
Figure 3. Electrical measurements on plasmonic solar cells. Data are shown for a-Si:H with two different intrinsic layer thicknesses. (a) a-Si:H thickness 340 nm and (b) a-Si:H thickness 160 nm. Curves are shown for square grid patterns of 250 nm diameter plasmonic scatterers at pitches of 500 nm and 700 nm, the flat reference cell, and (in (b)) the randomly textured Asahi cell.

We attribute this improvement to the decreased bulk recombination in thin layers, demonstrating a potentially additional advantage of the use of thin active layers aside from the reduced costs.[26] At the same time, the fill factors have increased to 0.64. The 500 nm pitch, 250 nm diameter samples now show an increase in J_{sc} of 46 % over the 160 nm thick flat cell. The best cell measured again had 250 nm diameter plasmonic scatterers and 500 nm pitch. This cell has an efficiency of 6.6 %, which is similar to the maximum efficiency found for the thick cell. While J_{sc} is lower in the thin cells, the increased V_{oc} and fill factor cause the overall efficiency to remain the same between the two thicknesses. This demonstrates conclusively that plasmonic back reflectors can be used to maintain efficiency while scaling to thinner solar cells.

Remarkably, Fig. 3(b) also shows that J_{sc} for the patterned cell with 500 nm pitch is significantly larger than for the randomly textured cell with Asahi-U type of texture. Because the nanopatterned cells and the randomly textured Asahi sample both have comparable fill factor and V_{oc}, we can exclude a difference in semiconductor quality as an explanation for the improved J_{sc}. We conclude that light trapping in the 500 nm pitch patterned cell is more efficient than in the randomly textured sample.

To further study the nature of the photocurrent enhancement, we measured external quantum efficiency (EQE) spectra, defined as the number of collected charge carriers per incident photon, using a Xenon lamp under light bias corresponding to approximately one sun illumination and 0 V bias. Fig. 4(a) shows the EQE spectra for the same thin cells described in Fig. 3(b). The photocurrent enhancement occurs primarily in the 550 - 800 nm spectral range. While the EQE of both the 500 nm and the 700 nm pitch cells exceeds that of the flat reference cell, there is a pronounced difference between the curves in the wavelength range from 550 nm to 700 nm. The cell on the randomly textured Asahi substrate has a very smooth EQE response, while the patterned devices exhibit peaked features in the EQE curve, of which the peak wavelengths are reproducible for each pitch (see Supplementary Information). The inset of Fig. 4(a) shows EQE spectra of these two cells recorded with higher spectral resolution using a supercontinuum laser source filtered by a grating spectrometer. The complex structure of the 500 nm pitch sample remains clearly visible compared to the smooth EQE spectrum of the randomly textured Asahi sample. Notably, the EQE of the 500 nm pitch cell exceeds that of the randomly textured Asahi sample in the 550 - 650 nm spectral range where there is significant power in the solar spectrum. From 650 nm to 800 nm the features in the spectra of the nanopatterned cell sharpen and alternately exceed and fall below the curve for the randomly textured Asahi cell.

8.4 Electromagnetic simulations of thin film solar cells

We use full-field finite difference electromagnetic simulations to study the optical contribution of the nanostructures, with the cell layer thicknesses and optical constants taken from experimental values. Figure 4(b) shows the calculated carrier generation rate modeled as $G_{opt} = \varepsilon"|\mathbf{E}|^2 / 2\hbar$ normalized by the incident photon flux across the 350 – 800 nm spectral range of photovoltaic activity for these cells. The inset shows a cross-section of the geometry used to describe the two patterned cells, where the nanostructures are taken to be hemispheres and the unit cell is chosen with either 500 nm or 700 nm pitch. The surface structure for the randomly textured Asahi cell was modeled using the AFM data shown in Fig. 2. The optical model accurately reproduces the spectral shape of the curves, including the enhanced absorption of the 500 nm pitch cell relative to the randomly textured cell and the reduced absorption for the 700 nm pitch cell. The enhancement and many of the peaked features are reproduced well in the simulation, and deviations may be due to minor variations in layer thickness, pitch, and optical constants.
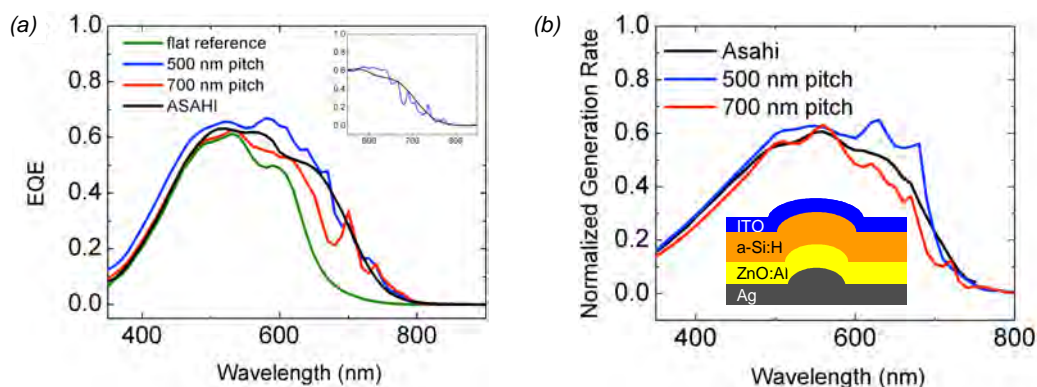
Figure 4. External quantum efficiency spectra of nanopatterned and randomly textured cells from measurement and simulation. (a) Measured EQE spectra for cells of 160 nm thickness, under one sun illumination at 0V bias. The primary enhancement in photocurrent over the flat reference cell occurs from 550 - 800 nm. The 500 nm pitch cell shows higher EQE than the randomly textured Asahi cell. The inset of a shows EQE measurements of these two cells at higher spectral resolution. (b) Electromagnetic simulations of the generation rate spectra for the same set of devices.

The overall spectral correspondence between the electromagnetic simulation and the EQE measurements strongly suggests that the EQE enhancement is due to increased absorption from light trapping.

To further investigate the nature of the light trapping mechanism for the nanopatterned and randomly textured Asahi glass samples we measured EQE spectra as a function of incident angle for the thinner cells. Figure 5 shows intensity maps of these angle-resolved EQE spectra, for angle of incidence between -45° and +45° from the substrate normal and for a range of illumination wavelengths from 550 nm to 850 nm, for the randomly textured Asahi cell (a) and the 500 nm pitch cell (b). The EQE curves at normal incidence were found to agree well with the measurements shown in Fig. 4. Some variation with angle of incidence is expected for all cells due to the angular response of the anti-reflection coating present on the cells. However, while it is evident that the randomly textured Asahi cell has a relatively isotropic spectral response to angle of incidence, the 500 nm pitch cell exhibits more complex behavior. The enhanced EQE for the patterned cell in the 550 - 650 nm range (inset in Fig. 4(a)) is observed, and can be seen to extend to at least +/- 20 degrees. From 650 nm to 800 nm the spectral photocurrent features become sharper, and show a stronger angular dependence. The dispersive features measured in Fig. 5(b) are clear evidence of coupling between light scattered by the grating and the waveguide modes supported by the high-index a-Si:H layer of the solar cell.
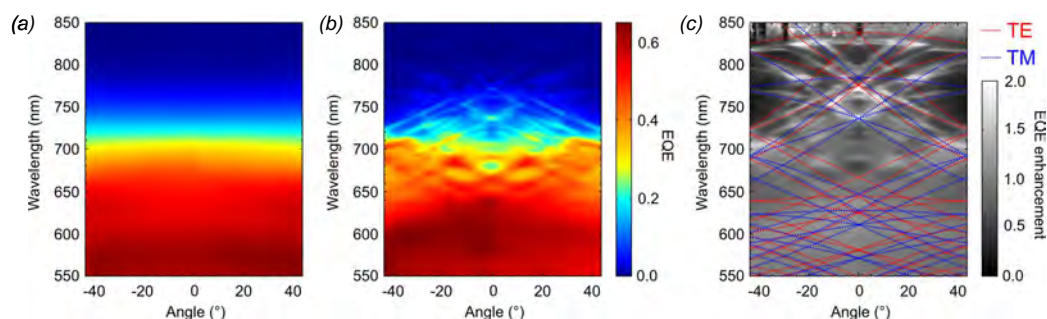
Figure 5. Angle-resolved photocurrent spectroscopy. Measured EQE versus incident wavelength and incident angle for cells with 160 nm a-Si:H thickness. (a) Randomly textured Asahi cell and (b) nanopatterned cell with a pitch of 500 nm. The Asahi cell shows a rather isotropic angular response, while the nanopatterned sample shows clear evidence of grating coupling to waveguide modes. (c) The EQE enhancement for the nanopatterned sample, the ratio of (b) to (a); the calculated folded-zone dispersion diagram of the lowest-order TE and TM modes is superimposed.

We calculated the dispersion curves for the waveguide modes present in a representative planar device with 500 nm periodicity. The calculations were performed using the experimentally determined layer thicknesses and optical constants. In Fig. 5(c), branches corresponding to the TE and TM modes with the highest modal overlap with the a-Si:H are shown, folded back to the angular range of interest by taking diffraction by the two-dimensional periodic structure into account. The curves are superimposed over an intensity map of the relative enhancement of the EQE of the patterned cell compared to the randomly textured Asahi cell. Clearly, the pattern of dispersive bands observed in the EQE measurements agrees well with the calculated waveguide mode dispersion. In particular, the bands of enhanced absorption in the 700 - 850 nm range are well explained by the model, including the crossings at 740 nm and 770 nm. Deviations between measurement and calculation are attributed to small differences in optical constants and the fact that the calculation does not include surface corrugation and associated mode coupling. Additional spectral features observed in the EQE spectra could possibly be associated with absorption due to local field enhancements in the nanostructures. The measurement clearly shows that for these wavelengths, coupling to modes guided by the a-Si:H layer is responsible for increased absorption in the cell. In the spectral range 550 - 650 nm, where the EQE of the patterned cell exceeds that of the randomly textured Asahi substrate, calculations show a high density of modes. The fact that in this region no sharp features are observed in the measurements is due to the large number of modes present, which are strongly broadened because of large absorption of a-Si:H in this spectral region.

We note that as a final important benefit of these plasmonic solar cells, this ultrathin design reduces the well-known Staebler-Wronski degradation effect[27] that has limited the long-term performance of a-Si:H photovoltaics so far. Ultrathin n-i-p devices, with thicknesses such as demonstrated above, possess high internal electric fields, which are known to exhibit no or only minimal light-induced degradation.[4,28,29]

8.5 Conclusions

In summary, we have demonstrated ultrathin a-Si:H solar cells employing light trapping using plasmonic back reflectors. Light scattering from the nanopatterned back contact enhances the photocurrent, while the reduced cell thickness causes an increase in open circuit voltage and the potential for long-term stability. The efficiency of cells with intentionally patterned back contacts can exceed that of randomly textured cells. Future work will focus on further optimization of the nanopattern design. The concepts described here are applicable to any type of thin-film solar cell, including commonly used photovoltaic cells made from materials such as polycrystalline Si, CdTe, and $CuIn_xGa_{1-x}Se_2$.

Methods

The master substrate of nanopatterns was made using electron beam lithography on a Si wafer. A bilayer stamp was molded from the master, consisting of a thin high-modulus poly-di-methyl-siloxane (PDMS) layer holding the nanopatterns and a low-modulus PDMS layer to bond the rubber to a 200 μm thick glass support for in-plane stiffness. The stamp was used to emboss a 100 nm thick layer of silica sol-gel on AF45 glass substrates using substrate conformal imprint lithography (SCIL). The sol-gel layer solidified at room temperature by forming a silica network, while reaction products diffuse into the rubber stamp. After stamp release the sol-gel was post cured at 200 °C. The patterned area was 10 cm by 4 cm, with patterned and flat reference cells tiled in 6 mm x 6 mm sections. The sol-gel patterns together with the Asahi U-type glass were overcoated with Ag and ZnO:Al via sputtering, and 13.56 MHz plasma enhanced

chemical vapor deposition was used to deposit the n-i-p a-Si:H layers. An array of 4 mm × 4 mm squares of ITO was sputtered through a contact mask, and finger contacts were evaporated over the ITO using a second contact mask. The final cell area of each device was 0.13 cm^2. Device characterization was performed using a solar simulator under one sun illumination (AM1.5, 100 mW/cm^2) and EQE measurements were performed using monochromatic light from a halogen lamp with one sun light bias applied. Angle-resolved EQE measurements were performed using a supercontinuum laser source filtered by a grating spectrometer with a passband of ~3 nm and a sample stage providing eucentric rotation about the point of illumination. The illumination was focused to a spot diameter of approximately 500 μm at low numerical aperture.

References

[1]   A. Shah, P. Torres, R. Tscharner, N. Wyrsch, and H. Keppner, *Photovoltaic technology: the case for thin-film solar cells*, Science **285**, 692 (1999)

[2]   R.H. Franken, R.L. Stolk, H. Li, C.H.M. van der Werf, J.K. Rath, and R.E.I. Schropp, *Understanding light trapping by light scattering textured back electrodes in thin film n-i-p-type silicon solar cells*, J. Appl. Phys. **102**, 014503 (2007)

[3]   J. Müller, B. Rech, J. Springer, and M. Vanecek, *TCO and light trapping in silicon thin film solar cells*, Sol. Energy **77**, 917 (2004)

[4]   R.E.I. Schropp, and M. Zeman, *Amorphous and microcrystalline silicon solar cells: modeling, materials, and device technology*, Kluwer Academic Publishers (1998)

[5]   E. Yablonovitch, and G.D. Cody, *Intensity enhancement in textured optical sheets for solar-cells*, IEEE Trans. on Electron Devices **29**, 300 (1982)

[6]   H.R. Stuart, and D.G. Hall, *Island size effects in nanoparticle-enhanced photodetectors*, Appl. Phys. Lett. **73**, 3815 (1998)

[7]   S. Pillai, K.R. Catchpole, T. Trupke, and M.A. Green, *Surface plasmon enhanced silicon solar cells*, J. Appl. Phys. **101**, 093105 (2007)

[8]   K.R. Catchpole, and A. Polman, *Design principles for particle plasmon enhanced solar cells*, Appl. Phys. Lett. **93**, 191113 (2008)

[9]   F.J. Beck, A. Polman, and K.R. Catchpole, *Tunable light trapping for solar cells using localized surface plasmons*, J. Appl. Phys. **105**, 114310 (2009)

[10]   D. Derkacs, S.H. Lim, P. Matheu, W. Mar, and E.T. Yu, *Improved performance of amorphous silicon solar cells via scattering from surface plasmon polaritons in nearby metallic nanoparticles*, Appl. Phys. Lett. **89**, 093103 (2006)

[11]   P. Matheu, S.H. Lim, D. Derkacs, C. McPheeters, and E.T. Yu, *Metal and dielectric nanoparticle scattering for improved optical absorption in photovoltaic devices*, Appl. Phys. Lett. **93**, 113108 (2008)

[12]   K. Nakayama, K. Tanabe, and H.A. Atwater, *Plasmonic nanoparticle enhanced light absorption in GaAs solar cells*, Appl. Phys. Lett. **93**, 121904 (2008)

[13]   Y. Kanamori, M. Sasaki, and K. Hane, *Broadband antireflection gratings fabricated upon silicon substrates*, Opt. Lett. **24**, 1422 (1999)

[14]   Y.-F. Huang, S. Chattopadhyay, Y.-J. Jen, C.-Y. Peng, T.-A. Liu, Y.-K. Hsu, C.-L. Pan, H.-C. Lo, C.H. Hsu, Y.-H. Chang, C.-S. Lee, K.-H. Chen, and L.C. Chen, *Improved broadband and quasi-omnidirectional anti-reflection properties with biomimetic silicon nanostructures*, Nature Nanotechnology **2**, 770 (2007)

[15]   V.E. Ferry, L.A. Sweatlock, D. Pacifici, and H.A. Atwater, *Plasmonic nanostructure design for efficient light coupling into solar cells*, Nano Lett. **8**, 4391 (2008)

[16]   P.N. Saeta, V.E. Ferry, D. Pacifici, J.N. Munday, and H.A. Atwater, *How much can guided modes enhance absorption in thin solar cells?*, Opt. Express **17**, 20975 (2009)

[17] J. Zhu, C.-M. Hsu, Z. Yu, S. Fan, and Y. Cui, *Nanodome solar cells with efficient light management and self-cleaning*, Nano Lett., DOI: 10.1021/nl9034237 (2009)

[18] O. Isabella, A. Campa, M.C.R. Heijna, W. Soppa, R. van Ervan, R.H. Franken, H. Borg, and M. Zeman, *Diffraction gratings for light trapping in thin-film silicon solar cells*, 23rd European Photovoltaic Solar Energy Conference **2025,** (2008)

[19] C. Eisele, C.E. Nebel, and M. Stutzmann, *Periodic light coupler gratings in amorphous thin film solar cells*, J. Appl. Phys. **89**, 7722 (2001)

[20] C. Haase, and H. Stiebig, *Thin-film silicon solar cells with efficient periodic light trapping texture*, Appl. Phys. Lett. **91**, 061116 (2007)

[21] V.E. Ferry, M.A. Verschuuren, H.B.T. Li, R.E.I. Schropp, H.A. Atwater, and A. Polman, *Improved red-response in thin film a-Si:H solar cells with soft-imprinted plasmonic back reflectors*, Appl. Phys. Lett. **95**, 183503 (2009)

[22] C. Stuart, and Y. Chen, *Roll in and roll out: a path to high-throughput nanoimprint lithography*, ACS Nano **3**, 2062 (2009)

[23] M. Verschuuren, and H. van Sprang, *3D photonic structures by sol-gel imprint lithography*, Mater. Res. Soc. Sym. Proc. **1002**, N03 (2007)

[24] H.B.T Li, C.H.M. van der Werf, J.K. Rath, and R.E.I. Schropp, *Hot wire CVD of nanocrystalline silicon solar cells on rough substrates*, Thin Solid Films **517**, 3476 (2009)

[25] K. Sato, Y. Gotoh, Y. Wakayama, Y. Hayashi, K. Adachi, and H. Nishimura, *Highly textured SnO$_2$:F TCO films for a-Si solar cells*, Rep. Res. Lab. Asahi Glass Co. Ltd. **42**, 129 (1992)

[26] P. Campbell, and M.A. Green, *The limiting efficiency of silicon solar-cells under concentrated sunlight*, IEEE Trans. Electron Devices **2**, 234 (1986)

[27] D.L. Staebler, and C.R. Wronski, *Reversible conductivity changes in discharge-produced amorphous silicon*, Appl. Phys. Lett. **31**, 292 (1977)

[28] A.V. Shah, H. Schade, M. Vanecek, J. Meier, E. Vallat-Sauvain, N. Wyrsch, U. Kroll, C. Droz, and J. Bailat, *Thin-film silicon solar cell technology*, Prog. Photovolt: Res. Appl. **12**, 113 (2004)

[29] P. Lechner, W. Frammelsberger, W. Psyk, R. Geyer, H. Maurus, D. Lundszien, H. Wagner, and B. Eichhorn, *Status of performance of thin film silicon solar cells and modules*, 23rd European Photovoltaic Solar Energy Conference, **2025** (2008)

8.6 Supplementary information

1. *J-V Measurements*

Here we present additional details of the J-V measurements for the two thicknesses of cells measured. The nanopatterned substrate contained cells with 4 diameters of scatterers and two pitches. As originally patterned in the glass, the diameters were 100 nm, 125 nm, 150 nm, and 175 nm, and after Ag coating these increased to approximately 200 nm, 225 nm, 250 nm, and 290 nm. The flat reference cells were built into the same substrate. The patterns were distributed across the substrate to minimize the effects of deposition inhomogeneity. The J_{sc} measurements were taken from the integrated EQE measurements, which is often a slight underestimate of the real J_{sc}.

For the cells of 340 nm a-Si:H thickness, V_{oc} is comparable across all the cells measured, and in the 840 – 850 mV range with standard deviations from 5-10 mV. The fill factors are comparable across all measured cells as well, in the 0.55-0.56 range with standard deviations of 0.01. The major difference between the patterns is in J_{sc}, as expected for cells with varying degrees of light trapping. There is a comparatively small change on average between particle diameters, and a slightly more substantial effect from pitch.

Thickness (nm)	Diameter (nm)	Pitch (nm)	V_{oc} (V)	FF	J_{sc} (mA/cm^2)	Eff.(%)
340	flat		0.844 (0.004)	0.58 (0.01)	10.5	5.14
340	200	700	0.847 (0.005)	0.56 (0.01)	12.78	6.06
340	225	700	0.846 (0.009)	0.56 (0.01)	12.8	6.06
340	250	700	0.843 (0.01)	0.55 (0.002)	13.34	6.19
340	200	500	0.850 (0.007)	0.56 (0.007)	13.13	6.25
340	225	500	0.848 (0.005)	0.56 (0.010)	13.23	6.28
340	250	500	0.848 (0.007)	0.55 (0.01)	13.85	6.58
340	290	500	0.846 (0.01)	0.55 (0.01)	13.52	6.29

Table S1. Summary of J-V measurements for cells with 340 nm thick a-Si:H. Standard deviations are shown in parentheses beside the average values. The J_{sc} values were determined from the integrated spectral response measurements.

Thickness (nm)	Diameter (nm)	Pitch (nm)	V_{oc} (V)	FF	J_{sc} (mA/cm^2)	Eff.(%)
160	flat		0.890 (0.01)	0.68 (0.01)	7.86	4.76
160	200	700	0.867 (0.028)	0.65 (0.008)	10.2	5.75
160	225	700	0.884 (0.028)	0.66 (0.011)	10.57	6.17
160	250	700	0.882 (0.0024)	0.65 (0.010)	10.2	5.85
160	290	700	0.882 (0.028)	0.65 (0.027)	10.2	5.85
160	200	500	0.885 (0.007)	0.65 (0.008)	10.2	5.85
160	225	500	0.877 (0.019)	0.63 (0.034)	11.8	6.52
160	250	500	0.883 (0.001)	0.64 (0.015)	11.6	6.56
160	290	500	0.886 (0.001)	0.66 (0.004)	11.2	6.55
160	Asahi		0.869 (0.008)	0.64 (0.008)	10.8	6.00

Table S2. Summary of J-V measurements for cells with 160 nm thick a-Si:H. Standard deviations are shown below the average values. The J_{sc} values were determined from the integrated spectral response measurements.
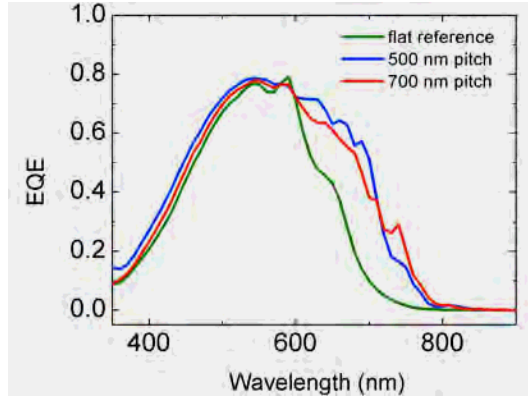
Figure S1. External quantum efficiency spectra of cells with 340 nm thick a-Si:H.

A similar effect is seen for the thinner cells of 160 nm thickness. V_{oc} is again comparable across the cells measured, in the 880 – 890 mV range, with standard deviations around 20 mV. These V_{oc}'s are higher than those found in the thicker cells. The fill factors are higher as well, around 0.65 with 0.01 standard deviation. The difference between the diameters is very slight, but there is a more substantial difference between the two pitches in J_{sc}. The Asahi cell has an intermediate J_{sc}, with comparable (or slightly lower) V_{oc} and fill factor.

2. *EQE Measurements*

For the thicker cells (Fig. S1), the increase in photocurrent occurs primarily from 600 - 800 nm spectral range. From 350 nm to 600 nm there is little difference between the curves, as most of this light is absorbed directly in the cell before reaching the back contact. This also indicates that the carrier collection is not hindered by the nanopatterned back contact. Since these cells are thicker, the onset of differences between the spectra begins around 600 nm, rather than at 550 nm as shown in Fig. 3 in the main text.
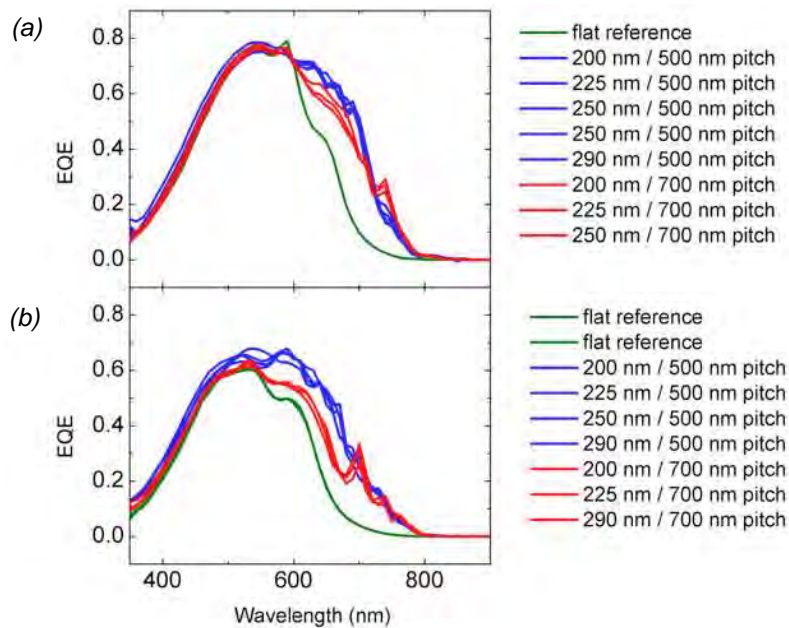
Figure S2. EQE spectra for all patterns measured. Measurements for the 340 nm thick a-Si:H cells are shown in (a), and the 160 nm thick cells are shown in (b). The first number in the legend is the diameter of the Ag hemisphere, and the second the pitch of the particles. The shape and magnitude of the spectra show very little change with diameter, but the features on the red side of the spectra are repeatable within each set of pitches.

The small features observed on the red side of the spectra are observed in all of the cells of each pitch, and are independent of particle diameter. Overall, from 600 - 800 nm the EQE increases by 87 % in the 500 nm pitch cell compared to the flat reference cell, not accounting for differences in the solar spectrum power over this range. Comparing the two patterned cells, the 500 nm pitch cell has the highest EQE from 600 nm to 700 nm, while the 700 nm pitch cells have higher EQE in the 700 - 800 nm range. Since the power in the solar spectrum is higher in the spectral range between 600 and 700 nm this will produce a larger J_{sc} for the 500 nm pitch sample, as observed in Fig. 3.

For both sets of cells, the features in the EQE spectra are repeatable within each pitch. Fig. S2 shows EQE measurements for cells of each diameter and pitch, as well as the flat reference cell from each. There are slight differences with diameter, but the differences are much smaller than the change in pitch. All of the cells with nanopatterns of 500 nm pitch substantially exceed the cells with nanopatterns of 700 nm pitch, and of the flat reference cells.

To check for differences in the reference cells, several EQE measurements were made for cells at various locations over the substrate, shown in Fig. S3. The randomly textured Asahi substrate was of the same length as the nanopatterned substrate, and positioned next to the nanopatterned substrate during a-Si:H deposition. The clear reproducibility of the reference cells indicates that thickness variation across the substrate is not the source of the observed J_{sc} differences.

3. *FDTD details*

Finite-difference time domain simulations (FDTD) were performed using commercially available software (Lumerical). The layer thicknesses were taken from cell cross sections (such as Fig. 1d). The optical constants of the ITO and ZnO:Al were taken as 2.08 + 0.004i and 1.93 + 0.004i, respectively, with slight dispersion measured using ellipsometry. The optical data for a-Si:H was taken from measured values. Ag was modeled using a Lorentz-Drude model. The simulation geometry for the randomly textured cells was taken from measured AFM data, and used to construct the surface.
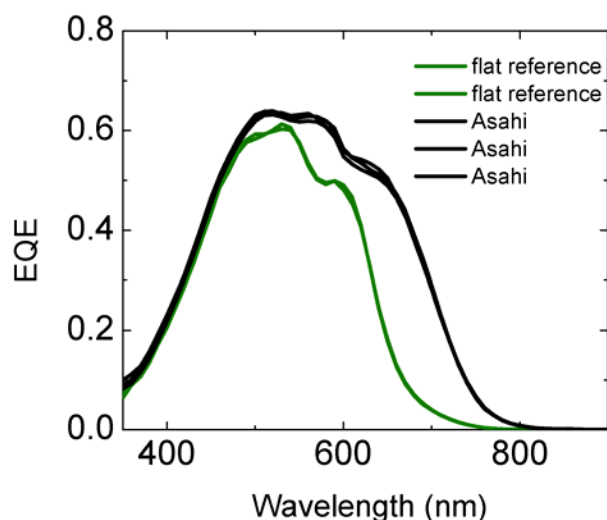
Figure S3. EQE spectra for flat and randomly textured Asahi reference cells of 160 nm a-Si:H thickness. EQE measurements for a number of each type of reference cell taken at various points across the substrate.

Summary

Nanotechnology focuses on the fabrication, characterization and modeling of structures and processes on length scales below 100 nm and is used in almost every scientific discipline. Conventional nanofabrication techniques such as e-beam lithography or focused ion beam milling are routinely used in research experiments. However, they are not suited for fabrication of large-area nanopatterns at low cost. Nanoimprinting may be developed as a versatile inexpensive technique for fabricating nanostructures in which a master pattern is replicated via a stamping process using rigid stamps. However, existing nanoimprint methods which use rigid stamps cannot print large areas.

In this thesis we present Substrate Conformal Imprint Lithography (SCIL) as a novel wafer-scale nanoimprint method with nanoscale resolution which combines the resolution and accuracy of rigid stamps with the flexibility of soft stamp methods. We characterize the SCIL technique in detail and apply it in nanophotonics, the study of the interaction and control of light with dielectric, semiconductor and metal structures which are comparable in size of smaller than the vacuum wavelength of light.

Chapter 1 describes existing nanoimprint methods. It discusses the limitations of rigid stamps such as sensitivity to particle contaminations and substrate bow and the limits in resolution and accuracy for soft stamps. Substrate Conformal Imprint Lithography (SCIL) is introduced which combines the advantages of rigid and soft stamps.

Chapter 2 describes the SCIL soft-nanoimprint process in detail. We introduce a novel silica sol-gel imprint resist and study the sol-gel chemistry for optimal imprint performance. The development of a new soft rubber stamp material is described which enables sub-10 nm resolution in imprinted sol-gel features. We demonstrate that SCIL replicated grating patterns show an average pitch variation over an 25×25 mm area that is less than 0.1 nm. We demonstrate sub–50 nm overlay alignment of two layers imprinted using SCIL.

Chapter 3 demonstrates the versatility of the SCIL soft-nanoimprint method, such as nano patterns with a 30 nm pitch and imprinted single features with an aspect ratio of as high as 5. Very low-aspect ratio features (1/640) with 2 nm variation in topology are also demonstrated. We show that imprinted sol-gel patterns can be transferred into underlying materials while maintaining sub-10 nm resolution. We demonstrate homogeneously imprinted patterns over 150 mm diameter wafers and demonstrate pattern tone inversion on this scale. Two methods are demonstrated to pattern noble metals in particle arrays and sub-wavelength hole arrays. SCIL is applied on non-continuous substrates to produce photonic crystal InGaN LEDs which exhibit a strong modification of the emission pattern.

Chapter 4 demonstrates a route towards 3D woodpile type photonic crystals. A process is developed in which directly imprinted silica gratings are subsequently planarized with a polymer using a surface energy driven process. Using this methods we stack multiple grating layers and show a four-layer woodpile type structure with 70 nm features on a 240 nm pitch which is temperature stable up to 1000 °C.

Chapter 5 treats single-mode polarization-stabilized Vertical Cavity Surface Emitting Lasers (VCSELs) covered with imprinted gratings. We compare the SCIL nanoimprint process to e-beam lithography by comparing the electro-optical performance of polarization-stable VCELs with sub-micron gratings that are produced by both techniques. The lasers produced by SCIL exhibit equal performance as devices produced by e-beam lithography which shows that our imprint process has the same high fidelity as conventional e-beam lithography. We also prepare VCSELs with sub-wavelength gratings that cannot be made by e-beam lithography and thereby increase the laser efficiency by 29 % compared to conventional sub-micron diffractive gratings.

Chapter 6 demonstrates a novel fabrication route to large-area nano hole arrays, which exhibit extraordinary optical transmission attributed to the coupling of surface plasmon polaritions. The confinement of light to the metal surface in and around the holes makes hole arrays interesting as angle independent color filters and for sensor applications. We show that as the dielectric surrounding of a hole array becomes more symmetric, the surface plasmon mediated transmission increases and broadens.

Chapter 7 studies the improved red light absorption in thin-film hydrogenated amorphous silicon (a-Si:H) solar cells with plasmonic back mirrors. Thin film a-Si:H solar cells are made on SCIL structured silver mirrors and smooth silver mirrors for reference. Patterning increases the energy conversion efficiency to 6.2 %, an increase of 26 % compared to smooth reference cells. This increase is due to an enhanced absorption in the 600-800 nm wavelength range. The patterned mirror diffracts non-absorbed light into off normal angles, thereby increasing the optical path length and carrier generation rate.

Chapter 8 studies the performance of ultra thin silicon solar cells. We use SCIL to pattern substrates which a large variety of nano patterns on which thin film a-Si:H solar cells are processed with a thickness of 160 and 340 nm. A 160 nm thick silicon cell is also made on randomly textured glass. The best patterned cells with 160 nm thick silicon exhibit an energy conversion efficiency of 6.6 %, equal to that of the best thicker cells and 37.8% better than flat cells. Crucially, some regular patterns exhibited improved efficiency over cells made on randomly textured glass, which we attribute to coupling of back reflected light to waveguide modes in the silicon.

Overall, this thesis demonstrates the top down fabrication of large-area nanoscale patterns by Substrate Conformal Imprint Lithography (SCIL) that are used to demonstrate lasers, LEDs, plasmonic hole arrays and solar cells with improved performance.

Samenvatting

Nanotechnologie bestudeert de fabricage, karakterisatie en het modelleren van structuren op lengteschalen kleiner dan 100 nm en wordt toegepast in bijna elke wetenschappelijke discipline. In het nanotechnologieonderzoek worden structuren met afmetingen op de nanoschaal gemaakt met behulp van technieken zoals elektronenbundellithografie en ionenbundelsputteren. Helaas zijn deze technieken niet geschikt om tegen lage kosten structuren met afmetingen op de nanoschaal te patroneren op grote oppervlakken. Nanoimprintlithografie is een techniek die in potentie grote oppervlakken kan patroneren met nanometerresolutie tegen lage kosten. Deze techniek is een replicatieproces en maakt gebruik van een stempel om patronen met nanometerresolutie aan te brengen op substraten. Tot op heden gebruikt deze methode echter rigide stempels die geen grote oppervlakken kunnen patroneren.

In dit proefschrift presenteren wij Substraat-Conforme Imprint Lithografie (SCIL), een nieuwe imprintmethode die grote oppervlakken kan patroneren met aan de ene kant de resolutie van rigide stempels en aan de andere kant de flexibiliteit van zachte stempels. We bestuderen de SCIL-methode en passen deze toe in het vakgebied van de nanofotonica, de studie van de interactie van licht met diëlektrische-, halfgeleider- en metaalstructuren die afmetingen hebben kleiner dan de golflengte van het licht.

Hoofdstuk 1 behandelt bestaande nanoimprinttechnieken. We behandelen de voor- en nadelen van rigide stempels, zoals gevoeligheid voor deeltjes en substraat non-uniformiteit en beschrijven de resolutielimiet van zachte stempels. Vervolgens introduceren we SCIL, die de voordelen van harde en zachte stempels combineert.

Hoofdstuk 2 behandelt de SCIL-techniek in detail. We introduceren een nieuwe anorganische imprintlak die gebaseerd is op sol-gel chemie. We ontwikkelen een harder siliconenrubber stempelmateriaal dat het mogelijk maakt om sub-10 nm structuren te repliceren in sol-gel lagen. Hiermee demonstreren we dat een met SCIL gerepliceerde tralie een gemiddelde afwijking in de steek heeft die minder is dan 0.1 nm over een oppervlak van 25×25 mm. Daarnaast demonstreren we dat met SCIL twee opeenvolgende lagen ten opzichte van elkaar uitgelijnd kunnen worden met een resolutie die beter is dan 50 nm.

Hoofdstuk 3 demonstreert de veelzijdigheid van SCIL. Zo laten we gerepliceerde patronen zien op een steek van 30 nm en gerepliceerde patronen met een hoge aspectverhouding van 5. Het repliceren van extreem lage aspectverhoudingen (1/640) is ook mogelijk en dit laten we zien door tralies te repliceren die geplanariseerd zijn binnen 2 nm. Verder gebruiken we gerepliceerde sol-gel patronen als etsmasker en laten we zien dat de sub-10 nm resolutie behouden blijft nadat het sol-gel patroon doorgeëtst is in een onderliggende laag. Substraten met een diameter van 150 mm worden homogeen gepatroneerd en demonstreren de inversie van de patroontoon op deze schaal. Daarnaast worden twee methoden geïntroduceerd om edele metalen te patroneren en deze worden gedemonstreerd door roosters van nano-gaten en nano-deeltjes in metaal te fabriceren. De SCIL-techniek maakt het mogelijk om niet-continue substraten te patroneren en op deze manier maken we op InGaN gebaseerde fotonisch kristal LEDs die een sterk gemodificeerd emissiepatroon vertonen.

Hoofdstuk 4 demonstreert een relatief eenvoudige route om driedimensionale "woodpile type" fotonische kristallen te maken. Het proces gebruikt SCIL om siliciumoxide sol-gel tralies te patroneren. Deze tralies worden vervolgens geplaniseerd met een polymeer door middel van een proces dat gedreven wordt door oppervlakte-energie. Door het stapelen van de tralies bouwen we een woodpile type structuur bestaande uit vier lagen met een traliesteek van 240 nm en lijnbreedtes van 70 nm. Deze structuur is thermisch stabiel tot 1000 °C.

Hoofdstuk 5 onderzoekt polarisatie-gestabiliseerde lasers met een verticale trilholte en goed gedefinieerde ruimtelijke en temporele coherentie. De polarisatiestabilisatie wordt verkregen door een tralie te patroneren in één van de laserspiegels. De periode van de tralie is 550 nm en de golflengte van het laserlicht is 850 nm. Het elektro-optisch gedrag van lasers, waarvan de tralies zijn gepatroneerd door middel van elektronenbundel lithografie en SCIL, wordt vergeleken. De lasers die gepatroneerd zijn met SCIL hebben identieke prestaties als lasers die met elektronenbundellithografie zijn gepatroneerd. Door gebruik te maken van SCIL is het mogelijk om lasers te fabriceren met tralies die een periode hebben die kleiner is dan de diffractielimiet en welke in de praktijk niet met elektronenbundellithografie gefabriceerd kunnen worden. Deze lasers hebben een 29 % hogere efficiency dan lasers met conventionele tralies die wel diffractie vertonen.

Hoofdstuk 6 beschrijft een nieuwe fabricageroute om op grote oppervlakken edele metalen te patroneren met een rooster van gaatjes die een diameter hebben die kleiner is dan de golflengte van het licht. Deze structuren ondersteunen oppervlakteplasmonpolaritonen, elektromagnetische oppervlaktegolven die gekoppeld zijn aan de geleidingselektronen van het metaal. Door de koppeling van licht naar plasmonen wordt de transmissie door de gaten sterk verhoogd. De concentratie van licht aan het metaaloppervlak maakt deze roosters interessant om toe te passen in hoekonafhankelijke kleurenfilters en sensoren. We laten zien dat, wanneer de diëlektrische omgeving van de roosters meer symmetrisch wordt, de transmissie toeneemt en verbreedt.

Hoofdstuk 7 bestudeert de verbeterde absorptie van rood licht in waterstof bevattende dunne film amorf-silicium (a-Si:H) zonnecellen met plasmonische reflectoren. De a-Si:H zonnecellen worden gedeponeerd op met SCIL gestructureerde zilveren reflectoren en ter controle op vlakke reflectoren. De gepatroneerde cellen hebben een energie conversierendement van 6.2 %, wat een verbetering is van 26 % ten opzichte van de referentiecellen met vlakke reflectoren. Deze toename wordt veroorzaakt door een toegenomen absorptie van licht met een golflengte tussen de 600 nm en 800 nm. In de gepatroneerde cel reflecteert het niet-geabsorbeerde licht in diffractieordes die onder een hoek staan met de normaal, waardoor de optische padlengte vergroot wordt.

Hoofdstuk 8 bestudeert de efficiency van ultradunne waterstof bevattende amorf-silicium zonnecellen. Met SCIL worden substraten gepatroneerd met verschillende patronen in een zilveren reflector. Hierop worden a-Si:H lagen gedeponeerd met een dikte van 160 en 340 nm. Ook wordt er een 160 nm dikke a-Si:H laag gedeponeerd op een substraat met een willekeurig patroon in de reflector. De beste gepatroneerde zonnecellen met een dikte van 160 nm hebben een energie conversierendement van 6.6 %, wat gelijk is aan de prestatie van de beste dikkere cellen, en 37.8 % hoger dan de dunne vlakke referentiecellen met een rendement van 4.8 %. Cruciaal hierbij is dat sommige gepatroneerde cellen een hoger rendement hebben dan cellen die op de willekeurige patronen zijn gedeponeerd. Deze verbetering schrijven we toe aan gereflecteerd licht in diffractieordes dat koppelt aan lichtgeleidingmodes in de siliciumlaag.

Samenvattend, demonstreert dit proefschrift de gecontroleerde fabricage van structuren op een nanoschaal over grote oppervlakken met behulp van Substraat-Conforme Imprint Lithografie (SCIL) die gebruikt worden om de prestatie van lasers, LEDs, plasmonische gatenroosters en zonnecellen te verbeteren.

Acknowledgements

About the author

Marc Verschuuren was born on September 17, 1977 in Tilburg, The Netherlands. He obtained his VWO (secondary education) at the "Mill-Hill College" in Goirle in 1997. Marc went on to study chemical engineering at the Fontys Hogescholen in Eindhoven. In 1999 he performed a 5 month internship at TNO Science and Industry in Eindhoven on the topic of "dual-cure" UV-curable hard coatings. During this time he built an infrastructure for in-situ study of the curing behavior of these coatings using Fourier transform infrared spectroscopy. In 2000 he performed a five month internship at the Yscor steel factory located in Vanderbijlpark, South-Africa. During this period he studied coal crushing efficiency and the extraction efficiency of the coke residue distillation plant. Marc concluded his study with an internship at the Centrum Vezelversterkte Kunststoffen at the Fontys Hogescholen, on the subject of vacuum foil injection molding of carbon fiber composites for application in sailing yachts. In 2002 he received his Bachelor of Science degree. From October 2001 Marc is employed at Philips Research in Eindhoven, presently as research scientist in the Photonic Materials & Devices group. During this time he worked on a diversity of subjects including, printable active matrix LCD, low friction and decorative iron soles sol-gel coatings, ceramic phosphors for LED applications, photonic crystal LEDs and Substrate Conformal Imprint Lithography. In these projects the common subjects were micro- and nano-patterning (leading to SCIL), surface chemistry and the optical behavior of materials and devices. In 2006 he received the title "distinguished employee of the year" for the technology transfer and commercialization of SCIL. At present he is project leader of the SCIL research project which aims to develop and commercialize the SCIL technology and applications.

PHILIPS   FOM Institute **AMOLF**

Affiliations.

Dr. H.A. van Sprang
Philips Research
Photonic Materials & Devices
High Tech Campus 4, 5656 AE, Eindhoven The Netherlands.

Prof. Dr. A. Polman
Center for Nanophotonics
FOM-institute AMOLF
Science Park 104, 1098 XG, Amsterdam, The Netherlands